Synthesis, Characterization, Transport and Electronic Structure Studies of Transition Metal Dichalcogenides

Corrected Copy

Thesis submitted for the degree of

Doctor of Philosophy (Science)

in

Physics (Experimental)

by

Indrani Kar

Department of Physics

University of Calcutta

2022

"It doesn't matter how beautiful your theory is, it doesn't matter how smart you are. If it doesn't agree with experiment, it's wrong."

— Richard Phillips Feynman

Dedicated to Maa and Baba...

List of Publications

1. Metal-chalcogen bond-length induced electronic phase transition from semiconductor to topological semimetal in ZrX_2 (X = Se and Te); **Indrani Kar**, Joydeep Chatterjee, Luminita Harnagea, Y. Kushnirenko, A. V. Fedorov, Deepika Shrivastava, B. Büchner, P. Mahadevan, and S. Thirupathaiah; *Phys. Rev. B* **101**, 165122 (2020).

2. Experimental evidence of stable $2H$ phase on the surface of layered $1T'$-$TaTe_2$; **Indrani Kar**, Kapildeb Dolui, Luminita Harnagea, Y. Kushnirenko, G. Shipunov, N. C. Plumb, M. Shi, B. Büchner, and S. Thirupathaiah; *J. Phys. Chem. C* **125**, 1150 (2021).

3. Observation of weak Kondo effect and angle dependent magnetoresistance in layered antiferromagnetic V_5S_8 single crystal; **Indrani Kar**, Sayan Routh, Soumya Ghorai, Shubham Purwar, and Setti Thirupathaiah; *Solid State Communications* **369**, 115209 (2023).

4. Observation of surface Dirac state in transition metal dichalcogenide $NiTe_2$ using ARPES; **Indrani Kar**, Luminita Harnagea, Soma Banik, Surjeet Singh, and Setti Thirupathaiah; *AIP Conference Proceedings* **2265**, 030361 (2020).

5. Crossover from linear to quadratic magnetoresistance in $NiTe_2$; **Indrani Kar** and Setti Thirupathaiah; *Mater. Today: Proc.* **65**, 70-73 (2022).

6. Observation of Kondo effect in transition metal dichalcogenides VX_2 (X=Se & Te) due to low-temperature weak ferromagnetism; **Indrani Kar**, Susanta Ghosh, Shuvankar Gupta, Sudip Chakraborty, and Setti Thirupathaiah (under review).

Acknowledgments

During my journey of education from the beginning, I met so many people who taught me the importance of education, inspired me to do research and gave continuous support. I would like to take this opportunity to acknowledge those upholders without whom I could not see this memorable day.

At first, I would like to express my heartiest gratitude to my supervisor, Dr. Thirupathaiah Setti, for his excellent guidance and continuous supervision on my research work for last five years. His valuable suggestions and advice are beneficial for research as well as for my future career and life. I am fortunate enough to be the first student of such a nice person who helped me in every difficulties throughout my PhD journey.

Now, I would also like to offer thanks to my PhD coursework teachers Dr. Atindra Nath Pal, Dr. Manoranjan Kumar, Late Prof. Sugata Mukherjee, Prof. Kalyan Mandal, Prof. Ranjan Choudhuri of the S. N. Bose Centre for their excellent teaching in coursework classes which helped me a lot to understand scientific problems and general rules of research. I must thank the S. N. Bose Centre, as a whole, for providing me the opportunity to do research with good research facilities, clean and peaceful environment, comfortable accommodation, nice canteen and beautiful garden with all along. I would like to thank "Muktangan" for arranging different extracurricular activities which act as ointment during our stressful research life. I also thank the department of science and technology (DST), Government of India for providing me fellowship regularly for the entire period of my Ph.D programme.

I wholeheartedly acknowledge Dr. Tapas Ganguly and Dr. Soma Banik from RRCAT, Indore, India for their support to provide me with the ARPES measurement facilities for my research work. I am grateful to Yevhen Kushnirenko, Grigory Shipunov, A. V. Fedorov, Volodymyr Bezguba, S. V. Borisenko, B. Büchner from IFW Dresden, Germany, and Nicholas C. Plumb, Ming Shi from Paul Scherrer Institute, Switzerland for providing ARPES measurement facilities and active cooperations. Also, I would like to thank Dr. Luminita Harnegea and Dr. Surjeet Singh from IISER Pune, India for providing me with high-quality single crystals at the very beginning of my research career when we did not have crystal growth facilities. I am grateful to Prof. Chandan Majumdar, Suvankar Gupta, and Sudip Chakraborty from SINP,

Kolkata, India for performing SQUID measurements on my samples. I would like to thank Prof. Priya Mahadevan, Dr. Joydeep Chatterjee, Dr. Deepika Shrivastava from SNBNCBS, Kolkata, India, and Dr. Kapildeb Dolui from the University of Delaware, Newark, USA for their theoretical collaboration. I am also grateful to all the technical staff Nandi babu, Urmi di, Sourav da, Debarghya di, Joy da, Shakti da, and Dipayan da for their technical help.

It is my pleasure to acknowledge the members of "Quantum Material Lab", Susmita Changdar, Achintya Low, Sayan Routh, Shubham Purwar, Sushanta Ghosh, and Soumya Ghorai for providing an excellent research-friendly atmosphere. Also, I am thankful to Dr. Pankaj Maheswari, Dr. Reena Goyal, and Dr. Ayana Mukhopadhyay for their nice suggestions and discussions during their stay in our lab.

My special regards to all my teachers at primary, high school, undergraduate and postgraduate levels and especially to Mandal Babu, Bhabatosh Babu, Manoj Babu, Jagannath Babu, Harihar Babu, Manas Sir, Bikash Sir, Mohitosh Babu, Deben Babu, A.C. Sir, T.B. Sir, S.C. Sir, S.M. Sir who not only enriched my knowledge but also inspired me to grow as a human being. I gratefully acknowledge Kamalpur Primary School, Kamalpur Netaji High School, Bankura Christian College, and Burdwan University for providing me with the perfect ambiance and educational support.

I have been blessed with many good friends and this journey would not be possible without each of them. I extend my word of thanks to my seniors Sumanti di, Anita di, Debasmita di, Jayita di, and Kajal di who supported me a lot during my early days at SNBNCBS. I would like to thank all my friends, seniors, and juniors of SNB Social, SNB Mess, Cultural group, and Muktangan. I would like to thank Dulal da, Utpal da, and all staff of SNB Students Mess, Bhagirathi Canteen for providing healthy and tasty foods which helped me a lot to reduce the tiredness and stress of the whole day. I am grateful to all the cleaning staff, gardeners, and plumbing staff who gifted us a clean hostel room, a beautiful garden, and well-decorated campus every day for the last five years. I am grateful to each member of the Accounts, Purchase, Library, Security, Dean's office, administration, and engineering cell. It is incomplete without mentioning my friends; Jayashree, Riya, Mamoni, Moumita, Antara, Aisha, Siddhartha, and Rahul.

I also confess my sincere indebtedness to the all reviewers of the examination committee for spending their valuable time to evaluate my thesis.

A special mention has to be made of a special person, Abhik who helped me face all the difficulties that came my way during these years. Apart from the emotional support, he has also helped me academically in many ways from day one of my Ph.D. journey. Only he knows the complete story of my Ph.D. life and he is the closest person who helped me extremely to reach here. His struggle and his motivational words inspired me a lot and his love gave me the strength to overcome difficult situations. Thank you Abhik. I am fortunate to have you in my life. Lastly, two people who have

been my pillars of strength – my parents. My father (M.Sc. in Physics from Visva-Bharati University), was my home teacher from the beginning of my education. He is the man behind my all successes who grew the thirst for understanding science and loving science inside me. Despite having busy life being headmaster of a Govt. aided high school, he managed to teach me Physics along with Mathematics and Chemistry so nicely from the very beginning. I couldn't reach here without care, guidance and support of my mother who never gave up on me, and pushed me to be my very best. I feel lucky to have them as my parents. They are two of the most understanding and undemanding people on earth. They never let me feel the need to think about anything else other than my work. I owe, not only this thesis but everything that I have ever done in my life to them. Since my childhood I have always taken them for granted, knowing that no words of gratitude could ever be enough. But today I would like to spell it out. Thank you Ma, thank you Baba just for being my parents. I love you. I would like to convey my uttermost respect and gratitude to my paternal uncle Prof. Haranath Kar from MNNIT, Allahabad who was my motivation to proceed in research from school life and gave me valuable suggestions about research in many ways during my Ph.D. life. Finally, I would like to convey my uttermost respect and gratitude to all my family members, especially dada, boro mama, mejo mama, choto mama, Babita di, Jagannath Jamaibabu, Ranjita di, Jaideep da, Kaku and Kakima (Abhik's parents). I would like to convey my regards to my late paternal and maternal grandparents (thakuma, thakurda, dadu & dida) who are constantly blessing me from the eternal world and enriched me with so much love, and affection. Last but not the least, my thesis is incomplete without mentioning Ranu, Piu, Surya, Sonu, Chandrani, and Priyanka who always brought a smile to my face after a tiring day at work.

Once again, I acknowledge my deep gratitude to everybody who helped me or supported me anyhow at any circumstances during my PhD life, because of whom I could able to complete the thesis which I am going to submit. I feel apologized that I could not mention everyone personally one by one. Many Thanks to all.

With regards,
Indrani Kar
Department of Condensed Matter and Materials Physics
S. N. Bose National Centre for Basic Sciences
Kolkata, India
November, 2022

Abstract

Transition metal dichalcogenides (TMDCs) are available with a wide range of electronic properties starting from the metallic, to the semimetallic, to the semiconducting, and to the Mott insulators. This group of materials are of great research interests due to their potential applications in spintronics and optoelectronics devices. In addition, the diverse electronic properties of TMDCs include charge density wave (CDW), spin density wave (SDW), magnetism, superconductivity, and topological properties. In recent years, band engineering is widely applied on this group of materials due to weak van der Waals forces between the layers to uncover the exotic physical properties. Thus, examining the electronic band structure of these materials is crucial for the microscopic understanding of their peculiar physical properties.

In this work, we performed angle resolved photoemission spectroscopy (ARPES) studies on various TMDCs such as $ZrSe_2$, $ZrTe_2$, $TaTe_2$, and $NiTe_2$ to understand their low-energy electronic band structure in the vicinity of the Fermi level. ARPES studies on $ZrTe_2$ demonstrate free charge carriers at the Fermi level, which is further confirmed by the density functional theory (DFT) calculations. An equal hole and electron carrier density estimated from the ARPES data, points to $ZrTe_2$ being a semimetal. The DFT calculations further suggest a band inversion between Te-p and Zr-d states at the Γ point, hinting at the nontrivial band topology in $ZrTe_2$. Thus, our studies suggest that $ZrTe_2$ is a topological semimetal. Also, a comparative band structure study is done on $ZrSe_2$, which shows a semiconducting nature of the electronic structure with an indirect band gap of 0.9 eV between the $\Gamma(A)$ and $M(L)$ high-symmetry points. From this comparative study between $ZrTe_2$ and $ZrSe_2$ we conclude that the metal-chalcogen bond length plays a crucial role in tuning the electronic properties from a semiconductor ($ZrSe_2$) to a topological semimetal ($ZrTe_2$)

From the ARPES studies on $TaTe_2$ which is one of the CDW materials from the group V TMDCs, we find that the Fermi surface (FS) topology of $TaTe_2$ is quite complicated compared to its isovalent compounds such as TaS_2, $TaSe_2$, and isostructural compound $NbTe_2$. Most importantly, we discover that the surface electronic structure of $1T'$-$TaTe_2$ has more resemblance to the $2H$-$TaTe_2$, while the bulk electronic structure has more resemblance to the hypothetical $1T$-$TaTe_2$. These experimental ob-

servations are thoroughly compared with the DFT calculations performed on $1T$-, $2H$-, and $2H$ (monolayer)/$1T$-$TaTe_2$. We further notice that the Fermi surface topology is temperature independent up to 180 K, confirming that the 2H phase on the surface is stable up to 180 K and the CDW order is not due to the Fermi surface nesting. Also, our ARPES data on $NiTe_2$ clearly show a surface Dirac point observed at a binding energy of 1.45 eV which is consistent with an earlier theoretical prediction. Thus, our results for the first time experimentally show that $NiTe_2$ is a topological TMDC. Our ARPES data further suggest a metallic nature of $NiTe_2$. We find that overall, the electronic structure of $NiTe_2$ has similarities with the other topological TMDCs like $PdTe_2$, $PtTe_2$, and $PtSe_2$.

In addition to ARPES studies on the above mentioned TMDCs, we also have grown high quality single crystals of few TMDCs such as $NiTe_2$, VTe_2, VSe_2, and V_5S_8 and studied their electrical-transport, magnetotransport, and magnetic properties. From our electrical-transport and magnetotransport measurements on $NiTe_2$ single crystals, we find a Debye temperature $\theta_D \approx 230$ K using an extended Bloch-Grüneisen (BG) formula. The resistivity data fitting with the BG formula indicates that resistance in this system is dominated by s-d electron–phonon scattering. Also, from the magnetoresistance (MR) measurements we observe a crossover from linear MR dependence on B (MR$\propto$B) to a quadratic MR dependence on B (MR$\propto B^2$) at an applied magnetic field of B $\approx$ 3.5 T.

From our electrical resistivity, magnetotransport, and magnetic properties studies on TMDCs VSe_2 and VTe_2, we draw a comprehensive comparison between them. We observe the Kondo effect in both systems due to weak ferromagnetic ordering at low temperatures, resulting into a low-temperature resistivity upturn due to the Kondo effect with a Kondo temperature of 6 K for VSe_2 and 12 K for VTe_2. From the field dependent resistance measurements we find that the data is fitted best with a modified Hamann equation corrected by the quantum Brillouin function for VSe_2, while the data is fitted best with a modified Hamann equation corrected by the classical Langevin function for VTe_2. We attribute the differing formalisms for the same Kondo effect in different materials to their extrinsic sample properties rather than to the intrinsic nature of the material. Interestingly, we observe a contrasting MR property between these systems across the Kondo temperature. That means, a negative MR is found in both systems in the Kondo state. In the normal state the MR is positive for VSe_2, while it is negligible for VTe_2. In addition, both systems show weak ferromagnetism at low temperatures due to intercalated V atoms. Further, we find that V_5S_8 shows a low temperature resistivity upturn due to Kondo effect at a Kondo temperature of 6 K despite being an antiferromagnetic system. Similar to VSe_2 and VTe_2, V_5S_8 also shows a anisotropic negative MR at low temperatures while at high temperatures the MR disappears.

List of Figures

Contents

Synthesis, Characterization, Transport and Electronic Structure Studies of Transition Metal Dichalcogenides

Abstract

Transition metal dichalcogenides (TMDCs) are available with exotic physical properties such as charge density wave (CDW), spin density wave (SDW), magnetism, superconductivity, and topological properties. Thus, examining the electronic band structure of these materials is crucial for microscopic understanding of their exotic physical properties.

In this work, we performed angle-resolved photoemission spectroscopy studies (ARPES) on $ZrSe_2$, $ZrTe_2$, $TaTe_2$, and $NiTe_2$ to understand their low-energy electronic structure. Our studies suggest that $ZrTe_2$ is a topological semimetal whereas $ZrSe_2$ is semiconductor. We conclude that the metal-chalcogen bond length plays a crucial role in tuning the electronic properties from semiconductor ($ZrSe_2$) to a topological semimetal ($ZrTe_2$). From ARPES studies on charge density wave (CDW) material $TaTe_2$, we discover that the surface electronic structure of $1T'$-$TaTe_2$ has more resemblance to the $2H$-$TaTe_2$, while bulk electronic structure has more resemblance to hypothetical $1T$-$TaTe_2$. The Fermi surface topology is temperature independent up to 180 K, confirming that the $2H$ phase on the surface is stable up to 180 K and the CDW order is not due to the Fermi surface nesting. ARPES data on $NiTe_2$ clearly show a surface Dirac point observed at a binding energy of 1.45 eV which is consistent with an earlier theoretical prediction.

Also, we have grown high quality single crystals of $NiTe_2$, VTe_2, VSe_2, and V_5S_8 and studied their electrical-transport, magnetotransport, and magnetic properties. From resistivity data on $NiTe_2$, we find that resistance is dominated by s-d electron–phonon scattering and estimated Debye temperature $\theta_D \approx 230$ K using an extended Bloch-Grüneisen (BG) formula. Magnetoresistance (MR) shows a crossover from linear MR dependence to a quadratic MR dependence on applied magnetic field (B) at ≈ 3.5 T. From resistance measurements we observe Kondo effect at very low temperature region in VTe_2, VSe_2, and V_5S_8 due to magnetic exchange interactions.

Reference

1. Choi *et al.*, *Materials Today* **20**, 116–130 (2017).
2. Kar *et al.*, *Phys. Rev. B* **101**, 165122 (2020).
3. Kar *et al.*, *J. Phys. Chem. C* **125**, 1150 (2021).
4. Kar *et al.*, *AIP Conference Proceedings* **2265**, 030361 (2020).
5. Kar *et al.*, *Mater. Today: Proc.* **65**, 70-73 (2022).

Indrani Kar

Chapter 1

Introduction

The field of transition metal dichalcogenides (TMDCs) [1] is fascinating to the research community from a long back as it contains compounds of differing electronic properties like metallic [2], semimetallic [3], semiconducting [4], and Mott insulators [5]. In the bulk layered TMDCs, the monolayers are stacked by weak van der Waals force and the layers are easily cleavable. By changing the layer numbers, rotating the angle between the layers, or stacking the layer on different substrate (heterostructure) the electronic properties can be tuned. Hence, TMDCs are potential candidates for band engineering [6] and applications in spintronics [7], optoelectronics [8]. For example, the bandgap of MoS_2 changes from an indirect bandgap of 1.29 eV to a direct bandgap of 1.8 eV as it goes from bulk to monolayer. It is found that the monolayer MoS_2 enhances the photoluminescence (PL) due to the presence of direct band gap [9] and the bilayer MoS_2 generates five to eight-fold increase in PL compared to the monolayer [10]. Again, by changing the twisting-angle of bilayer PL can be enhanced further [11].

In addition, the diverse electronic properties of TMDCs include the CDW [12], SDW [13], magnetism [14], superconductivity [15], and topological properties [16]. Tunable bandgap [17] is one of the widely discussed topics of TMDCs. From the last few years, quasi 2-dimensional (2D) TMDCs have drawn significant technological research interests sparked by the demonstration of monolayer MoS_2 based transistors [18].

H																	He
Li	Be											B	C	N	O	F	Ne
Na	Mg	3	4	5	6	7	8	9	10	11	12	Al	Si	P	S	Cl	Ar
K	Ca	Sc	Ti	V	Cr	Mn	Fe	Co	Ni	Cu	Zn	Ga	Ge	As	Se	Br	Kr
Rb	Sr	Y	Zr	Nb	Mo	Tc	Ru	Rh	Pd	Ag	Cd	In	Sn	Sb	Te	I	Xe
Cs	Ba	La-Lu	Hf	Ta	W	Re	Os	Ir	Pt	Au	Hg	Tl	Pb	Bi	Po	At	Rn
Fr	Ra	Ac-Lr	Rf	Db	Sg	Bh	Hs	Mt	Ds	Rg	Cn	Uut	Fl	Uup	Lv	Uus	Uuo

Figure 1.1: The transition metals and the three chalcogen elements that mostly crystallize in layered structure are highlighted in the periodic table. Gradient colored Co, Rh, Ir, and Ni indicate that only $CoTe_2$, $RhTe_2$, $IrTe_2$ and $NiTe_2$ form layered structures.

The various structural phases of TMDCs result in a broad range of electronic properties, both from the electronic band structure (metallic or insulating) and the emergence of correlated topological phases [2–5, 16]. The physical and structural properties of TMDCs vary depending on the group of the transition metal element. The TMDCs, $TiSe_2$, $ZrSe_2$, and $HfSe_2$ are semiconductors, whereas $TiTe_2$, $ZrTe_2$, and $HfTe_2$ are metallic, formed from the group IV transition metals [19]. The discovery of CDW phase in the group V TMDCs, both in $2H$ and $1T$ phases of TaS_2, $TaSe_2$, and $2H$ phase of $NbSe_2$, led to renewed interest in this direction [20]. In the $2H$ phase of $NbSe_2$, TaS_2, and $TaSe_2$, superconductivity coexists with the CDW phase at low temperature [21]. Monolayer NbS_2 shows SDW state [13]. In addition to CDW phase some are Mott insulators [22]. TMDCs formed by the group VI transition metals Mo and W combined with S and Se in their thermodynamically stable $2H$ phase, MoS_2, $MoSe_2$, WS_2, and WSe_2 are semiconductors [23]. On the other hand, $MoTe_2$ and WTe_2 are well known as type-II Weyl semimetals [2]. TMDCs from the group VII, TcS_2, $TcSe_2$, and $TcTe_2$ are indirect band gap semiconductors with the band gaps within the infrared region of the electromagnetic spectrum. In the same series, the compounds ReS_2, $ReSe_2$, and $ReTe_2$ also possess semiconducting behaviour [24]. Further, from the group IX TMDCs, $IrTe_2$ shows superconductivity [15]. TMDCs formed by the group X transition metals $NiTe_2$, $PtTe_2$, $PtSe_2$, and $PdTe_2$ are reported to be type-II Dirac semimetals [25].

1.1 Structure of TMDCs

TMDCs consist of a transition-metal (M) and two chalcogen (X = S, Se or Te) atoms, described by the chemical formula of MX_2. In layered TMDCs, the monolayers of MX_2 are stacked by weak van der Waals forces. Hence, the layers are easily cleavable, known as quasi-2D system. Each MX_2 monolayer typically has a thickness of $6\mathring{A}$ to $7\mathring{A}$. The bonding between M and X is covalent and M is bonded with six X atoms. Depending on the geometry of covalent bonding, the TMDCs are mainly available in five polymorphs such as $1T$, $1T'$, $1T_d$, $2H$, and $3R$ [1, 26–28]. The letters denote the crystallographic system; T for trigonal, H for hexagonal, T' for monoclinic and triclinic, T_d for orthorhombic, and R for rhombohedral. The number denotes total number of TMDC monolayers per unit cell. $1T$ phase shows octahedral coordination whereas $2H$ and $3R$ phases show trigonal prismatic coordination. $1T'$, $1T_d$ show distorted octahedral coordination.

In the $1T$ phase, six X atoms octahedrally arranged around the central M atom. Most of the TMDCs are available in this $1T$ phase with trigonal crystal structure having the space group of $P\bar{3}m1$. These TMDCs are ZrX_2, HfX_2, TiX_2, VSe_2, VS_2,

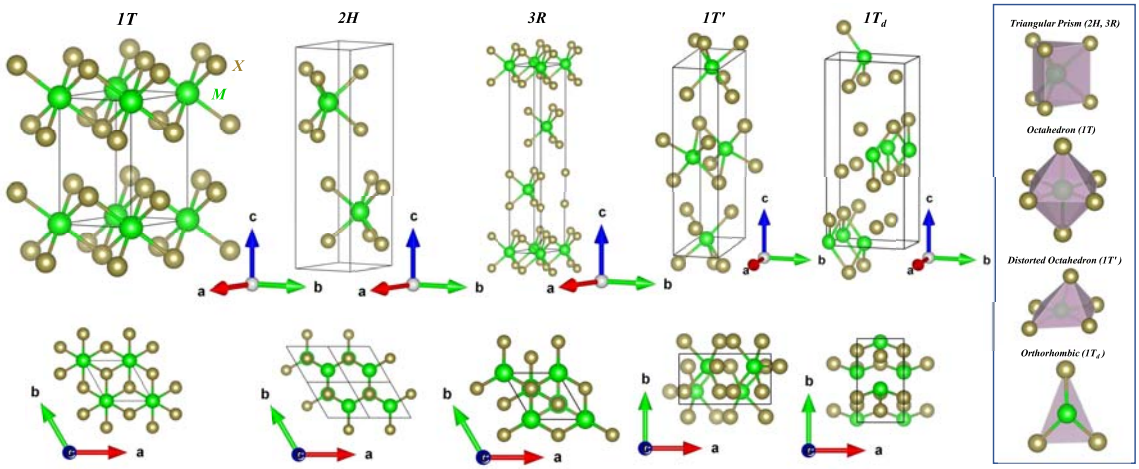

Figure 1.2: Crystal structure of $1T$, $2H$, $3R$, $1T'$, and $1T_d$ polytypes in top panel. Bottom panel shows projection of crystal structure on ab-plane. The octahedral ($1T$), trigonal prismatic ($2H$, $3R$), distorted octahedral ($1T'$) and orthorhombic (T_d) geometries are shown in the blue colored box.

$TaSe_2$, TaS_2, $CrTe_2$, $CrSe_2$, MoS_2, $IrTe_2$, $NiTe_2$, $CoTe_2$, $RhTe_2$, $PdTe_2$, PtX_2 (X=S, Se, Te).

$1T'$ phase is a distorted form of $1T$ phase. The available TMDCs in this phase are VTe_2, $NbTe_2$, $TaTe_2$, CrS_2, $MoTe_2$ with monoclinic crystal structure and triclinic ReX_2 (X= S, Se, Te).

$1T_d$ is also a distorted form of $1T$ phase. Two type-II Weyl semimetals, $MoTe_2$ and WTe_2 are available in this phase having orthorhombic structure with the space group of $Pnm2_1$. PdS_2 and $PdSe_2$ from the group XI are also available in this phase having orthorhombic crystal structure with the space group of P_{bca} [29].

In the $2H$ phase, six X atoms are symmetrically arranged around the central M atom to form a triangular prism. M is the centre and X are the vertices of the triangular prism. Here, the number two indicates that the unit cell has two TMDC monolayers in this phase. Mostly, TMDCs in low dimension (monolayer, bilayer, few layer) are available in this phase. In bulk, $NbSe_2$, NbS_2, TaS_2, $TaSe_2$, MoX_2, WS_2, WSe_2 are available in the $2H$ phase.

In the $3R$ phase, six X atoms are arranged around the central M atom similar to the $2H$ phase but the unit cell structure is quite different from the $2H$-phase as shown in Fig. 1.2. Here, two extra TMDC monolayers are inserted between the two TMDC monolayers of the $2H$ phase. The total number of TMDC monolayers present in a unit cell of $3R$ phase is three. Very few TMDCs show this $3R$ phase. In nature some of the MoS_2 compounds are available in this phase and $MoSe_2$, WS_2 are stabilized in this phase under high pressure.

Recently, another new phase $2M$ is found in WS_2 [30]. Here, the number two

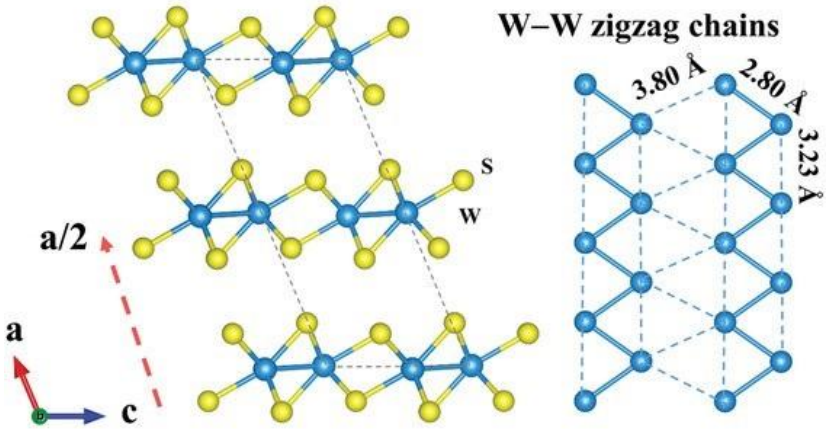

Figure 1.3: Crystal structure of $2M$-phase WS_2 [30].

indicates that unit cell has two TMDC monolayers in this phase and the letter M indicates the monoclinic crystal structure. The monolayer of $2M$ WS_2 is similar to the $1T'$-phase but the crystal structure is different from the $1T'$-phase. Here, the stacking manner is different as shown in Fig. 1.3.

Apart from the van der Waals layered compounds there are some pyrite structured TMDCs such as; MnX_2, FeS_2 (less), $FeTe_2$, RuX_2, OsX_2, CoX_2, NiX_2, RhX_2, $IrSe_2$, IrS_2. Among the TMDCs, some are also found in marcasite structure like MnS_2, FeX_2, $RuTe_2$, $CoSe_2$, $CoTe_2$, $NiSe_2$.

1.2 Importance of TMDCs

TMDCs are enriched with a broad range of exotic physical properties such as topological semimetal, superconductor, direct bandgap semiconductor, Mott insulator and so on.

1.2.1 Metal/Semimetal

Most of the TMDCs are available as metal or semimetal in their bulk state. These metallic TMDCs attract the research community due to presence of exotic physical properties such as type-II Dirac and Weyl semimetal, CDW, superconductivity and magnetism. Also, the physical properties are tunable by applying external pressure or strain [31] and by doping or intercalation [32–36]. By changing the thickness from bulk to monolayer the physical properties changes [37–45].

Topological Properties

The discovery of Dirac fermions [46, 47], Weyl fermions [48, 49], Majorana fermions [50, 51], and exotic new fermions beyond Dirac or Weyl fermions [52] in condensed matter systems enriched potential applications in spintronics and quantum computing as they exhibit a rich variety of novel phenomena, such as large linear MR [25], chiral magnetic effects [53], quantum anomalous Hall effect [54], topological Hall effect [55], and so on.

Fermions: In particle physics, the fundamental particles [56] are classified in two categories. One is Bosons having integral spin values and it follows Bose-Einstein statistics. Another one is Fermions having half integral spin values and follows Fermi-Dirac statistics. Fermions are classified into two categories: Leptons (electrons, muons, neutrinos and tau) and Quarks (up, down, strange, charm, top, bottom). Quarks are combined to form composite particles known as hadrons such as proton, neutron. Quarks participate in strong neuclear force.

Fermions are classified into different categories in quantum field theory such as Dirac fermions, Weyl fermions, and Majorana fermions [57].

Dirac Fermion: Dirac fermions obey Dirac equation [58] where mass and spin of particles are considered. These particles have four degrees of freedom, corresponding to two particle-antiparticle states and two spin states. These particles are observed in Dirac semimetals.

Weyl Fermion: Weyl fermions obey Weyl equation which is the simplified version of Dirac equation considering the particle mass is negligible. These massless particles have two degrees of freedom, corresponding to one-handedness state (left-handed or right-handed) and a single spin state. Weyl fermions do not have antiparticles. Chiral anomaly is observed within these particles, where the number of left-handed and right-handed particles can change under certain conditions. These particles are observed in topological insulators and Weyl semimetals.

Majorana Fermion: Majorana fermions are hypothetical charge-neutral particles. These particles follow Majorana equation which is a modified version of Dirac equation. In this equation, the particle and antiparticle wavefunctions are identical and the wavefunction is real-valued. Experimental evidence for Majorana fermions has been suggested in some exotic systems, such as topological superconductors [59].

Depending on the behaviour of fermions and electronic structure, the materials are classified into different subcategories such as Dirac semimetal, Weyl semimetal, topological insulator, topological semimetal.

Dirac Semimetal: In Dirac semimetals [46, 60], valence band and conduction band touch each other at a point near the Fermi level with a zero bandgap. This point is called Dirac point. Dirac point is protected by time reversal symmetry and spatial inversion symmetry. A conical dispersion is observed at Dirac point where energy

varies linearly with momentum. Here the charge carriers move as massless fermions which is described by relativistic Dirac equation. Dirac semimetals are of two types: type-I and type-II [61]. In type -I Dirac semimetal, the valence and conduction bands touch each other at discrete points in the momentum space and the Dirac cone has isotropic three dimentional dispersion. In type-II Dirac semimetals, the Dirac cone is tilted in momentum space and leads to anisotropic three dimentional dispersion. Three dimentional topological Dirac semimetals have pair of Dirac cones and carry a quantized topological invariant [62, 63].

Weyl Semimetal: In Weyl semimetals [64], valence band and conduction band touch at two points in momentum space with opposite chirality. These points are called Weyl points which are the source and sink of Berry flux and act as monopole and anti-monopole of Berry curvature. Similar to Dirac semimetals, conical band dispersion is observed near the Weyl points where energy varies linearly with momentum. Weyl points are protected either by time reversal symmetry or spatial inversion symmetry. Weyl points are topologically protected which means the robustness to various perturbation and disorder. In Weyl semimetals Fermi arcs are observed on the surface states which are topologically protected. A topological Dirac semimetal can be converted into a Weyl semimetal by breaking time-reversal symmetry or inversion symmetry [63]. By breaking one of these symmetries, the Dirac cone will split into two Weyl points with opposite chirality. Similar to Dirac semimetal, Weyl semimetals are of two types : type-I and type-II [61]. In type -I Weyl semimetal, the Weyl points are formed at discrete points in pair with opposite chirality in the momentum space and the Weyl nodes have isotropic three dimentional dispersion. In type-II Weyl semimetals, the Weyl nodes are tilted in momentum space and lead to anisotropic three dimentional dispersion.

Topological insulator: Topological insulators [65] has unique electronic structure where bulk state behaves as insulator and surface state is conducting. The bandgap of valence band and conduction band is similar as insulator but there is a gapless surface state within the bandgap. Electric current can conduct with high mobility through the surface states. The surface states are topologically protected.

Topological superconductor: Similar to topological insulators, topological superconductors have gapped bulk state and gapless suface state in superconducting phase [66, 67]. In these topological superconductors, the excitations across the gapless surface state are governed by Majorana equation where the wave function is real [67]. The theoretical physicists called these excitations as Majorana fermions [68].

Group X TMDCs, $NiTe_2$, $PdTe_2$, $PtTe_2$, and $PtSe_2$ have been confirmed as topological type-II Dirac semimetals [25, 69, 71–84]. Superconducting $PdTe_2$ has a type-II Dirac point at a binding energy of 0.5 eV and another surface Dirac point at a binding energy of 1.7 eV [76]. Also, $PtTe_2$ and $PtSe_2$ are type-II Dirac semimetals [69, 72, 73, 78] hav-

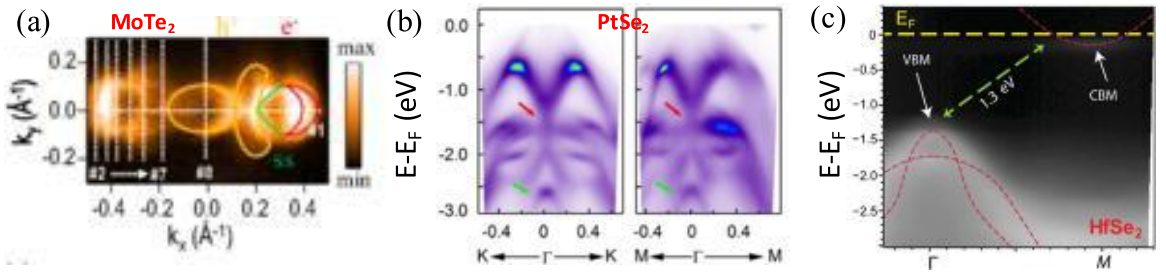

Figure 1.4: ARPES measurements on different TMDCs. (a) Shows the Fermi surface (FS) map of $MoTe_2$. Solid curves represent bulk Fermi sheets, while the dashed curve represents a Fermi arc from the surface [3]. (b) Energy dispersive maps of $PtSe_2$ along the Γ-K and Γ-M directions. Red arrow indicates the Dirac point and green arrow indicates the deep topological surface states [69]. (c) $HfSe_2$ shows indirect bandgap along Γ to M direction. Dashed red lines denote the calculated band structure using DFT along the Γ to M direction [70].

ing a Dirac point at a binding energy of 0.86 eV for $PtTe_2$ and 1.48 eV for $PtSe_2$ [69]. Deep topological surface states along with Dirac surface states are also observed in $PtTe_2$ and $PtSe_2$ [69, 76–78]. In $NiTe_2$ the location of a type-II bulk Dirac point is estimated 20 meV above the Fermi level (E_F) while the Dirac surface states are present at a binding energy of 1.4 eV [25, 80, 82].

Group VI TMDCs, WTe_2 and $MoTe_2$ are reported as topological type-II Weyl semimetal in the T_d phase [3, 85–88].

Apart from type-II Dirac or Weyl semimetals, VTe_2 from group V and $ZrTe_2$ from group IV are known as topological semimetals due to the presence of band inversion [89–91]. WS_2 in the $2M$ phase from group VI is a topological superconductor due to presence of topological surface states [30, 92] and predicted the possible presence of Majorana bound states [93]. Previous study predicted $IrTe_2$ from group IX to be a topological superconductor as it shows very high linear magnetoresistance along with superconducting transition at 2.5 K [15]. Also, by applying pressure or doping or intercalation, topological phases in layered TMDCs can be tuned [31]. In going from bulk to monolayer the electronic structure can be tuned to a topological state [44, 45]. Some of the TMDCs are predicted as topological insulators in twisted bilayer, monolayer, or in presence of defects or strain [94–97].

Charge Density Wave

CDW is the modulation of conduction electrons below a certain temperature (T_{CDW}) [98–100]. Below T_{CDW}, the periodicity and the density of charge at the lattice points of metals are rearranged. The origin of CDW in 1D system was theoretically explained by Rudolf Peierls [98–101]. Peierls distortion and Fermi surface nesting are the two

main aspects behind the CDW ordering. Also, electron-phonon coupling was suggested for the formation of CDW ordering in quasi 1D systems like, $ZrTe_3$ [102] and CuTe [103]. Still the mechanism of a CDW in higher dimensional materials is unsettled. This phenomena was first observed in metallic 1D linear chain system [104–106]. Inorganic transition metal trichalcogenide, $NbSe_3$ [104] and organic tetrathiafulvalene-tetracyanoquinodimethane (TTF-TCNQ) [105, 106] are first to show CDW in quasi 1D system.

Among layered TMDCs, group V TMDCs are well known for the presence of CDW ordering. Also, in some compounds of this group, $NbSe_2$ and $NbTe_2$ show a superconducting transition. For instance, VTe_2 shows a normal to commensurate CDW (C-CDW) transition at 474 K [107–109], while $NbTe_2$ shows a transition to a incommensurate CDW (IC-CDW) at 550 K and a IC-CDW to C-CDW transition at room temperature [110, 111], in addition to a superconducting transition at $\approx$ 0.5 K [112, 113]. On the other hand, $TaTe_2$ shows a normal to IC-CDW transition at 170 K [114–116]. Similarly, VSe_2 shows a IC-CDW transition at around 110 K and a IC-CDW to C-CDW at 70 K [117–120]. $NbSe_2$ shows a IC-CDW transition at 33 K and superconductivity at 7.2 K [121]. $TaSe_2$ shows a IC-CDW transition at 600 K and a C-CDW transition at 473 K in the 1T phase [122], while a IC-CDW transition at 122 K and a C-CDW transition at 90 K found in the 2H phase [123, 124]. Theoretical calculations suggested the presence of superconductivity at the extremely low temperature of 0.1 K in $2H$-$TaSe_2$ [125]. VS_2 is reported to show a CDW transition below 304 K in $1T$ phase [126–128]. Though NbS_2 is not found to show clear CDW order, but a report strongly suggested it to be at the verge of CDW order following the diverse electronic properties in NbS_2 [129, 130]. However, TaS_2 shows IC-CDW phase below 550 K and a nearly commensurate CDW (NC-CDW) phase below 350 K and C-CDW phase below 180 K was found in the 1T phase [131], while a short range CDW transition is found below 75 K in the 2H phase [132]. Hence, to understand the CDW phenomena or to understand the correlation between superconductivity and a CDW, this group V TMDCs are ideal to study.

Apart from the group V TMDCs, $TiSe_2$ from the group IV TMDCs undergoes a C-CDW transition at 200 K [133, 134]. A CDW can be induced in TMDCs by applying pressure or by doping or intercalation as observed in the Ni-doped $ZrTe_2$ compound [32]. Besides, it has a layer dependency [135, 136].

Superconductivity

The sudden drop of d.c. electrical resistivity to zero when the sample is cooled to a sufficiently low temperature is observed in many metals and alloys in addition to the Meissner effect. This phenomenon is known as superconductivity. It was first

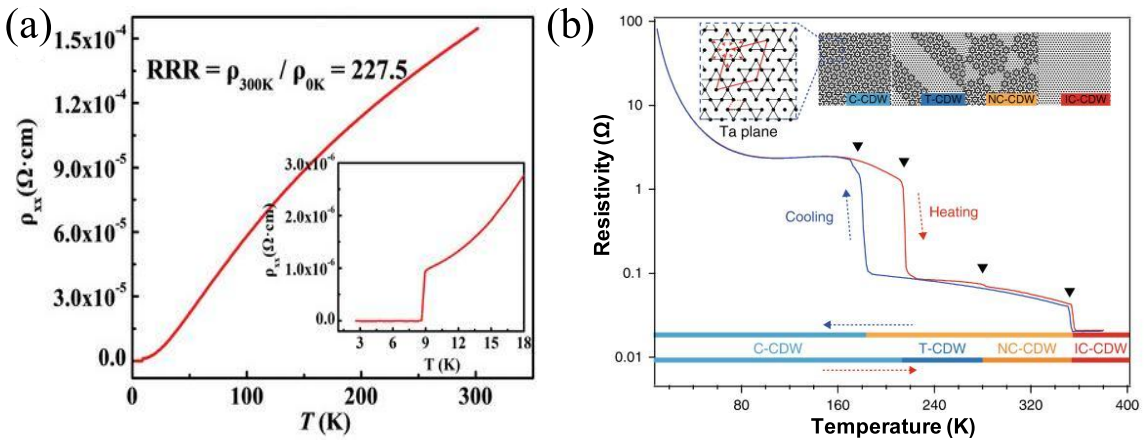

Figure 1.5: Resistivity measurements on different TMDCs. (a) Superconductivity of $2M$-WS_2 [30]. (b) Different types of CDW transitions and Mott Insulator transition in $1T$-TaS_2 [131].

observed by Kamerlingh Onnes in 1911 in mercury [137]. He found that at 4.2 K the resistance in a solid mercury wire immersed in liquid helium suddenly vanished. Superconductivity is an order state of metal below a certain temperature (T_C). The origin of superconductivity was explained by Bardeen, Cooper, and Schrieffer in terms of the Cooper pair [138]. Also, the theory by Ginzburg and Landau is used to describe superconductivity [139]. The concept of superconductivity has a wide range of technical applications. A superconducting transition is observed in some layered TMDCs at low temperatures. Group V TMDCs, $NbTe_2$ and $NbSe_2$ show superconducting transition at ≈ 0.5 K [112, 113] and 7.2 K [121], respectively. High quality single crystals of $2H$-NbS_2 show a superconducting transition at around 6 K [140]. Theoretical calculations predicted superconductivity at extremely low temperature of 0.1 K in $2H$-$TaSe_2$ [125]. Apart from the group V TMDCs, WS_2 in $2M$ phase from group VI, $IrTe_2$ from group IX and $PdTe_2$ from group X are widely discussed as topological superconductors, having a transition at 8.8 K (highest among the TMDCs) [30, 92, 93], 2.5 K [15] and 1.7 K [76–78, 141] respectively. Superconductivity is induced or the transition temperature increased in many layered TMDCs under the external pressure [142–144], by doping or intercalation of Ni, Ti, Re, Pd, Pt, Cu, Fe, Co, Mn, Sn, Cr [32, 144–153]. Also, by changing the layer thickness the superconductivity can be introduced or T_c can be enhanced [154].

Magnetism

Magnetism [155, 156] in solid arises due to spin and orbital motions of electrons and spins of nucleus. The motion of charged particles is equivalent to electric current which produces magnetic field. Magnetism is classified in five categories depending on the

number of unpaired valence electrons present in the atoms of the solid and orientations of the neighbouring magnetic moments.

1. Diamagnetism: In diamagnetic materials all the electrons within atoms are paired up, resulting in a zero net magnetic moment. In presence of external magnetic field a small current is induced in the opposite direction. This small current generates a magnetic field which opposes the applied magnetic field. Magnetic susceptibility of these materials is very small and negative. Most of the organic compounds, water, silver, gold are few examples of diamagnetic materials.

2. Paramagnetism: In paramagnetic materials, atoms, ions or molecules have unpaired electrons which produces permanent magnetic moments. These moments are randomly oriented in absence of external magnetic field and the net magnetization becomes zero. In presence of external magnetic field, the magnetic moments aligned in the direction of applied magnetic field. Magnetic susceptibility of these materials is very small and positive. Oxygen, Alluminium, Platinum are few examples of paramagnetic materials.

3. Ferromagnetism: Similar to paramagnetic materials, ferromagnetic materials also have permanent magnetic moments. Ferromagnetic materials have tiny domains. In each domain, the magnetic moments are aligned in particular direction even in the absence of magnetic field. The orientation of domains are different from each other within a ferromagnetic material. The net magnetization of a ferromagnetic material is non zero even in absence of magnetic field below a certain critical temperature. This is called spontaneous magnetization and the critical temperature is called the Curie temperature (T_C). This type of alignment accurs due to exchange interaction between magnetic ions. In presence of magnetic field, all the magnetic moments aligned along the direction of magnetic field. Magnetic susceptibility of these materials is large and positive. Magnetic susceptibility becomes infinite at T_C. Fe, Ni, Co are most common examples of ferromagnetic materials.

4. Antiferromagnetism: In antiferromagnetic materials magnetic moments of the neighbouring moments are aligned in an antiparallel arragement due to negative exchange integral unlike to ferromagnetic materials. In absense of magnetic field, net magnetization is zero as the neighbourings moments cancel each other. In presence of magnetic field, a small magnetization occurs and increases with temperature. This magnetization becomes maximum at a critical temperature which is called Néel temperature (T_N). Above this temperature magnetization decreases which is an indication of paramagnetic state. Magnetic susceptibility

of these materials is high and positive. Magnetic susceptibility becomes maximum at T_N with a finite value. Cr is one common example of antiferromagnetic material [157].

5. Ferrimagnetism: Ferrimagnetism is similar to antiferromagnetism except that the magnitude of magnetic moments of two neighbouring atoms are not equal. As a result the net magnetization becomes nonzero in absence of magnetic field. Fe_3O_4 is one common example of ferrimagnetic material [158].

The discovery of 2D magnetic systems are of great research interests for the last few years because of their versatile technological applications. By stacking layers of different magnetic materials or by twisting the layers or by making heterostructures of magnetic materials, magnetic properties or magnetic ordering can be tuned. Among layered TMDCs, magnetism is rare in bulk, whereas many TMDCs posses magnetism in lower dimensions such as monolayer VSe_2 [37], VTe_2 thin film [38], nanomaterial $2H$-$NbSe_2$ [159], atomically thin $1T$-NbS_2 [160], and so on. Theoretical and experimental studies predicted that bulk $2H$-$NbSe_2$ is close to the ferromagnetic instability [161, 162]. Metastable $1T$-$CrTe_2$ has ferromagnetic transition at 310 K [163]. Theoretical studies predicted that metastable $1T$-$CrSe_2$ is antiferromagnetic [164] and metastable $1T'$-CrS_2 is a ferromagnetic semiconductor [165]. Some self-intercalated TMDCs show magnetic ordering. For instance, monoclinic Cr_5Te_8 shows a paramagnetic to ferromagnetic transition at $\approx$ 220K [166–168]. Trigonal Cr_5Te_8 shows a competing nature between ferromagnetism and antiferromagnetism [169–171]. Monoclinic V_5S_8 is an antiferromagnetic, metallic compound [172–176]. V_5S_8 and Cr_5Te_8 are layered TMDC compounds where one transition metal is intercalated between four VS_2 and $CrTe_2$ layers respectively. Apart from these, TMDCs show magnetic ordering induced by doping or intercalation of Sc, Ti, V, Cr, Mn, Fe, Co, Ni [33–36]. Also, the magnetic properties differ between bulk and monolayer in TMDCs [37–40].

1.2.2 Semiconductor

When the valance band maxima (VBM) and conduction band minima are separated by a small energy gap of 0.1 to 2 eV and the value of electrical resistivity varies in the range of 10^{-2} to 10^{9} Ω-cm at room temperature it is called semiconductor. The electrical resistivity of semiconductor is strongly temperature dependent and perfect semiconductors become insulator at absolute zero temperature. The discovery of semiconductors was sparked by applications in transistors, light emitting diodes (LED), photovoltaic cells, detectors, thermistors, switches, etc.

For more than five decades Silicon is one of the widely used semiconductors in the field of electronics due to its abundance and moderate bandgap. Recently 2D-

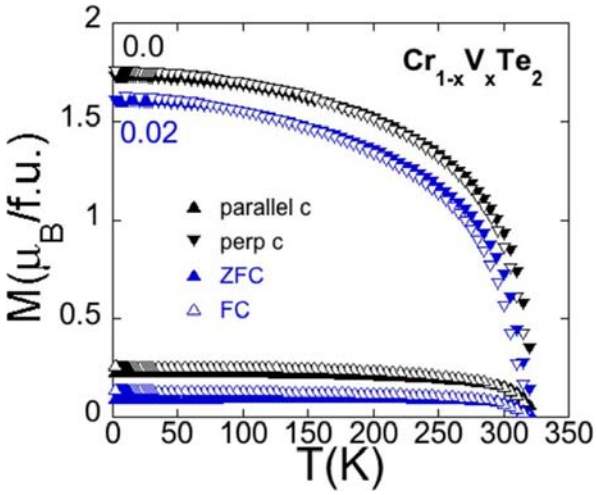

Figure 1.6: Magnetization measurements on ferromagnetic $1T$-$Cr_{1-x}V_xTe_2$ samples with an applied magnetic field of 1 kOe [163].

semiconductors have received much attention from the application point of view in nanoscale devices. $HfSe_2$, HfS_2, $ZrSe_2$, ZrS_2, TiS_2 are some of the indirect bandgap semiconductors from the group IV TMDCs [70, 177–180]. TMDCs from the group VI; MoX_2, WS_2, WSe_2 are indirect bandgap semiconductor in the $2H$ phase [181, 182]. PtS_2 from group X TMDCs is an indirect bandgap semiconductor with bandgap of 0.25 eV [183]. PdS_2 from the same group is predicted to be an indirect bandgap semiconductor [184, 185]. From the group VII TMDCs, bulk ReS_2 is a direct bandgap semiconductor whereas the electrical properties of bulk $ReSe_2$ is still under debate [186, 187]. From the same group, $ReTe_2$ is theoretically predicted to be an indirect bandgap semiconductor in the monolayer limit and there is no report available in bulk state [188]. The radioactive layered compounds $TcTe_2$, $TcSe_2$, and TcS_2 are less studied. Theoretically these are predicted as semiconductor in bulk state [189]. The bandgap of TMDCs are strongly layer dependent and sensitive to external pressure, doping, and intercalation [41–43].

1.2.3 Metal-Insulator Crossover

At room temperature none of the TMDCs are insulators. However, some of the TMDCs show metal-insulator transition at very low temperatures. For example, the ground state of bulk $1T$-TaS_2 is a band insulator though upon heating it enters into Mott insulator state within a narrow temperature range of 217-233 K [131]. Also, some TMDCs at very low temperature show a resistivity upturn due to (i) the Kondo effect [190], (ii) weak localization (WL) [191], or (iii) electron-electron interaction (EEI) [192]. So far, VTe_2 [193], VSe_2 [120, 194], and $ZrTe_2$ [195] are reported to show Kondo effect induced by self intercalation of transition metal elements between the layers. Also,

defect induced WL is observed in VSe_2 [196].

Kondo effect: The presence of magnetic impurities in some nonmagnetic metals or alloys gives rise to low temperature resistivity upturn which is known as Kondo effect [155, 156]. In normal metal and alloys, the resistivity decreases with the decreasing temperature as the inelastic scattering of electrons decreases with decreasing temperature. However, in some metals and alloys resistivity suddenly starts to increase logarithmically with decreasing temperature at low temperature region. Jun Kondo first explained that the Kondo effect arises due to the exchange coupling between the magnetic ions and the conduction electrons. The magnetic ions induce magnetizations in the conduction electrons and this magnetization causes exchange interaction between the magnetic ions and induced magnetized conduction electrons.

Mott insulator: In normal metals resistance decreases with decreasing temperature but in some metals resistance starts to increase abruptly at low temperature and becomes insulator due to strong electron-electron interaction. This state is known as Mott insulator [156, 197]. Since conventional band theory does not consider strong electron-electron interaction, it can not predict these insulators theoretically [198]. In this state, the valence electrons are strongly localized and unable to move freely due to repulsive Coulombic interaction between electrons. As a result, the material behaves as insulator, even though it may have a partially filled valence band. This type of metal-insulator transition was first expained by Sir Nevill Francis Mott. This transition is observed in transition metal based materials which have partially filled d or f electron orbitals, such as VO_2 [199], NiO [200].

1.3 Overview of the Thesis

The exotic physics of TMDC materials stems mainly from the interplay among various quantum mechanical effects, charge and spin excitations, orbital fluctuations, topological properties of the electronic band structure, etc. The primary aim of the thesis is to grow high quality single crystals and study their physical and electronic properties in order to understand the physics of these materials.

In this PhD thesis, we worked on the TMDC systems such as $ZrSe_2$, $ZrTe_2$, $TaTe_2$, $NiTe_2$, VTe_2, VSe_2, and VS_2 due to their topological properties. Our studies suggest that $ZrTe_2$ is a topological semimetal, while $ZrSe_2$ is found to be a semiconductor with an indirect band gap of 0.9 eV between the Γ(A) and $M(L)$ high-symmetry points. $TaTe_2$ is a CDW system, showing completely different electronic band structure from its isostructural compound $NbTe_2$ and isovalent compounds $TaSe_2$ and TaS_2. Surface states of $TaTe_2$ resemble the $2H$ phase electronic structure, while the bulk states replicate the $1T$ phase electronic structure of $TaTe_2$. Further, we realize that the band

structure of $TaTe_2$ is temperature independent above and below the CDW transition temperature. Next, $NiTe_2$ is a topological type-II Dirac semimetal showing the presence of a Dirac point at a binding energy of 1.45 eV as measured from the angle resolved photoemission spectroscopy (ARPES). From the magnetotransport studies of $NiTe_2$, we observe a crossover from a quadratic to a linear dependence on the applied magnetic field as we increase the field. Also, we estimated a Debye temperature of 230 K from resistivity data using BG fitting from $NiTe_2$. A comparative study has been performed on the CDW compounds VSe_2 and VTe_2 systems which show a Kondo effect at low temperatures. Magneto-transport and magnetic properties studies on antiferromagnetic 1T′-VS_2 (V_5S_8) have been performed. Single crystals have been grown using the chemical vapor transport (CVT) method. V_5S_8 shows a low temperature upturn as observed in its isovalent compounds VTe_2 and VSe_2, as well an antiferromagnetic transition is observed at around 28 K with a spin-flop (SF) transition at $\approx$ 3.5 T when the field is perpendicular to the *ab*-plane.

In the Chapter 2, we give a brief idea of single crystal growth techniques. Also we present the experimental details of energy dispersive X-ray analysis (EDX), X-ray diffraction analysis (XRD), electrical transport, thermal transport, dc-magnetic measurements, and electronic structure studies using X-ray photoemission spectroscopy (XPS) and angle-resolved photoemission spectroscopy (ARPES).

Chapter 3 presents the low-energy electronic structure of bulk $ZrTe_2$ and $ZrSe_2$ using high-resolution ARPES. To understand electronic contribution and for comparison with our results, we took help through collaboration for band structure calculations using DFT. From the Fermi surface topology of $ZrSe_2$, we observe only electron pockets located at the M(L) point, while the hole pockets are noticed well below the Fermi level at a binding energy of $\approx$1 eV. $ZrSe_2$ is a semiconductor with an indirect band gap of 0.9 eV between the Γ(A) and M(L) high-symmetry points. In contrast to $ZrSe_2$, on the Fermi surface map of $ZrTe_2$, we observe several well disconnected hole and electron pockets at the Γ(A) and M(L) points, respectively. Further, in $ZrTe_2$, we realize three holelike nondegenerate band dispersions near the Γ(A) point and an electronlike band dispersion at the M(L) point. An equal number of hole and electron carrier density estimated from our ARPES data using Luttinger's theorem suggests $ZrTe_2$ to be a semimetal. In addition, DFT calculations on $ZrTe_2$ in presence of spin-orbit coupling (SOC) predict band inversion between the Te *p* and Zr *d* bands near the Γ point, pointing $ZrTe_2$ to be a topological semimetal. In order to understand the origin of semimetallic state in $ZrTe_2$ and semiconducting state in $ZrSe_2$, our collaborators quantified the electronic structure by mapping it onto a tight-binding model. This allows us to relate the electronic structure changes in going from $ZrSe_2$ to $ZrTe_2$ to the change in the metal-chalcogen bond lengths.

Chapter 4 presents magneto-transport and ARPES studies on type-II Dirac semimetal

$NiTe_2$, to understand the electronic structure and transport behaviour. We have grown single crystals of $NiTe_2$ using the flux-growth method with Te as a flux. The electronic structure is similar in its sister compounds, $PdTe_2$, $PtTe_2$ and $PtSe_2$. All of them show a pair of Dirac points. ARPES reveals that it is metallic as the bands are crossing the Fermi level. An interesting feature indicating conical band dispersion is observed at a binding energy near about 1.45 eV. Another band crossing is not observed from ARPES as it is located 0.08 eV above the Fermi level. The electrical transport behaviour shows a metallic nature in agreement with ARPES results. The BG fitting to the resistivity data suggests a dominant s-d electron-phonon scattering in these systems. Further, we estimated a Debye temperature of 230 K. Also, from the magnetotransport studies, we observe a crossover from quadratic to linear dependence of the MR on the applied magnetic field as we increase the field, could mainly be due to the linear band dispersions near the Fermi level.

Chapter 5 presents ARPES studies on CDW candidate $TaTe_2$ to understand the change of electronic structure at the CDW transition and to examine whether it is a Dirac semimetal as speculated by quantum oscillations. The Fermi surface of $1T'$-$TaTe_2$ has a hexagonal symmetry, which is in contradiction to its monoclinic crystal structure. To fully understand the experimentally obtained electronic band structure of $TaTe_2$, we have disentangled the surface states from the bulk with the help of slab calculations done by our collaborator. We realized that the surface states resemble the $2H$ phase electronic structure, while the bulk states replicate the $1T$ phase electronic structure of $TaTe_2$. This is an interesting discovery as $TaTe_2$ does exist neither in the $1T$ phase nor in the $2H$ phase as per the observation of the crystal structure. The Fermi surface topology hardly changes across the CDW transition temperature, except that over a full temperature cycle, the spectral intensity was reduced for the surface states due to sample aging. Thus, we realize that the band structure of $TaTe_2$ is temperature independent above and below the CDW transition temperature.

In the Chapter 6, we present the electrical transport, magnetotransport, and magnetic properties studies on the transition metal dichalcogenides VSe_2 and VTe_2 and draw a comprehensive comparison between them. We observe the Kondo effect in both systems due to exchange interaction between localized moments and conduction electrons at low temperature, resulting into a resistance upturn at 6 K for VSe_2 and 12 K for VTe_2. From the field dependent resistance measurements we find that the data is fitted best with the modified Hamann equation corrected by the quantum Brillouin function for VSe_2, while the data is fitted best with a modified Hamann equation corrected by the classical Langevin function for VTe_2. We attribute the differing formalisms for the same Kondo effect in VSe_2 and VTe_2 to their extrinsic sample properties rather than the intrinsic nature of the material. Interestingly, we observe a contrasting MR property between these systems across the Kondo temperature. That means, negative

MR is found in both systems in the Kondo state. In the normal state the MR is positive for VSe_2, while it is negligible for VTe_2. In addition, both systems show weak ferromagnetism at low temperature due to intercalated V atoms.

The compound V_5S_8 can also be represented as $V_{1.25}S_2$, a transition metal dichalcogenide (TMDC) with excess V. Very few TMDCs show magnetism and/or Kondo effect. Among them, the sister compounds of V_5S_8, VSe_2 and VTe_2, are recently proved to show ferromagnetism in addition to the low temperature resistivity upturn due to the Kondo effect. In this study, we show the Kondo effect in V_5S_8 due to exchange interaction between localized moments and conduction electrons. We find isotropic magnetic properties above T_N, while a strong magnetic anisotropy is noticed below T_N. In addition, below T_N we find an out-of-plane ($H \parallel c$) SF transition triggered at a critical field of 3.5T that is absent for $H \perp c$. A negative MR is noticed in the antiferromagnetic state, while it is negligible in the paramagnetic state. An angle-dependent magnetoresistance is found to be highly anisotropic in the antiferromagnetic state.

In Chapter 8, we summarize our experimental observations.

Bibliography

[1] J. A. Wilson and A. D. Yoffe, "The transition metal dichalcogenides discussion and interpretation of the observed optical, electrical and structural properties," *Advances in Physics*, vol. 18, pp. 193–335, may 1969.

[2] P. Li, Y. Wen, X. He, Q. Zhang, C. Xia, Z.-M. Yu, S. A. Yang, Z. Zhu, H. N. Alshareef, and X.-X. Zhang, "Evidence for topological type-II Weyl semimetal WTe_2," *Nature Communications*, vol. 8, dec 2017.

[3] S. Thirupathaiah, R. Jha, B. Pal, J. S. Matias, P. K. Das, P. K. Sivakumar, I. Vobornik, N. C. Plumb, M. Shi, R. A. Ribeiro, and D. D. Sarma, "$MoTe_2$: An uncompensated semimetal with extremely large magnetoresistance," *Physical Review B*, vol. 95, jun 2017.

[4] H. Wang, C. Li, P. Fang, Z. Zhang, and J. Z. Zhang, "Synthesis, properties, and optoelectronic applications of two-dimensional MoS_2 and MoS_2-based heterostructures," *Chemical Society Reviews*, vol. 47, no. 16, pp. 6101–6127, 2018.

[5] L. Perfetti, P. A. Loukakos, M. Lisowski, U. Bovensiepen, H. Berger, S. Biermann, P. S. Cornaglia, A. Georges, and M. Wolf, "Time Evolution of the Electronic Structure of 1T-TaS_2 through the Insulator-Metal Transition," *Physical Review Letters*, vol. 97, aug 2006.

[6] W. Choi, N. Choudhary, G. H. Han, J. Park, D. Akinwande, and Y. H. Lee, "Recent development of two-dimensional transition metal dichalcogenides and their applications," *Materials Today*, vol. 20, pp. 116–130, apr 2017.

[7] R. Cheng, S. Jiang, Y. Chen, Y. Liu, N. Weiss, H.-C. Cheng, H. Wu, Y. Huang, and X. Duan, "Few-layer molybdenum disulfide transistors and circuits for high-speed flexible electronics," *Nature Communications*, vol. 5, oct 2014.

[8] W. Wu, L. Wang, Y. Li, F. Zhang, L. Lin, S. Niu, D. Chenet, X. Zhang, Y. Hao, T. F. Heinz, J. Hone, and Z. L. Wang, "Piezoelectricity of single-atomic-layer MoS_2 for energy conversion and piezotronics," *Nature*, vol. 514, pp. 470–474, oct 2014.

[9] A. Splendiani, L. Sun, Y. Zhang, T. Li, J. Kim, C.-Y. Chim, G. Galli, and F. Wang, "Emerging Photoluminescence in Monolayer MoS_2," *Nano Letters*, vol. 10, pp. 1271–1275, apr 2010.

[10] S. Zhang, W. Wang, L. Guan, X. Niu, J. Yao, X. Yan, B. Xing, Y. Yu, J. Sha, and Y. Wang, "Photoluminescence enhancement by stacking bi-layer MoS_2 without interlayer coupling," *Journal of Luminescence*, vol. 213, pp. 388–394, sep 2019.

[11] S. Huang, X. Ling, L. Liang, J. Kong, H. Terrones, V. Meunier, and M. S. Dresselhaus, "Probing the Interlayer Coupling of Twisted Bilayer MoS_2 Using Photoluminescence Spectroscopy," *Nano Letters*, vol. 14, pp. 5500–5508, sep 2014.

[12] M. Hossain, Z. Zhao, W. Wen, X. Wang, J. Wu, and L. Xie, "Recent Advances in Two-Dimensional Materials with Charge Density Waves: Synthesis, Characterization and Applications," *Crystals*, vol. 7, p. 298, oct 2017.

[13] F. Güller, V. L. Vildosola, and A. M. Llois, "Spin density wave instabilities in the NbS_2 monolayer," *Physical Review B*, vol. 93, mar 2016.

[14] X. Zhu, Y. Guo, H. Cheng, J. Dai, X. An, J. Zhao, K. Tian, S. Wei, X. C. Zeng, C. Wu, and Y. Xie, "Signature of coexistence of superconductivity and ferromagnetism in two-dimensional $NbSe_2$ triggered by surface molecular adsorption," *Nature Communications*, vol. 7, apr 2016.

[15] X. Zhang, J. Wang, Y. Liu, W. Zheng, and J. Wang, "Superconductivity in large spin-orbit coupled material $IrTe_2$," *Journal of Physics and Chemistry of Solids*, vol. 128, pp. 245–250, may 2019.

[16] J. Jiang, Z. K. Liu, Y. Sun, H. F. Yang, C. R. Rajamathi, Y. P. Qi, L. X. Yang, C. Chen, H. Peng, C. C. Hwang, S. Z. Sun, S. K. Mo, I. Vobornik, J. Fujii, S. S. P. Parkin, C. Felser, B. H. Yan, and Y. L. Chen, "Signature of type-II Weyl semimetal phase in $MoTe_2$," *Nature Communications*, vol. 8, jan 2017.

[17] A. Ramasubramaniam, D. Naveh, and E. Towe, "Tunable band gaps in bilayer transition-metal dichalcogenides," *Physical Review B*, vol. 84, nov 2011.

[18] B. Radisavljevic, A. Radenovic, J. Brivio, V. Giacometti, and A. Kis, "Single-layer MoS_2 transistors," *Nature Nanotechnology*, vol. 6, pp. 147–150, jan 2011.

[19] A. Ghafari, M. Moustafa, G. D. Santo, L. Petaccia, and C. Janowitz, "Opposite dispersion bands at the Fermi level in $ZrSe_2$," *Applied Physics Letters*, vol. 112, p. 182105, apr 2018.

[20] M.-T. Suzuki and H. Harima, "Electronic band structure of 1T-$TaSe_2$ in CDW phase," *Journal of Magnetism and Magnetic Materials*, vol. 272-276, pp. E653–E654, may 2004.

[21] K. Takita and K. Masuda, "Charge density wave transition and superconductivity in 2H-$NbSe_2$. Direct measurement of the penetration depth in a layered superconductor," *Journal of Low Temperature Physics*, vol. 58, pp. 127–142, jan 1985.

[22] C. Zhang, K. C. Santosh, Y. Nie, C. Liang, W. G. Vandenberghe, R. C. Longo, Y. Zheng, F. Kong, S. Hong, R. M. Wallace, and K. Cho, "Charge Mediated Reversible Metal–Insulator Transition in Monolayer $MoTe_2$ and $W_xMo_{1-x}Te_2$ Alloy," *ACS Nano*, vol. 10, pp. 7370–7375, jul 2016.

[23] A. Eftekhari, "Tungsten dichalcogenides (WS_2, WSe_2, and WTe_2): materials chemistry and applications," *Journal of Materials Chemistry A*, vol. 5, no. 35, pp. 18299–18325, 2017.

[24] C. M. Fang, G. A. Wiegers, C. Haas, and R. A. de Groot, "Electronic structures of , and in the real and the hypothetical undistorted structures," *Journal of Physics: Condensed Matter*, vol. 9, pp. 4411–4424, may 1997.

[25] C. Xu, B. Li, W. Jiao, W. Zhou, B. Qian, R. Sankar, N. D. Zhigadlo, Y. Qi, D. Qian, F.-C. Chou, and X. Xu, "Topological Type-II Dirac Fermions Approaching the Fermi Level in a Transition Metal Dichalcogenide $NiTe_2$," *Chemistry of Materials*, vol. 30, pp. 4823–4830, jun 2018.

[26] N. Lu, C. Zhang, C.-H. Lee, J. P. Oviedo, M. A. T. Nguyen, X. Peng, R. M. Wallace, T. E. Mallouk, J. A. Robinson, J. Wang, K. Cho, and M. J. Kim, "Atomic and Electronic Structures of WTe_2 Probed by High Resolution Electron Microscopy and ab Initio Calculations," *The Journal of Physical Chemistry C*, vol. 120, pp. 8364–8369, apr 2016.

[27] R. J. Toh, Z. Sofer, J. Luxa, D. Sedmidubský, and M. Pumera, "3R phase of MoS_2 and WS_2 outperforms the corresponding 2H phase for hydrogen evolution," *Chemical Communications*, vol. 53, no. 21, pp. 3054–3057, 2017.

[28] H. Yang, S. W. Kim, M. Chhowalla, and Y. H. Lee, "Structural and quantum-state phase transitions in van der Waals layered materials," *Nature Physics*, vol. 13, pp. 931–937, jul 2017.

[29] J. Sun, H. Shi, T. Siegrist, and D. J. Singh, "Electronic, transport, and optical properties of bulk and mono-layer $PdSe_2$," *Applied Physics Letters*, vol. 107, p. 153902, oct 2015.

[30] Y. Fang, J. Pan, D. Zhang, D. Wang, H. T. Hirose, T. Terashima, S. Uji, Y. Yuan, W. Li, Z. Tian, J. Xue, Y. Ma, W. Zhao, Q. Xue, G. Mu, H. Zhang, and F. Huang, "Discovery of Superconductivity in 2M WS_2 with Possible Topological Surface States," *Advanced Materials*, p. 1901942, jun 2019.

[31] W. Liu, A. Luo, G. Zhong, J. Zou, and G. Xu, "Prediction of new topological superconductor candidate 1T-Ti$(Se_{1-y}Te_y)_2$," *Phys. Rev. Research*, vol. 4, p. 023127, May 2022.

[32] L. E. Correa, P. P. Ferreira, L. R. de Faria, T. T. Dorini, M. S. da Luz, Z. Fisk, M. S. Torikachvili, L. T. F. Eleno, and A. J. S. Machado, "Evidence for multiband superconductivity and charge density waves in Ni-doped $ZrTe_2$," *Journal of Alloys and Compounds*, vol. 907, p. 164477, jun 2022.

[33] R. H. Friend, A. R. Beal, and A. D. Yoffe, "Electrical and magnetic properties of some first row transition metal intercalates of niobium disulphide," *The Philosophical Magazine: A Journal of Theoretical Experimental and Applied Physics*, vol. 35, pp. 1269–1287, may 1977.

[34] P. Kumar, R. Skomski, and R. Pushpa, "Magnetically Ordered Transition-Metal-Intercalated WSe_2," *ACS Omega*, vol. 2, pp. 7985–7990, nov 2017.

[35] L. S. Xie, S. Husremovic, O. Gonzalez, I. M. Craig, and D. K. Bediako, "Structure and Magnetism of Iron- and Chromium-Intercalated Niobium and Tantalum Disulfides," *J. Am. Chem. Soc.*, vol. 144, pp. 9525–9542, apr 2022.

[36] S. Mankovsky, K. Chadova, D. Ködderitzsch, J. Minár, H. Ebert, and W. Bensch, "Electronic, magnetic, and transport properties of Fe-intercalated $2H$-TaS_2 studied by means of the KKR-CPA method," *Phys. Rev. B*, vol. 92, p. 144413, Oct 2015.

[37] M. Bonilla, S. Kolekar, Y. Ma, H. C. Diaz, V. Kalappattil, R. Das, T. Eggers, H. R. Gutierrez, M.-H. Phan, and M. Batzill, "Strong room-temperature ferromagnetism in VSe_2 monolayers on van der Waals substrates," *Nature Nanotechnology*, vol. 13, pp. 289–293, feb 2018.

[38] P. M. Coelho, K. Lasek, K. N. Cong, J. Li, W. Niu, W. Liu, I. I. Oleynik, and M. Batzill, "Monolayer Modification of VTe_2 and Its Charge Density Wave," *The Journal of Physical Chemistry Letters*, vol. 10, pp. 4987–4993, aug 2019.

[39] N.-N. Sun and H.-Y. Wang, "Theoretical investigation of the ferromagnetism on VS_2 monolayers with exchange anisotropy," *Journal of Magnetism and Magnetic Materials*, vol. 477, pp. 232–236, may 2019.

[40] L. Meng, Z. Zhou, M. Xu, S. Yang, K. Si, L. Liu, X. Wang, H. Jiang, B. Li, P. Qin, P. Zhang, J. Wang, Z. Liu, P. Tang, Y. Ye, W. Zhou, L. Bao, H.-J. Gao, and Y. Gong, "Anomalous thickness dependence of Curie temperature in air-stable two-dimensional ferromagnetic 1T-$CrTe_2$ grown by chemical vapor deposition," *Nature Communications*, vol. 12, feb 2021.

[41] A. Chaves, J. G. Azadani, H. Alsalman, D. R. da Costa, R. Frisenda, A. J. Chaves, S. H. Song, Y. D. Kim, D. He, J. Zhou, A. Castellanos-Gomez, F. M. Peeters, Z. Liu, C. L. Hinkle, S.-H. Oh, P. D. Ye, S. J. Koester, Y. H. Lee, P. Avouris, X. Wang, and T. Low, "Bandgap engineering of two-dimensional semiconductor materials," *npj 2D Materials and Applications*, vol. 4, aug 2020.

[42] H. Guo, N. Lu, L. Wang, X. Wu, and X. C. Zeng, "Tuning Electronic and Magnetic Properties of Early Transition-Metal Dichalcogenides via Tensile Strain," *The Journal of Physical Chemistry C*, vol. 118, pp. 7242–7249, mar 2014.

[43] A. Ciarrocchi, A. Avsar, D. Ovchinnikov, and A. Kis, "Thickness-modulated metal-to-semiconductor transformation in a transition metal dichalcogenide," *Nature Communications*, vol. 9, mar 2018.

[44] P. Tsipas, D. Tsoutsou, S. Fragkos, R. Sant, C. Alvarez, H. Okuno, G. Renaud, R. Alcotte, T. Baron, and A. Dimoulas, "Massless Dirac Fermions in $ZrTe_2$ Semimetal Grown on InAs(111) by van der Waals Epitaxy," *ACS Nano*, vol. 12, pp. 1696–1703, jan 2018.

[45] A. Huang, C.-H. Chen, C.-H. Chang, and H.-T. Jeng, "Topological Phase and Quantum Anomalous Hall Effect in Ferromagnetic Transition-Metal Dichalcogenides Monolayer 1T-VSe_2," *Nanomaterials*, vol. 11, p. 1998, aug 2021.

[46] S. Borisenko, Q. Gibson, D. Evtushinsky, V. Zabolotnyy, B. Büchner, and R. J. Cava, "Experimental Realization of a Three-Dimensional Dirac Semimetal," *Phys. Rev. Lett.*, vol. 113, p. 027603, Jul 2014.

[47] Z. K. Liu, B. Zhou, Y. Zhang, Z. J. Wang, H. M. Weng, D. Prabhakaran, S.-K. Mo, Z. X. Shen, Z. Fang, X. Dai, Z. Hussain, and Y. L. Chen, "Discovery of a Three-Dimensional Topological Dirac Semimetal, Na_3Bi," *Science*, vol. 343, pp. 864–867, feb 2014.

[48] H. Weng, C. Fang, Z. Fang, B. A. Bernevig, and X. Dai, "Weyl Semimetal Phase in Noncentrosymmetric Transition-Metal Monophosphides," *Phys. Rev. X*, vol. 5, p. 011029, Mar 2015.

[49] N. Xu, H. M. Weng, B. Q. Lv, C. E. Matt, J. Park, F. Bisti, V. N. Strocov, D. Gawryluk, E. Pomjakushina, K. Conder, N. C. Plumb, M. Radovic, G. Autès, O. V. Yazyev, Z. Fang, X. Dai, T. Qian, J. Mesot, H. Ding, and M. Shi, "Observation of Weyl nodes and Fermi arcs in tantalum phosphide," *Nature Communications*, vol. 7, mar 2016.

[50] L. Fu and C. L. Kane, "Superconducting Proximity Effect and Majorana Fermions at the Surface of a Topological Insulator," *Phys. Rev. Lett.*, vol. 100, p. 096407, Mar 2008.

[51] J. J. He, T. K. Ng, P. A. Lee, and K. T. Law, "Selective Equal-Spin Andreev Reflections Induced by Majorana Fermions," *Phys. Rev. Lett.*, vol. 112, p. 037001, Jan 2014.

[52] B. Bradlyn, J. Cano, Z. Wang, M. G. Vergniory, C. Felser, R. J. Cava, and B. A. Bernevig, "Beyond Dirac and Weyl fermions: Unconventional quasiparticles in conventional crystals," *Science*, vol. 353, aug 2016.

[53] A. A. Zyuzin and A. A. Burkov, "Topological response in Weyl semimetals and the chiral anomaly," *Phys. Rev. B*, vol. 86, p. 115133, Sep 2012.

[54] J. Wang, B. Lian, and S.-C. Zhang, "Quantum anomalous Hall effect in magnetic topological insulators," *Physica Scripta*, vol. T164, p. 014003, aug 2015.

[55] J. Jiang, D. Xiao, F. Wang, J.-H. Shin, D. Andreoli, J. Zhang, R. Xiao, Y.-F. Zhao, M. Kayyalha, L. Zhang, K. Wang, J. Zang, C. Liu, N. Samarth, M. H. W. Chan, and C.-Z. Chang, "Concurrence of quantum anomalous Hall and topological Hall effects in magnetic topological insulator sandwich heterostructures," *Nature Materials*, vol. 19, pp. 732–737, feb 2020.

[56] B. R. Martin and G. Shaw, *Particle physics*. John Wiley & Sons, 2016.

[57] P. B. Pal, "Dirac, majorana, and weyl fermions," *American Journal of Physics*, vol. 79, no. 5, pp. 485–498, 2011.

[58] M. Peskin, *An introduction to quantum field theory*. CRC press, 2018.

[59] M. Leijnse and K. Flensberg, "Introduction to topological superconductivity and Majorana fermions," *Semiconductor Science and Technology*, vol. 27, no. 12, p. 124003, 2012.

[60] S. M. Young, S. Zaheer, J. C. Y. Teo, C. L. Kane, E. J. Mele, and A. M. Rappe, "Dirac Semimetal in Three Dimensions," *Phys. Rev. Lett.*, vol. 108, p. 140405, Apr 2012.

[61] H.-X. Wang, Y. Chen, Z. H. Hang, H.-Y. Kee, and J.-H. Jiang, "Type-II Dirac photons," *npj Quantum Materials*, vol. 2, sep 2017.

[62] B.-J. Yang and N. Nagaosa, "Classification of stable three-dimensional Dirac semimetals with nontrivial topology," *Nature Communications*, vol. 5, sep 2014.

[63] Z. K. Liu, J. Jiang, B. Zhou, Z. J. Wang, Y. Zhang, H. M. Weng, D. Prabhakaran, S.-K. Mo, H. Peng, P. Dudin, T. Kim, M. Hoesch, Z. Fang, X. Dai, Z. X. Shen, D. L. Feng, Z. Hussain, and Y. L. Chen, "A stable three-dimensional topological Dirac semimetal Cd_3As_2," *Nature Materials*, vol. 13, pp. 677–681, may 2014.

[64] S. Jia, S.-Y. Xu, and M. Z. Hasan, "Weyl semimetals, Fermi arcs and chiral anomalies," *Nature Materials*, vol. 15, pp. 1140–1144, oct 2016.

[65] M. Z. Hasan and J. E. Moore, "Three-dimensional topological insulators," *Annu. Rev. Condens. Matter Phys.*, vol. 2, no. 1, pp. 55–78, 2011.

[66] Y. Cui, S. Wu, Q. Zhu, G. Xiao, B. Liu, J. Wu, G. Cao, and Z. Ren, "Metal-insulator-like transition, superconducting dome and topological electronic structure in Ga-doped Re_3Ge_7," *npj Quantum Materials*, vol. 6, aug 2021.

[67] M. Sato and Y. Ando, "Topological superconductors: a review," *Reports on Progress in Physics*, vol. 80, no. 7, p. 076501, 2017.

[68] C. Beenakker and L. Kouwenhoven, "A road to reality with topological superconductors," *Nature Physics*, vol. 12, pp. 618–621, jun 2016.

[69] K. Zhang, M. Yan, H. Zhang, H. Huang, M. Arita, Z. Sun, W. Duan, Y. Wu, and S. Zhou, "Experimental evidence for type-II Dirac semimetal in $PtSe_2$," *Physical Review B*, vol. 96, sep 2017.

[70] M. J. Mleczko, C. Zhang, H. R. Lee, H.-H. Kuo, B. Magyari-Köpe, R. G. Moore, Z.-X. Shen, I. R. Fisher, Y. Nishi, and E. Pop, "$HfSe_2$ and $ZrSe_2$: Two-dimensional semiconductors with native high-κ oxides," *Science Advances*, vol. 3, p. e1700481, aug 2017.

[71] M. K. Hooda, C. S. Yadav, and D. Samal, "Electronic and topological properties of group-10 transition metal dichalcogenides," *Journal of Physics: Condensed Matter*, vol. 33, p. 103001, dec 2020.

[72] A. Politano, G. Chiarello, B. Ghosh, K. Sadhukhan, C.-N. Kuo, C. S. Lue, V. Pellegrini, and A. Agarwal, "3D Dirac Plasmons in the Type-II Dirac Semimetal $PtTe_2$," *Physical Review Letters*, vol. 121, aug 2018.

[73] H. Huang, S. Zhou, and W. Duan, "Type-II Dirac fermions in the $PtSe_2$ class of transition metal dichalcogenides," *Physical Review B*, vol. 94, sep 2016.

[74] K. Kim, S. Kim, J. S. Kim, H. Kim, J.-H. Park, and B. I. Min, "Importance of the van Hove singularity in superconducting $PdTe_2$," *Physical Review B*, vol. 97, apr 2018.

[75] R. C. Xiao, P. L. Gong, Q. S. Wu, W. J. Lu, M. J. Wei, J. Y. Li, H. Y. Lv, X. Luo, P. Tong, X. B. Zhu, and Y. P. Sun, "Manipulation of type-I and type-II Dirac points in $PdTe_2$ superconductor by external pressure," *Physical Review B*, vol. 96, aug 2017.

[76] H.-J. Noh, J. Jeong, E.-J. Cho, K. Kim, B. Min, and B.-G. Park, "Experimental Realization of Type-II Dirac Fermions in a $PdTe_2$ Superconductor," *Physical Review Letters*, vol. 119, jul 2017.

[77] F. Fei, X. Bo, R. Wang, B. Wu, J. Jiang, D. Fu, M. Gao, H. Zheng, Y. Chen, X. Wang, H. Bu, F. Song, X. Wan, B. Wang, and G. Wang, "Nontrivial Berry phase and type-II Dirac transport in the layered material $PdTe_2$," *Physical Review B*, vol. 96, jul 2017.

[78] O. Clark, M. Neat, K. Okawa, L. Bawden, I. Marković, F. Mazzola, J. Feng, V. Sunko, J. Riley, W. Meevasana, J. Fujii, I. Vobornik, T. Kim, M. Hoesch, T. Sasagawa, P. Wahl, M. Bahramy, and P. King, "Fermiology and Superconductivity of Topological Surface States in $PdTe_2$," *Physical Review Letters*, vol. 120, apr 2018.

[79] W. Zheng, R. Schönemann, N. Aryal, Q. Zhou, D. Rhodes, Y.-C. Chiu, K.-W. Chen, E. Kampert, T. Förster, T. J. Martin, G. T. McCandless, J. Y. Chan, E. Manousakis, and L. Balicas, "Detailed study of the Fermi surfaces of the type-II Dirac semimetallic candidates XTe_2 (X =Pd, Pt)," *Physical Review B*, vol. 97, jun 2018.

[80] M. Nurmamat, S. V. Eremeev, X. Wang, T. Yoshikawa, T. Kono, M. Kakoki, T. Muro, Q. Jiang, Z. Sun, M. Ye, and A. Kimura, "Bulk Dirac cone and highly anisotropic electronic structure of $NiTe_2$," *Physical Review B*, vol. 104, oct 2021.

[81] I. Kar, L. Harnagea, S. Banik, SurjeetSingh, and S. Thirupathaiah, "Observation of surface Dirac state in transition metal dichalcogenide $NiTe_2$ using ARPES," in *DAE SOLID STATE PHYSICS SYMPOSIUM 2019*, AIP Publishing, 2020.

[82] B. Ghosh, D. Mondal, C.-N. Kuo, C. S. Lue, J. Nayak, J. Fujii, I. Vobornik, A. Politano, and A. Agarwal, "Observation of bulk states and spin-polarized topological surface states in transition metal dichalcogenide Dirac semimetal candidate $NiTe_2$," *Physical Review B*, vol. 100, nov 2019.

[83] Q. Liu, F. Fei, B. Chen, X. Bo, B. Wei, S. Zhang, M. Zhang, F. Xie, M. Naveed, X. Wan, F. Song, and B. Wang, "Nontopological origin of the planar Hall effect in the type-II Dirac semimetal $NiTe_2$," *Physical Review B*, vol. 99, apr 2019.

[84] P. J. Orders, J. Liesegang, R. C. G. Leckey, J. G. Jenkin, and J. D. Riley, "Angle-resolved photoemission from the valence bands of $NiTe_2$, $PdTe_2$ and $PtTe_2$," *Journal of Physics F: Metal Physics*, vol. 12, pp. 2737–2753, nov 1982.

[85] M. N. Ali, J. Xiong, S. Flynn, J. Tao, Q. D. Gibson, L. M. Schoop, T. Liang, N. Haldolaarachchige, M. Hirschberger, N. P. Ong, and R. J. Cava, "Large, non-saturating magnetoresistance in WTe_2," *Nature*, vol. 514, pp. 205–208, sep 2014.

[86] K. Deng, G. Wan, P. Deng, K. Zhang, S. Ding, E. Wang, M. Yan, H. Huang, H. Zhang, Z. Xu, J. Denlinger, A. Fedorov, H. Yang, W. Duan, H. Yao, Y. Wu, S. Fan, H. Zhang, X. Chen, and S. Zhou, "Experimental observation of topological Fermi arcs in type-II Weyl semimetal $MoTe_2$," *Nature Physics*, vol. 12, pp. 1105–1110, sep 2016.

[87] Y. Wu, D. Mou, N. H. Jo, K. Sun, L. Huang, S. L. Bud'ko, P. C. Canfield, and A. Kaminski, "Observation of Fermi arcs in the type-II Weyl semimetal candidate WTe_2," *Phys. Rev. B*, vol. 94, p. 121113, Sep 2016.

[88] S. Thirupathaiah, R. Jha, B. Pal, J. S. Matias, P. K. Das, I. Vobornik, R. A. Ribeiro, and D. D. Sarma, "Temperature-independent band structure of WTe_2 as observed from angle-resolved photoemission spectroscopy," *Phys. Rev. B*, vol. 96, p. 165149, Oct 2017.

[89] N. Mitsuishi, Y. Sugita, M. S. Bahramy, M. Kamitani, T. Sonobe, M. Sakano, T. Shimojima, H. Takahashi, H. Sakai, K. Horiba, H. Kumigashira, K. Taguchi, K. Miyamoto, T. Okuda, S. Ishiwata, Y. Motome, and K. Ishizaka, "Switching of band inversion and topological surface states by charge density wave," *Nature Communications*, vol. 11, may 2020.

[90] I. Kar, J. Chatterjee, L. Harnagea, Y. Kushnirenko, A. V. Fedorov, D. Shrivastava, B. Büchner, P. Mahadevan, and S. Thirupathaiah, "Metal-chalcogen bond-length induced electronic phase transition from semiconductor to topological semimetal in ZrX_2 (X=Se and Te)," *Physical Review B*, vol. 101, apr 2020.

[91] Y. Tian, N. Ghassemi, and J. H. Ross, "Topological nodal line in $zrte_2$ demonstrated by nuclear magnetic resonance," *Phys. Rev. B*, vol. 102, p. 165149, Oct 2020.

[92] Y. W. Li, H. J. Zheng, Y. Q. Fang, D. Q. Zhang, Y. J. Chen, C. Chen, A. J. Liang, W. J. Shi, D. Pei, L. X. Xu, S. Liu, J. Pan, D. H. Lu, M. Hashimoto, A. Barinov, S. W. Jung, C. Cacho, M. X. Wang, Y. He, L. Fu, H. J. Zhang, F. Q. Huang, L. X. Yang, Z. K. Liu, and Y. L. Chen, "Observation of topological superconductivity in a stoichiometric transition metal dichalcogenide 2M-WS_2," *Nature Communications*, vol. 12, may 2021.

[93] Y. Yuan, J. Pan, X. Wang, Y. Fang, C. Song, L. Wang, K. He, X. Ma, H. Zhang, F. Huang, *et al.*, "Evidence of anisotropic Majorana bound states in 2M-WS_2," *Nature Physics*, vol. 15, no. 10, pp. 1046–1051, 2019.

[94] X. Li, S. Zhang, and Q. Wang, "Topological insulating states in 2D transition metal dichalcogenides induced by defects and strain," *Nanoscale*, vol. 9, no. 2, pp. 562–569, 2017.

[95] F. Wu, T. Lovorn, E. Tutuc, I. Martin, and A. MacDonald, "Topological Insulators in Twisted Transition Metal Dichalcogenide Homobilayers," *Physical Review Letters*, vol. 122, feb 2019.

[96] D. Varsano, M. Palummo, E. Molinari, and M. Rontani, "A monolayer transition-metal dichalcogenide as a topological excitonic insulator," *Nature nanotechnology*, vol. 15, no. 5, pp. 367–372, 2020.

[97] J. Zeng, H. Liu, H. Jiang, Q.-F. Sun, and X. C. Xie, "Multiorbital model reveals a second-order topological insulator in $1H$ transition metal dichalcogenides," *Phys. Rev. B*, vol. 104, p. L161108, Oct 2021.

[98] R. E. Thorne, "Charge-Density-Wave Conductors," *Physics Today*, vol. 49, pp. 42–47, may 1996.

[99] G. Grüner, "The dynamics of charge-density waves," *Reviews of Modern Physics*, vol. 60, pp. 1129–1181, oct 1988.

[100] R. E. Peierls, *Quantum Theory of Solids*. Oxford University Press, feb 2001.

[101] X. Zhu, J. Guo, J. Zhang, and E. W. Plummer, "Misconceptions associated with the origin of charge density waves," *Advances in Physics: X*, vol. 2, pp. 622–640, may 2017.

[102] Y. Hu, F. Zheng, X. Ren, J. Feng, and Y. Li, "Charge density waves and phonon-electron coupling in $ZrTe_3$," *Physical Review B*, vol. 91, apr 2015.

[103] K. Zhang, X. Liu, H. Zhang, K. Deng, M. Yan, W. Yao, M. Zheng, E. F. Schwier, K. Shimada, J. D. Denlinger, Y. Wu, W. Duan, and S. Zhou, "Evidence for a Quasi-One-Dimensional Charge Density Wave in CuTe by Angle-Resolved Photoemission Spectroscopy," *Physical Review Letters*, vol. 121, nov 2018.

[104] P. Monçeau, N. P. Ong, A. M. Portis, A. Meerschaut, and J. Rouxel, "Electric Field Breakdown of Charge-Density-Wave—Induced Anomalies in $NbSe_3$," *Physical Review Letters*, vol. 37, pp. 602–606, sep 1976.

[105] E. Abrahams, J. Sólyom, and F. Woynarovich, "The Landau theory of phase transitions in TTF-TCNQ (tetrathiafulvalene-tetracyanoquinodimethane)," *Physical Review B*, vol. 16, pp. 5238–5249, dec 1977.

[106] A. J. Berlinsky, "Introduction to Highly Conducting One-Dimensional Solids," in *Highly Conducting One-Dimensional Solids*, pp. 1–16, Springer US, 1979.

[107] K. D. Bronsema, G. W. Bus, and G. A. Wiegers, "The crystal structure of vanadium ditelluride, $V_{(1+x)}Te_2$," *Journal of Solid State Chemistry*, vol. 53, pp. 415–421, jul 1984.

[108] T. Ohtani, K. Hayashi, M. Nakahira, and H. Nozaki, "Phase transition in $V_{1+x}Te_2$ ($0.04 \leq x \leq 0.11$)," *Solid State Communications*, vol. 40, pp. 629–631, nov 1981.

[109] T. Ohtani, S. Onoue, and M. Nakahira, "Phase relationships and properties in the V-Te system," *Materials research bulletin*, vol. 19, no. 10, pp. 1367–1375, 1984.

[110] H. Chen, Z. Li, X. Fan, L. Guo, and X. Chen, "Quantum linear magnetoresistance in $NbTe_2$," *Solid State Communications*, vol. 275, pp. 16–20, jul 2018.

[111] C. Battaglia, H. Cercellier, F. Clerc, L. Despont, M. G. Garnier, C. Koitzsch, P. Aebi, H. Berger, L. Forró, and C. Ambrosch-Draxl, "Fermi-surface-induced lattice distortion in $NbTe_2$," *Physical Review B*, vol. 72, nov 2005.

[112] S. Nagata, T. Abe, S. Ebisu, Y. Ishihara, and K. Tsutsumi, "Superconductivity in the metallic layered compound $NbTe_2$," *Journal of Physics and Chemistry of Solids*, vol. 54, pp. 895–899, aug 1993.

[113] M. H. Van Maaren and G. M. Schaeffer, "Some new superconducting group V^a dichalcogenides," *Physics Letters A*, vol. 24, no. 12, pp. 645–646, 1967.

[114] H. Chen, Z. Li, L. Guo, and X. Chen, "Anisotropic magneto-transport and magnetic properties of low-temperature phase of $TaTe_2$," *EPL (Europhysics Letters)*, vol. 117, p. 27009, jan 2017.

[115] C. Chen, H.-S. Kim, A. S. Admasu, S.-W. Cheong, K. Haule, D. Vanderbilt, and W. Wu, "Trimer bonding states on the surface of the transition-metal dichalcogenide $TaTe_2$," *Physical Review B*, vol. 98, nov 2018.

[116] Y. Liu, W. J. Lu, D. F. Shao, L. Zu, X. C. Kan, W. H. Song, and Y. P. Sun, "Structural, electrical, and thermoelectric properties of distorted 1T-$Ta_{1-x}Nb_xTe_2$ single crystals," *EPL (Europhysics Letters)*, vol. 109, p. 17003, jan 2015.

[117] A. H. Thompson and B. G. Silbernagel, "Magnetic properties of VSe_2: Inferences from the study of metal-rich $V_{1+\delta}Se_2$ compounds," *Journal of Applied Physics*, vol. 49, pp. 1477–1479, mar 1978.

[118] L. F. Schneemeyer and M. J. Sienko, "The effect of niobium substitution on charge density wave anomalies in vanadium diselenide," *Journal of the Less Common Metals*, vol. 62, pp. 343–348, nov 1978.

[119] A. H. Thompson and B. G. Silbernagel, "Correlated magnetic and transport properties in the charge-density-wave states of VSe_2," *Physical Review B*, vol. 19, pp. 3420–3426, apr 1979.

[120] J. Pandey and A. Soni, "Electron-phonon interactions and two-phonon modes associated with charge density wave in single crystalline 1T-VSe_2," *Physical Review Research*, vol. 2, jul 2020.

[121] T. Valla, A. V. Fedorov, P. D. Johnson, P. A. Glans, C. McGuinness, K. E. Smith, E. Y. Andrei, and H. Berger, "Quasiparticle Spectra, Charge-Density Waves, Superconductivity, and Electron-Phonon Coupling in 2H- $NbSe_2$," *Physical review letters*, vol. 92, no. 8, p. 086401, 2004.

[122] F. J. Di Salvo, J. A. Wilson, B. G. Bagley, and J. V. Waszczak, "Effects of doping on charge-density waves in layer compounds," *Physical Review B*, vol. 12, no. 6, p. 2220, 1975.

[123] T. Kumakura, H. Tan, T. Handa, M. Morishita, and H. Fukuyama, "Charge density waves and superconductivity in 2H-$TaSe_2$," *Czechoslovak Journal of Physics*, vol. 46, pp. 2611–2612, may 1996.

[124] F. Borsa, D. R. Torgeson, and H. R. Shanks, "Charge-density wave amplitudes in $2H - NbSe_2$ and $2H - TaSe_2$ determined by ^{77}Se NMR," *Phys. Rev. B*, vol. 15, pp. 4576–4579, May 1977.

[125] C.-S. Lian, C. Heil, X. Liu, C. Si, F. Giustino, and W. Duan, "Coexistence of Superconductivity with Enhanced Charge Density Wave Order in the Two-Dimensional Limit of $TaSe_2$," *The Journal of Physical Chemistry Letters*, vol. 10, pp. 4076–4081, jul 2019.

[126] T. Tsuda, H. Yasuoka, Y. Kitaoka, and F. J. Di Salvo, "^{51}V NMR study of the phase transition in 1T-VS_2," *Journal of Magnetism and Magnetic Materials*, vol. 31, pp. 1101–1102, 1983.

[127] M. Mulazzi, A. Chainani, N. Katayama, R. Eguchi, M. Matsunami, H. Ohashi, Y. Senba, M. Nohara, M. Uchida, H. Takagi, and S. Shin, "Absence of nesting in the charge-density-wave system 1T-VS_2 as seen by photoelectron spectroscopy," *Physical Review B*, vol. 82, aug 2010.

[128] X. Sun, T. Yao, Z. Hu, Y. Guo, Q. Liu, S. Wei, and C. Wu, "In situ unravelling structural modulation across the charge-density-wave transition in vanadium disulfide," *Physical Chemistry Chemical Physics*, vol. 17, no. 20, pp. 13333–13339, 2015.

[129] M. Leroux, M. Le Tacon, M. Calandra, L. Cario, M.-A. Méasson, P. Diener, E. Borrissenko, A. Bosak, and P. Rodière, "Anharmonic suppression of charge density waves in 2H-NbS_2," *Physical Review B*, vol. 86, p. 155125, Oct 2012.

[130] M. Leroux, L. Cario, A. Bosak, and P. Rodière, "Traces of charge density waves in NbS_2," *Physical Review B*, vol. 97, may 2018.

[131] Y. D. Wang, W. L. Yao, Z. M. Xin, T. T. Han, Z. G. Wang, L. Chen, C. Cai, Y. Li, and Y. Zhang, "Band insulator to Mott insulator transition in 1T-TaS_2," *Nature communications*, vol. 11, no. 1, pp. 1–7, 2020.

[132] J. Joshi, H. M. Hill, S. Chowdhury, C. D. Malliakas, F. Tavazza, U. Chatterjee, A. R. H. Walker, and P. M. Vora, "Short-range charge density wave order in 2H- TaS_2," *Physical Review B*, vol. 99, no. 24, p. 245144, 2019.

[133] B. Hildebrand, T. Jaouen, M.-L. Mottas, G. Monney, C. Barreteau, E. Giannini, D. R. Bowler, and P. Aebi, "Local Real-Space View of the Achiral 1T-$TiSe_2$ $2 \times 2 \times 2$ Charge Density Wave," *Phys. Rev. Lett.*, vol. 120, p. 136404, Mar 2018.

[134] F. J. Di Salvo, D. E. Moncton, and J. V. Waszczak, "Electronic properties and superlattice formation in the semimetal $TiSe_2$," *Phys. Rev. B*, vol. 14, pp. 4321–4328, Nov 1976.

[135] C. van Efferen, J. Berges, J. Hall, E. van Loon, S. Kraus, A. Schobert, T. Wekking, F. Huttmann, E. Plaar, N. Rothenbach, K. Ollefs, L. M. Arruda, N. Brookes, G. Schönhoff, K. Kummer, H. Wende, T. Wehling, and T. Michely, "A full gap above the Fermi level: the charge density wave of monolayer VS_2," *Nature Communications*, vol. 12, nov 2021.

[136] J. Yang, W. Wang, Y. Liu, H. Du, W. Ning, G. Zheng, C. Jin, Y. Han, N. Wang, Z. Yang, M. Tian, and Y. Zhang, "Thickness dependence of the charge-density-wave transition temperature in VSe_2," *Applied Physics Letters*, vol. 105, p. 063109, aug 2014.

[137] H. K. ONNES, "The superconductivity of mercury," *Comm. Phys. Lab. Univ. Leiden*, vol. 122, pp. 122–124, 1911.

[138] J. Bardeen, L. N. Cooper, and J. R. Schrieffer, "Theory of Superconductivity," *Phys. Rev.*, vol. 108, pp. 1175–1204, Dec 1957.

[139] L. D. Landau and V. L. Ginzburg, "On the theory of superconductivity," *Zh. Eksp. Teor. Fiz.*, vol. 20, p. 1064, 1950.

[140] K. Onabe, M. Naito, and S. Tanaka, "Anisotropy of Upper Critical Field in Superconducting 2H-NbS_2," *Journal of the Physical Society of Japan*, vol. 45, pp. 50–58, jul 1978.

[141] M. S. Bahramy, O. J. Clark, B.-J. Yang, J. Feng, L. Bawden, J. M. Riley, I. Marković, F. Mazzola, V. Sunko, D. Biswas, *et al.*, "Ubiquitous formation of bulk Dirac cones and topological surface states from a single orbital manifold in transition-metal dichalcogenides," *Nature materials*, vol. 17, no. 1, pp. 21–28, 2018.

[142] J. Guo, C. Huang, H. Luo, H. Yang, L. Wei, S. Cai, Y. Zhou, H. Zhao, X. Li, Y. Li, K. Yang, A. Li, P. Sun, J. Li, Q. Wu, R. J. Cava, and L. Sun, "Observation of three superconducting transitions in the pressurized CDW-bearing compound $TaTe_2$," *Phys. Rev. Materials*, vol. 6, p. L051801, May 2022.

[143] B. Wang, Y. Liu, K. Ishigaki, K. Matsubayashi, J. Cheng, W. Lu, Y. Sun, and Y. Uwatoko, "Pressure-induced bulk superconductivity in a layered transition-metal dichalcogenide 1T-tantalum selenium," *Phys. Rev. B*, vol. 95, p. 220501, Jun 2017.

[144] K. Manikandan, R. Pervin, C. Saravanan, M. Sathiskumar, N. Chakraborty, P. M. Shirage, S. Mondal, V. Srihari, H. K. Poswal, and S. Arumugam, "Influence of pressure on the transport, magnetic, and structural properties of superconducting $Cr_{0.0009}NbSe_2$ single crystal," *RSC Advances*, vol. 10, no. 22, pp. 13112–13125, 2020.

[145] B. S. de Lima, R. R. de Cassia, F. B. Santos, L. E. Correa, T. W. Grant, A. L. R. Manesco, G. W. Martins, L. T. F. Eleno, M. S. Torikachvili, and A. J. S. Machado, "Properties and superconductivity in Ti-doped $NiTe_2$ single crystals," *Solid State Communications*, vol. 283, pp. 27–31, nov 2018.

[146] M. Mandal and R. P. Singh, "Emergent superconductivity by Re doping in type -II Weyl semimetal $NiTe_2$," *Journal of Physics: Condensed Matter*, vol. 33, p. 135602, jan 2021.

[147] J. J. Yang, Y. J. Choi, Y. S. Oh, A. Hogan, Y. Horibe, K. Kim, B. I. Min, and S.-W. Cheong, "Charge-Orbital Density Wave and Superconductivity in the Strong Spin-Orbit Coupled $IrTe_2$:Pd," *Phys. Rev. Lett.*, vol. 108, p. 116402, Mar 2012.

[148] S. Pyon, K. Kudo, and M. Nohara, "Superconductivity Induced by Bond Breaking in the Triangular Lattice of $IrTe_2$," *Journal of the Physical Society of Japan*, vol. 81, p. 053701, may 2012.

[149] H. Luo, J. Strychalska-Nowak, J. Li, J. Tao, T. Klimczuk, and R. J. Cava, "S-Shaped Suppression of the Superconducting Transition Temperature in Cu-Intercalated $NbSe_2$," *Chemistry of Materials*, vol. 29, pp. 3704–3712, apr 2017.

[150] R. Pervin, M. Krishnan, A. K. Rana, S. Arumugam, and P. M. Shirage, "Effect of Cr atoms in vortex dynamics of $NbSe_2$ superconductor and study of second magnetization peak effect," *Materials Research Express*, vol. 5, p. 076001, jul 2018.

[151] S. C. Ganguli, H. Singh, R. Ganguly, V. Bagwe, A. Thamizhavel, and P. Raychaudhuri, "Orientational coupling between the vortex lattice and the crystalline lattice in a weakly pinned $Co_{0.0075}NbSe_2$ single crystal," *Journal of Physics: Condensed Matter*, vol. 28, p. 165701, mar 2016.

[152] S. Naik, G. K. Pradhan, S. G. Bhat, B. C. Behera, P. S. A. Kumar, S. L. Samal, and D. Samal, "The effect of Sn intercalation on the superconducting properties of 2H-$NbSe_2$," *Physica C: Superconductivity and its Applications*, vol. 561, pp. 18–23, jun 2019.

[153] M. Iavarone, R. Di Capua, G. Karapetrov, A. E. Koshelev, D. Rosenmann, H. Claus, C. D. Malliakas, M. G. Kanatzidis, T. Nishizaki, and N. Kobayashi, "Effect of magnetic impurities on the vortex lattice properties in $NbSe_2$ single crystals," *Phys. Rev. B*, vol. 78, p. 174518, Nov 2008.

[154] E. Navarro-Moratalla, J. O. Island, S. Mañas-Valero, E. Pinilla-Cienfuegos, A. Castellanos-Gomez, J. Quereda, G. Rubio-Bollinger, L. Chirolli, J. A. Silva-Guillén, N. Agraït, G. A. Steele, F. Guinea, H. S. J. van der Zant, and E. Coronado, "Enhanced superconductivity in atomically thin TaS_2," *Nature Communications*, vol. 7, mar 2016.

[155] N. W. Ashcroft and N. D. Mermin, *Solid state physics*. Cengage Learning, 2022.

[156] C. Kittel, *Introduction to solid state physics*. John Wiley & sons, inc, 2005.

[157] J. Chen, D. Singh, and H. Krakauer, "Local-density description of antiferromagnetic Cr," *Physical Review B*, vol. 38, pp. 12834–12836, dec 1988.

[158] K. Kato, S. Iida, K. Yanai, and K. Mizushima, "Ferrimagnetic ferroelectricity of Fe_3O_4," *Journal of Magnetism and Magnetic Materials*, vol. 31-34, pp. 783–784, feb 1983.

[159] E. Martino, C. Putzke, M. König, P. J. W. Moll, H. Berger, D. LeBoeuf, M. Leroux, C. Proust, A. Akrap, H. Kirmse, C. Koch, S. Zhang, Q. Wu, O. V. Yazyev, L. Forró, and K. Semeniuk, "Unidirectional Kondo scattering in layered NbS_2," *npj 2D Materials and Applications*, vol. 5, nov 2021.

[160] R. Gill, "Superconductivity and ferromagnetism in nanomaterial $NbSe_2$," in *AIP Conference Proceedings*, Author(s), 2017.

[161] R. Pervin, M. Krishnan, A. Sonachalam, and P. M. Shirage, "Coexistence of superconductivity and ferromagnetism in defect-induced $NbSe_2$ single crystals," *Journal of Materials Science*, vol. 54, pp. 11903–11912, jun 2019.

[162] D. Wickramaratne, S. Khmelevskyi, D. F. Agterberg, and I. I. Mazin, "Ising Superconductivity and Magnetism in $NbSe_2$," *Phys. Rev. X*, vol. 10, p. 041003, Oct 2020.

[163] D. C. Freitas, R. Weht, A. Sulpice, G. Remenyi, P. Strobel, F. Gay, J. Marcus, and M. Núñez-Regueiro, "Ferromagnetism in layered metastable $1T$-$CrTe_2$," *Journal of Physics: Condensed Matter*, vol. 27, p. 176002, apr 2015.

[164] C. M. Fang, C. F. van Bruggen, R. A. de Groot, G. A. Wiegers, and C. Haas, "The electronic structure of the metastable layer compound," *Journal of Physics: Condensed Matter*, vol. 9, pp. 10173–10184, nov 1997.

[165] K. Chen, J. Deng, Y. Yan, Q. Shi, T. Chang, X. Ding, J. Sun, S. Yang, and J. Z. Liu, "Diverse electronic and magnetic properties of CrS_2 enabling strain-controlled 2D lateral heterostructure spintronic devices," *npj Computational Materials*, vol. 7, may 2021.

[166] X. Zhang, T. Yu, Q. Xue, M. Lei, and R. Jiao, "Critical behavior and magnetocaloric effect in monoclinic Cr_5Te_8," *Journal of Alloys and Compounds*, vol. 750, pp. 798–803, 2018.

[167] K. Lukoschus, S. Kraschinski, C. Näther, W. Bensch, and R. K. Kremer, "Magnetic properties and low temperature X-ray studies of the weak ferromagnetic monoclinic and trigonal chromium tellurides Cr_5Te_8," *Journal of Solid State Chemistry*, vol. 177, no. 3, pp. 951–959, 2004.

[168] Z.-L. Huang, W. Kockelmann, M. Telling, and W. Bensch, "A neutron diffraction study of structural and magnetic properties of monoclinic Cr_5Te_8," *Solid state sciences*, vol. 10, no. 8, pp. 1099–1105, 2008.

[169] Y. Wang, J. Yan, J. Li, S. Wang, M. Song, J. Song, Z. Li, K. Chen, Y. Qin, L. Ling, H. Du, L. Cao, X. Luo, Y. Xiong, and Y. Sun, "Magnetic anisotropy and topological Hall effect in the trigonal chromium tellurides Cr_5Te_8," *Phys. Rev. B*, vol. 100, p. 024434, Jul 2019.

[170] Y. Liu and C. Petrovic, "Anomalous Hall effect in the trigonal Cr_5Te_8," *Phys. Rev. B*, vol. 98, p. 195122, Nov 2018.

[171] X.-H. Luo, W.-J. Ren, and Z.-D. Zhang, "Magnetic properties and magnetocaloric effect of a trigonal Te-rich Cr_5Te_8 single crystal," *Journal of Magnetism and Magnetic Materials*, vol. 445, pp. 37–43, 2018.

[172] A. B. De Vries and C. Haas, "Magnetic susceptibility and nuclear magnetic resonance of vanadium sulfides," *Journal of Physics and Chemistry of Solids*, vol. 34, no. 4, pp. 651–659, 1973.

[173] B. G. Silbernagel, R. B. Levy, and F. R. Gamble, "Magnetic properties of V_5S_8: An NMR study," *Phys. Rev. B*, vol. 11, pp. 4563–4570, Jun 1975.

[174] H. Nozaki and Y. Ishizawa, "An evidence of spin flopping in V_5S_8 by magnetoresistance experiments," *Physics Letters A*, vol. 63, no. 2, pp. 131–132, 1977.

[175] Y. Kitaoka and H. Yasuoka, "NMR investigations on the spin fluctuations in itinerant antiferromagnets. II. V_3S_4 and V_5S_8," *Journal of the Physical Society of Japan*, vol. 48, no. 6, pp. 1949–1956, 1980.

[176] M. Nakanishi, K. Yoshimura, K. Kosuge, T. Goto, T. Fujii, and J. Takada, "Anomalous field-induced magnetic transitions in V_5X_8 (X=S,Se)," *Journal of Magnetism and Magnetic Materials*, vol. 221, no. 3, pp. 301–306, 2000.

[177] M. Moustafa, T. Zandt, C. Janowitz, and R. Manzke, "Growth and band gap determination of the ZrS_xSe_{2-x} single crystal series," *Physical Review B*, vol. 80, jul 2009.

[178] X. Zhao, T. Wang, G. Wang, X. Dai, C. Xia, and L. Yang, "Electronic and magnetic properties of 1T-HfS_2 by doping transition-metal atoms," *Applied Surface Science*, vol. 383, pp. 151–158, oct 2016.

[179] H. Wang, Z. Qiu, W. Xia, C. Ming, Y. Han, L. Cao, J. Lu, P. Zhang, S. Zhang, H. Xu, and Y.-Y. Sun, "Semimetal or Semiconductor: The Nature of High Intrinsic Electrical Conductivity in TiS_2," *The Journal of Physical Chemistry Letters*, vol. 10, pp. 6996–7001, oct 2019.

[180] K. Chen, M. Song, Y.-Y. Sun, H. Xu, D.-C. Qi, Z. Su, X. Gao, Q. Xu, J. Hu, J. Zhu, R. Zhang, J. Wang, L. Zhang, L. Cao, Y. Han, and Y. Xiong, "Defects controlled doping and electrical transport in TiS_2 single crystals," *Applied Physics Letters*, vol. 116, p. 121901, mar 2020.

[181] A. J. Grant, T. M. Griffiths, G. D. Pitt, and A. D. Yoffe, "The electrical properties and the magnitude of the indirect gap in the semiconducting transition metal dichalcogenide layer crystals," *Journal of Physics C: Solid State Physics*, vol. 8, pp. L17–L23, jan 1975.

[182] B. S. Kim, J.-W. Rhim, B. Kim, C. Kim, and S. R. Park, "Determination of the band parameters of bulk 2H-MX_2 (M= Mo, W; X= S, Se) by angle-resolved photoemission spectroscopy," *Scientific reports*, vol. 6, no. 1, pp. 1–7, 2016.

[183] Y. Zhao, J. Qiao, P. Yu, Z. Hu, Z. Lin, S. P. Lau, Z. Liu, W. Ji, and Y. Chai, "Extraordinarily strong interlayer interaction in 2D layered PtS_2," *Advanced materials*, vol. 28, no. 12, pp. 2399–2407, 2016.

[184] S. Lebègue, T. Björkman, M. Klintenberg, R. M. Nieminen, and O. Eriksson, "Two-Dimensional Materials from Data Filtering and Ab Initio Calculations," *Phys. Rev. X*, vol. 3, p. 031002, Jul 2013.

[185] Y. Wang, Y. Li, and Z. Chen, "Not your familiar two dimensional transition metal disulfide: structural and electronic properties of the PdS_2," *Journal of Materials Chemistry C*, vol. 3, no. 37, pp. 9603–9608, 2015.

[186] B. Jariwala, D. Voiry, A. Jindal, B. A. Chalke, R. Bapat, A. Thamizhavel, M. Chhowalla, M. Deshmukh, and A. Bhattacharya, "Synthesis and Characterization of ReS_2 and $ReSe_2$ Layered Chalcogenide Single Crystals," *Chemistry of Materials*, vol. 28, pp. 3352–3359, may 2016.

[187] L. S. Hart, J. L. Webb, S. Dale, S. J. Bending, M. Mucha-Kruczynski, D. Wolverson, C. Chen, J. Avila, and M. C. Asensio, "Electronic bandstructure and van der Waals coupling of $ReSe_2$ revealed by high-resolution angle-resolved photoemission spectroscopy," *Scientific Reports*, vol. 7, jul 2017.

[188] M. YAĞMURCUKARDEŞ, "Stable anisotropic single-layer of $ReTe_2$: a first principles prediction," *TURKISH JOURNAL OF PHYSICS*, vol. 44, pp. 450–457, oct 2020.

[189] P. F. Weck, E. Kim, and K. R. Czerwinski, "Semiconducting layered technetium dichalcogenides: insights from first-principles," *Dalton Transactions*, vol. 42, no. 43, p. 15288, 2013.

[190] J. Kondo, "Resistance Minimum in Dilute Magnetic Alloys," *Progress of Theoretical Physics*, vol. 32, pp. 37–49, jul 1964.

[191] L. Maritato, C. Adamo, C. Barone, G. M. D. Luca, A. Galdi, P. Orgiani, and A. Y. Petrov, "Low-temperature resistivity of $La_{0.7}Sr_{0.3}MnO_3$ ultra thin films: Role of quantum interference effects," *Physical Review B*, vol. 73, mar 2006.

[192] J. Joseph, C. Bansal, K. J. Reddy, and A. Rajanikanth, "Electron–electron interaction dominated resistivity minimum in quasi-continuous Ag nanocluster films," *AIP Advances*, vol. 10, p. 125223, dec 2020.

[193] X. Ding, J. Xing, G. Li, L. Balicas, K. Gofryk, and H.-H. Wen, "Crossover from Kondo to Fermi-liquid behavior induced by high magnetic field in 1T-VTe_2 single crystals," *Physical Review B*, vol. 103, mar 2021.

[194] S. Barua, M. C. Hatnean, M. R. Lees, and G. Balakrishnan, "Signatures of the Kondo effect in VSe_2," *Scientific Reports*, vol. 7, sep 2017.

[195] Y. Wang, C. Xie, J. Li, Z. Du, L. Cao, Y. Han, L. Zu, H. Zhang, H. Zhu, X. Zhang, Y. Xiong, and W. Zhao, "Weak Kondo effect in the monocrystalline transition metal dichalcogenide $ZrTe_2$," *Phys. Rev. B*, vol. 103, p. 174418, May 2021.

[196] Q. Cao, F. F. Yun, L. Sang, F. Xiang, G. Liu, and X. Wang, "Defect introduced paramagnetism and weak localization in two-dimensional metal VSe_2," *Nanotechnology*, vol. 28, p. 475703, oct 2017.

[197] B. H. Brandow, "Electronic structure of Mott insulators," *Advances in Physics*, vol. 26, pp. 651–808, sep 1977.

[198] N. Tsuda, K. Nasu, A. Fujimori, and K. Siratori, "Electron-Electron Interaction and Electron Correlation," in *Springer Series in Solid-State Sciences*, pp. 119–155, Springer Berlin Heidelberg, 2000.

[199] M. M. Qazilbash, M. Brehm, B.-G. Chae, P.-C. Ho, G. O. Andreev, B.-J. Kim, S. J. Yun, A. V. Balatsky, M. B. Maple, F. Keilmann, H.-T. Kim, and D. N. Basov, "Mott Transition in VO_2 Revealed by Infrared Spectroscopy and Nano-Imaging," *Science*, vol. 318, pp. 1750–1753, dec 2007.

[200] V. I. Anisimov, M. A. Korotin, and E. Z. Kurmaev, "Band-structure description of Mott insulators (NiO, MnO, FeO, CoO)," *Journal of Physics: Condensed Matter*, vol. 2, pp. 3973–3987, apr 1990.

Chapter 2

Experimental Details

2.1 Single Crystal Growth

Figure 2.1: (a) Diffusion pump used for vacuum sealing. (b) Sealing of a quartz tube under vacuum using Oxygen and liquefied petroleum gas (LPG) together. (c) Muffle furnace with a maximum allowable temperature of 1250°C. (d) 3-zone gradient tube furnace with a maximum allowable temperature of 1100°C.

2.1.1 Chemical Vapor Transport

Bunsen first discussed about the formation of minerals by the chemical vapor transport method (CVT) in nature without the influence of human [1, 2]. He noticed the formation of crystalline Fe_2O_3 in presence of volcanic gases containing gaseous hydrogen chloride. In laboratory, Van Arkel and de Boer first applied the CVT method for the preparation of pure Ti, Hf, Zr, and Th metal in 1925 [3]. In CVT method, stoichiometric amount of compounds are mixed and loaded in a quartz tube with a transport agent. Then, the quartz tube is sealed under vacuum and kept inside a gradient tube furnace. The precursors are kept at one side and transported from one end to another end with the help of vaporized transport agent. Mostly crystallized Iodine is used as transport agent which vaporizes above 457.5 K. Also, chloride, bromide of metals such as VCl_3, $CoCl_2$, $TaCl_5$, $CoBr_2$, $TeCl_4$ are used as transport agent which break down and form Chlorine or Bromine gases [4–6]. Depending on the nature of reaction, transport takes place such as for endothermic process (absorbs heat and cools the surrounding) transportation is from hot(T_1) to cold end (T_2) whereas for exothermic process (releases heat and heated the surrounding) it is in the reverse direction. The schematic diagram of the CVT process in a conventional two-zone furnace is shown in Fig. 2.2. Most of the TMDCs are reported to grow by the CVT method using various transport agents [4–7].

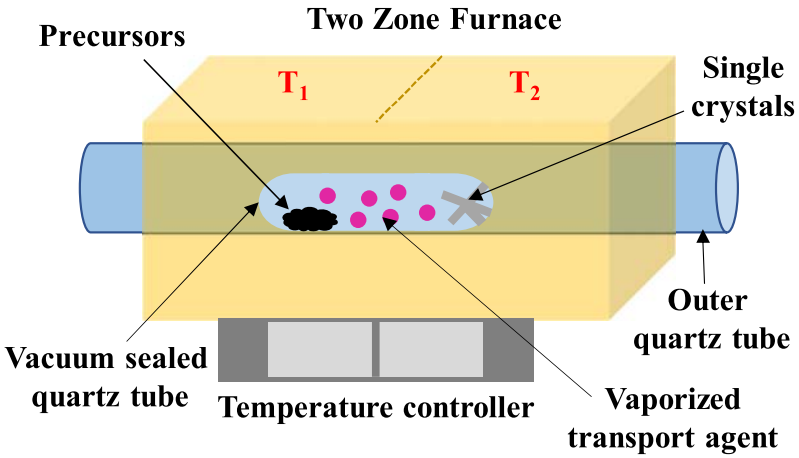

Figure 2.2: Schematic diagram of the CVT process in a conventional two-zone gradient tube furnace. This image is adapted from refernce [8].

2.1.2 Flux Growth Method

The flux growth method is also known as high temperature solution growth method [9]. Using this method, the components (solute) of the desired compound are dissolved

in the flux (solvent). Generally, the flux can be various metals like Sn, Bi, Te, Pt, compounds like MgI_2, or salts like NaCl, KCl, CsCl, AuCl, $ZnCl_2$ [10, 11]. The flux is selected based on solubility, inertness, melting temperature, toxicity, reaction with the container material, removableness, price, viscosity, density, and polarity. If the flux is one of the elements of the desired compound then it is called self-flux. In the self-flux process the components are not mixed in stoichiometric ratio. If the flux is a salt then the method is called salt-flux. In this method, the mixture is loaded in a crucible made of metals like Fe, Ni, Ta, W, Mo, Pt or oxides (Al_2O_3, MgO, ZrO_2), quartz, graphite, nitrides (BN) [12] and heated to very high temperature to melt the flux to dissolve the components within the flux. The whole process is done under vacuum. Finally, the mixture is cooled down slowly for the growth of single crystals and then the crystals are separated from the flux after centrifuging the tube by flipping the tube upside down. The schematic diagram of flux-growth method is shown in Fig. 2.3. The flux growth method is applied to grow TMDCs like VTe_2, $NiTe_2$, WTe_2 [13–15].

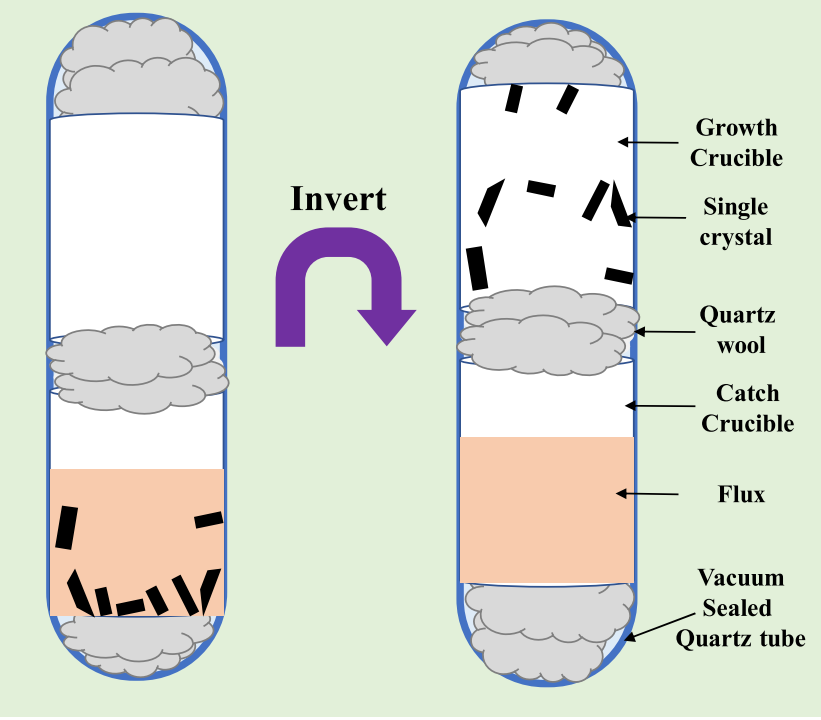

Figure 2.3: Schematic diagram of the flux-growth method. The position of the quartz tube during heat treatment is shown in the leftside image and the rightside image shows the postion of quartz tube during centrifuge process. This image is adapted from reference [16].

2.2 Compositional Characterization

2.2.1 EDX and FESEM Measurements

Energy dispersive X-ray analysis (EDX) is a technique used to determine the chemical composition of a sample. In this technique, at first, the sample is bombarded by electrons with high kinetic energy of 20-25 KeV. Thus, the electrons inside the sample get excited from lower energy levels to higher energy level or ejected from the inner shell completely. As a result, electron deficiencies are created in those inner shells. To compensate these void spaces, electrons from a higher energy level jump to the holes created in the low energy levels by emitting X-ray, the energy of which is equivalent to the energy difference between the two states.

EDX is attached to a field emission scanning electron microscopes (FESEM) to check the surface of a sample. The EDX or FESEM measurements are mostly done under vacuum of 10^{-6} mbar at room temperature using X-ray with a photon energy 20-25 KV. Generally, Silicon Lithium (Si(Li)) X-Ray Detectors are used to count the number of emitted X-rays. A schematic presentation of FESEM and EDX is shown in Fig. 2.4. Atomic spectra of each atom in the periodic table is unique from one another. Hence, by evaluating the energies of emitted X-rays, the elements can be identified. The EDX spectra usually shows peaks corresponding to the energy levels of higher X-ray counts, where each peak indicates different energy level of elements present within the sample. By evaluating relative intensities (counts) of these peaks, the atomic percentage of the sample is calculated.

We used the FEI Quanta^{TM} FEG 250 instrument for EDX analysis as shown in Fig. 2.5. The analysis is performed at several positions of sample surface to check the compositional homogeneity.

2.3 Structural Characterization

2.3.1 XRD Measurements

X-ray diffraction analysis (XRD) is a technique used to determine the crystal structure, phase, and crystallographic plane of single crystals. Crystals are regular arrays of atoms. When X-rays of wavelength λ incident on a plane of crystal at a certain angle θ to the plane, atoms scatter incident X-rays, primarily through interaction with the atom's electrons. This phenomenon is known as elastic scattering. Each electrons of that plane produce spherical waves. These waves produce constructive and destructive interference as determined by the Bragg's law [18] in Eq. 2.1

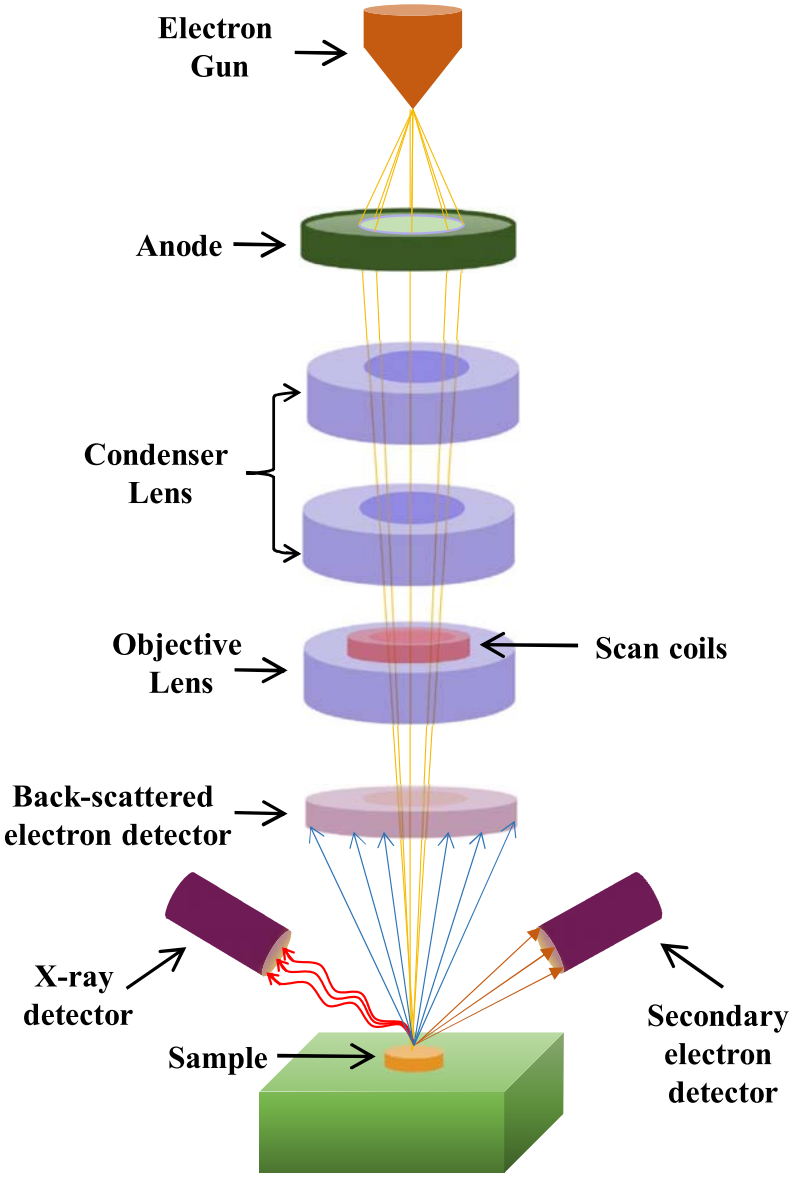

Figure 2.4: The schematic diagram of Energy dispersive X-ray analysis (EDX). This image is adapted from reference [17].

$$2dsin\theta = n\lambda \tag{2.1}$$

Here, d is the inter-planar spacing of the crystal, θ is the angle of diffraction, n denotes the order of diffraction, and λ is wavelength of the incident X-ray beam. Using this technique, monochromatic X-rays hit the sample and the incident X-rays make an XRD pattern according to Bragg's law. In case of polycrystal or powder sample,

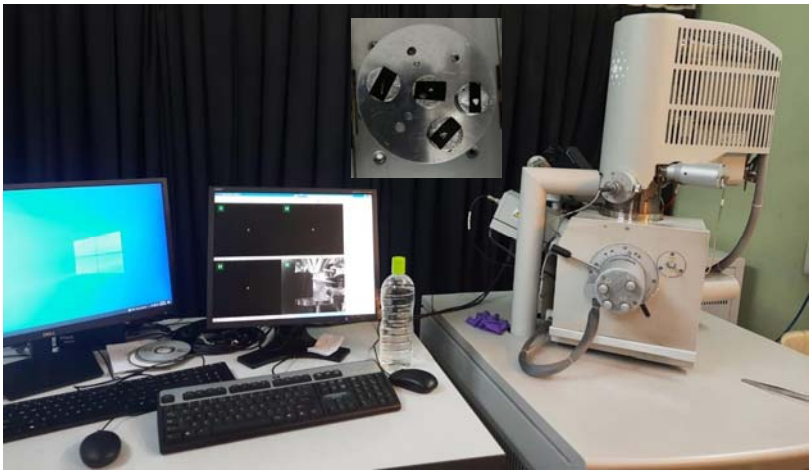

Figure 2.5: The image of FEI Quanta^{TM} FEG 250 instrument, available under the central equipment facilities of SNBNCBS. Inset shows samples are attached to the sample holder using conducting carbon tape.

the planes are randomly oriented. Hence, XRD pattern shows several peaks of several orientations. In case of a single crystal, planes are arranged parallel to each other and XRD pattern shows peaks in a single orientation only. The schematic diagram of X-ray diffraction measurements is shown in Fig. 2.6 (a). In general, a monochromatic beam of X-rays, Cu-K$_\alpha$ of wavelength $\lambda \approx 1.54\mathring{A}$ is used.

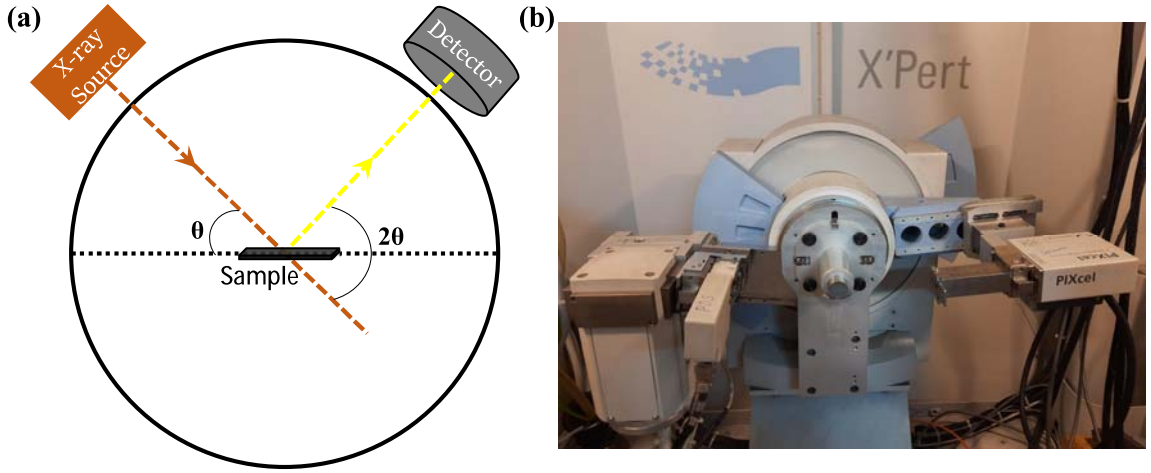

Figure 2.6: (a) The schematic diagram of X-ray diffraction measurements (XRD). This image is adapted from xrd.co. (b) The image of PANalytical X'Pert Pro instrument, available under the central equipment facilities of SNBNCBS.

We have used the Rigaku MiniFlex II (θ–2θ system), the PANalytical X'Pert Pro (θ–θ system), and the Rigaku smartLab 9 kW (θ–θ system) X-ray diffractometer using Cu-K$_\alpha$ radiation ($\lambda = 1.54$ $\mathring{A}$) to characterize the samples. The image of PANalytical X'Pert Pro instrument is shown in Fig. 2.6 (b). In θ–2θ scan, the X-ray source is fixed while the sample rotates at $\theta°$/min and the detector moves at $2\theta°$/min. In θ–θ scan,

the sample stage is fixed while both the X-ray source and the detector rotate at an angular speed of θ°/min simultaneously.

2.4 Thermal Transport Measurements

2.4.1 DSC Measurements

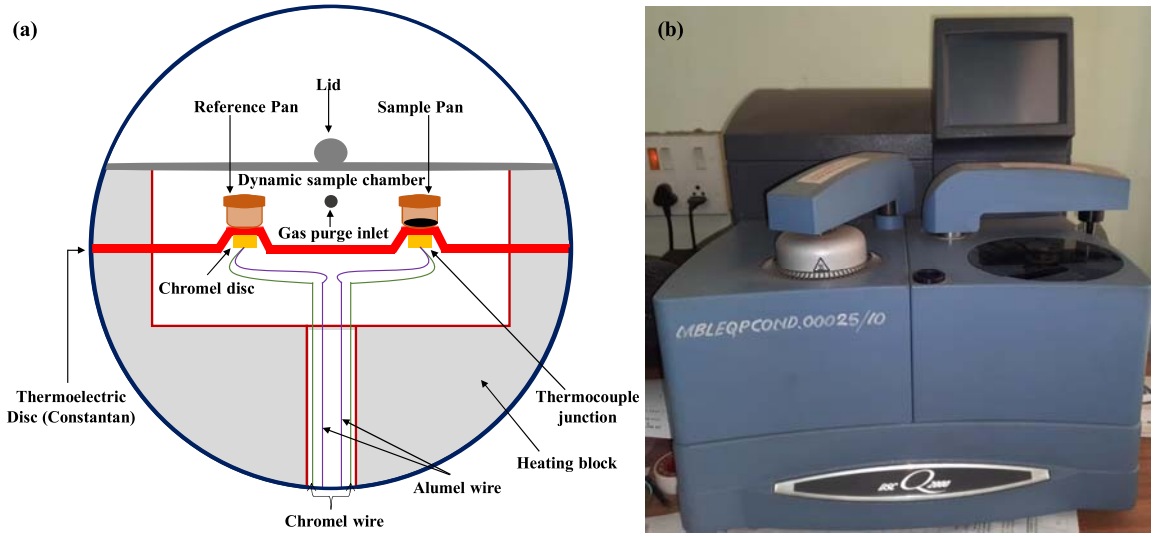

Figure 2.7: (a) The schematic diagram of a heat-flux DSC. This image is adapted from reference [19]. (b) The image of the Q2000 heat-flux DSC instrument, available under the central equipment facilities of SNBNCBS.

A Calorimeter is a tool to measure the amount of heat absorbed or produced in a reaction of chemical or electrical or mechanical. Also, it is used to measure the heat capacity of a material. The differential scanning calorimeter (DSC) is one of the most used calorimeter to study the type of phase transition of a sample such as the first order or second order transitions. The DSC operates in two methods [19], the first one is the heat-flux DSC (the schematic presentation and image of the instrument are shown in Fig.2.7) and the second one is the power compensated DSC (the schematic presentation is shown in Fig. 2.8). In the heat flux DSC, the sample pan and the reference pan are heated simultaneously in same furnace. The temperature difference is measured by a thermocouple and converted into heat flow rate via a calibration process. In the power compensated DSC, sample pan and the reference pan are heated separately in two separate furnaces in such a way that the temperature remain same in both pans. The difference in thermal power needed to keep them at the same temperature is measured and plotted as a function of temperature. From these measurements, we can get quantitative and qualitative information about the type of a phase transition, physical and chemical changes involving exothermic (heat release) or endothermic (heat

absorption) processes or changes in the heat capacity [20]. We used the Q2000 heat-flux DSC for our measurements at a temperature scan rate of 5-10 K/min within the temperature range of 113 K to 773 K as shown in Fig.2.7.

The sample is mounted on a thermoelectric disc encapsulated by a thermal conducting metal pan made of Al, Pt etc. An empty pan made of same metal as the sample pan is mounted on the thermoelectric disc as reference pan inside a furnace. The sample pan and reference pan are heated simultaneously by varying the furnace temperature. The heat transferred from the furnace to the sample pan and reference pan is measured by a thermocouple made up of chromel (an alloy made of Ni and Cr with weight ratio of approximately 9:1) and alumel (an alloy made of Ni, Al, Mn, Si with weight ratio of approximately 9.5:2:2:1) wires. The heat flow amount q is measured using Ohm's law using the relation $q = \Delta T/R$. Here, R is the thermal resistance of the thermoelectric disc and ΔT is the temperature difference between sample pan and reference pan which is proportional to the voltage difference between the thermocouple junctions. For refrigerated cooling systems (RCS), liquid nitrogen is used.

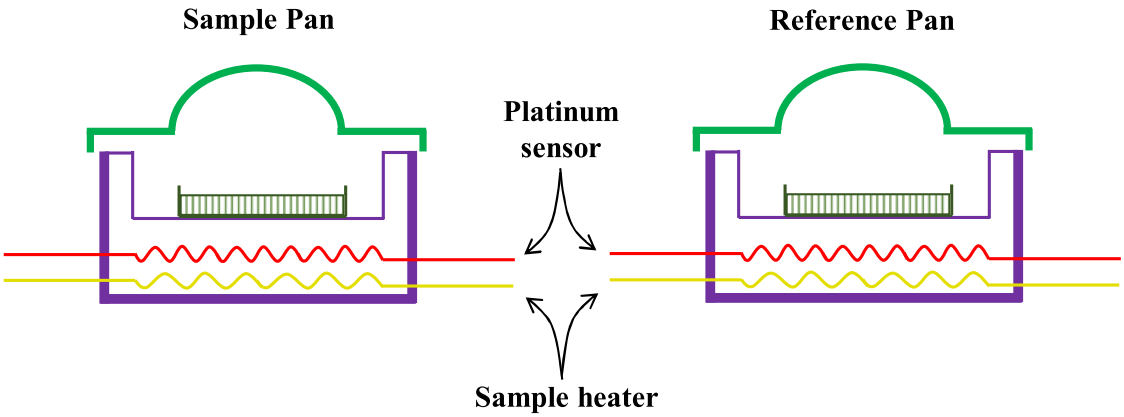

Figure 2.8: The schematic diagram of a power compensated DSC. This image is adapted from reference [19].

2.5 Electrical Transport Measurements

The layered TMDC materials explored in this thesis are metallic in nature having very low resistances ($\approx$ mΩ). To measure the resistivity of these samples we use a four probe low resistance circuit method [21] to avoid the contact resistance associated with the sample and the leads. A schematic representation of this method is shown in Fig. 2.9, where the a.c. current is passed through the outer two leads, while the voltage drop is measured across the inner two leads. Using ac excitations the change of polarity corresponding to the frequency of the ac signal and emf generated due to

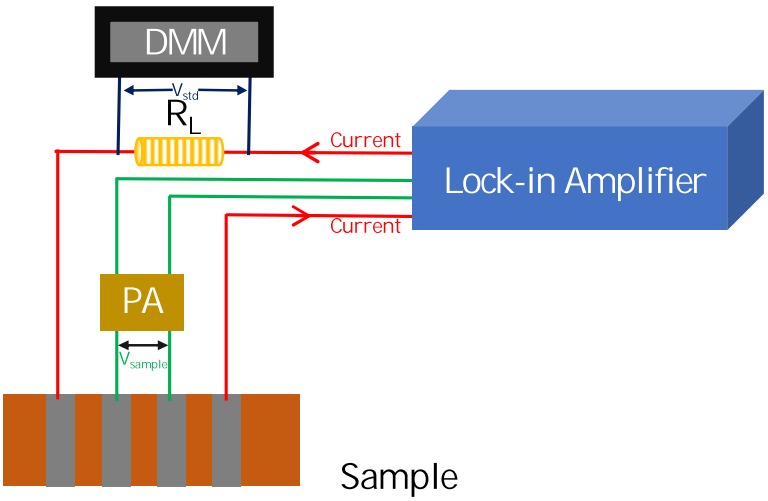

Figure 2.9: The schematic representation of four probe method used for resistivity measurement. DMM stands for digital multimeter

thermoelectric effect get canceled at the contacts. Since the same value of current is passing through the sample (R_{sample}) and the standard resistance (R_L), it can be written that $V_{sample}/R_{sample} = V_{std}/R_L$. Here, V_{sample} and V_{std} are the voltage drops across R_L and the inner two leads of the sample respectively. In an other way, it can be written as $R_{sample} = \frac{V_{sample}}{V_{std}} R_L$. Thus by measuring V_{sample} and V_{std}, we can get the value of sample resistance.

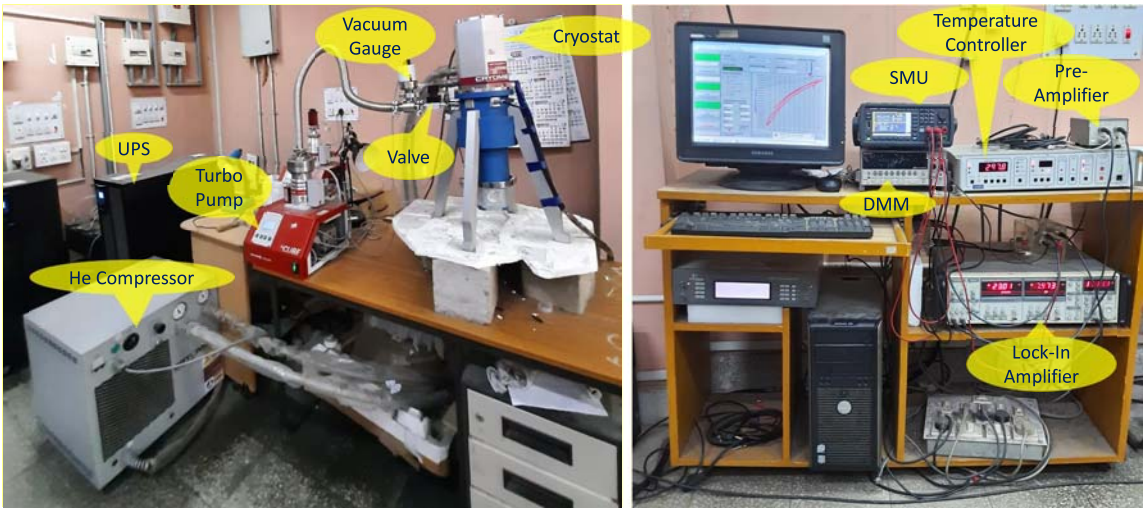

Figure 2.10: The low temperature resistivity set-up in our lab along with supporting instruments.

Also, electrical transport measurements were done in a physical property measurement system (PPMS) (Quantum Design^{TM} PPMS-9T) using standard puck and rotator set up as shown in Fig. 2.11 with the electrical current applied along the plane of sample (*ab*-plane). Magnetic field was applied at different polar angles with the axis

perpendicular to the *ab*-plane for magneto-transport measurements up to 9 T. Four copper (Cu) leads were connected to the sample by vacuum compatible silver epoxy (Epo-Tek H2OE). The sample temperature was varied between 2K and 330 K during the measurements. Also, we have performed a.c. resistivity measurement using a in-house resistivity set up as shown in Fig. 2.10. In this set up, a digital signal processing (DSP) lock-in amplifier [Stanford Research Systems 830 (SR830)] is used as a.c. current source through the outer two leads and to measure the voltage across inner two leads of the sample. The voltage drop across the inner two leads is transferred through a SR554 transformer preamplifier to the lock-in amplifier. The a.c. current of the order of few mA having frequency 111.11 Hz is sent through a load resistance (R_L) of the order of few kΩ. The voltage drop across the R_L is measured using Keithly 2000 digital multimeter (DMM). To reach lowest possible temperature (≈4 K), a closed cycle cryostat (CCR) of Oxford Instrument^{TM} (Optistat AC-V®) with pulsed tube refrigerator (PTR) is used. Also, for controlled heating an Oxford Instrument^{TM} ITC-503 temperature controller is used. A Rh-Fe thermometer is mounted on the sample mounting stage of the cryostat to detect the temperature of the sample environment. The whole set up is connected via General Purpose Interface Bus (GPIB) to a computer and the measurement is controlled using a program developed in LabVIEW^{TM}. Using this set up we can measure the resistivity within the temperature range of 4-325 K with a ramp rate of 1 K/min during heating.

2.6 DC Magnetic Measurements

2.6.1 VSM Measurements

The vibrating sample magnetometer (VSM) is a tool to measure the magnetization of a sample as a function of magnetic field and temperature. This was invented in 1955 by Simon Foner at Lincoln labs MIT. The VSM works on the principle of Faraday's law of induction which states that an emf (ϵ) is induced when magnetic flux (Φ_B) across the coil is changes with time, written as $\epsilon = -\frac{d\Phi_B}{dt}$. The direction of induced emf is governed by Lenz's law. Figure 2.12 (a) shows the schematic diagram of the VSM.

The sample is mounted on a thin nonmagnetic stick made of quartz or glass and kept at the centre of the magnetic poles. This stick is connected to the transducer assembly which vibrates the sample vertically in accordance with the sinusoidal signal generated by an oscillator. Under the application of magnetic field (B), a magnetic moment (m) is induced in the sample. Due to the vibration of sample, an emf is generated according to Faraday's law of induction associated with the variation of magnetic flux density linked with the pick-up coils. The induced emf can be written as $\epsilon = -\frac{d\Phi_B}{dz}\frac{dz}{dt}$. Here, z is the sample position along the z axis with respect to the centre of the electromagnet. Under

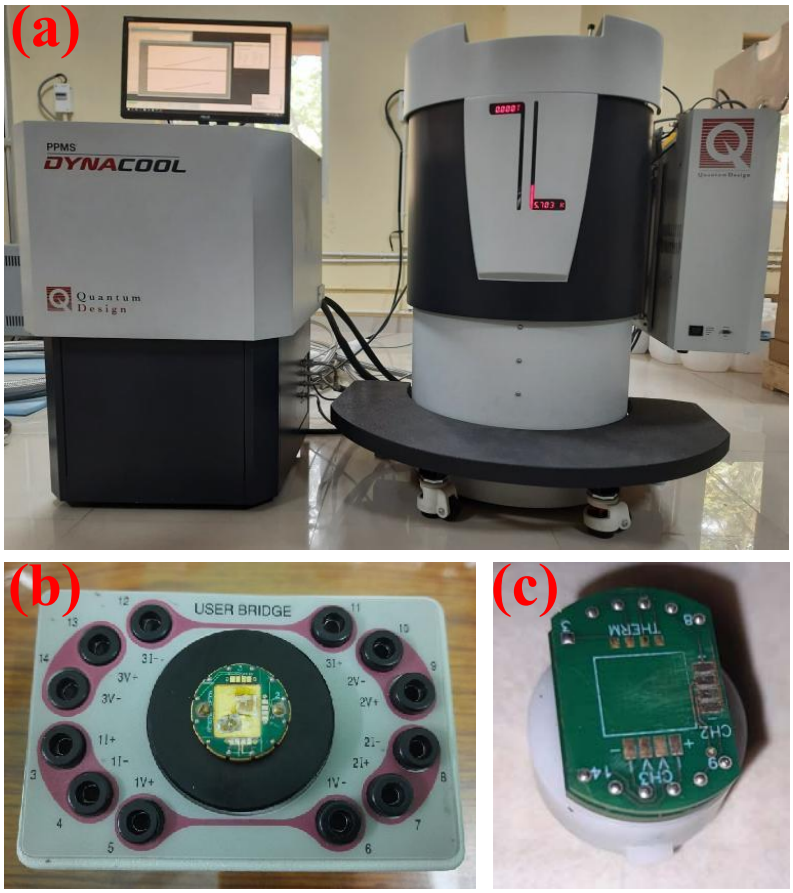

Figure 2.11: (a) Picture of the Quantum Design^{TM} PPMS-9T instrument available under technical research centre at SNBNCBS. (b) The picture of the ETO puck mounted on a puck-wiring test station. Two samples are connected to the ETO puck. (c) Picture of the rotator puck.

the application of sinusoidal oscillation, $Acos(\omega t)$ to sample stick, ϵ can be written as, $\epsilon = KmA\omega sin(\omega t)$ where K is the coupling constant, m is the magnetic moment of the sample, $\omega = 2\pi\nu$ where ν is the frequency of oscillation of the sample stick and A is the amplitude of oscillation. VSM can sense very low magnetic moment down to order of 10^{-5}-10^{-6} emu [23].

VSM measurements were performed using Quantum Design PPMS (Quantum Design^{TM} PPMS-9T) based VSM set up with magnetic field up to 9 Tesla by varying the temperature between 2 and 300 K during the measurements. Also, high temperature VSM measurement in the range of 300-1000 K is possible with a different set up in PPMS. We also used the Lake Shore Cryotronics^{TM} based VSM as shown in Fig. 2.12 (b) with a magnetic field up to 1.6 Tesla within the temperature range of 80-400 K for low temperature measurements and 300-1273 K for high temperature measurements. The temperature dependence of magnetization at different magnetic fields in zero-field-cooled (ZFC) and field-cooled (FC) protocol in the warming cycle has been carried out

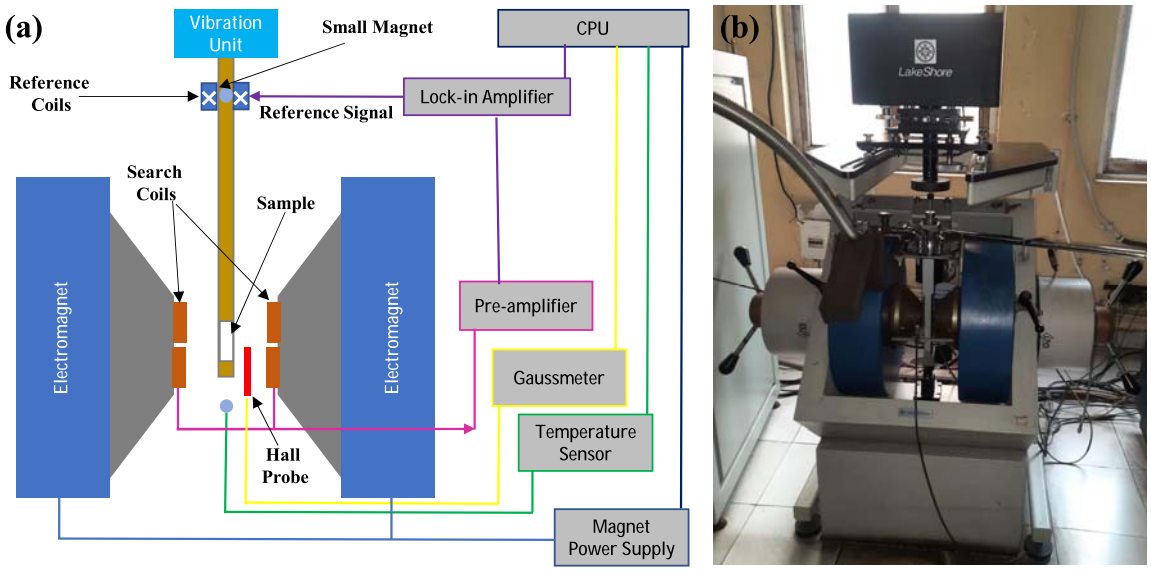

Figure 2.12: (a) Schematic diagram of vibrating sample magnetometer (VSM). This image is adapted from reference [22]. (b) Image of Lake Shore Cryotronics^{TM} based VSM instrument, available under the central equipment facilities of SNBNCBS.

and field dependence of magnetization(M(H)) has also been carried out for different temperatures in VSM.

2.6.2 SQUID Measurements

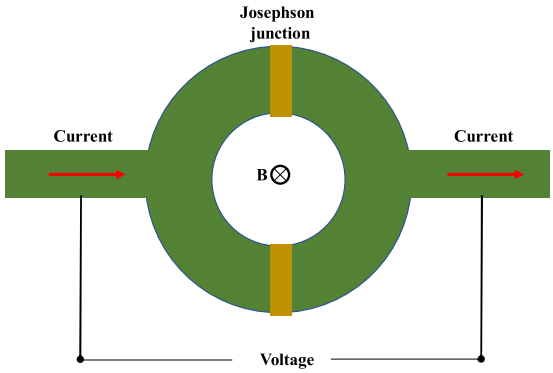

Figure 2.13: Schematic diagram of DC-SQUID loop containing two Josephson junctions. This image is adapted from reference [24].

The superconducting quantum interference device (SQUID) is a very sensitive magnetometer used to measure very low magnetic moment of sample [23]. SQUID operates on the basis of flux quantization (magnetic flux quantum, $\phi = h/2e = 2.0678 \times 10^{-15} Tm^2$ where e is the charge of electron and h is the Plank constant) and Josephson effect. SQUID is of two types, one is DC-SQUID based on DC Josephson effect and RF-SQUID based on AC Josephson effect. The Josephson effect is a

macroscopic quantum phenomena where tunneling of Cooper pairs of electron occurs through a junction between two superconductors in absence of applied voltage where the junction is made of insulating layer (S-I-S) or non-superconducting metal (S-N-S), or a physical constriction that weakens the superconductivity at the junction (S-C-S). A current flows through the Josephson junction even in the absence of applied voltage which is proportional to the sine of the Josephson phase(phase difference accross the junction), it is called DC Josephson effect. When a DC voltage is applied across the Josephson junction, the current passing through the junction oscillates with a characteristic frequency proportional to the voltage applied across the junction. This phenomenon is known as AC Josephson effect. In case of DC-SQUID, a superconducting loop is cut off by two insulating layers placed parallel as shown in Fig. 2.13. As a result two Josephson junctions form within the loop. Under application of perpendicular magnetic field to the plane of the loop, the loop generates current due to quantization of flux. The generated critical current and the output voltage difference are periodic function of external applied magnetic flux. The schematic diagram of SQUID is shown in Fig. 2.14.

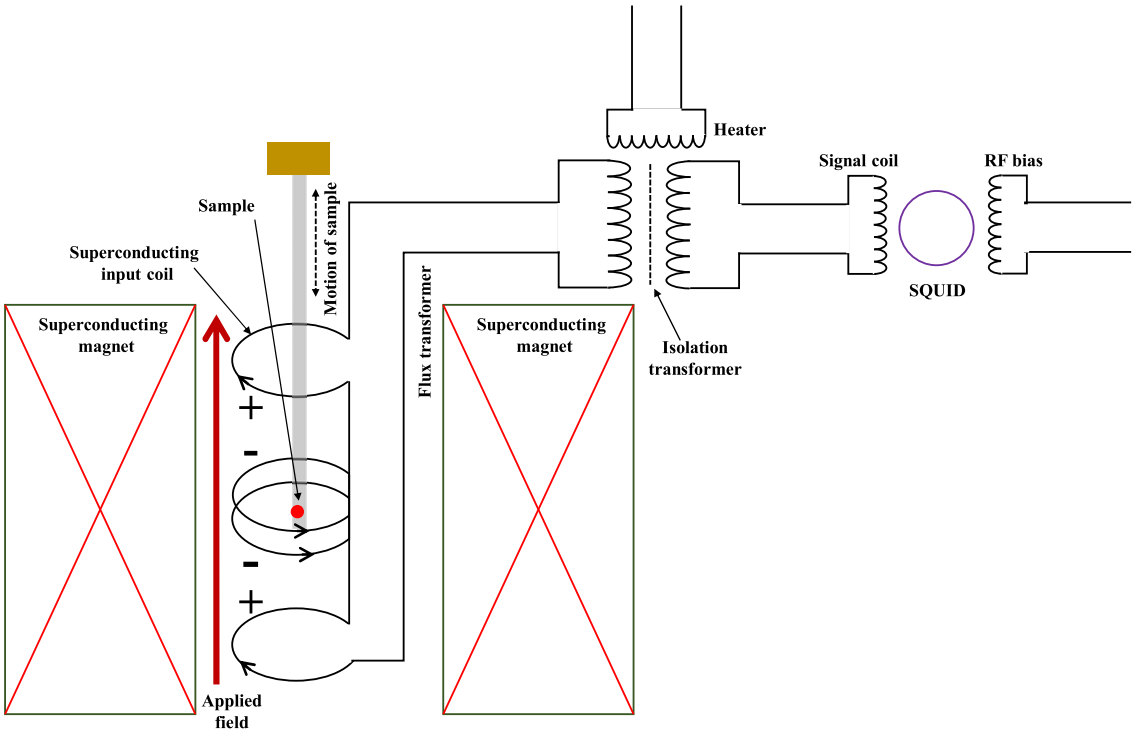

Figure 2.14: Schematic representation of superconducting quantum interference device (SQUID). This image is adapted from Quantum Design MPMS 3 user's manual.

We used the Quantum Design^{TM} magnetic property measurement system (MPMS) based SQUID to measure magnetization of a sample with a magnetic field up to 7 Tesla by varying the sample temperature between 2-300 K during the measurements. Here,

the magnetic field is generated by a superconducting coil. Similar to VSM, the sample is mounted on a thin nonmagnetic stick made of quartz or glass and kept at the centre of the superconducting coil. The stick is oscillated along z-axis using a vibrator. Hence, magnetic flux enclosed by the pick-up coils changes due to the magnetic moment of the vibrating sample. The SQUID sensor and superconductive pick-up coils are coupled to each other inductively. Hence the output voltage of SQUID is the reflection of the pick-up coil signal. The SQUID magnetometer can sense very low magnetic moment which are not detectable using conventional VSM. Temperature dependence of magnetization in ZFC and FC protocol in the warming cycle has been carried out under different magnetic fields and field dependence of magnetization [M(H)] has also been carried out for different temperatures.

2.7 Electronic Structure Studies

2.7.1 XPS Measurements

X-ray photoemission spectroscopy follows the photoelectric effect theory which was discovered by Heinrich Rudolf Hertz in 1887 [26] and explained by Albert Einstein in 1905 [25]. The photoelectric effect theory states that when photon of kinetic energy $h\nu$ hits a metal it emits photoelectrons of kinetic energy $h\nu - \phi - E_B$ where E_B is the binding energy (BE) of the electron measured relative to the chemical potential. ϕ is the work function of the material. A schematic representation of photoemission spectroscopy is shown in Fig. 2.15. If the photon energy source is X-ray, mainly generated by Al k_α or synchrotron radiation, it is called X-ray photoemission spectroscopy (XPS). If the photon energy source is ultraviolet ray, mostly generated by Helium lamp or synchrotron radiation, it is called ultraviolet photoemission spectroscopy (UPS). The penetration depth of XPS is more than 1000 $\mathring{A}$. Hence, it collects electronic structure information from surface and bulk. XPS spectra of each atom in the periodic table is unique from one other. Hence, by evaluating the binding energy of the emitted electrons, the element present in the system can be identified. The XPS spectrum usually indicates different energy level of elements present within the sample. By evaluating relative intensities (counts) of these peaks, the atomic percentage of the sample can be measured as well. From XPS, we can get the information of elements present in the material, chemical composition, information on doping or intercalation etc by measuring the kinetic energy and the intensity of emitted photoelectrons.

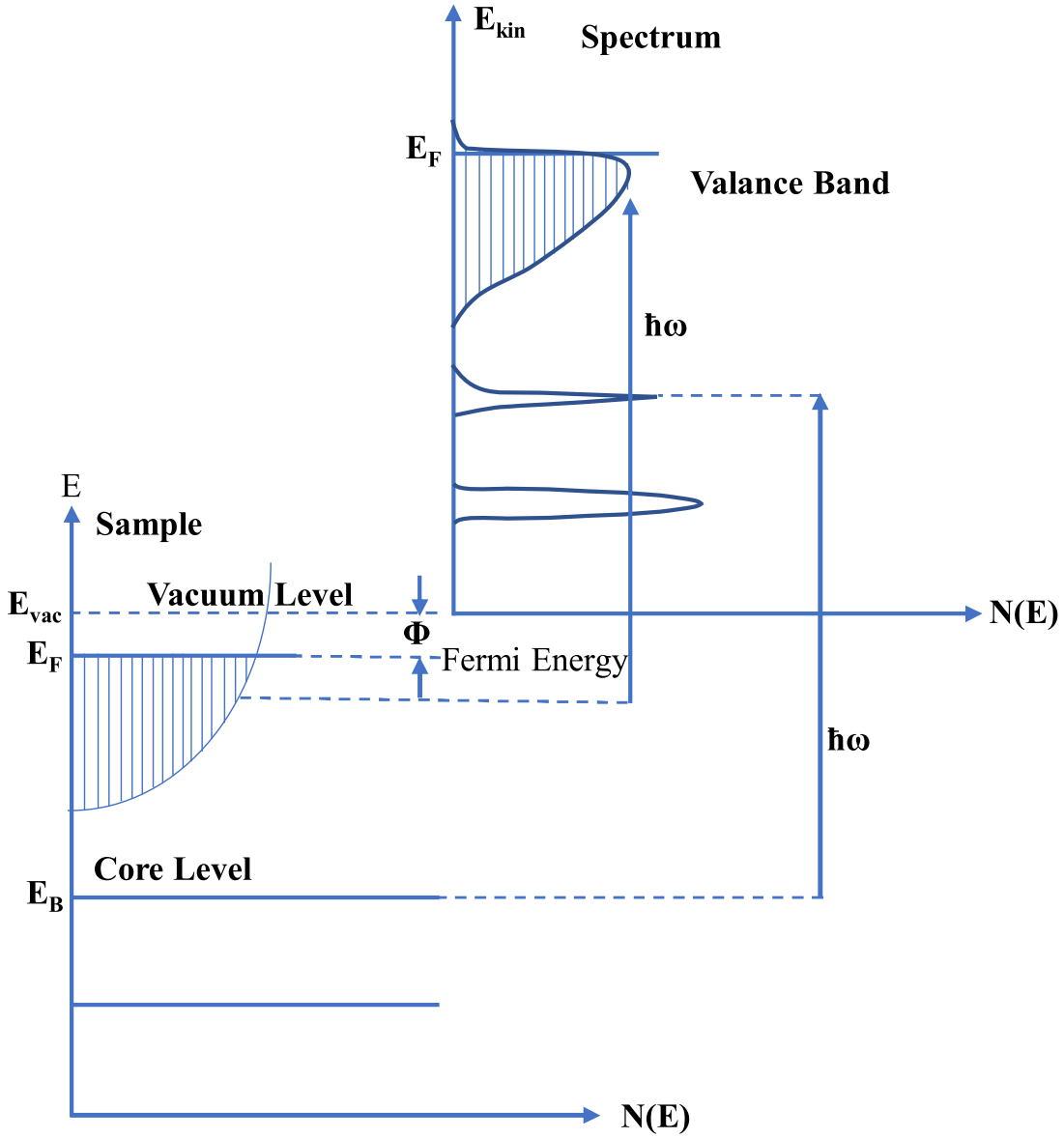

Figure 2.15: A schematic representation of the relation between energy levels in a solid and the electron distribution of photoelectrons produced by photons of energy $\hbar\omega$. This image is reproduced from reference [25].

2.7.2 ARPES Measurements

Angle resolved photoemission spectroscopy (ARPES) [25] is also based on the photoelectric effect theory with an upgradation. Here, emission angle, kinetic energy and intensity of emitted electrons are measured simultaneously. As a result, we can get the electronic band dispersions in the energy-momentum plot of a material directly. In conventional ARPES, ultraviolet ray generated by Helium lamp or synchrotron radiation is used mostly with photon energy within the range of 20-200 eV. The universal curve of the inelastic mean free path of electrons in Fig. 2.16 shows that the penetra-

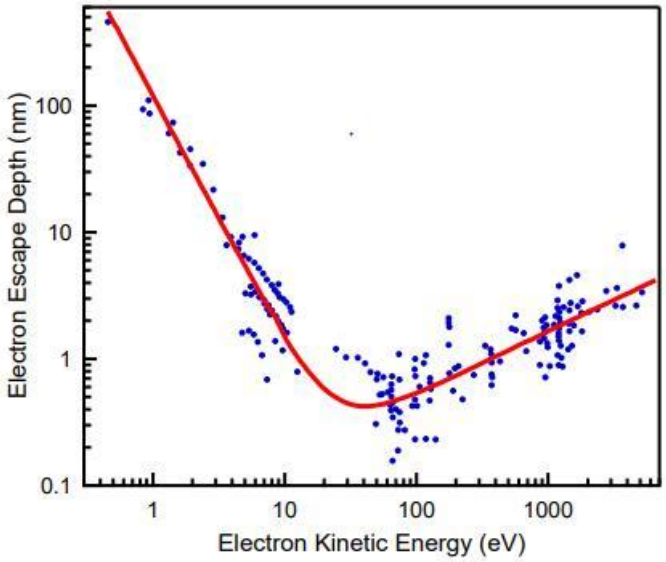

Figure 2.16: "The universal curve" of the inelastic mean-free path of electrons within a solid as a function of kinetic energy are plotted for a broad range of solids. This figure is taken from reference [27]

tion depth of electrons within the photon energy range of 20-200 eV is 5-10 $\mathring{A}$. Hence, ARPES is a surface sensitive tool to directly probe surface states as well as the bulk band structure of materials.

In ARPES, the probability of a transition from initial to final state can be described by two models [25]: the three-step model and the one-step model. The schematic representation of these models are shown in Fig. 2.17. The three-step model is most commonly used phenomenological approach which was described by Berglund and Spicer [28, 29]. The three steps of this model are,
1^{st} step: optical excitation of a photoelectron in the solid,
2^{nd} step: transport of the photoelectron to the surface,
3^{rd} step: escape of the photoelectron into the vacuum.

On the other hand, the one-step model is a quantum mechanical approach where an optical transition between initial and final states consists of many body wave functions and obeys necessary boundary conditions at the surface of the solid. Because of the complexity involved in the one-step model, most of the experimental results are described in terms of the three-step model.

The spherical deflection analyzer is one of the important components of ARPES set-up. It plays the crucial role to measure and analyze kinetic energy and momentum of the emitted photoelectrons from the sample. It consists of two concentric hemispheres as shown in Fig. 2.18 with a mean radius of two concentric hemispheres $R_0 = (R_1+R_2)/2$, where R_1 and R_2 are the radii of inner and outer hemispheres respectively. Here, the photoelectrons emitted at various angles are focused by an electron lens to

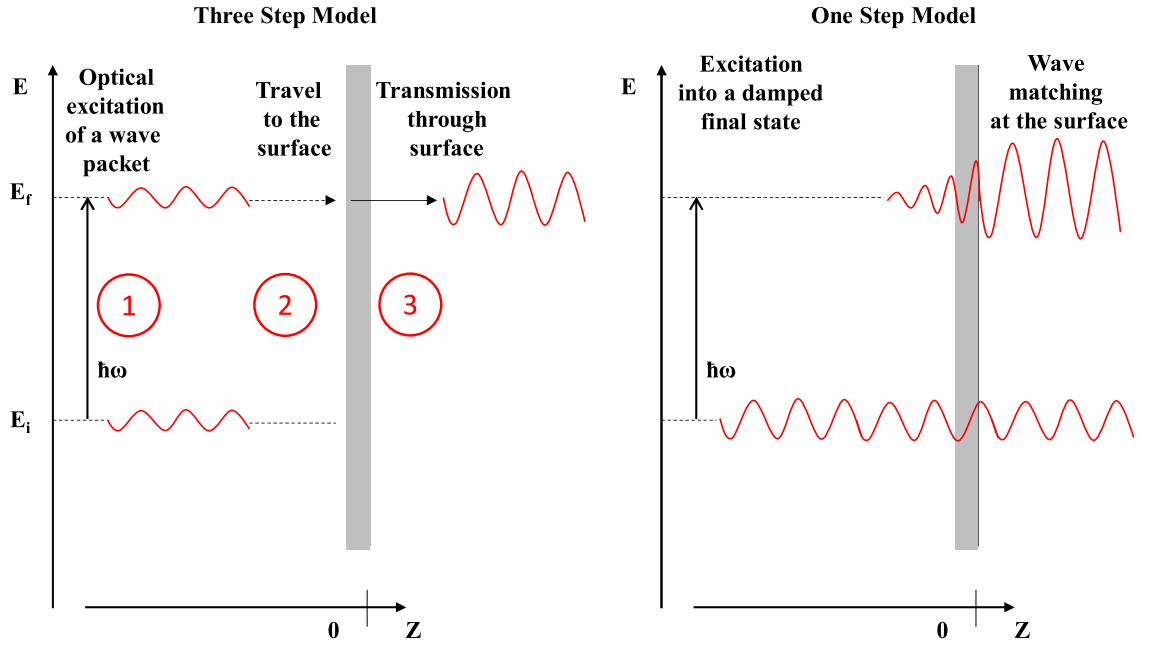

Figure 2.17: A schematic representation of three-step and two-step model in photoemission spectroscopy. This figure is reproduced from reference [25].

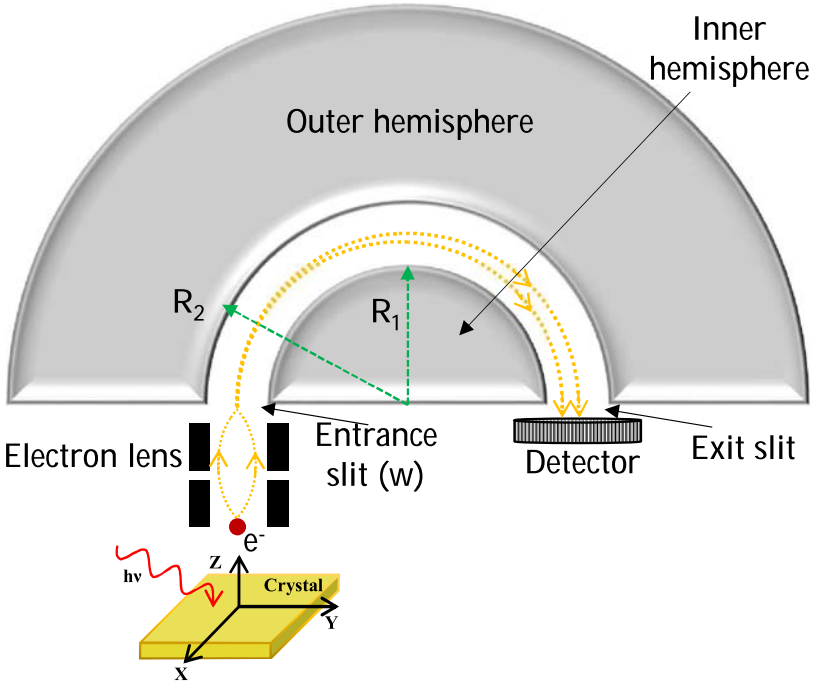

Figure 2.18: A schematic diagram of a hemispherical electron analyzer. This image is adapted from references [25, 30].

the entrance slit of the analyzer. These photoelectrons follow different trajectories inside the hemisphere and hit the two dimensional detector as a function of the kinetic energy. The detector simultaneously measures the counts (intensity) as a function of

escape angle and kinetic energy. Hence, a 3D map is generated to get band structure information in terms of energy-momentum diagram. The energy resolution of a hemispherical electron analyzer can be estimated using the formula $\Delta E = \frac{\omega E_P}{R_0}$. Here, w is the width of entrance slit and E_P is pass energy of the photoelectrons. Photoelectrons with a kinetic energy E_{kin} are accelerated or decelerated without changing the actual energy spread using preretardation stage before entrance slit. In this way the energy resolution increases by a factor E_{kin}/E_P. Also, smaller size of hemisphere can be used for energy detection.

The geometry of ARPES is shown in Fig. 2.19(a). The relation between momentum vector components ($k_\parallel$, $k_\perp$) while transmitting through the sample surface to vacuum is shown in Fig. 2.19(b). Here,
k^{in} is the momentum vector of the electron inside the crystal
$k_\parallel^{in}$ is the parallel component of momentum vector of the electron inside the crystal
$k_\perp^{in}$ is the perpendicular component of momentum vector of the electron inside the crystal
k^{out} is the momentum vector of the electron in vacuum
$k_\parallel^{out}$ is the parallel component of momentum vector of the electron in vacuum
$k_\perp^{out}$ is the perpendicular component of momentum vector of the electron in vacuum

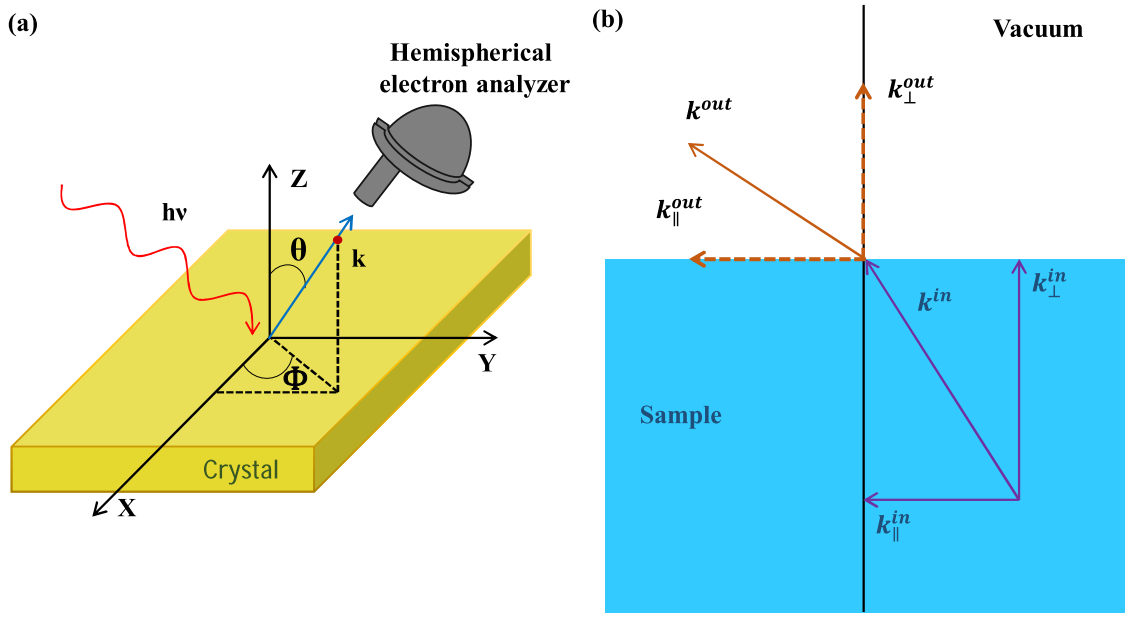

Figure 2.19: (a) A schematic representation of angle-resolved photoemission spectroscopy (ARPES) geometry. (b) The schematic diagram of momentum vector (k) components ($k_\parallel$, $k_\perp$) while transmitting through the sample surface to vacuum. This figure is reproduced from reference [31].

According to law of conservation of kinetic energy of photoelectrons can be written

as,

$$E_{kin} = \frac{\hbar^2 k^{in\,2}}{2m} - V_0 \tag{2.2}$$

Or,

$$E_{kin} = \frac{\hbar^2 k_{\parallel}^{in\,2} + k_{\perp}^{in\,2}}{2m} - V_0 \tag{2.3}$$

Here, V_0 is known as inner potential which can be estimated from band mapping along vertical direction or theoretical calculations. Also, kinetic energy of photoelectrons can be written as,

$$E_{kin} = \frac{\hbar^2 k_{\parallel}^{out\,2} + k_{\perp}^{out\,2}}{2m} \tag{2.4}$$

According to the three-step model of photoemission, the parallel component of momentum remain unchanged during transmission from crystal to vacuum i.e.,

$$k_{\parallel}^{out} = k_{\parallel}^{in} \tag{2.5}$$

Hence, by equating Eq. 2.3 and Eq. 2.4, we can get

$$\frac{\hbar^2 k_{\perp}^{out\,2}}{2m} = \frac{\hbar^2 k_{\perp}^{in\,2}}{2m} - V_0 \tag{2.6}$$

Hence, one can obtain the perpendicular component of internal momentum vector in terms of perpendicular component of outer momentum vector using Eq. 2.7

$$k_{\perp}^{in} = \sqrt{k_{\perp}^{out\,2} + \frac{2m}{\hbar^2} V_0} \tag{2.7}$$

Now, the perpendicular component of momentum vector in vacuum can be written as $k_{\perp}^{out} = \sqrt{\frac{2mE_{kin}}{\hbar^2}} cos\theta$.

So, Eq. 2.7 can be written as,

$$k_{\perp}^{in} = \sqrt{\frac{2m}{\hbar^2}(E_{kin} cos^2\theta + V_0)} \tag{2.8}$$

The parallel component of momentum vector in vacuum has two parts such as k_x^{out} and k_y^{out} where $k_x^{out} = \sqrt{\frac{2mE_{kin}}{\hbar^2}} sin\theta cos\phi$ and $k_y^{out} = \sqrt{\frac{2mE_{kin}}{\hbar^2}} sin\theta sin\phi$. From Fig. 2.19 (a), it can be noticed that the angle ϕ can be adjusted to very small value (≈ 0) by rotating the sample stage. Then the parallel component can be written as Eq. 2.9 using Eq. 2.5 where $k_{\parallel}^{in}$ could be either k_x^{in} and k_y^{in}. Conventionally, it is called as $k_{\parallel}^{in}$.

$$k_{\parallel}^{in} = \sqrt{\frac{2m}{\hbar^2} E_{kin}} sin\theta \tag{2.9}$$

By measuring the emission angles (θ) and kinetic energies simultaneously of photo-electrons using hemispherical analyzer and detector as shown in Fig. 2.18, we can get in-plane energy-momentum plot using Eq. 2.9. To get out-of-plane energy-momentum plot, one has to vary the photon energies. Then, by using Eq. 2.8 and inner potential one can get out-of-plane energy-momentum plot.

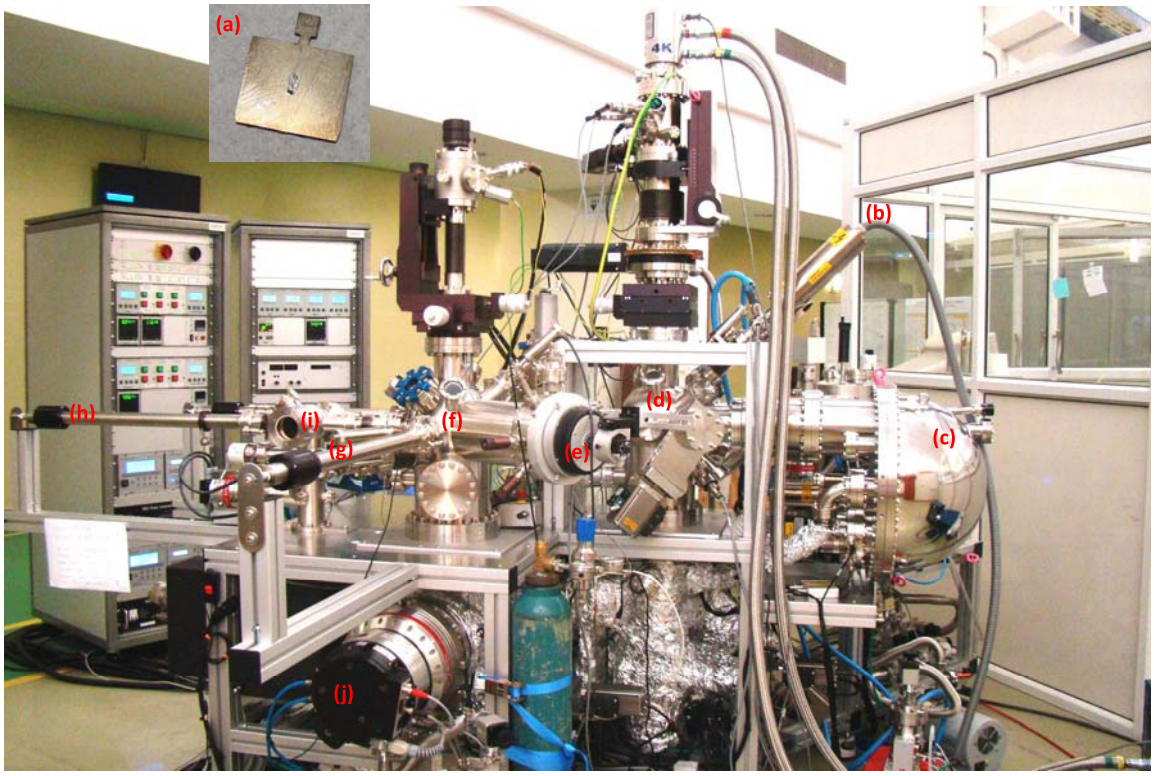

Figure 2.20: ARPES experimental station attached with XPS and LEED facilities, Indus-2, RRCAT, India. (a) is the sample holder with the sample glued on it, (b) is the X-ray source, (c) is the hemispherical electron analyzer, (d) is the main chamber, (e) is the LEED camera, (f) is the sample preparation chamber, (g) is the cleaving rod, (h) is the transfer rod, (i) is sample isertion chamber, (j) is a turbo pump.

We performed ARPES measurements using He light source of photon energies 21.2 eV and 40.8 eV and synchrotron light source with energy resolution of 10 meV. The samples were cleaved *in situ* in the sample preparation chamber to get a clean and smooth surface. Then, the data were recorded at a chamber vacuum of the order of 9×10^{-11} mbar. The sample temperature was varied in the range of 1 K and 300 K during the experiment. Schematic representation of ARPES experimental station at Indus-2, RRCAT, India is shown in Fig. 2.20.

Bibliography

[1] R. Bunsen, "Vulkanische exhalation," *J. prakt. Chem*, vol. 56, p. 53, 1852.

[2] K. Tsutsumi, "X-ray-diffraction study of the periodic lattice distortion associated with a charge-density wave in 1T-VSe_2," *Physical Review B*, vol. 26, pp. 5756–5759, nov 1982.

[3] A. E. van Arkel and J. H. de Boer, "Darstellung von reinem Titanium-, Zirkonium-, Hafnium- und Thoriummetall," *Zeitschrift für anorganische und allgemeine Chemie*, vol. 148, pp. 345–350, sep 1925.

[4] A. Ubaldini and E. Giannini, "Improved chemical vapor transport growth of transition metal dichalcogenides," *Journal of Crystal Growth*, vol. 401, pp. 878–882, sep 2014.

[5] K. S. Nikonov, M. N. Brekhovskikh, A. V. Egorysheva, T. K. Menshchikova, and V. A. Fedorov, "Chemical vapor transport growth of vanadium(IV) selenide and vanadium(IV) telluride single crystals," *Inorganic Materials*, vol. 53, pp. 1126–1130, oct 2017.

[6] J. Jiang, Z. K. Liu, Y. Sun, H. F. Yang, C. R. Rajamathi, Y. P. Qi, L. X. Yang, C. Chen, H. Peng, C. C. Hwang, S. Z. Sun, S. K. Mo, I. Vobornik, J. Fujii, S. S. P. Parkin, C. Felser, B. H. Yan, and Y. L. Chen, "Signature of type-II Weyl semimetal phase in $MoTe_2$," *Nature Communications*, vol. 8, jan 2017.

[7] K. Nikonov, N. Ehlen, B. Senkovskiy, N. Saigal, A. Fedorov, A. Nefedov, C. Wöll, G. D. Santo, L. Petaccia, and A. Grüneis, "Synthesis and spectroscopic characterization of alkali–metal intercalated $ZrSe_2$," *Dalton Transactions*, vol. 47, no. 9, pp. 2986–2991, 2018.

[8] P. Schmidt, M. Binnewies, R. Glaum, and M. Schmidt, *Chemical vapor transport reactions–methods, materials, modeling.* InTech Rijeka, 2013.

[9] D. Elwell, H. J. Scheel, and E. Kaldis, "Crystal growth from high temperature solutions," *Journal of The Electrochemical Society*, vol. 123, no. 9, p. 319C, 1976.

[10] J. Koruza, H. Liu, M. Höfling, M.-H. Zhang, and P. Veber, "(K,Na)NbO_3-based piezoelectric single crystals: Growth methods, properties, and applications," *Journal of Materials Research*, vol. 35, pp. 990–1016, jan 2020.

[11] J. Wang, P. Yox, and K. Kovnir, "Flux Growth of Phosphide and Arsenide Crystals," *Frontiers in Chemistry*, vol. 8, apr 2020.

[12] J.-Q. Yan, "Flux growth utilizing the reaction between flux and crucible," *Journal of Crystal Growth*, vol. 416, pp. 62–65, apr 2015.

[13] X. Ding, J. Xing, G. Li, L. Balicas, K. Gofryk, and H.-H. Wen, "Crossover from Kondo to Fermi-liquid behavior induced by high magnetic field in 1T-VTe_2 single crystals," *Physical Review B*, vol. 103, mar 2021.

[14] C. Xu, B. Li, W. Jiao, W. Zhou, B. Qian, R. Sankar, N. D. Zhigadlo, Y. Qi, D. Qian, F.-C. Chou, and X. Xu, "Topological Type-II Dirac Fermions Approaching the Fermi Level in a Transition Metal Dichalcogenide $NiTe_2$," *Chemistry of Materials*, vol. 30, pp. 4823–4830, jun 2018.

[15] Y. Tao, J. A. Schneeloch, A. A. Aczel, and D. Louca, "T_d to $1T'$ structural phase transition in the WTe_2 Weyl semimetal," *Phys. Rev. B*, vol. 102, p. 060103, Aug 2020.

[16] A. F. May, J. Yan, and M. A. McGuire, "A practical guide for crystal growth of van der Waals layered materials," *Journal of Applied Physics*, vol. 128, no. 5, p. 051101, 2020.

[17] A. Baron Al-Hassan, *Synthesis and Characterization of methyl ammonium lead tri halide Perovskite Compounds and their Applications in Photonic Devices.* PhD thesis, 03 2019.

[18] C. Kittel, *Introduction to solid state physics*, vol. 8.

[19] M. Abd-Elghany and T. M. Klapötke, "A review on differential scanning calorimetry technique and its importance in the field of energetic materials," *Physical Sciences Reviews*, vol. 3, no. 4, 2018.

[20] P. Gabbott, ed., *Principles and Applications of Thermal Analysis*. Blackwell Publishing Ltd, jan 2008.

[21] K. Instruments, "Low Level Measurements Handbook," *Precision DC Current, Voltage and Resistance Measurements, 7th ed.; Keithley Instruments Inc.: Cleveland, OH, USA*, p. 245, 2013.

[22] L. Benito, J. I. Arnaudas, and A. del Moral, "High-sensitivity vector magnetometer for measuring magnetic torque at low temperatures," *Review of Scientific Instruments*, vol. 77, p. 025101, feb 2006.

[23] S. Foner, "Versatile and Sensitive Vibrating-Sample Magnetometer," *Review of Scientific Instruments*, vol. 30, pp. 548–557, jul 1959.

[24] P. Marcon and K. Ostanina, "Overview of Methods for Magnetic Susceptibility Measurement," *Progress in Electromagnetics Research Symposium*, 01 2012.

[25] S. Hüfner, *Photoelectron Spectroscopy*. Springer Berlin Heidelberg, 1996.

[26] H. Hertz, "Ueber einen Einfluss des ultravioletten Lichtes auf die electrische Entladung," *Annalen der Physik und Chemie*, vol. 267, no. 8, pp. 983–1000, 1887.

[27] X. J. Zhou, "Angle-Resolved Photoemission Spectroscopy on Electronic Structure and Electron-Phonon Coupling in Cuprate Superconductors," *Submitted to Book Chapter in Handbook of High-Temperature Superconductivity: Theory and Experiment (2007)*, 4 2010.

[28] W. E. Spicer, "Photoemissive, Photoconductive, and Optical Absorption Studies of Alkali-Antimony Compounds," *Phys. Rev.*, vol. 112, pp. 114–122, Oct 1958.

[29] W. E. Spicer, "Photoemission and related properties of the alkali-antimonides," *Journal of Applied Physics*, vol. 31, no. 12, pp. 2077–2084, 1960.

[30] A. Damascelli, Z. Hussain, and Z.-X. Shen, "Angle-resolved photoemission studies of the cuprate superconductors," *Rev. Mod. Phys.*, vol. 75, pp. 473–541, Apr 2003.

[31] B. Lv, T. Qian, and H. Ding, "Angle-resolved photoemission spectroscopy and its application to topological materials," *Nature Reviews Physics*, vol. 1, no. 10, pp. 609–626, 2019.

Chapter 3

ARPES Studies on ZrX_2 (X = Se and Te)

3.1 Introduction

Transition metal dichalcogenides (TMDCs) [1–3] are gaining a great deal of research interests, especially, from the past few decades due to their potential applications in spintronics [4–8] as well in the optoelectronics [9–13] because of their wide range of electronic properties starting from the metallic [14–16], to the semimetallic [17–20], to the semiconducting [21–24], and to the Mott-insulators [25–27], obtained mainly by the band engineering [28–30]. In addition, the diversity of electronic properties of TMDCs includes the CDW [31, 32], the magnetism [33–35], and the superconductivity [36–38].

Tunable band gap in layered TMDCs is one of the major research topics in recent days from both the theory and experiment [39–42]. It is known that the band gap in IVB TMDCs (TiX_2, ZrX_2, and HfX_2, where X = S, Se, and Te) change with the strain [43]. However, among the IVB TMDCs, ZrX_2 compounds in their monolayer thickness show peculiarity beyond a critical pressure. That means, instead of increasing band gap with the increasing pressure, it starts decreasing beyond the critical pressure. On the other hand, the monolayer thickness $ZrTe_2$ transforms from metal to a semiconductor beyond a critical pressure. Hence, understanding the pressure effects on the electronic structure of TMDCs has a significance in their band engineering [44]. Specifically, performing ARPES studies under external pressure is a non-trivial method [45, 46]. However, studying the electronic structure using ARPES under the application of chemical pressure induced by the substitution of an isovalent atom is highly viable [47]. So far there exists very few ARPES reports in this direction [48–52]. Moreover, these studies report only the electronic structure of $Zr(Se_{1-x}S_x)_2$ which are semiconductors. Although several theoretical reports on $ZrTe_2$ predicted it to be a metal [53–55], so far no ARPES study exists on this compound in bulk phase confirm-

Most of this chapter is published as: I. Kar *et al.*, Phys. Rev. B **101**, 165122 (2020).

ing the same, except that a recent ARPES study on monolayer $ZrTe_2$ deposited on InAs (111) substrate showing linear Dirac states near the Fermi level at the Γ-point [56]. Thus, a thorough understanding of the electronic structure of bulk $ZrTe_2$ has interests from other reasons as well, whether $ZrTe_2$ is another topological system like $ZrTe_5$ [57–61]. Therefore, ARPES studies on the bulk $ZrTe_2$ are essential to understand whether $ZrTe_2$ is a simple metal or a topological semimetal.

In this chapter, we report on the low-energy electronic structure of bulk $ZrTe_2$ and $ZrSe_2$ using high resolution angle resolved photoemission spectroscopy and compare it with density functional theory performed by our theoretical collaborators. On the Fermi surface map of $ZrTe_2$, we observe several well disconnected hole and electron pockets at $\Gamma(A)$ and $M(L)$ points, respectively. Further, in $ZrTe_2$, we realize three holelike non-degenerate band dispersions near the $\Gamma(A)$ point and an electronlike band dispersion at the $M(L)$. DFT calculations performed by our theoretical collaborators predict all hole pockets are composed by the Te p orbital characters and the electron pocket is composed by the Zr d_{z^2} orbital character. An equal number of hole and electron carrier density estimated from our ARPES data using Luttinger's theorem [62, 63] suggests $ZrTe_2$ to be a semimetal. In addition, DFT calculations performed by our theoretical collaborators on $ZrTe_2$ in presence of SOC predict band inversion between Te p and Zr d characters near Γ point, pointing $ZrTe_2$ to a topological semimetal. In contrast to $ZrTe_2$, from the Fermi surface topology of $ZrSe_2$ we observe only electron pockets located at the $M(L)$ point, while the hole pockets are noticed well below the Fermi level at a binding energy of ≈ 1 eV. Nevertheless, our studies on $ZrSe_2$ are inline with the existing reports that it is a semiconductor with an indirect band gap of 0.9 eV between $\Gamma(A)$ and $M(L)$ high symmetry points [51, 52, 64]. In order to understand the origin of semimetallic state in $ZrTe_2$ and semiconducting state in $ZrSe_2$, our theoretical collaborators quantified the electronic structure by mapping it onto a tight-binding model. They relate the electronic structure changes in going from $ZrSe_2$ to $ZrTe_2$ to the change in the metal-chalcogen bond lengths.

3.2 Experimental Details

High quality single crystals of $ZrSe_2$ and $ZrTe_2$ were grown by the CVT method using iodine as a transport agent [65] at IISER, Pune by our collaborator. In the first step, stoichiometric quantities of elements, Zr (sponge, $\geq$ 99.9%, metals basis, Sigma Aldrich) with Se (shot, Alfa Aesar, 99.999%, metals basis) or Te (ingot, 99.99%, metals basis, Alfa Aesar), were loaded into an alumina crucible and subsequently sealed in a quartz ampoule under vacuum. The ampoule was slowly heated to 500 °C, with a rate of 50 °C/h, kept there for 5 h and then heated further to 900 °C. This temperature has

been maintained for a period of 2 days, in order to complete the reaction between Zr and the chalcogen (Se/Te). The polycrystalline powders of $ZrSe_2$ and $ZrTe_2$ were used for the single crystal growth. The powdered samples were placed and sealed under vacuum in quartz ampoules together with pieces of crystallized iodine (5 mg/cm^3). The ampoules had subsequently been loaded in a three-zone furnace, where a gradient of temperature of 100 °C was maintained between the source (880 °C) and the sink (780 °C) zone. After 10 days of transport, many single crystals with dimensions as large as 5 mm × 5 mm × 0.1 mm were obtained at the cold part of the ampoule. Crystal structure, morphology and chemical composition of the single crystals were determined using XRD and scanning electron microscope (SEM) equipped with an EDX, see Figure 3.1. From EDX, the studied samples in this contribution have the chemical compositions of $Zr_{1.02}Se_2$ and $Zr_{1.16}Te_2$ with 2% and 16% excess Zr per formula unit, respectively. Both the compounds crystallized in the space group of $P\bar{3}m1$ (164), with lattice parameters at room temperature as $a = b = 3.945$ $\mathring{A}$ and $c = 6.624$ $\mathring{A}$ for $ZrTe_2$ and $a = b = 3.766$ $\mathring{A}$ and $c = 6.150$ $\mathring{A}$ for $ZrSe_2$.

Angle resolved photoemission spectroscopy measurements were carried out at the UE-112 beam-line equipped with 1^3-ARPES end station located in BESSY II (Helmholtz zentrum Berlin) synchrotron radiation center [66, 67] by Dr. Thirupathaiah Setti. Photon energies for the measurements were varied between 30 eV to 110 eV. The energy resolution was set between 10 and 15 meV depending on the excitation energy. Data were recorded at a chamber vacuum of the order of 1×10^{-10} mbar and the sample temperature was kept at 1 K during the measurements. We employed various photon polarizations in order to extract the electronic structure comprehensively. Measuring geometry of s and p-polarized photons with respect to the scattering plane (SP) and analyzer entrance slit (ES) is shown in Fig. 3.1(f). s-polarized light has odd parity and p-polarized light has even parity with respect to scattering plane. This means that the wave oscillates parallel to the scattering plane for p-polarized light and perpendicular to the scattering plane for s-polarized light. Even parity orbitals are visible with p-polarized light such as s, p_x, p_z, d_{xz}, $d_{x^2-y^2}$, d_{z^2}. Odd parity orbitals are visible with s-polarized light such as p_y, d_{xy}, d_{yz}.

Figure 3.1(a) shows the trigonal crystal structure of ZrX_2. Figure 3.1(b) shows the projected Zr-chalcogen layer on the ab-plane where one can notice each Zr ion is octahedrally coordinated with six Te (Se) ions. From the EDX measurements on $ZrTe_2$ and $ZrSe_2$ we derived the chemical formulae of $Zr_{1.02}Se_2$ and $Zr_{1.16}Te_2$, respectively, suggesting that there is a 2% of Se (excess Zr) and a 16% of Te (excess Zr) deficiency from the stoichiometric compositions. Such a chalcogen deficiency or excess Zr in these systems generally leads to excess electron carrier density. Nevertheless, from our EDX we noticed that the samples are homogeneous. As shown in Figures 3.1(g) and 3.1(h), we performed XPS on $ZrTe_2$ and $ZrSe_2$, respectively. Most of the atomic core levels are

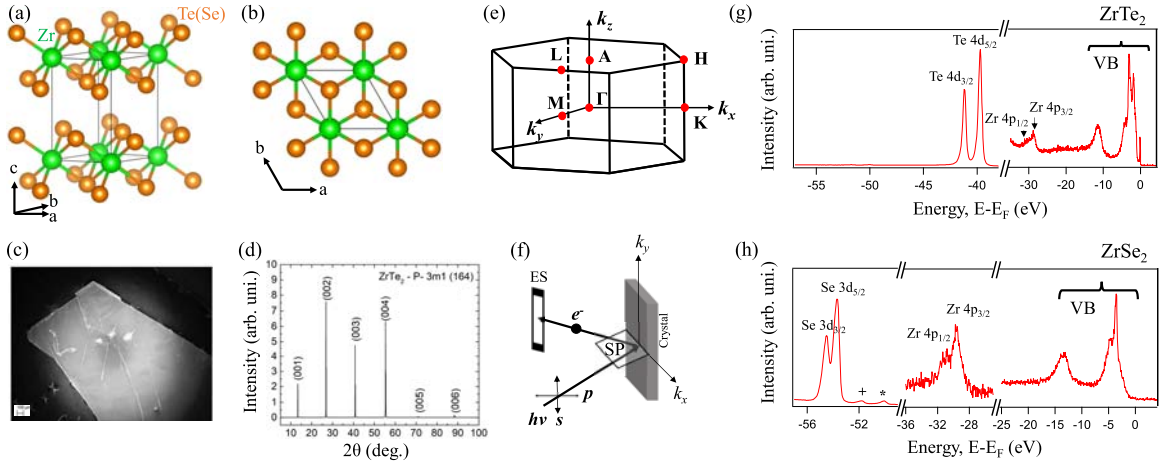

Figure 3.1: (a) Trigonal crystal structure of $ZrTe_2$ and $ZrSe_2$. (b) ZrX_2 layer projected on the *ab*-plane, showing the metal-chalcogen hexagonal pattern. (c) Scanning electron microscope image of the $ZrTe_2$ single crystal with a spacial resolution of 100 μm. (d) X-ray diffractogram of $ZrTe_2$ single crystal. (e) 3D view of the hexagonal Brillouin zone with high symmetry points. (f) Measuring geometry of photoemission spectroscopy, defining the *s* and *p*-polarized photons with respect to the scattering plane (SP) and analyzer entrance slit (ES). Core level photoemission spectra of (g) $ZrTe_2$ and (h) $ZrSe_2$. In (h), the symbols + and $\star$ represent the Iodine impurity peaks of $4p_{3/2}$ and $4p_{5/2}$, respectively.

assigned to their respective binding energies for $ZrTe_2$. However, for $ZrSe_2$, we noticed significant intensity peaks at binding energies of 52 eV and 50.6 eV, pointed by + and $\star$, respectively, that are negligibly visible in $ZrTe_2$. These peaks are identified as the Iodine $4p_{3/2}$ (+) and $4p_{5/2}$ ($\star$) states. Note here that Iodine was used as a transport agent for growing these crystals, hence, some of the Iodine atoms may have stuck in between the $ZrSe_2$ layers during the crystal growth process. But nevertheless, as we discuss below presence of Iodine in $ZrSe_2$ has no net effect on its electronic structure. Apart from this, we do not find any other impurity peaks from the XPS of $ZrSe_2$ and as well from $ZrTe_2$.

Figure 3.2 shows ARPES data of $ZrTe_2$. Fermi surface map of $ZrTe_2$ in the $k_x - k_y$ plane is shown in Figure 3.2(a), measured with *p*-polarized light using a photon energy of hν=100 eV. The Fermi surface has hexagonal symmetry which is consistent with the hexagonal crystal structure. As can be observed in Fig. 3.2(a) the Fermi surface of $ZrTe_2$ consists of well disconnected Fermi pockets located at the Γ and M points. In order to understand nature of these Fermi pockets we have taken the energy distribution maps (EDMs) along the cuts #1 and #2 as shown in Fig. 3.2(a). From the EDMs shown in Figure 3.2(b) three holelike band dispersions, α_1, α_2, and α_3, are found at $\Gamma(A)$ and an electronlike band dispersion, β, is found at $M(L)$ high symmetry points. From the polarization dependent EDMs as shown in Fig. 3.2(b), with *s*-polarized light

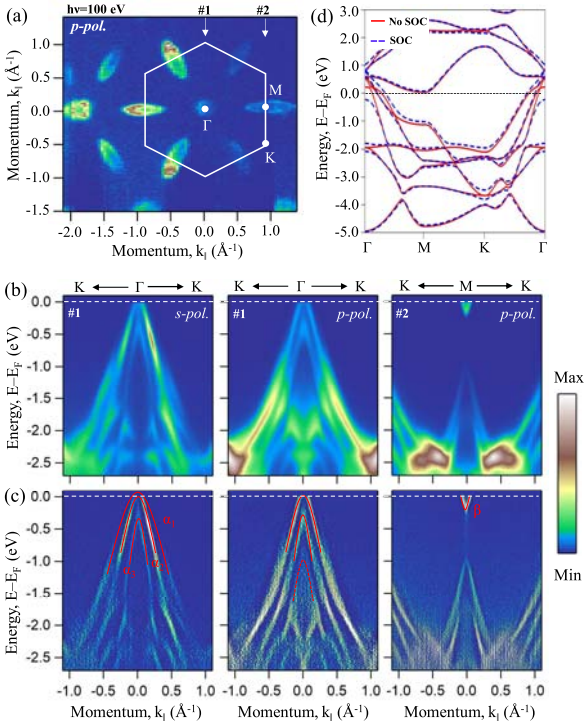

Figure 3.2: In-plane electronic structure of $ZrTe_2$. (a) Fermi surface map measured using p polarized light with a photon energy hν = 100 eV. (b) Energy distribution maps (EDMs) taken along the cuts #1 and #2 as shown in (a). (c) Second derivatives of (b). In (c) the red-dashed curves are eye-guides showing the band dispersions. (d) Energy-momentum plot of $ZrTe_2$ calculated using density functional theory with (blue) and without (red) including spin-orbit coupling.

we noticed all three hole pockets with reduced intensity for α_1 and α_3 and high intensity for α_2, whereas with p-polarized light we noticed predominantly two hole pockets (α_2 and α_3). Orbital resolved band structure performed by our theoretical collaborators (see Figure 3.7) in the absence of SOC suggest that the hole pocket α_1 is composed by Te p_x, the hole pocket α_2 is composed by Te p_y, and the hole pocket α_3 is composed by Te p_z character. However, in the presence of SOC the orbital contribution to the hole pockets is more complex as can be observed in Fig. 3.7. Thus, assigning orbital characters to the experimental band structure for $ZrTe_2$ is non-trivial. Next, an high intense electron pocket (β) has been recorded using p-polarized light which is composed by the even parity orbital Zr d_{z^2} character. Figure 3.2(d) shows calculated band structure with and without including spin-orbit coupling. As we can see from Fig. 3.2(d), three holelike and an electronlike band dispersions are predicted at $\Gamma(A)$ and $M(L)$ high symmetry points. Therefore, calculated band structure is qualitatively in agreement with the experimental data.

Despite being a layered system, we further performed photon energy dependent ARPES measurements on $ZrTe_2$ to unravel the out-of-plane (k_z) band structure. Fig-

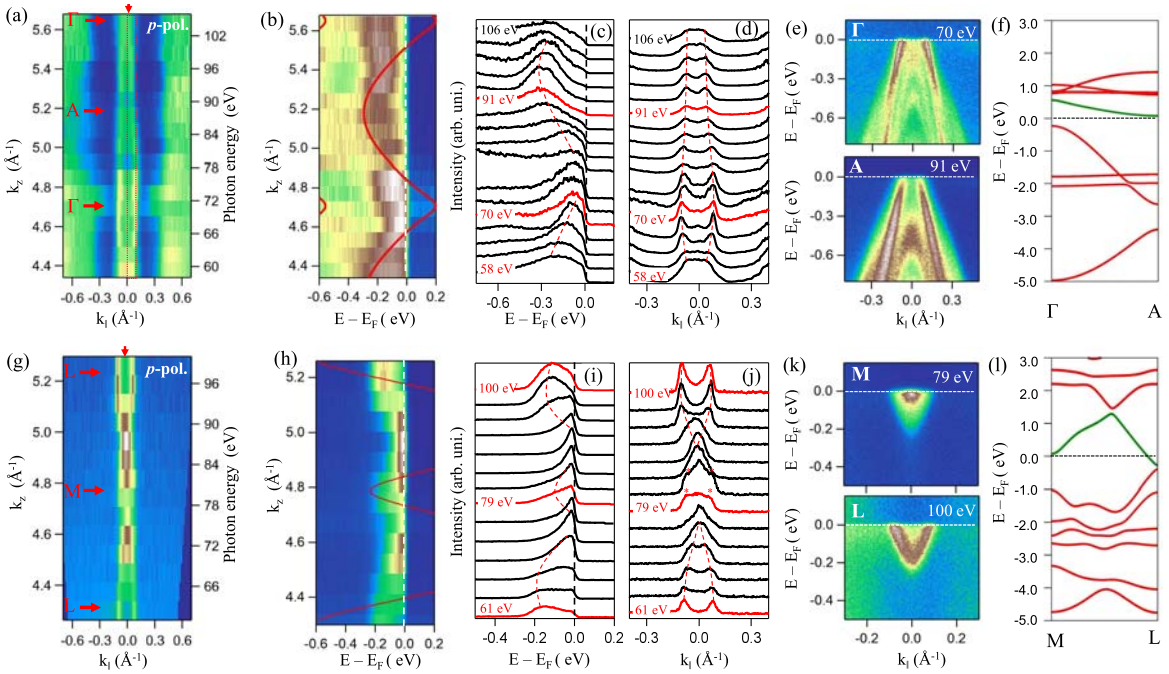

Figure 3.3: Out-of-plane (k_z) electronic structure of $ZrTe_2$. (a) k_z Fermi surface map measured using p-polarized light in the ΓMAL plane. (b) EDM taken along the $\Gamma - A$ high symmetry line. (c) Photon energy dependent energy distribution curves (EDCs) extracted from (b). (d) Photon energy dependent momentum distribution curves (MDCs) extracted from (a). (e) EDMs taken from Γ and A high symmetry points. (f) Energy-momentum plot from the calculations along the $\Gamma - A$ high symmetry line. (g) k_z Fermi surface map measured using p-polarized light in the $MKHL$ plane. (h) EDM taken along the $M - L$ high symmetry line. (i) Photon energy dependent EDCs extracted from (h). (j) Photon energy dependent MDCs extracted from (g). (k) EDMs taken from M and L high symmetry points. (l) Energy-momentum plot from the calculations along the $M - L$ high symmetry line. In (b) and (h) the DFT band structure along $\Gamma - A$ and $M - L$ is overlapped on the ARPES data by shifting the calculated Fermi level 0.3 eV towards lower binding energy. Note that since the band renormalization effects are not consider, only a qualitative agreement is found between theory and experiment.

ure 3.3(a) shows Fermi surface map of $ZrTe_2$ in the ΓMLA plane measured with photon energies ranging from 58 to 106 eV in step of 3 eV using p-polarized light. Following the equation, $k_z = \sqrt{\frac{2m}{\hbar^2}}\sqrt{V_0 + E_k \cos^2\theta}$, here m is the electron mass, $\hbar$ is the Planck's constant, E_k is the photoelectron kinetic energy, θ is escape angle of the photoelectron from the sample surface normal, and V_0 is the inner potential of the sample which is considered to be 16 eV, we found that the photon energies 70±3 eV and 91±3 eV correspond to the high symmetry points of Γ and A, respectively. Figure 3.3(b) shows EDM taken along the $\Gamma - A$ direction as shown by the down arrow in Fig. 3.3(a) extracted by a momentum integration of 0.05 $\mathring{A}^{-1}$. From this EDM one can clearly notice that there is significant k_z dispersion in going from Γ to A for the hole pocket which has a partial

contribution from Zr d_{z^2} along with Te $p_x(p_y)$ under SOC [see Fig. 3.7]. This is further demonstrated using photon energy dependent energy distribution curves (EDCs) as shown in Figure 3.3(c). Figure 3.3(d) shows photon energy dependent Momentum distribution curves (MDCs) extracted from Fig. 3.3(a). We estimated a Fermi vector of hole pocket $k_F \approx 0.09$ $\mathring{A}^{-1}$ at the Γ-point, while a Fermi vector $k_F \approx 0.06$ $\mathring{A}^{-1}$ is estimated at the A-point. This observation again confirms significant k_z dispersion of the hole pocket. Figure 3.3(e) shows EDMs from Γ (70 eV) and A (91 eV) high symmetry points. This observation is consistent with DFT calculations performed by our theoretical collaborators along $\Gamma - A$ direction as shown in Fig. 3.3(f), where one can see a significant k_z dispersion for the hole pocket (green color band dispersion).

Similarly, Figure 3.3(g) shows k_z Fermi surface map in the $MKLH$ plane measured with photon energies ranging from 61 eV to 100 eV in step of 3 eV using p-polarized light. From these data we found that the photon energy 79 eV detects bands from the M-point whereas the photon energies 61 and 100 eV detect the bands from the L-point. Figure 3.3(h) shows EDM along the $M - L$ orientation and Figure 3.3(i) shows photon energy dependent EDCs taken from Fig. 3.3(h). Figure 3.3(j) shows photon energy dependent MDCs. We estimate a Fermi vector $k_F \approx 0.08$ $\mathring{A}^{-1}$ for the electron pocket at the L-point, while no Fermi vector for the electron pocket is found at the M-point. This observation is suggesting that the k_z dispersion of the electron pocket composed by Zr d_z^2 orbital character is relatively stronger. Further, in Fig. 3.3(j) we could identify a couple of peaks shown by $\star$ symbol on the MDC curves taken around the M point. These peaks are caused by the reminiscent spectral intensity of the electron pocket from the L-point. This is because, in ARPES the photon energy dependent data generally suffer from the k_z resolution due to vertical transition of the photoelectrons. Thus, the k_z dependent ARPES data generally consist of overlapping states in the k_z direction. Figure 3.3(k) shows EDMs from M (79±3 eV) and L (100±3 eV) high symmetry points. This observation is consistent with DFT calculations performed by our theoretical collaborators along $M - L$ direction as shown in Fig. 3.3(l), where one can see a significant k_z dispersion for the electron pocket (green color band dispersion).

Next, ARPES data of $ZrSe_2$ is shown in Figure 3.4. Figure 3.4(a) shows the Fermi surface map measured with a photon energy of hν = 100 eV using p-polarized light in the $k_x - k_y$ plane. Figure 3.4 (b) shows energy-momentum plot of $ZrSe_2$ from DFT calculations. On the Fermi surface, we could identify six Fermi pockets located at six $M(L)$-points in a hexagonal symmetry. On the other hand, we did not find any spectral intensity at the $\Gamma(A)$ point. To further elucidate the nature of the band dispersions at the $M(L)$ and $\Gamma(A)$ points, we measured energy distribution maps along the direction as shown in Fig. 3.4 (a). Figures 3.4 (c) and (d) are such EDMs measured with photon energy of hν = 100 eV using p- and s polarized lights, respectively. From these EDMs it is clear that there are three well resolved holelike band dispersions, α_1, α_2, and

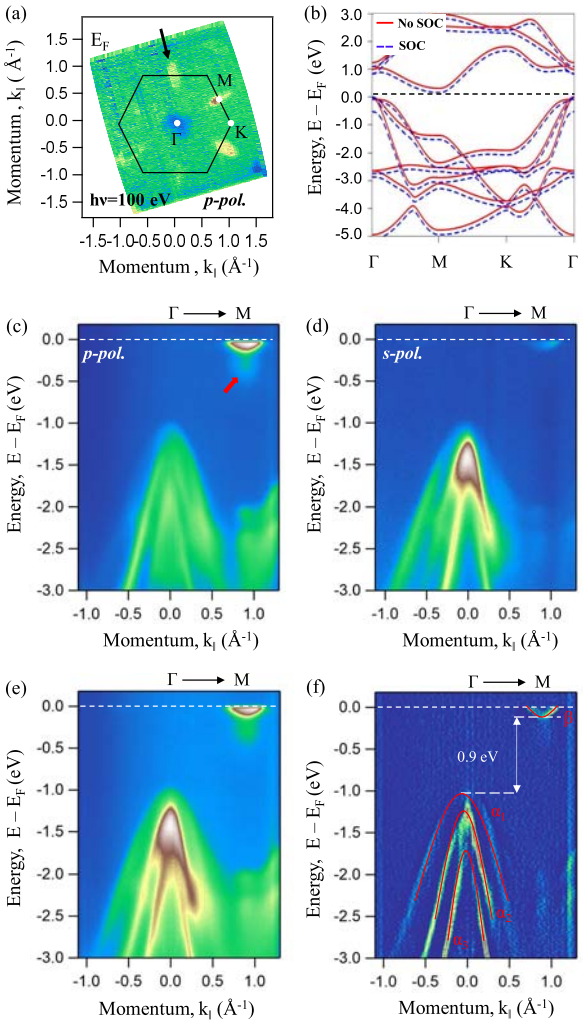

Figure 3.4: ARPES spectra of $ZrSe_2$. (a) Fermi surface map measured using p-polarized light with a photon energy of hν = 100 eV. (b) Energy-momentum plot from the first-principles calculations. (c) EDM cut taken along the direction as shown in (a) measured using p-polarized light. (d) Same as (c) but measured using s-polarized light. (e) Sum of (c) and (d). (f) Second derivative of (e).

α_3, near the $\Gamma(A)$-point with the valance band top well below the Fermi level, at a binding energy of $E_B \approx 1$ eV. Further, we found an electronlike band dispersion, β, crossing the Fermi level with a Fermi vector k_F=0.06$\mathring{A}^{-1}$ at the $M(L)$-point. This electron pocket is almost disappearing when measured with s-polarized light as shown in Figure 3.4 (d). The orbital resolved band structure of $ZrSe_2$ performed by our theoretical collaborators (see Figure 3.5) suggests that the holelike band dispersions are composed by Se p_x, p_y, and p_z orbital characters, while the electronlike band near the $M(L)$-point is composed by the Zr d_z^2 orbital character. Thus, the electron pocket is more intense when measured using p-polarized light compared to s-polarized light as in the current measuring geometry near the Fermi level the p-polarized light detects predominantly even parity orbital characters like d_z^2, p_x and p_z whereas the s-polarized

light detects p_y character. Figure 3.4 (e) shows the sum of EDMs from Figs. 3.4 (c) and (d). Figure 3.4 (f) is the second derivative of Fig. 3.4 (e). From Figs. 3.4 (e) and (f) we estimated an indirect band gap of 0.9 eV between the top of holelike (valance) band, α_1, near the $\Gamma(A)$ point and the bottom of electronlike (conduction) band, β, near the $M(L)$-point. These observations are in good agreement with earlier ARPES studies on this system, i.e., $ZrSe_2$ is a semiconductor with an indirect band gap [49–52]. In addition, near the $M(L)$ point, from the ARPES data a bright spectral feature has been noticed at a binding energy of 0.3 eV [shown by red arrow in Fig. 3.4(c)], which is not predicted from DFT calculations performed by our theoretical collaborators. But similar spectral feature has been observed in an earlier ARPES report on $ZrSe_2$ [52].

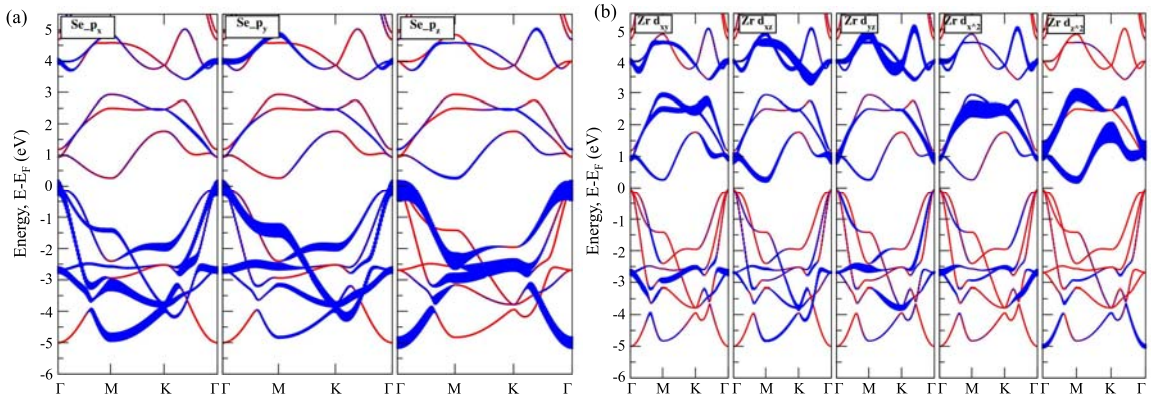

Figure 3.5: Orbital resolved calculated band structure of $ZrSe_2$ without SOC for (a) Se p states (b) Zr d states. The blue color represents the strength of contributions.

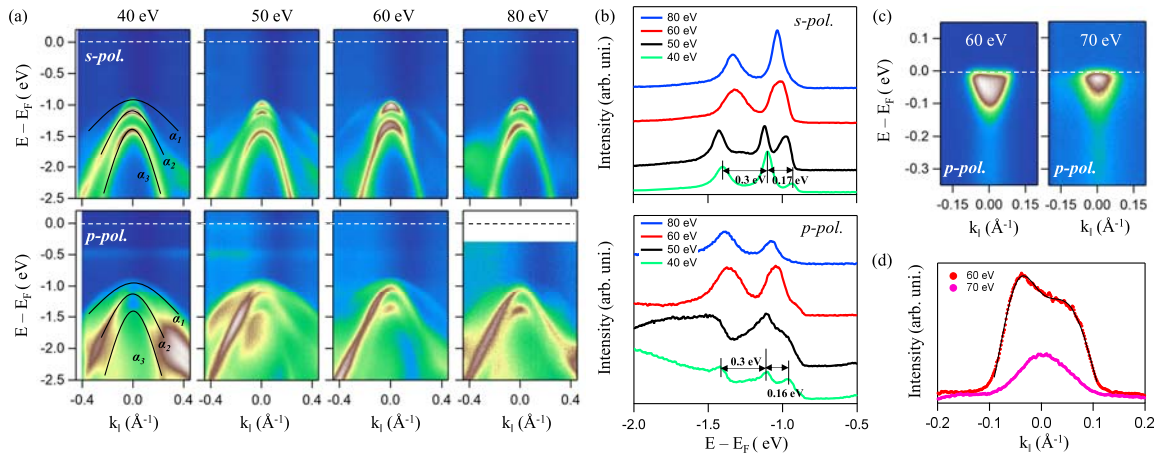

Figure 3.6: Photon energy dependent ARPES spectra of $ZrSe_2$. (a) Photon energy dependent EDMs measured using s-polarized (top panel) and p-polarized light (bottom panel) at the zone center. (b) Photon energy dependent EDCs from s- and p-polarized lights. (c) Photon energy dependent EDMs taken for the electron pocket. (d) MDCs extracted by integrating over 10 meV about the Fermi level, taken from (c).

Top panels in Figure 3.6 (a) show photon energy dependent EDMs taken along the

zone center using s-polarized light. Similarly, bottom panels in figure 3.6 (a) show photon energy dependent EDMs taken along the zone center using p-polarized light. Using inner potential of 10.9 eV [50], we identify that 40 eV, 50 eV, 60 eV and 80 eV photon energies, along $\Gamma - A$ direction, detect the bands at k_z values of 13.65 $\frac{\pi}{c'}$, 15.05 $\frac{\pi}{c'}$, 16.33 $\frac{\pi}{c'}$, and 18.63 $\frac{\pi}{c'}$. Similarly, in Fig. 3.6 (c), the photon energies 60 eV and 70 eV, along $M - L$ direction, detect the bands at k_z values of 15.75 $\frac{\pi}{c'}$ and 16.97 $\frac{\pi}{c'}$, respectively. Here, $c' = 2c$ and $c = 6.150$ $\mathring{A}$. From the EMDs of both polarizations, we do notice three well resolved hole pockets at the zone centre. As discussed above, the p-polarized light should detect two holelike bands composed of the even parity orbitals p_x and p_z and the s-polarized light should detect one holelike band composed of odd parity orbital p_y. But since the crystal is not oriented in any high symmetry direction, the photoemission process does not follow the parity dependent selection rules and moreover the orbital contribution to the low-energy band structure of $ZrSe_2$ under SOC is more complex. Hence, we do see all three bands from both p- and s- polarized lights. Top panel in Figure 3.6 (b) shows photon energy dependent EDCs taken at $k_{\|}$=0 from the EDMs of s-polarized light. Similarly, bottom panel in Figure 3.6 (b) shows photon energy dependent EDCs taken at $k_{\|}$=0 from the EDMs of p-polarized light. From the EDCs shown in Fig. 3.6 (b) one can clearly see that the three holelike bands are well separated. For instance from the EDCs of 40 eV in Fig. 3.6 (b), one peak has been observed at a binding energy of 1.4 eV, corresponding to the top of holelike band α_3. Another two peaks have been observed at binding energies of 1.1 eV and 0.93 eV, corresponding to the top of holelike bands α_2 and α_1, respectively. Similar observations were made with 50 eV photon energy. However, when measured with 60 and 80 eV the band separation is not that clear due to either the matrix element effects or k_z dispersion. Figure 3.6 (c) shows EDMs of the electron pocket measured using p-polarized light with 60 eV and 70 eV. Figure 3.6 (d) shows MDCs extracted near the Fermi level from the EDMs of Fig. 3.6 (c). From the MDC of 60 eV we estimated a Fermi vector of $k_F \approx 0.05$ $\mathring{A}^{-1}$, while the MDC of 70 eV shows no Fermi vector for the electron pocket. This suggest that the electron pocket composed of Zr d_{z^2} character has significant k_z dispersion in $ZrSe_2$.

3.3 Discussions

Despite sharing the same trigonal crystal structure, the low-energy electronic structures of $ZrTe_2$ and $ZrSe_2$ are clearly differing from one another. $ZrTe_2$ has a metallic band structure with overlapping valance and conduction bands above the Fermi level at the $\Gamma(A)$ point, composed by Te p and Zr d orbitals, respectively. On the other hand, $ZrSe_2$ has a semiconducting nature of the band structure with an indirect band gap

of E_g=0.9 eV between the $\Gamma(A)$ and $M(L)$ high symmetry points, with the valance and conduction bands composed of Se p and Zr d orbitals, respectively. In agreement with a previous ARPES report on $ZrSe_2$ [52], a tiny spectral feature near the $M(L)$-point at a binding energy of 0.3 eV has been observed. This feature is more intense when measured with p-polarized light than the s-polarized light, suggesting that it is composed by an even parity orbital. However, experimentally we are unable to pin point its band dispersion neither to electronlike nor to holelike. Further, this feature is not predicted from the DFT calculations performed by our theoretical collaborators, thus cannot be of the intrinsic origin. As the XPS data of $ZrSe_2$ (see Fig. 3.1) shows Iodine peaks, perhaps, this Iodine impurity could be a plausible source of this strange spectral feature in $ZrSe_2$ than the back-folding of the bands from the $M(L)$ to $\Gamma(A)$ as suggested in the Ref. [52]. Moreover, an earlier ARPES study on $ZrSe_2$ showed Fermi level lying in between valence and conduction band [64], whereas from our study we found that the Fermi level is moved to the conduction band. This could be due to the Se deficiency in $ZrSe_2$ as observed from the EDX measurements, which is giving rise to the net electron doping.

Spin-orbit coupling seems to be significantly affecting the low-energy electronic structure of these compounds. Especially, in $ZrSe_2$ the DFT calculations without SOC suggest two of the three hole pockets are degenerate, i.e., the two hole pockets composed by p_x and p_y are degenerate while the third hole pocket composed by p_z is well separated from them. The ARPES data of $ZrSe_2$ show three well separated hole pockets near the Γ point. This can only be reproduced in DFT calculations with the inclusion of SOC. In addition, the ARPES data of $ZrSe_2$ suggest a SOC splitting of hole pockets to as high as 0.17 eV. This observation is in very good agreement with the SOC split size of 0.16 eV for the same hole pockets reported by an earlier ARPES study on $ZrSe_2$ [50]. On the other hand, DFT calculations with SOC performed by our theoretical collaborators only produced a SOC splitting size of 0.085 eV (see Fig. 3.2).

We further would like to show DFT calculations performed by our theoretical collaborators [see Figure 3.7] on $ZrTe_2$ in which we identify a band inversion between Zr d and Te p states at the Γ point. As discussed above, in $ZrSe_2$ a clear separation is noticed between the valence and conduction bands composed by Se p and Zr d states, respectively. In $ZrTe_2$, the Zr d_{z^2} state comes closer to the valance band and in fact touches the valance band at Γ. Further, in the presence of SOC we clearly observe a band inversion in $ZrTe_2$ in such a way that the Te p_y state moves up to the conduction band, while the Zr d_{z^2} moves further down to the valance band. As a result, a band gap of 10 meV is noticed [see inset in Fig. 3.7(b)].

Next, coming to the discussion on the electronic structure of $ZrTe_2$, for the first time we report here the ARPES studies on bulk $ZrTe_2$. The only existing ARPES study is on monolayer thickness $ZrTe_2$ film deposited on InAs (111), suggesting a Dirac like

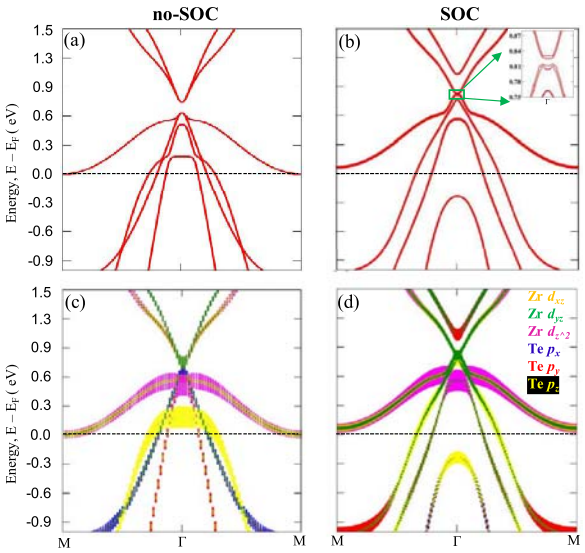

Figure 3.7: Calculated band structure of $ZrTe_2$ (a) without SOC and (b) with SOC. (c) and (d) are same as (a) and (b) but with orbital information. Inset in (b) shows a gap of 10 meV opening at the Γ point due to the band inversion under the SOC.

linear bands at the $\Gamma(A)$ point [56]. Interestingly, DFT calculations performed by our theoretical collaborators predict a band inversion between Zr d and Te p states at the $\Gamma(A)$ point, hinting at a possible non-trivial band structure in $ZrTe_2$ despite experimentally failing to detect any linear Dirac surface states. Furthermore, with the help of in-plane and out-of-plane ARPES data and Luttinger's theorem [62, 63] we calculated the number of hole and electron carriers enclosed by the hole and electron Fermi pockets. According to this theorem the carrier density is directly proportional to the volume enclosed by the Fermi surface in a uniform system of noninteracting Fermmions. The carrier density per unit cell can be written as the ratio of volume enclosed by the Fermi surface and total volume of the Brillouin zone. Our calculation results to hole carrier density $n_h = 0.003$ per unit cell ($1.1 \times 10^{19}/cm^3$) and electron carriers $n_e = 0.0026$ per unit cell ($0.95 \times 10^{19}/cm^3$). Our estimated electron carrier density value is very close to the value of the order of $10^{19}/cm^3$ reported for $Cu_{0.3}ZrTe_{1.2}$ [55], but much higher than the value of $5.07 \times 10^{15}/cm^3$ reported for $ZrTe_2$ [68]. In any case, carrier density reported in Ref. [68] is rather pointing $ZrTe_2$ to a semiconductor, while $ZrTe_2$ is widely known as a metal as also confirmed by the present study. Nearly equal number of hole and electron carrier density as derived from our ARPES data in addition to the band inversion as seen from the DFT calculations performed by our theoretical collaborators is suggesting that $ZrTe_2$ is a topological semimetal.

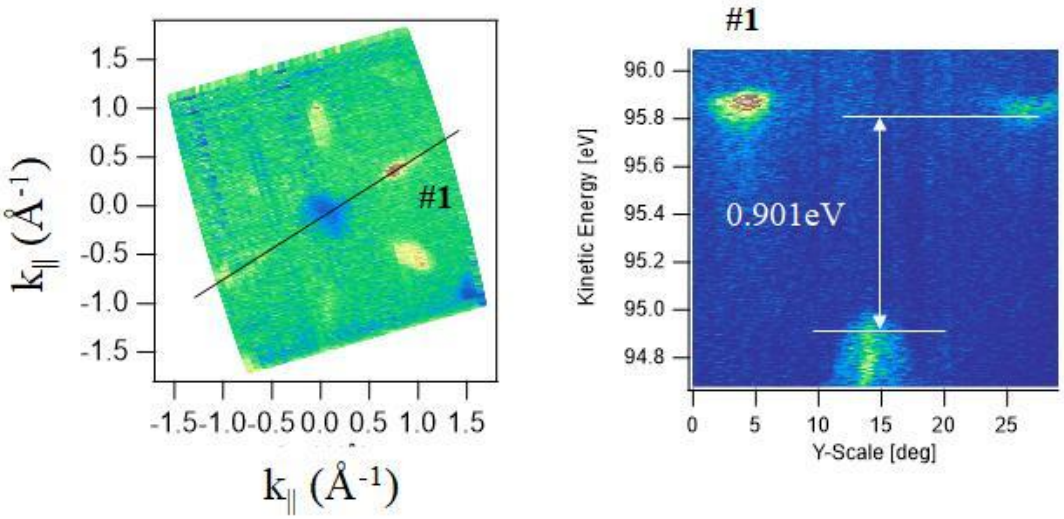

Figure 3.8: ARPES data of $ZrSe_2$. The figure suggests the gap between valence and conduction band to be 0.9 eV. The data is measured using p-polarized light with a photon energy of 100 eV.

3.4 Conclusions

In conclusion, we systematically studied the low-energy electronic structure of $ZrTe_2$ and $ZrSe_2$ using angle resolved photoemission spectroscopy and compared with density functional theory calculations performed by our theoretical collaborators. ARPES data of $ZrTe_2$ suggest several well disconnected hole and electron pockets at $\Gamma(A)$ and $M(L)$ points, respectively. From the ARPES data of $ZrTe_2$, we realize three holelike non-degenerate band dispersions near the $\Gamma(A)$ point and an electronlike band dispersion at the $M(L)$ point. The experimental observations are in good agreement with the DFT calculations performed by our theoretical collaborators. An equal number of hole and electron carrier density as estimated from our ARPES data suggesting $ZrTe_2$ to be a semimetal. In addition, the DFT calculations of $ZrTe_2$ in the presence of spin-orbit coupling suggest a band inversion between Te p and Zr d bands near Γ point, hinting $ZrTe_2$ to be a topological semimetal. On the other hand, from the Fermi surface topology of $ZrSe_2$ we observe only the electron pockets located at $M(L)$ point, while the hole pockets are noticed well below the Fermi level. Our studies on $ZrSe_2$ further suggest it to be a semiconductor with an indirect band gap of 0.9 eV between $\Gamma(A)$ and $M(L)$ high symmetry points (see Figure 3.8). Also, calculations performed by our theoretical collaborators demonstrate that the metal-chalcogen bond-length plays a vital role on the electronic structure changes of ZrX_2 (X = Se and Te) in such a way that an electronic phase transition takes place from semiconductor to topological semimetal in going from $ZrSe_2$ to $ZrTe_2$.

Bibliography

[1] R. G. Dickinson and L. Pauling, "THE CRYSTAL STRUCTURE OF MOLYBDENITE," *Journal of the American Chemical Society*, vol. 45, pp. 1466–1471, jun 1923.

[2] J. A. Wilson and A. D. Yoffe, "The transition metal dichalcogenides discussion and interpretation of the observed optical, electrical and structural properties," *Advances in Physics*, vol. 18, pp. 193–335, may 1969.

[3] L. F. Mattheiss, "Band Structures of Transition-Metal-Dichalcogenide Layer Compounds," *Physical Review B*, vol. 8, pp. 3719–3740, oct 1973.

[4] R. Späh, U. Elrod, M. Lux-Steiner, E. Bucher, and S. Wagner, "pnjunctions in tungsten diselenide," *Applied Physics Letters*, vol. 43, pp. 79–81, jul 1983.

[5] D. Jiménez, "Drift-diffusion model for single layer transition metal dichalcogenide field-effect transistors," *Applied Physics Letters*, vol. 101, p. 243501, dec 2012.

[6] Q. H. Wang, K. Kalantar-Zadeh, A. Kis, J. N. Coleman, and M. S. Strano, "Electronics and optoelectronics of two-dimensional transition metal dichalcogenides," *Nature Nanotechnology*, vol. 7, pp. 699–712, nov 2012.

[7] H. Zeng, J. Dai, W. Yao, D. Xiao, and X. Cui, "Valley polarization in MoS_2 monolayers by optical pumping," *Nature Nanotechnology*, vol. 7, pp. 490–493, jun 2012.

[8] R. Cheng, S. Jiang, Y. Chen, Y. Liu, N. Weiss, H.-C. Cheng, H. Wu, Y. Huang, and X. Duan, "Few-layer molybdenum disulfide transistors and circuits for high-speed flexible electronics," *Nature Communications*, vol. 5, oct 2014.

[9] S. J. Li, J. C. Bernède, J. Pouzet, and M. Jamali, "thin films prepared by solid state reaction (induced by annealing) between the constituents in thin film form," *Journal of Physics: Condensed Matter*, vol. 8, pp. 2291–2304, apr 1996.

[10] M. S. Fuhrer and J. Hone, "Measurement of mobility in dual-gated MoS_2 transistors," *Nature Nanotechnology*, vol. 8, pp. 146–147, mar 2013.

[11] W. Wu, L. Wang, Y. Li, F. Zhang, L. Lin, S. Niu, D. Chenet, X. Zhang, Y. Hao, T. F. Heinz, J. Hone, and Z. L. Wang, "Piezoelectricity of single-atomic-layer MoS_2 for energy conversion and piezotronics," *Nature*, vol. 514, pp. 470–474, oct 2014.

[12] C. Gong, Y. Zhang, W. Chen, J. Chu, T. Lei, J. Pu, L. Dai, C. Wu, Y. Cheng, T. Zhai, L. Li, and J. Xiong, "Electronic and Optoelectronic Applications Based on 2D Novel Anisotropic Transition Metal Dichalcogenides," *Advanced Science*, vol. 4, p. 1700231, oct 2017.

[13] M. A. Khan and M. N. Leuenberger, "Optoelectronics with single layer group-VIB transition metal dichalcogenides," *Nanophotonics*, vol. 7, pp. 1589–1600, sep 2018.

[14] A. T. Neal, Y. Du, H. Liu, and P. D. Ye, "Two-Dimensional $TaSe_2$ Metallic Crystals: Spin–Orbit Scattering Length and Breakdown Current Density," *ACS Nano*, vol. 8, pp. 9137–9142, sep 2014.

[15] Z. Zhang, J. Niu, P. Yang, Y. Gong, Q. Ji, J. Shi, Q. Fang, S. Jiang, H. Li, X. Zhou, L. Gu, X. Wu, and Y. Zhang, "Van der Waals Epitaxial Growth of 2D Metallic Vanadium Diselenide Single Crystals and their Extra-High Electrical Conductivity," *Advanced Materials*, vol. 29, p. 1702359, aug 2017.

[16] J. Zhang, B. Yang, H. Zheng, X. Han, and Y. Yan, "Large magnetic anisotropy and strain induced enhancement of magnetic anisotropy in monolayer $TaTe_2$," *Physical Chemistry Chemical Physics*, vol. 19, no. 35, pp. 24341–24347, 2017.

[17] M. N. Ali, J. Xiong, S. Flynn, J. Tao, Q. D. Gibson, L. M. Schoop, T. Liang, N. Haldolaarachchige, M. Hirschberger, N. P. Ong, and R. J. Cava, "Large, non-saturating magnetoresistance in WTe_2," *Nature*, vol. 514, pp. 205–208, sep 2014.

[18] J. Jiang, Z. K. Liu, Y. Sun, H. F. Yang, C. R. Rajamathi, Y. P. Qi, L. X. Yang, C. Chen, H. Peng, C. C. Hwang, S. Z. Sun, S. K. Mo, I. Vobornik, J. Fujii, S. S. P. Parkin, C. Felser, B. H. Yan, and Y. L. Chen, "Signature of type-II Weyl semimetal phase in $MoTe_2$," *Nature Communications*, vol. 8, jan 2017.

[19] S. Thirupathaiah, R. Jha, B. Pal, J. S. Matias, P. K. Das, P. K. Sivakumar, I. Vobornik, N. C. Plumb, M. Shi, R. A. Ribeiro, and D. D. Sarma, "$MoTe_2$: An uncompensated semimetal with extremely large magnetoresistance," *Physical Review B*, vol. 95, jun 2017.

[20] H. Ma, P. Chen, B. Li, J. Li, R. Ai, Z. Zhang, G. Sun, K. Yao, Z. Lin, B. Zhao, R. Wu, X. Tang, X. Duan, and X. Duan, "Thickness-Tunable Synthesis of Ultrathin Type-II Dirac Semimetal $PtTe_2$ Single Crystals and Their Thickness-Dependent Electronic Properties," *Nano Letters*, vol. 18, pp. 3523–3529, may 2018.

[21] X. guaug Zheng, H. Kuriyaki, and K. Hirakawa, "Electrical Anisotropy of Layered Compound $ZrSe_2$ and $HfSe_2$," *Journal of the Physical Society of Japan*, vol. 58, pp. 622–626, feb 1989.

[22] Y.-C. Lin, D. O. Dumcenco, Y.-S. Huang, and K. Suenaga, "Atomic mechanism of the semiconducting-to-metallic phase transition in single-layered MoS_2," *Nature Nanotechnology*, vol. 9, pp. 391–396, apr 2014.

[23] H. M. Hill, A. F. Rigosi, K. T. Rim, G. W. Flynn, and T. F. Heinz, "Band Alignment in MoS_2/WS_2 Transition Metal Dichalcogenide Heterostructures Probed by Scanning Tunneling Microscopy and Spectroscopy," *Nano Letters*, vol. 16, pp. 4831–4837, jul 2016.

[24] M. Salavati, "Electronic and mechanical responses of two-dimensional HfS_2, $HfSe_2$, ZrS_2, and $ZrSe_2$ from first-principles," *Frontiers of Structural and Civil Engineering*, vol. 13, pp. 486–494, jul 2018.

[25] T. Pillo, J. Hayoz, H. Berger, R. Fasel, L. Schlapbach, and P. Aebi, "Interplay between electron-electron interaction and electron-phonon coupling near the Fermi surface of 1T-TaS_2," *Physical Review B*, vol. 62, pp. 4277–4287, aug 2000.

[26] L. Perfetti, P. A. Loukakos, M. Lisowski, U. Bovensiepen, H. Berger, S. Biermann, P. S. Cornaglia, A. Georges, and M. Wolf, "Time Evolution of the Electronic Structure of 1T-TaS_2 through the Insulator-Metal Transition," *Physical Review Letters*, vol. 97, aug 2006.

[27] C. Zhang, K. C. Santosh, Y. Nie, C. Liang, W. G. Vandenberghe, R. C. Longo, Y. Zheng, F. Kong, S. Hong, R. M. Wallace, and K. Cho, "Charge Mediated Reversible Metal–Insulator Transition in Monolayer $MoTe_2$ and $W_xMo_{1-x}Te_2$ Alloy," *ACS Nano*, vol. 10, pp. 7370–7375, jul 2016.

[28] K. F. Mak, C. Lee, J. Hone, J. Shan, and T. F. Heinz, "Atomically Thin MoS_2: A New Direct-Gap Semiconductor," *Physical Review Letters*, vol. 105, sep 2010.

[29] A. Kumar and P. K. Ahluwalia, "Electronic structure of transition metal dichalcogenides monolayers 1H-MX_2 (M = Mo, W; X = S, Se, Te) from ab-initio theory: new direct band gap semiconductors," *The European Physical Journal B*, vol. 85, jun 2012.

[30] W. Choi, N. Choudhary, G. H. Han, J. Park, D. Akinwande, and Y. H. Lee, "Recent development of two-dimensional transition metal dichalcogenides and their applications," *Materials Today*, vol. 20, pp. 116–130, apr 2017.

[31] M. Porer, U. Leierseder, J.-M. Ménard, H. Dachraoui, L. Mouchliadis, I. E. Perakis, U. Heinzmann, J. Demsar, K. Rossnagel, and R. Huber, "Non-thermal separation of electronic and structural orders in a persisting charge density wave," *Nature Materials*, vol. 13, pp. 857–861, jul 2014.

[32] L. J. Li, W. J. Zhao, B. Liu, T. H. Ren, G. Eda, and K. P. Loh, "Enhancing charge-density-wave order in 1T-$TiSe_2$ nanosheet by encapsulation with hexagonal boron nitride," *Applied Physics Letters*, vol. 109, p. 141902, oct 2016.

[33] Y. Ma, Y. Dai, M. Guo, C. Niu, Y. Zhu, and B. Huang, "Evidence of the Existence of Magnetism in Pristine VX_2 Monolayers (X = S, Se) and Their Strain-Induced Tunable Magnetic Properties," *ACS Nano*, vol. 6, pp. 1695–1701, jan 2012.

[34] X. Zhu, Y. Guo, H. Cheng, J. Dai, X. An, J. Zhao, K. Tian, S. Wei, X. C. Zeng, C. Wu, and Y. Xie, "Signature of coexistence of superconductivity and ferromagnetism in two-dimensional $NbSe_2$ triggered by surface molecular adsorption," *Nature Communications*, vol. 7, apr 2016.

[35] H. Xiang, B. Xu, Y. Xia, J. Yin, and Z. Liu, "Strain tunable magnetism in SnX_2 (X = S, Se) monolayers by hole doping," *Scientific Reports*, vol. 6, dec 2016.

[36] Y. I. Joe, X. M. Chen, P. Ghaemi, K. D. Finkelstein, G. A. de la Peña, Y. Gan, J. C. T. Lee, S. Yuan, J. Geck, G. J. MacDougall, T. C. Chiang, S. L. Cooper, E. Fradkin, and P. Abbamonte, "Emergence of charge density wave domain walls above the superconducting dome in 1T-$TiSe_2$," *Nature Physics*, vol. 10, pp. 421–425, apr 2014.

[37] C.-X. Liu, "Unconventional Superconductivity in Bilayer Transition Metal Dichalcogenides," *Physical Review Letters*, vol. 118, feb 2017.

[38] S. C. de la Barrera, M. R. Sinko, D. P. Gopalan, N. Sivadas, K. L. Seyler, K. Watanabe, T. Taniguchi, A. W. Tsen, X. Xu, D. Xiao, and B. M. Hunt, "Tuning Ising superconductivity with layer and spin–orbit coupling in two-dimensional transition-metal dichalcogenides," *Nature Communications*, vol. 9, apr 2018.

[39] A. Ramasubramaniam, D. Naveh, and E. Towe, "Tunable band gaps in bilayer transition-metal dichalcogenides," *Physical Review B*, vol. 84, nov 2011.

[40] R. Das, B. Rakshit, S. Debnath, and P. Mahadevan, "Microscopic model for the strain-driven direct to indirect band-gap transition in monolayer MoS_2 and ZnO," *Physical Review B*, vol. 89, mar 2014.

[41] H. C. Movva, T. Lovorn, B. Fallahazad, S. Larentis, K. Kim, T. Taniguchi, K. Watanabe, S. K. Banerjee, A. H. MacDonald, and E. Tutuc, "Tunable Γ-K Valley Populations in Hole-Doped Trilayer WSe_2," *Physical Review Letters*, vol. 120, Mar. 2018.

[42] M. Aghajanian, A. A. Mostofi, and J. Lischner, "Tuning electronic properties of transition-metal dichalcogenides via defect charge," *Scientific Reports*, vol. 8, sep 2018.

[43] H. Guo, N. Lu, L. Wang, X. Wu, and X. C. Zeng, "Tuning Electronic and Magnetic Properties of Early Transition-Metal Dichalcogenides via Tensile Strain," *The Journal of Physical Chemistry C*, vol. 118, pp. 7242–7249, mar 2014.

[44] L. ping Feng, N. Li, M. hao Yang, and Z. tang Liu, "Effect of pressure on elastic, mechanical and electronic properties of WSe_2: A first-principles study," *Materials Research Bulletin*, vol. 50, pp. 503–508, feb 2014.

[45] M. Yi, D. Lu, J.-H. Chu, J. G. Analytis, A. P. Sorini, A. F. Kemper, B. Moritz, S.-K. Mo, R. G. Moore, M. Hashimoto, W.-S. Lee, Z. Hussain, T. P. Devereaux, I. R. Fisher, and Z.-X. Shen, "Symmetry-breaking orbital anisotropy observed for detwinned $Ba(Fe_{1-x}Co_x)_2As_2$ above the spin density wave transition," *Proceedings of the National Academy of Sciences*, vol. 108, pp. 6878–6883, apr 2011.

[46] Y. Zhang, C. He, Z. R. Ye, J. Jiang, F. Chen, M. Xu, Q. Q. Ge, B. P. Xie, J. Wei, M. Aeschlimann, X. Y. Cui, M. Shi, J. P. Hu, and D. L. Feng, "Symmetry breaking via orbital-dependent reconstruction of electronic structure in detwinned NaFeAs," *Physical Review B*, vol. 85, feb 2012.

[47] S. Thirupathaiah, E. D. L. Rienks, H. S. Jeevan, R. Ovsyannikov, E. Slooten, J. Kaas, E. van Heumen, S. de Jong, H. A. Dürr, K. Siemensmeyer, R. Follath, P. Gegenwart, M. S. Golden, and J. Fink, "Dissimilarities between the electronic structure of chemically doped and chemically pressurized iron pnictides from an angle-resolved photoemission spectroscopy study," *Physical Review B*, vol. 84, jul 2011.

[48] H. E. Brauer, H. I. Starnberg, L. J. Holleboom, and H. P. Hughes, "The electronic structure of $ZrSe_2$ and Cs_xZrSe_2 studied by angle-resolved photoelectron spectroscopy," *Journal of Physics: Condensed Matter*, vol. 7, pp. 7741–7760, oct 1995.

[49] M. Moustafa, T. Zandt, C. Janowitz, and R. Manzke, "Growth and band gap determination of the ZrS_xSe_{2-x} single crystal series," *Physical Review B*, vol. 80, jul 2009.

[50] M. Moustafa, A. Ghafari, A. Paulheim, C. Janowitz, and R. Manzke, "Spin orbit splitting in the valence bands of ZrS_xSe_{2-x}: Angle resolved photoemission and density functional theory," *Journal of Electron Spectroscopy and Related Phenomena*, vol. 189, pp. 35–39, aug 2013.

[51] M. J. Mleczko, C. Zhang, H. R. Lee, H.-H. Kuo, B. Magyari-Köpe, R. G. Moore, Z.-X. Shen, I. R. Fisher, Y. Nishi, and E. Pop, "$HfSe_2$ and $ZrSe_2$: Two-dimensional semiconductors with native high-κ oxides," *Science Advances*, vol. 3, p. e1700481, aug 2017.

[52] A. Ghafari, M. Moustafa, G. D. Santo, L. Petaccia, and C. Janowitz, "Opposite dispersion bands at the Fermi level in $ZrSe_2$," *Applied Physics Letters*, vol. 112, p. 182105, apr 2018.

[53] A. H. Reshak and S. Auluck, "Theoretical investigation of the electronic and optical properties of ZrX_2 (X=S, Se and Te)," *Physica B: Condensed Matter*, vol. 353, pp. 230–237, dec 2004.

[54] A. Kumar, H. He, R. Pandey, P. K. Ahluwalia, and K. Tankeshwar, "Pressure and electric field-induced metallization in the phase-engineered ZrX_2 (X = S, Se, Te) bilayers," *Physical Chemistry Chemical Physics*, vol. 17, no. 29, pp. 19215–19221, 2015.

[55] A. J. S. Machado, N. P. Baptista, B. S. de Lima, N. Chaia, T. W. Grant, L. E. Corrêa, S. T. Renosto, A. C. Scaramussa, R. F. Jardim, M. S. Torikachvili, J. A. Aguiar, O. C. Cigarroa, L. T. F. Eleno, and Z. Fisk, "Evidence for topological behavior in superconducting Cu_xZrTe_{2-y}," *Physical Review B*, vol. 95, apr 2017.

[56] P. Tsipas, D. Tsoutsou, S. Fragkos, R. Sant, C. Alvarez, H. Okuno, G. Renaud, R. Alcotte, T. Baron, and A. Dimoulas, "Massless Dirac Fermions in $ZrTe_2$ Semimetal Grown on InAs(111) by van der Waals Epitaxy," *ACS Nano*, vol. 12, pp. 1696–1703, jan 2018.

[57] M. H. Whangbo, F. J. DiSalvo, and R. M. Fleming, "Electronic structure of $ZrTe_5$," *Physical Review B*, vol. 26, pp. 687–689, jul 1982.

[58] G. Manzoni, L. Gragnaniello, G. Autès, T. Kuhn, A. Sterzi, F. Cilento, M. Zacchigna, V. Enenkel, I. Vobornik, L. Barba, F. Bisti, P. Bugnon, A. Magrez, V. Strocov, H. Berger, O. Yazyev, M. Fonin, F. Parmigiani, and A. Crepaldi, "Evidence for a Strong Topological Insulator Phase in $ZrTe_5$," *Physical Review Letters*, vol. 117, nov 2016.

[59] Y. Zhang, C. Wang, L. Yu, G. Liu, A. Liang, J. Huang, S. Nie, X. Sun, Y. Zhang, B. Shen, J. Liu, H. Weng, L. Zhao, G. Chen, X. Jia, C. Hu, Y. Ding, W. Zhao, Q. Gao, C. Li, S. He, L. Zhao, F. Zhang, S. Zhang, F. Yang, Z. Wang, Q. Peng, X. Dai, Z. Fang, Z. Xu, C. Chen, and X. J. Zhou, "Electronic evidence of temperature-induced Lifshitz transition and topological nature in $ZrTe_5$," *Nature Communications*, vol. 8, may 2017.

[60] L. Shen, M. X. Wang, S. C. Sun, J. Jiang, X. Xu, T. Zhang, Q. H. Zhang, Y. Y. Lv, S. H. Yao, Y. B. Chen, M. H. Lu, Y. F. Chen, C. Felser, B. H. Yan, Z. K. Liu, L. X. Yang, and Y. L. Chen, "Spectroscopic evidence for the gapless electronic structure in bulk $ZrTe_5$," *Journal of Electron Spectroscopy and Related Phenomena*, vol. 219, pp. 45–52, aug 2017.

[61] H. Xiong, J. A. Sobota, S.-L. Yang, H. Soifer, A. Gauthier, M.-H. Lu, Y.-Y. Lv, S.-H. Yao, D. Lu, M. Hashimoto, P. S. Kirchmann, Y.-F. Chen, and Z.-X. Shen, "Three-dimensional nature of the band structure of $ZrTe_5$ measured by high-momentum-resolution photoemission spectroscopy," *Physical Review B*, vol. 95, may 2017.

[62] J. M. Luttinger, "Fermi Surface and Some Simple Equilibrium Properties of a System of Interacting Fermions," *Physical Review*, vol. 119, pp. 1153–1163, aug 1960.

[63] M. Oshikawa, "Topological Approach to Luttinger's Theorem and the Fermi Surface of a Kondo Lattice," *Physical Review Letter*, vol. 84, pp. 3370–3373, Apr 2000.

[64] K. Nikonov, N. Ehlen, B. Senkovskiy, N. Saigal, A. Fedorov, A. Nefedov, C. Wöll, G. D. Santo, L. Petaccia, and A. Grüneis, "Synthesis and spectroscopic characterization of alkali–metal intercalated $ZrSe_2$," *Dalton Transactions*, vol. 47, no. 9, pp. 2986–2991, 2018.

[65] H. SCHÄFER, "Chemical Transport Processes as an Aid in Preparative Chemistry. Combination of Transport Reactions with Other Processes," in *Chemical Transport Reactions*, pp. 115–131, Elsevier, 1964.

[66] S. V. Borisenko, V. B. Zabolotnyy, A. A. Kordyuk, D. V. Evtushinsky, T. K. Kim, E. Carleschi, B. P. Doyle, R. Fittipaldi, M. Cuoco, A. Vecchione, and H. Berger, "Angle-resolved Photoemission Spectroscopy At Ultra-low Temperatures," *Journal of Visualized Experiments*, oct 2012.

[67] S. V. Borisenko, ""One-cubed" ARPES User Facility at BESSY II," *Synchrotron Radiation News*, vol. 25, pp. 6–11, sep 2012.

[68] D. N. Bhavsar, A. K. Dasadia, B. B. Nariya, M. K. Bhayani, A. R. Jani, A. B. Garg, R. Mittal, and R. Mukhopadhyay, "Electrical Properties of Zirconium Ditelluride Single Crystals," AIP, 2011.

Chapter 4

ARPES Studies on CDW Candidate, $TaTe_2$

4.1 Introduction

Investigation of the TMDCs is quite fascinating as these systems host a wide variety of structural, physical, and electronic properties [1–4]. Particularly, the structural polymorphism in TMDCs (1T, 2H, and 3R phases) play a significant role for their exotic physical properties such as CDW [5, 6], superconductivity [7], magnetic ordering [8], topological properties [9], and the valleytronics [10] by tuning the electronic band structure. Therefore, a thorough knowledge on the electronic band structure of TMDCs is vital for understanding their diverse electronic and physical properties.

TMDCs are in general formed by one transition metal atom (group IV, V, VI, VII, IX, and X) and two chalcogen atoms (S, Se, and Te) with the chemical formula of MX_2 (M=transition metal and X=chalcogen). Among these, the group V TMDCs, NbX_2 and TaX_2 are most attractive as they show interplay between the charge ordering (CDW) and the superconductivity both in the $1T$ and $2H$ phases [11]. The mechanism of charge ordering and the superconductivity in TMDCs are under debate. Fermi surface nesting [12], electron-phonon coupling [13], and the van Hove singularities [14] have been proposed as the origin of CDW ordering in these systems [15]. Though, the electronic properties are almost similar in both NbX_2 and TaX_2, their structural properties are rather different. That means, at room temperature, the bulk Ta(Nb)S_2 and Ta(Nb)Se_2 can be formed in the $1T$ and $2H$ phases with octahedral and trigonal prismatic coordination in the hexagonal crystal symmetry [4] having $(\sqrt{13} \times \sqrt{13})$ superstructure on the surface [16], while the bulk $TaTe_2$ and $NbTe_2$ are in the distorted octahedral coordination with the monoclinic crystal symmetry ($1T'$ phase) having (1×3) superstructure on the surface [17]. Also at low temperatures, the surface of Ta(Nb)Te_2 goes into the (3×3) superstructure with $1T'$ phase intact [18–20]. Further,

Most of this chapter is published as: I. Kar *et al.*, J. Phys. Chem. C **125**, 1150 (2021).

$TaTe_2$ shows IC-CDW phase below $T_{CDW} \approx 170K$ [13, 18, 19, 21], whereas $NbTe_2$ shows C-CDW order at room temperature but then turns into IC-CDW phase just above the room temperature [22, 23].

So far $TaTe_2$ and $NbTe_2$ are experimentally studied for their structural [5, 13, 17, 24], physical properties [18, 20], magnetic properties [25], and potential applications in the energy storage materials [26–28]. Further, unlike $TaTe_2$ which does not show superconductivity down to lowest possible temperature, $NbTe_2$ shows superconductivity below $\approx 0.5K$ [29]. Several theoretical calculations were performed to understand their structural transition and origin of CDW in these systems by studying the electronic band structure using the DFT calculations [13, 16, 20]. However, till date, one experimental ARPES report available on $NbTe_2$ [22] and none on $TaTe_2$. One quantum oscillation study discussing the speculative band structure of $TaTe_2$ is available [25]. Since ARPES studies are utmost needed to unambiguously understand the low-energy electronic structure of these systems, we performed ultra-high resolution ARPES studies on $TaTe_2$ to understand the origin of CDW transition and to examine whether it is a Dirac semimetal as speculated by the quantum oscillations [25].

In this chapter, we report on the low-energy electronic structure of $1T'$-$TaTe_2$ using high-resolution angle-resolved photoemission spectroscopy (ARPES) and compare it with density functional theory calculations performed by our theoretical collaborator. We observe that the Fermi surface of $1T'$-$TaTe_2$ is in the hexagonal symmetry, which is in contradiction to its monoclinic crystal structure. We observe a totally different electronic structure of $TaTe_2$ when compared with the isostructural compound $NbTe_2$. Further, despite being in the hexagonal symmetry the Fermi surface topology of $TaTe_2$ is quite different when compared to the isovalent compounds, $TaSe_2$ and TaS_2. To fully understand the experimentally obtained electronic band structure of $TaTe_2$, the surface states are disentangled from bulk with the help of the slab calculations performed by our theoretical collaborator. Thus, we realize that the surface states resemble the $2H$ phase electronic structure, while the bulk states replicate the $1T$ phase electronic structure of $TaTe_2$. This is an interesting discovery as $TaTe_2$ does exist neither in $1T$ phase nor in $2H$ phase as per the observation of crystal structure. We further notice that the $1T$ phase electronic structure shows substantial band dispersion in the k_z direction. We realize that the band structure of $TaTe_2$ is temperature independent above and below the CDW transition temperature.

4.2 Experimental Details

Single crystals of $TaTe_2$ were grown by chemical vapor transport method using iodine as transporting agent at IISER, Pune by our collaborator. The sample preparation

and storage were carried out in an Ar-filled glove box where the moisture and oxygen were maintained below 0.1 ppm. Polycrystalline sample of $TaTe_2$, obtained by reacting stoichiometric amounts of Ta powder (Sigma Aldrich , 99.9%, metals basis) and Te (ingot, 99.99%, metals basis, Alfa Aesar) under vacuum (10^{-5} Torr) at 750° C for 48 h, was used for the single crystal growth. The polycrystalline sample was then grinded in glove box, loaded and sealed under vacuum in a quartz ampoule together with the transporting agent (iodine – 5 mg/cm^3). Subsequently, the ampoule has been placed in a three-zone furnace, where a gradient temperature of 50° C has been maintained between the source (T_1 = 870° C) and the sink zones (T_2 = 820° C) for a period of 12 days. By this procedure platelet shaped single crystals with a typical lateral dimensions of 10-15 mm were obtained.

The chemical purity and composition were confirmed using SEM (ZEISS Gemini SEM 500) equipped with an EDX probe. The phase purity of the single crystal was checked using X-ray diffraction (Bruker D8 diffractometer, Cu Kα radiation) measurements.

ARPES measurements were carried out at 1^3-ARPES end station using UE112-PGM2b beamline equipped with a Scienta R4000 analyzer having angular resolution better than 0.2° located in BESSY II (Helmholtz zentrum Berlin) synchrotron radiation center [30, 31] by Dr. Thirupathaiah Setti. Photon energies for the measurements were varied between 50 to 100 eV. The energy resolution was set between 5 and 15 meV depending on the excitation energy. Data were recorded at a chamber vacuum better than 1×10^{-10} mbar. Sample was cleaved *in situ* before the measurements. The sample temperature was kept at 1 K during the measurements. Temperature dependent ARPES data were recorded at the SIS beamline located in Swiss Light Source [32] equipped with a Scienta R4000 electron analyzer with an angular resolution of better than 0.2° by Dr. Thirupathaiah Setti. The energy resolution was set at 10 meV. The sample was cleaved *in situ* before performing the measurements. The base pressure was better than 1×10^{-10} mbar during the measurements.

4.3 Results and Discussions

The crystal structure of $TaTe_2$ in the $1T'$ phase with monoclinic crystal symmetry is shown in Figure 4.1a at high temperature (T>170K) and in Figure 4.1b at low temperature (T<170K) reproduced from Ref.[18]. As can be seen from Figures 4.1a and 4.1b the crystal symmetry does not change but only the lattice constants do alter above and below the CDW order transition temperature (T≈170K). Figure 4.1c shows the hypothetical crystal structure of $TaTe_2$ in the $1T$ phase with the hexagonal crystal symmetry projected onto the *ab* plane. SEM image of $TaTe_2$ single crystal is shown

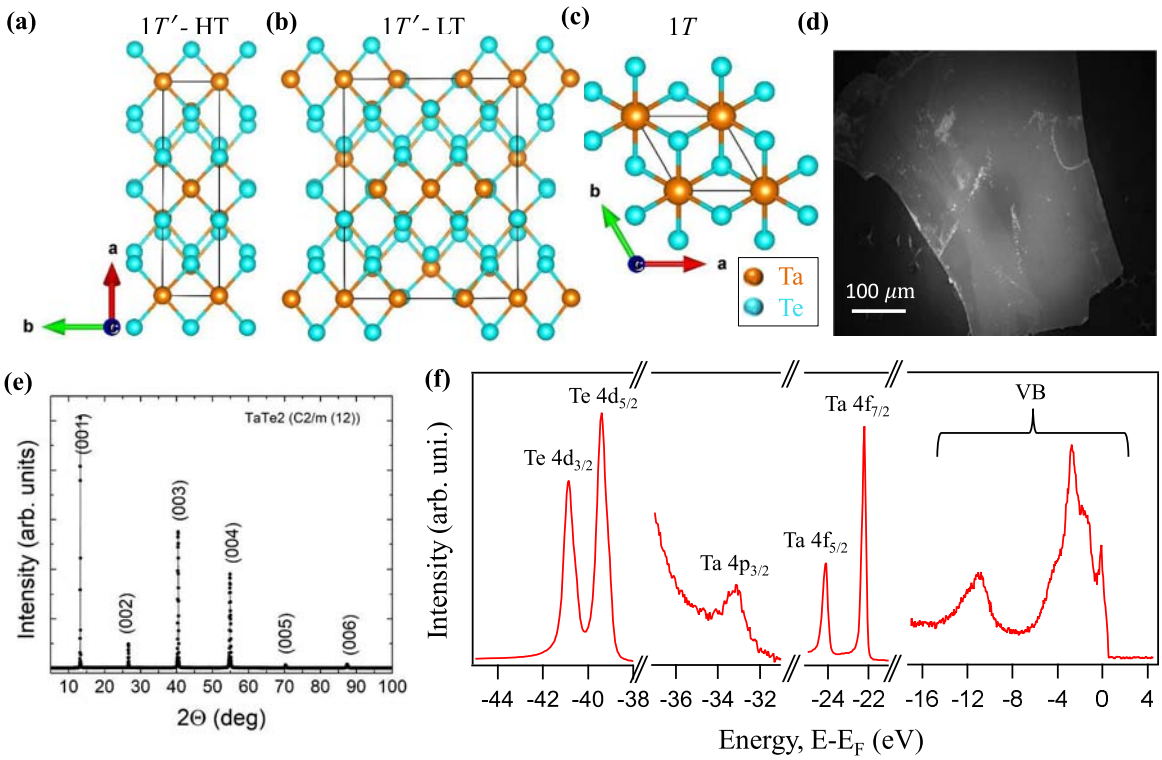

Figure 4.1: Distorted $1T$ phase ($1T'$) or the monoclinic crystal structure of $TaTe_2$ at high temperature (a) and at low temperature (b). (c) Hypothetical $1T$ phase crystal structure of $TaTe_2$ projected onto the ab-plane. (d) Scanning electron microscope image of the $1T'$-$TaTe_2$ single crystal. (e) X-ray diffractogram of $1T'$-$TaTe_2$ single crystal. (f) XPS measured with a photon energy of 100 eV. On the XPS, all core levels are identified either to Ta or Te atom.

in Figure 4.1d. From the EDX measurements, we derived the chemical composition as $Ta_{1.06}Te_2$. This suggests that there exists a 6% of excess Ta per unit cell. Such an excess amount of transition metal or chalcogen deficiency in these systems generally leads to excess electron carrier density. Otherwise, from the EDX and SEM data the sample is noticed as homogeneous. Figure 4.1e shows XRD pattern, measured at room temperature, indicating that $TaTe_2$ single crystal is crystallized in the space group of $C2/m(12)$, with lattice parameters as $a = 14.76$ Å, $b = 3.63$ Å, $c = 9.32$ Å, and $\beta = 110.89°$. The crystal surface normal is parallel to the c-axis, analogous to the earlier reports [20, 25]. Also, we performed XPS measurements on the cleaved $TaTe_2$ to check the purity of the sample, before performing the ARPES measurements as shown in Figure 4.1f. All observed core levels from XPS are referred to respective binding energies of Ta and Te atoms and no other impurity peaks are detected.

Fermi surface topology of $TaTe_2$ in the k_x-k_y plane is shown in Figure 4.2a, measured with a photon energy of 100 eV using p-polarized light at a sample temperature of 1K and corresponding constant energy contour taken at a binding energy of 100 meV below the Fermi level is shown in Figure 4.3a. As can be seen from these maps, the

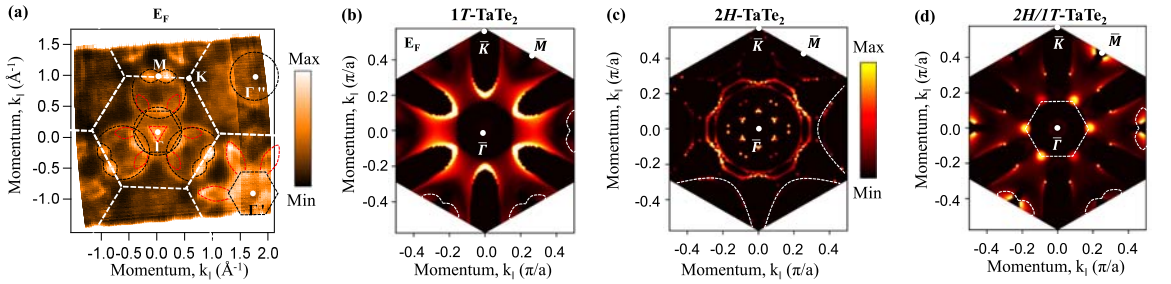

Figure 4.2: (a) Experimental Fermi surface map measured with a photon energy hν = 100 eV. (b), (c) and (d) Show the calculated spectral function distribution at the Fermi level plotted for semi-infinite slabs of $1T$, $2H$, and $2H$-monolayer placed on top of the semi-infinite $1T$-$TaTe_2$ slab, respectively.

Fermi pockets follow the hexagonal symmetry that is in contrast to its monoclinic crystal structure as observed from the XRD measurements (Figure 4.1e). The symmetry difference between the crystal and electronic structures could be related to the formation of bulk (3×1×3) supercell structure as reported earlier in the case of isostructural $1T'$-$NbTe_2$ [22]. Further, on the Fermi surface map, we could identify various Fermi pockets of circular-shaped, hexagonal-shaped, petal-shaped, half-circular-shaped, and triangular-shaped. In detail, at the Γ point we see a large circular-shaped Fermi pocket. Though we identify another large hexagonal-shaped Fermi pocket at the Γ point, due to the matrix element effects it is not very clear. But this hexagonal-shaped Fermi pocket is clearly visible as we move to the Γ′ point. Further, at the Γ point we do find six petal-shaped, three half-circle-shaped and one triangular-shaped Fermi pockets. Interestingly, as we move away from Γ to the Γ′ point we find a large hexagonal-shaped Fermi pocket that is not clear at the Γ point. Also, at Γ′, the size of the petal-shaped Fermi pockets is significantly enhanced compared to their size at Γ. We did not observe any half-circle-shaped Fermi pockets at Γ′. Next, at Γ″, we could readily observe one circular-shaped Fermi pocket of the same size to the one at Γ and with a careful observation we could also find the half-circular-shaped Fermi pockets. At the M point, we observe peanut-shaped Fermi pocket. Due to the matrix element effects out of six peanut-shaped Fermi pockets, only three are readily visible due to their high spectral intensity and the other three peanut-shaped pockets exist with reduced spectral intensity.

Since the ARPES is a surface sensitive technique, inevitably, it probes the surface electronic structure in addition to the bulk electronic structure. Therefore, it is crucial to disentangle the surface electronic structure from the bulk resulted from the surface reconstruction due to crystal cleavage under ultra-high chamber vacuum. For this purpose, slab calculations of $TaTe_2$ in its $1T$-phase, $2H$-phase, and $2H$-phase monolayer on top of the bulk $1T$-phase (hybrid-phase) $TaTe_2$ have been performed using the density functional theory by our theoretical collaborator. Thus, Figures 4.2b, 4.2c,

and 4.2d are the calculated spectral function intensity plots in the k_x-k_y plane at the Fermi level from the top surface layer of the semi-infinite slabs of $1T$, $2H$, and $2H$-monolayer placed on top of the semi-infinite $1T$-$TaTe_2$ slab (hybrid-phase), respectively. On comparing the experimental Fermi surface with those obtained from the slab calculations, we can find a qualitative agreement between experiment and theory. For instance, the circular-shaped and half-circular-shaped hole pockets are reproduced from the $2H$-phase. The peanut-shaped hole pocket can be noticed very well from the hybrid-phase, though we can see it from the $1T$-phase with reduced intensity. Next, the hexagonal-shaped hole pocket is visible only in the hybrid-phase. Nevertheless, the triangular-shaped electron pocket and the petal-shaped hole pockets are not visible from any of these slab calculations, possibly due to their bulk origin.

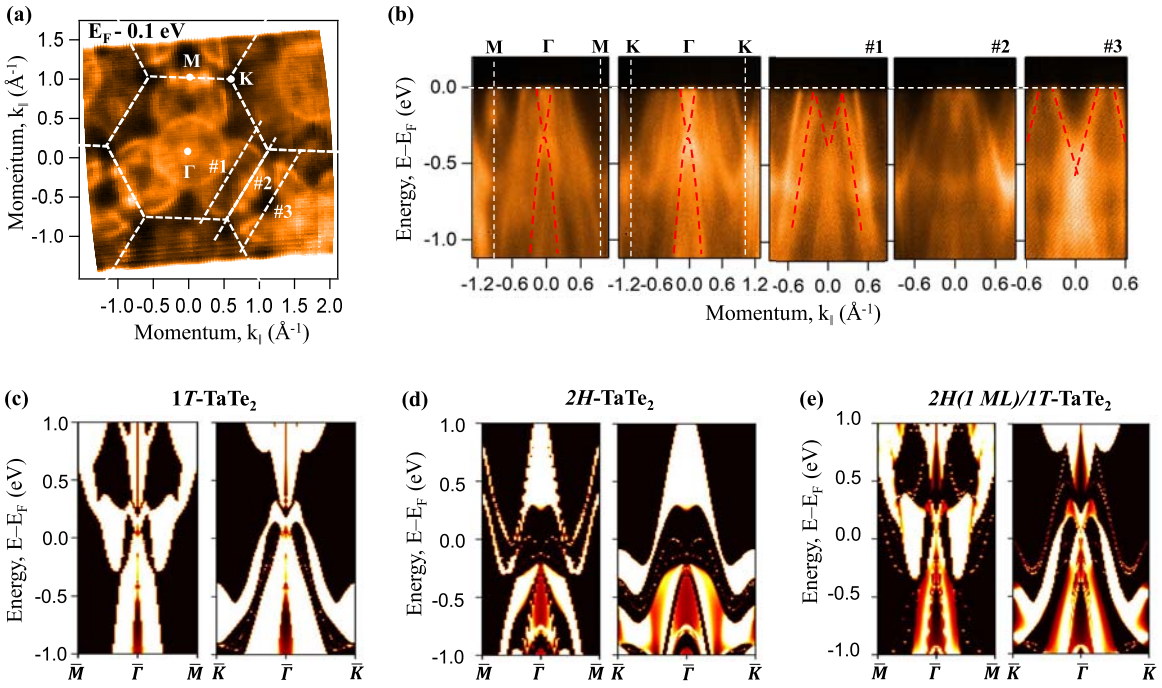

Figure 4.3: (a) Constant energy contour map taken at binding energy of 0.1 eV below E_F measured with a photon energy $h\nu = 100$ eV (b) EDMs taken along Γ-K, Γ-M, and along the cuts #1-#3 as shown in (a). (c), (d), and (e) are the calculated energy distribution maps along the high-symmetry lines of $\overline{\Gamma M}$ and $\overline{\Gamma K}$ plotted for the semi-infinite slabs of $1T$, $2H$, and $2H$-monolayer placed on top of the semi-infinite $1T$-$TaTe_2$ slab, respectively.

To elucidate the nature of band dispersions contributing to the Fermi pockets, we plotted in Figure 4.3b the experimentally obtained EDMs taken along ΓK, ΓM, #1, #2, and #3 directions as shown in Figure 4.3a. From these EDMs one can realize that at the Γ point the triangular shaped Fermi sheet has an electronlike band dispersion, while the larger circular- and hexagonal-shaped Fermi sheets have the holelike band dispersions. From the EDM cut #1 we can see that the petal-shaped and half-circle-

shaped Fermi sheets have the holelike band dispersions. Similarly, from the EDM cut #2 we find that the peanut-shaped Fermi sheet at the M point has the holelike band dispersions. Next, the EDM cut #3 identifies holelike band dispersion for the petal-shaped Fermi sheet corresponding to Γ'. Note here that the Fermi vector of the petal-shaped hole pocket is negligible at Γ as it does not cross the Fermi level, however, it has a finite Fermi vector of 0.1Å^{-1} near the Γ' point. Therefore, the petal-shaped hole pocket has significant k_z dispersion and must be originating from the bulk band structure. Similarly, the triangular-shaped hole pocket at Γ totally disappears at Γ' which is possible only if it is of the bulk nature. Thus, from our experimental data we can unambiguously conclude that the petal-shaped and triangular-shaped Fermi sheets are originated from the bulk bands, while the rest of Fermi sheets are originated from the surface bands. Importantly, overall, the experimental band dispersions are qualitatively in agreement with the calculated band structure of $2H$ (1 ML)/$1T$-$TaTe_2$ as shown in Figure 4.3e. In addition, for a better understanding of the calculated band dispersions, we plotted individual EDMs along the high-symmetry lines of $\overline{\Gamma M}$ and $\overline{\Gamma K}$ from the semi-infinite slab of $1T$-$TaTe_2$ (see Figure 4.3c) and $2H$-$TaTe_2$ (see Figure 4.3d). Thus, from Figure 4.3d it is clearly evident that the experimental band dispersion noticed at the M point (see Figure 4.3b) is originated from the $2H$ phase.

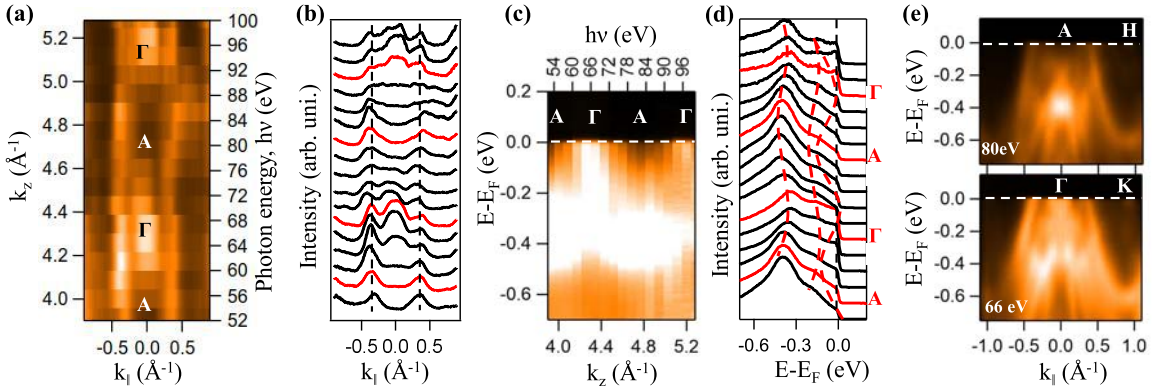

Figure 4.4: Out-of-plane (k_z) electronic structure of $TaTe_2$ measured at 1K. (a) k_z Fermi surface map in ΓKHA plane. (b) Photon energy dependent momentum distribution curves extracted from (a). (c) EDM taken along the Γ-A high symmetry line. (d) Photon energy dependent energy distribution curves extracted from (c).(e) EDMs taken from Γ-K and A-H high symmetry lines.

Figure 4.4 shows out-of-plane (k_z) ARPES measurements on $TaTe_2$. Figure 4.4a shows k_z Fermi surface map in $k_{\|}$-k_z plane measured with photon energy ranging from 52 to 100 eV with a step of 3 eV. High symmetry points Γ and A are located on the k_z map. Figure 4.4b depicts the photon energy dependent MDCs. From Figure 4.4b we can notice mainly three peaks, out of which two peaks (shown by the vertical-dashed lines) always present irrespective of the applied photon energy while the middle-peak appears significantly at the photon energies of 66 and 94 eV and then the peak

intensity gradually decreases as we move away from these photon energies to totally disappear at photon energies of 52 and 80 eV. Figure 4.4c shows EDM taken along the Γ-A direction. From Figure 4.4c we can notice that the band is crossing the Fermi level near Γ. Observation of the experimental k_z dispersions along the Γ-A high symmetry line are in very good agreement with the bulk band structure calculations of 1T-$TaTe_2$ (see Figure 4.5) performed by our theoretical collaborator. Figure 4.4d shows EDCs extracted from the EDM shown in Figure 4.4c. EDMs along Γ-K and A-H orientation are shown in Figure 4.4e. Following the equation $k_z = \sqrt{\frac{2m}{\hbar^2}(V_0 + E_k \cos^2\theta)}$ and considering the inner potential $V_0 = 11 \pm 2$ eV with a lattice constant $c = 9.30\mathring{A}$ of low temperature [18], we identified that the Γ point can be probed with photon energies hν = 66 and 92 eV, while the A point can be probed with photon energies 54 and 80 eV. Here, m is the rest mass of electron, $\hbar$ is the Planck's constant, E_k is the photoelectron kinetic energy, and θ is photoelectron emission angle with respect to the sample surface normal.

The 3D view of the calculated Fermi surface topology of bulk $TaTe_2$ in 1T and 2H are plotted in Figure 4.5 a and c, respectively to compare the experimental results with theory. Our ARPES data qualitatively agree with bulk 2H-$TaTe_2$ where one can find the circular-shaped, and half-circular-shaped hole pockets at the Γ point. The petal-shaped hole pocket noticed in 1T'-$TaTe_2$ is consistent with bulk 1T-$TaTe_2$. Though the triagular shaped electron pocket is not observed from the 1T-$TaTe_2$. Further, for better understanding of electronic band structure, the electronic band structure of bulk $TaTe_2$ in 1T and 2H are plotted in Figure 4.5 b and d, respectively. The experimental k_z dispersions along the Γ-A high symmetry line (see Figure 4.4c) are in very good agreement with the bulk band structure calculations of 1T-$TaTe_2$ as shown in Figure 4.5b. This observation suggests that triagular shaped electron pocket is coming from bulk origin.

Since $TaTe_2$ shows CDW order at 170 K [11], we have measured the ARPES data above and below the CDW transition temperature to understand the effect of electronic band structure on the CDW order. Figure 4.6 shows the FS maps measured with 100 eV photon energy using p polarized light. Left panel in Figure 4.6 shows the FS map measured at a sample temperature of 20 K, middle panel is the FS map measured at 180 K, and right panel is the FS map measured at 20 K immediately after cooling down from 180 K. As can be noticed from Figure 4.6, the FS topology hardly changes across the CDW transition temperature, except that over a full temperature cycle the spectral intensity reduced for the surface states (see right panel) due to sample aging.

Next, we compare the experimental band structure of $TaTe_2$ with the existing literature on the isovalent compounds like, 1T-TaS_2, 1T-$TaSe_2$ and the isostructural compound 1T'-$NbTe_2$. Despite being the FS topology of these compounds in the hexago-

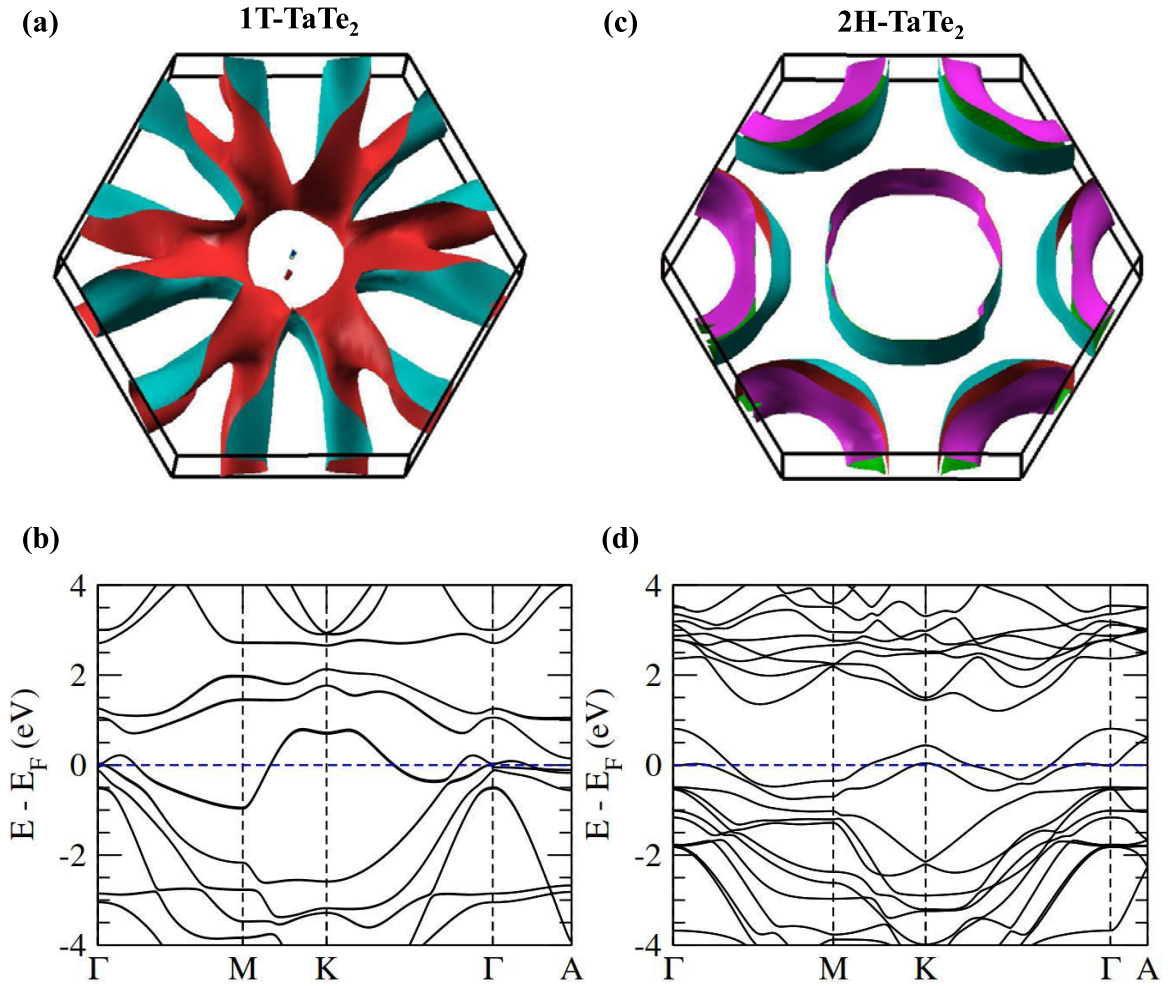

Figure 4.5: (a) 3D view of the calculated Fermi surface topology of bulk $1T$-$TaTe_2$. (b) Electronic band structure of bulk $1T$-$TaTe_2$. (c) 3D view of the calculated Fermi surface topology of bulk $2H$-$TaTe_2$. (d) Electronic band structure of bulk $2H$-$TaTe_2$.

nal symmetry we do not find any qualitative agreement with $TaTe_2$. We identify one circular-shaped and one hexagonal-shaped hole pockets at the Γ point from $TaTe_2$, whereas no such circular-shaped hole pockets have been found from $1T$-TaS_2 [33], $1T$-$TaSe_2$ [34, 35], and $1T'$-$NbTe_2$ [22]. However, the petal-shaped hole pocket noticed in $1T'$-$TaTe_2$ is consistent with these systems. Further, the electronic band dispersions of $TaTe_2$ do neither agree with $TaSe_2$ nor with TaS_2 which are formed by the isovalent substitution of Se/S at the Te site. This is rare to find drastic changes in the electronic structure by isovalently replacing the chalcogen atom in the TMDCs. It is known that a relative shifting of the valance and conduction bands with isovalent substitution takes place [9]. Hence, understanding the electronic structure of $TaTe_2$ has become very complex by simply comparing with the $1T$-phase of the other similar systems. Importantly, we notice from the total energy calculation of slab $1T$-$TaTe_2$ (20 monolayers) that the top surface layer of $1T$-$TaTe_2$ favourably transforms into the $2H$-phase. Moreover, the

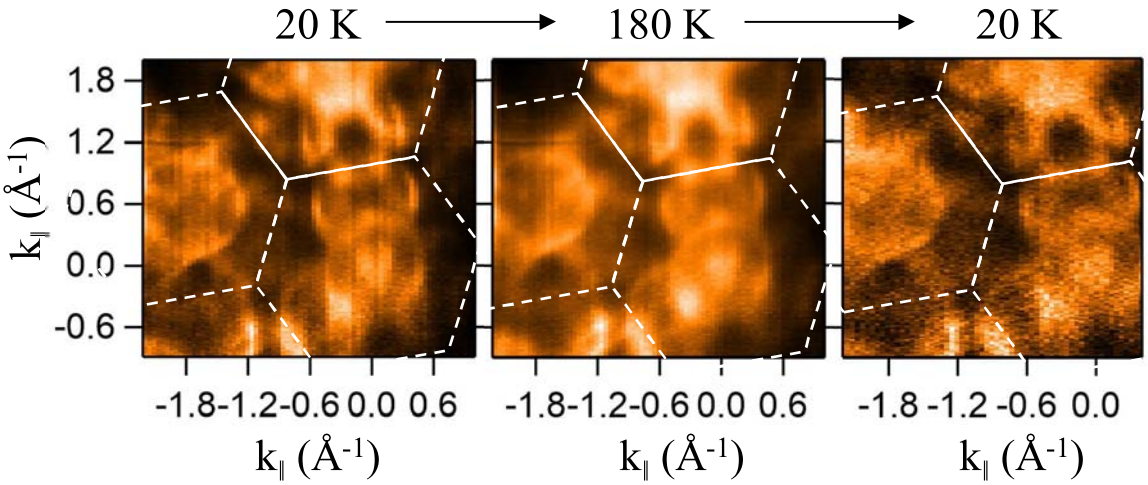

Figure 4.6: Temperature dependent Fermi surface (FS) topology of $TaTe_2$. FS measured at 20 K (left), 180 K (middle), and 20 K after cooling down from 180 K (right).

calculated spectral function of the stand alone $2H$ phase monolayer and the $2H$ phase surface monolayer on top of the semi-infinite $1T$- phase slab, matches quite well with our ARPES data. In addition, our ARPES data qualitatively agree with the ARPES data of $2H$-$TaSe_2$ [36, 37] and $2H$-TaS_2 [38] where one can find the circular-shaped, half-circular-shaped, and hexagonal-shaped hole pockets at the Γ point. Therefore, the surface states observed on top of the bulk $1T'$-$TaTe_2$ from our studies are originated by the surface reconstruction to form $2H$-$TaTe_2$.

Finally, we notice that the band structure of $TaTe_2$ hardly changes across the CDW transition temperature ($T_{CDW} \approx$ 170K) as shown in Figure 4.6, thus, ruling out the Fermi surface nesting mechanism as the origin of CDW ordering in this system. Perhaps, the electron-phonon scattering could be the reason for CDW phase in $TaTe_2$ as discussed in the previous reports [16, 22]. Also, it is worth to mention here that the $2H$-phase surface layer is stable even after raising the sample temperature up to 180 K and moving to back 20 K as the Fermi surface topology does not change much with the temperature. An earlier quantum oscillations study on $TaTe_2$ suggested the presence of topological Dirac cone in this system [25]. But from our systematic ARPES measurements and DFT calculations, we do not observe any signature of the suggested Dirac cone. On the other hand, some of the transport studies on $TaTe_2$ reported it to be a semimetal [25, 39, 40]. Our experimental studies qualitatively support this argument, if we ignore the large number of surface states, as we observe a bulk triangular-shaped electron pocket at the Γ point and six petal-shaped hole pockets surrounding it.

4.4 Conclusions

In conclusion, we have systematically studied the low-energy electronic structure of layered Tantalum ditelluride ($1T'$-$TaTe_2$) using angle-resolved photoemission spectroscopy and compared with density functional theory performed by our theoretical collaborator. We find that the Fermi surface topology of $TaTe_2$ is rather different when compared to the isovalant compounds of $TaTe_2$ such as TaS_2, $TaSe_2$, and isostructural compound like $NbTe_2$. Interestingly, we realize that the surface electronic structure of $1T'$-$TaTe_2$ has more resemblance to the $2H$-$TaTe_2$, while the bulk electronic structure $1T'$-$TaTe_2$ has more resemblance to the $1T$-$TaTe_2$. These experimental observations are systematically compared with our DFT calculations performed on $1T$-, $2H$- and $2H$ (monolayer)/$1T$-$TaTe_2$. We further notice that the Fermi surface topology is temperature independent up to 180 K, confirming that $2H$ phase on the top layer is very stable and the CDW order is not due to the Fermi surface nesting.

Bibliography

[1] H. Guo, N. Lu, L. Wang, X. Wu, and X. C. Zeng, "Tuning Electronic and Magnetic Properties of Early Transition-Metal Dichalcogenides via Tensile Strain," *The Journal of Physical Chemistry C*, vol. 118, pp. 7242–7249, mar 2014.

[2] H. Wang, H. Yuan, S. S. Hong, Y. Li, and Y. Cui, "Physical and chemical tuning of two-dimensional transition metal dichalcogenides," *Chemical Society Reviews*, vol. 44, no. 9, pp. 2664–2680, 2015.

[3] D. Voiry, A. Mohite, and M. Chhowalla, "Phase engineering of transition metal dichalcogenides," *Chemical Society Reviews*, vol. 44, no. 9, pp. 2702–2712, 2015.

[4] S. Manzeli, D. Ovchinnikov, D. Pasquier, O. V. Yazyev, and A. Kis, "2D transition metal dichalcogenides," *Nature Reviews Materials*, vol. 2, jun 2017.

[5] H. Luo, W. Xie, J. Tao, H. Inoue, A. Gyenis, J. W. Krizan, A. Yazdani, Y. Zhu, and R. J. Cava, "Polytypism, polymorphism, and superconductivity in $TaSe_{2-x}Te_x$," *Proceedings of the National Academy of Sciences*, vol. 112, mar 2015.

[6] M. Yoshida, J. Ye, Y. Zhang, Y. Imai, S. Kimura, A. Fujiwara, T. Nishizaki, N. Kobayashi, M. Nakano, and Y. Iwasa, "Extended Polymorphism of Two-Dimensional Material," *Nano Letters*, vol. 17, pp. 5567–5571, aug 2017.

[7] B. Sipos, A. F. Kusmartseva, A. Akrap, H. Berger, L. Forró, and E. Tutiš, "From Mott state to superconductivity in 1T-TaS_2," *Nature Materials*, vol. 7, pp. 960–965, nov 2008.

[8] Y. Ma, Y. Dai, M. Guo, C. Niu, Y. Zhu, and B. Huang, "Evidence of the Existence of Magnetism in Pristine VX_2 Monolayers (X = S, Se) and Their Strain-Induced Tunable Magnetic Properties," *ACS Nano*, vol. 6, pp. 1695–1701, jan 2012.

[9] I. Kar, J. Chatterjee, L. Harnagea, Y. Kushnirenko, A. V. Fedorov, D. Shrivastava, B. Büchner, P. Mahadevan, and S. Thirupathaiah, "Metal-chalcogen bond-length induced electronic phase transition from semiconductor to topological semimetal in ZrX_2 (X=Se and Te)," *Physical Review B*, vol. 101, apr 2020.

[10] J. R. Schaibley, H. Yu, G. Clark, P. Rivera, J. S. Ross, K. L. Seyler, W. Yao, and X. Xu, "Valleytronics in 2D materials," *Nature Reviews Materials*, vol. 1, aug 2016.

[11] M. Chhowalla, H. S. Shin, G. Eda, L.-J. Li, K. P. Loh, and H. Zhang, "The chemistry of two-dimensional layered transition metal dichalcogenide nanosheets," *Nature Chemistry*, vol. 5, pp. 263–275, mar 2013.

[12] M. D. Johannes and I. I. Mazin, "Fermi surface nesting and the origin of charge density waves in metals," *Physical Review B*, vol. 77, apr 2008.

[13] Y. Liu, D. F. Shao, L. J. Li, W. J. Lu, X. D. Zhu, P. Tong, R. C. Xiao, L. S. Ling, C. Y. Xi, L. Pi, H. F. Tian, H. X. Yang, J. Q. Li, W. H. Song, X. B. Zhu, and Y. P. Sun, "Nature of charge density waves and superconductivity in 1T-$TaSe_{2-x}Te_x$," *Physical Review B*, vol. 94, jul 2016.

[14] T. M. Rice and G. K. Scott, "New Mechanism for a Charge-Density-Wave Instability," *Physical Review Letters*, vol. 35, pp. 120–123, jul 1975.

[15] S. Barja, S. Wickenburg, Z.-F. Liu, Y. Zhang, H. Ryu, M. M. Ugeda, Z. Hussain, Z.-X. Shen, S.-K. Mo, E. Wong, M. B. Salmeron, F. Wang, M. F. Crommie, D. F. Ogletree, J. B. Neaton, and A. Weber-Bargioni, "Charge density wave order in 1D mirror twin boundaries of single-layer $MoSe_2$," *Nature Physics*, vol. 12, pp. 751–756, apr 2016.

[16] S. Sharma, L. Nordström, and B. Johansson, "Stabilization of charge-density waves in 1T-TaX_2 (X=S,Se,Te): First-principles total energy calculations," *Physical Review B*, vol. 66, nov 2002.

[17] B. E. Brown, "The crystal structures of $NbTe_2$ and $TaTe_2$," *Acta Crystallographica*, vol. 20, pp. 264–267, feb 1966.

[18] T. Sörgel, J. Nuss, U. Wedig, R. K. Kremer, and M. Jansen, "A new low temperature modification of $TaTe_2$—Comparison to the room temperature and the hypothetical 1T-$TaTe_2$ modification," *Materials Research Bulletin*, vol. 41, pp. 987–1000, may 2006.

[19] J. Feng, A. Tan, S. Wagner, J. Liu, Z. Mao, X. Ke, and P. Zhang, "Charge modulation and structural transformation in $TaTe_2$ studied by scanning tunneling microscopy/spectroscopy," *Applied Physics Letters*, vol. 109, p. 021901, jul 2016.

[20] J. J. Gao, J. G. Si, X. Luo, J. Yan, F. C. Chen, G. T. Lin, L. Hu, R. R. Zhang, P. Tong, W. H. Song, X. B. Zhu, W. J. Lu, and Y. P. Sun, "Origin of the structural phase transition in single-crystal $TaTe_2$," *Physical Review B*, vol. 98, dec 2018.

[21] L.-L. Wei, S.-S. Sun, K. Sun, Y. Liu, D.-F. Shao, W.-J. Lu, Y.-P. Sun, H.-F. Tian, and H.-X. Yang, "Charge Density Wave States and Structural Transition in Layered Chalcogenide $TaSe_{2-x}Te_x$," *Chinese Physics Letters*, vol. 34, p. 086101, aug 2017.

[22] C. Battaglia, H. Cercellier, F. Clerc, L. Despont, M. G. Garnier, C. Koitzsch, P. Aebi, H. Berger, L. Forró, and C. Ambrosch-Draxl, "Fermi-surface-induced lattice distortion in $NbTe_2$," *Physical Review B*, vol. 72, nov 2005.

[23] F. Clerc, C. Battaglia, H. Cercellier, C. Monney, H. Berger, L. Despont, M. G. Garnier, and P. Aebi, "Fermi surface of layered compounds and bulk charge density wave systems," *Journal of Physics: Condensed Matter*, vol. 19, p. 355002, aug 2007.

[24] J. van Landuyt, G. van Tendeloo, and S. Amelinckx, "The direct imaging of two-dimensional charge density waves and of commensurate superlattices in $NbTe_2$ and $TaTe_2$," *Physica Status Solidi (a)*, vol. 29, pp. K11–K13, may 1975.

[25] H. Chen, Z. Li, L. Guo, and X. Chen, "Anisotropic magneto-transport and magnetic properties of low-temperature phase of $TaTe_2$," *EPL (Europhysics Letters)*, vol. 117, p. 27009, jan 2017.

[26] D. Chakravarty, P. Kumar, V. S. Ugale, and D. J. Late, "Microwave-Assisted Synthesis of Few-Layered $TaTe_2$ and Its Application as Supercapacitor," *European Journal of Inorganic Chemistry*, vol. 2015, feb 2015.

[27] J. Zhang, B. Yang, H. Zheng, X. Han, and Y. Yan, "Large magnetic anisotropy and strain induced enhancement of magnetic anisotropy in monolayer $TaTe_2$," *Physical Chemistry Chemical Physics*, vol. 19, no. 35, pp. 24341–24347, 2017.

[28] X. Xue, X. Wang, and W. Mi, "Electric field effects on electronic structure of tantalum dichalcogenides van der Waals $TaS_2/TaSe_2$ and $TaSe_2/TaTe_2$ heterostructures," *Applied Surface Science*, vol. 455, pp. 963–969, oct 2018.

[29] M. H. V. Maaren and G. M. Schaeffer, "Some new superconducting group Va dichalcogenides," *Physics Letters A*, vol. 24, pp. 645–646, jun 1967.

[30] S. V. Borisenko, ""One-cubed" ARPES User Facility at BESSY II," *Synchrotron Radiation News*, vol. 25, pp. 6–11, sep 2012.

[31] S. V. Borisenko, V. B. Zabolotnyy, A. A. Kordyuk, D. V. Evtushinsky, T. K. Kim, E. Carleschi, B. P. Doyle, R. Fittipaldi, M. Cuoco, A. Vecchione, and H. Berger, "Angle-resolved Photoemission Spectroscopy At Ultra-low Temperatures," *Journal of Visualized Experiments*, oct 2012.

[32] U. Flechsig, L. Patthey, and T. Schmidt, "Performance measurements at the SLS spectroscopy beamline," in *AIP Conference Proceedings*, vol. 705, pp. 316–319, American Institute of Physics, 2004.

[33] A. S. Ngankeu, S. K. Mahatha, K. Guilloy, M. Bianchi, C. E. Sanders, K. Hanff, K. Rossnagel, J. A. Miwa, C. B. Nielsen, M. Bremholm, and P. Hofmann, "Quasi-one-dimensional metallic band dispersion in the commensurate charge density wave of 1T-TaS_2," *Physical Review B*, vol. 96, nov 2017.

[34] M. Bovet, D. Popović, F. Clerc, C. Koitzsch, U. Probst, E. Bucher, H. Berger, D. Naumović, and P. Aebi, "Pseudogapped Fermi surfaces of 1T-TaS_2 and 1T-$TaSe_2$: A charge density wave effect," *Physical Review B*, vol. 69, mar 2004.

[35] Y. Chen, W. Ruan, M. Wu, S. Tang, H. Ryu, H.-Z. Tsai, R. L. Lee, S. Kahn, F. Liou, C. Jia, O. R. Albertini, H. Xiong, T. Jia, Z. Liu, J. A. Sobota, A. Y. Liu, J. E. Moore, Z.-X. Shen, S. G. Louie, S.-K. Mo, and M. F. Crommie, "Strong correlations and orbital texture in single-layer 1T-$TaSe_2$," *Nature Physics*, vol. 16, pp. 218–224, jan 2020.

[36] S. V. Borisenko, A. A. Kordyuk, A. N. Yaresko, V. B. Zabolotnyy, D. S. Inosov, R. Schuster, B. Büchner, R. Weber, R. Follath, L. Patthey, and H. Berger, "Pseudogap and Charge Density Waves in Two Dimensions," *Physical Review Letters*, vol. 100, may 2008.

[37] H. Ryu, Y. Chen, H. Kim, H.-Z. Tsai, S. Tang, J. Jiang, F. Liou, S. Kahn, C. Jia, A. A. Omrani, J. H. Shim, Z. Hussain, Z.-X. Shen, K. Kim, B. I. Min, C. Hwang, M. F. Crommie, and S.-K. Mo, "Persistent Charge-Density-Wave Order in Single-Layer $TaSe_2$," *Nano Letters*, vol. 18, pp. 689–694, jan 2018.

[38] J. Zhao, K. Wijayaratne, A. Butler, J. Yang, C. D. Malliakas, D. Y. Chung, D. Louca, M. G. Kanatzidis, J. van Wezel, and U. Chatterjee, "Orbital selectivity causing anisotropy and particle-hole asymmetry in the charge density wave gap of 2H-TaS_2," *Physical Review B*, vol. 96, sep 2017.

[39] J. A. Wilson and A. D. Yoffe, "The transition metal dichalcogenides discussion and interpretation of the observed optical, electrical and structural properties," *Advances in Physics*, vol. 18, pp. 193–335, may 1969.

[40] L. H. Brixner, "Preparation and properties of the single crystalline AB_2-type selenides and tellurides of niobium, tantalum, molybdenum and tungsten," *Journal of Inorganic and Nuclear Chemistry*, vol. 24, no. 3, pp. 257–263, 1962.

Chapter 5

Magneto-transport and ARPES Studies on type-II Dirac semimetal, $NiTe_2$

5.1 Introduction

Discovery of Dirac and Weyl semimetals in condensed matter physics has attracted much attention from the research community. TMDCs are widely known for their diverse electronic properties including exotic topological states, such as, topological insulator [1, 2] or topological semimetals [3, 4]. Interestingly, in these systems, physical and electronic properties can be tuned by changing the sample thickness, twisting-angle between layers, making hetero-structures or by applying external perturbations like stress, strain, and pressure [5–15]. These systems are also considered to be quasi two-dimensional layered systems due to the weak van der Waals forces between the layers [16]. Among these, group X TMDC compounds, XZ_2 (X = Ni, Pd, Pt; Z = Se, Te) are of great research interest as they show linearly dispersive Dirac surface states [17–32]. Among them, $PdTe_2$ is a superconductor having a type-II Dirac point below the Fermi level. ARPES measurements on $PdTe_2$ clearly show a type-II Dirac point at a binding energy of 0.5 eV and another surface Dirac point at a binding energy of 1.7 eV [23]. Also, $PtTe_2$ and $PtSe_2$ are type-II Dirac semimetals [18–20, 25]. ARPES measurements on these systems show a Dirac point at a binding energy of 0.86 eV for $PtTe_2$ and 1.48 eV for $PtSe_2$ [20]. Deep topological surface states along with another Dirac cone are also observed in $PtTe_2$ and $PtSe_2$ [20, 25]. There are several ARPES measurements on $PtTe_2$, $PtSe_2$ and $PdTe_2$ suggesting that these are Dirac semimetals [20, 23–25]. On the other hand, so far only one report was available on the ARPES studies of $NiTe_2$ with no discussion on the presence of Dirac point

Most of this chapter is published as: [1] I. Kar *et al.*, AIP Conference Proceedings **2265** 030361 (2020), [2] I. Kar *et al.*, Mater. Today: Proc. **65**, (2022) 70-73.

in this system. They reported a comparative study among $NiTe_2$, $PdTe_2$ and $PtTe_2$. The valence band, composed of d-orbitals of transition metal, shifts to higher binding energy upon going from Ni to Pt [32]. Another theoretical study on $NiTe_2$ reported a pair of Dirac nodes in $NiTe_2$ very close to the Fermi level [27]. The calculated band structure shows a Dirac point at an energy of 0.08 eV above the Fermi level and surface state calculations using Wannier functions show another Dirac point at a binding energy of 1.6 eV below the Fermi level, connecting the bulk and surface state. Also, a quantum oscillations study revealed the existence of a nontrivial Berry phase connected with Dirac fermions [27]. In addition, it shows a large linear anisotropic MR and planar Hall effect as observed from the magneto-transport measurement [27, 31]. The non-saturating linear MR at higher magnetic fields is a novel phenomenon, which has potential applications in the spintronic technology such as magnetic field sensors and magnetic memory devices [33].

ARPES is a sophisticated tool to probe the electronic structure of a system directly. Hence, motivated by the previous theoretical study [27], we have performed ARPES measurements on $NiTe_2$ to observe the predicted Dirac surface states experimentally. Electrical transport in metals and semiconductors is one of the basic and frontline properties in the condensed matter systems as it consists of important information on the electronic phase transitions [34, 35]. Hence, keeping the literatures on $NiTe_2$ in the mind, we successfully synthesized $NiTe_2$ single crystals and performed electrical-transport and magneto-transport measurements to understand the electronic properties. The system is found to be metallic with dominant s-d electron-phonon scattering. The calculated Debye temperature using BG formula is $\Theta_D \approx$230 K. Below T $\approx$25 K, the BG fitting deviates from experimental data. A small resistivity upturn is observed at low temperature possibly due to the presence of electron-electron interaction [36, 37].

5.2 Experimental Details

High quality single crystals of $NiTe_2$ were synthesized using flux-growth method with Te as a flux at IISER, Pune by our collaborator. Also, we have synthesized single crystals of $NiTe_2$ following the same method. High purity nickel (Alfa Aesar, metal basis Ni, 99.9%) and tellurium (Signma Aldrich, metal basis Te, 99.997%), taken in a molar ratio of 1:8, were thoroughly mixed in an argon filled glove box. The precursors mixture was then sealed in a quartz ampoule under vacuum. The quartz ampoule was then slowly heated to 950°C for 10h, kept there for 48h to ensure homogenization and then slowly cooled to 595°C at a rate of 3°C/h. At this temperature the ampoule was removed from the oven. Then we separated large dark – grey single crystals with typical

lateral dimensions of 10 mm× 9 mm from the flux using surgical scalpel blade. The crystal purity, morphology, chemical composition were confirmed using SEM (Quanta 250 FEG) equipped with an EDX probe. The phase purity of the grown crystals was checked using X-ray diffraction (PANalytical X'Pert PRO diffractometer with Cu k_α-radiation).

ARPES measurements were carried out at the ARPES experimental station, Indus-2, RRCAT, Indore using a He light source of photon energy 21.2 eV and an energy resolution of 10 meV. The sample was cleaved in situ in the sample preparation chamber to get a clean and smooth surface. Then data were recorded at a chamber vacuum of the order of 9×10^{-11} mbar and the sample temperature was kept 15 K during the experiment.

Electrical transport were done in a PPMS (Quantum Design PPMS-9T) using a standard four-probe method, with the electrical current applied along the plane of sample (*ab*-plane). A magnetic field was applied at different polar angles with the axis perpendicular to the *ab*-plane for magneto-transport measurements up to 9 T. Four copper (Cu) leads were connected to the sample by vacuum compatible silver epoxy (Epo-Tek H2OE). The sample temperature was varied between 2 K and 310 K during the transport measurements.

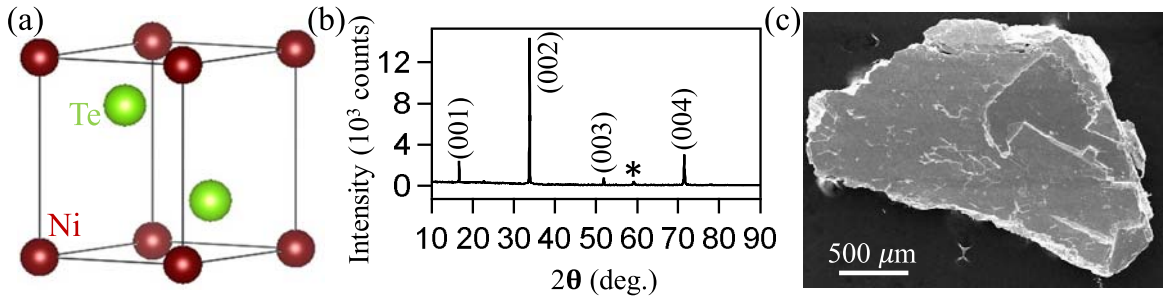

Figure 5.1: (a) Trigonal crystal structure of $NiTe_2$. (b) XRD of $NiTe_2$ single crystal. (c) Scanning electron microscope image of $NiTe_2$ single crystals.

5.3 Results and Discussions

Figure 5.1 (a) shows the trigonal crystal structure of $NiTe_2$. Figure 5.1 (b) shows XRD peaks. The strong diffraction peak can be indexed as $(00l)$. The $NiTe_2$ single crystals crystallize in the $1T$ phase with space group $P3\bar{m}1$ (164). From EDX measurements, we derived the chemical formula $Ni_{0.99}Te_{2.0}$ suggesting that there is a 1% deficiency of Ni (excess of Te) from the stoichiometric composition. Such an excess of Te or deficiency of Ni in these systems generally leads to excess hole carrier density. From the SEM as shown in Fig. 5.1 (c) and EDX we noticed that the sample is homogeneous.

Temperature dependent resistivity data is shown in Fig. 5.2(a), measured within the temperature range of 2 to 310 K. The resistivity data is fitted with the BG formula 5.1.

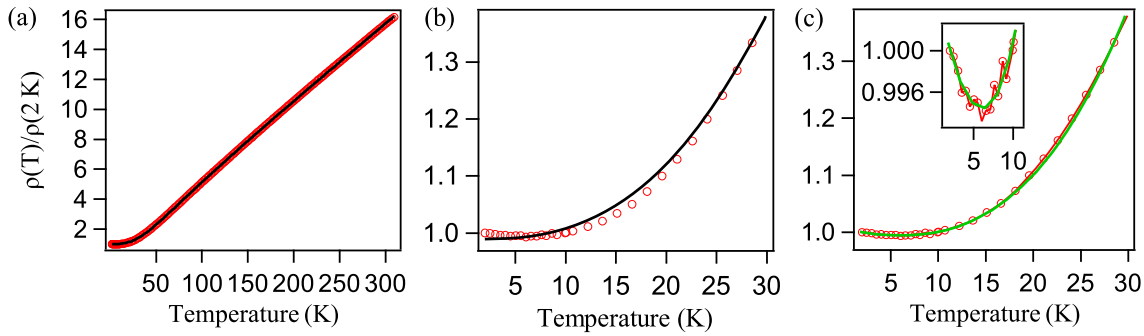

Figure 5.2: (a) Temperature dependent zero-field in-plane electrical resistivity normalized to the residual resistivity of $NiTe_2$. Black curve is the fitting result of Eq. 5.1. (b) Zoomed-in image of (a) below 30 K. (c) Temperature dependent zero-field in-plane electrical resistivity normalized to the residual resistivity plotted below 30 K. Green curve is the fitting result of Eq. 5.2. Inset shows small resistivity upturn below 10 K.

$$\rho(T) = \rho(0) + \alpha(T/\theta_D)^n \int_0^{\theta_D/T} \frac{x^n dx}{(e^x - 1)(1 - e^{-x})}. \tag{5.1}$$

In the above expression the first term, $\rho(0)$ is temperature independent residual resistivity due to impurity scattering and second term mainly discusses about various electronic interactions. α is a constant, proportional to the interaction strength and θ_D is the Debye temperature. Here, n =2 suggests the electron-electron interaction, n=3 suggests the electron-magnon or s-d interband electron scattering, and n =5 suggests the electron-phonon interaction [38]. From the fitting, we obtained the value of $n = 2.8 \pm 0.1$, which is close to n =3. Generally, T^3 dependence of resistivity (n=3) due to the electron-magnon scattering is observed in antiferromagnets [39]. Since $NiTe_2$ is a paramagnetic semimetal [40], electron-magnon scattering may not be the origin of T^3 dependence of resistivity. Therefore, the resistivity of $NiTe_2$ is dominated by s-d electron-phonon scattering [41–43]. Many other TMDCs like $2H$-NbS_2, $2H$-$NbSe_2$, T_d-WTe_2 also show a T^3 dependence of the resistivity at low temperature [44, 45]. From the fitting we obtained the value of $\theta_D = 230 \pm 2$ K which is in excellent agreement with the value of $\theta_D = 230$ K obtained from the heat capacity measurements on this system [27]. The linear temperature dependence of resistivity at high temperatures suggests that electron–phonon (e–ph) scattering is the dominant scattering mechanism at high temperatures. As can be noticed from Fig. 5.2(b), below 25 K, the fitting is not perfect. A small resistivity upturn at low temperature is shown in the inset of Fig. 5.2(c). This low temperature upturn may arise due to (i) the Kondo effect [46], (ii) WL [47], and (iii) EEI [36]. The resistivity upturn decreases with increasing applied magnetic field in the case of a Kondo effect or a WL. Isothermal MR curves of $NiTe_2$

single crystal at 2K and 10K are overlapping each other perfectly within 0 to 9T (MR at 10K is not shown). This indicates that the resistivity upturn remains the same for an applied magnetic field in the range from 0T to 9T. Also, we fitted this region with Kondo equation [46] and WL using Eq. 5.2 with p = 2, 3, 3/2 [47].

$$R = a + bT^3 - cT^{p/2}. \tag{5.2}$$

Apparently, these fittings are not compatible with our experimental data. Thus, ruling out WL and Kondo effect as the origin of the low temperature resistivity upturn. The electron-electron interaction is field-independent [46, 48]. The low temperature region is best fitted with Eq. 5.2 with p=1 as shown by the green curve in Fig. 5.2(c). A $T^{1/2}$ behavior of resistivity is expected to arise from electron-electron interaction in disordered systems [36, 37].

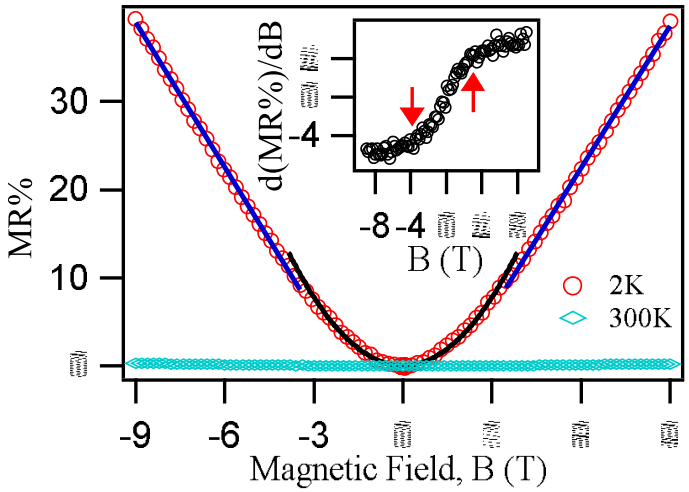

Figure 5.3: Transverse MR at 2 K and 300 K. Black solid line is parabolic fit and blue solid lines are linear fit. The inset shows the first derivative of the MR at 2 K.

Next, from the data shown in Fig. 5.3, we observe that the MR significantly changes with B at low temperatures. However, at room temperature the MR is negligible and almost constant with B, consistent with earlier reports [27, 31]. We further observe that the MR changes from quadratic to linear at an applied magnetic field of 3.5 T. This could be due to the topological properties of the system [27, 28, 30–32, 49]. In general, normal metals show quadratic MR dependence on B and get saturated at higher fields [46]. In case of some topological semimetals, the MR shows an unusual linear dependency without saturation at higher fields due to quantum effects [41, 50]. Here the MR can be written as $MR = \frac{\alpha B^2}{\beta + B^2} + \gamma |B|$ [27, 33]. The inset of Fig. 5.3 clearly shows a change in slope ($\frac{dMR\%}{dB}$) at ≈3.5 T (indicated by the red arrows). This kind of MR crossover from a quadratic to a linear dependence on B is also observed in other systems such as the topological insulator Bi_2Se_3, or the semimetal antimony

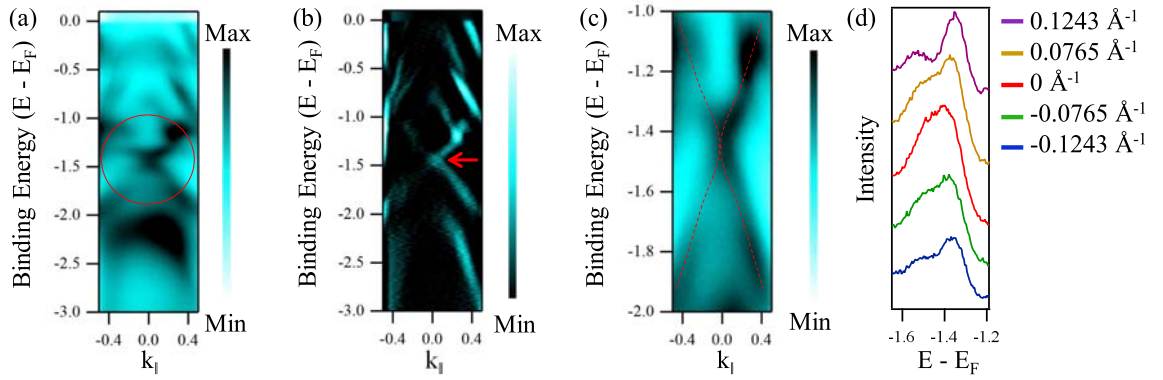

Figure 5.4: (a) EDM of $NiTe_2$ single crystal measured using photon energy of 21.2 eV at a sample temperature 8.9 K. (b) Second derivative of (a). (c) Zoomed-in image of the region marked by red dotted circle in (a). (d) EDCs of (a) taken at different momentum values.

crystal [48, 51]. Therefore, the MR crossover from classical quadratic dependence on B at lower fields to non-saturating linear dependence on B at higher fields is mainly due to the linear band dispersions near the Fermi level [27, 28, 30, 49].

In order to understand the electronic structure of $NiTe_2$ we measured an EDM. Figure 5.4(a) shows the EDM which reveals that it is metallic as the bands are crossing the Fermi level. An interesting feature indicating a conical band dispersion is observed at a binding energy near about 1.45 eV as shown by the red dotted circle. Our EDM supports the calculated surface spectrum using Wannier functions along $K - \Gamma - K$ direction as reported earlier [27]. In this work a type-II bulk Dirac point at 0.08 eV was predicted above the Fermi level along the Γ to A direction and a conical surface band dispersion at a binding energy of 1.6 eV, using a first principle calculation. Observing the type-II Dirac point above the Fermi level using ARPES is not possible. In Fig. 5.4(b) we performed a second derivative of the EDM. This figure clearly reveals the existence of Dirac point marked by red arrow. This figure exactly measures the position of Dirac cone at a binding energy of 1.45 eV which is 0.15 eV lower than the calculated value previously reported. This crystal has 1% excess Te, it is self-doped with hole carriers. Excess hole lowers the position of the Fermi level. This could be a possible reason for this slight deviation of the experimental value from the theoretical value. Figure 5.4(c) is a zoomed-in image of the region encircled by the red circle in Fig. 5.4(a) for better visualization of the Dirac states. Figure 5.4(d) is the plot of EDCs taken from Fig. 5.4(a) near the band crossing point for momentum values 0.1243, 0.0765, 0, -0.1243, and -0.0765 $\AA^{-1}$ within an energy range of -1.65 eV to -1.19 eV. From the EDCs we can see only one peak at a binding energy near about 1.45 eV for momentum value 0 $\AA^{-1}$. The observation of Dirac point is further confirmed from the EDCs shown in Fig. 5.4(d).

5.4 Conclusions

In conclusion, we have grown single crystals of $NiTe_2$ and performed electrical transport and magnetotransport studies on these single crystals. The BG fitting to the resistivity data suggests of a dominant s-d electron-phonon scattering in these systems [38]. Further, we estimated a Debye temperature of 230 K. Also, from the magnetotransport studies, we observe a crossover from quadratic to linear dependence on the applied magnetic field as we increase the field. Also, we have done ARPES measurements to understand the electronic structure. A similar electronic structure was observed in its sister compounds including $PdTe_2$, $PtTe_2$ and $PtSe_2$. All of them show a pair of Dirac points. For $PdTe_2$, a type-II Dirac point is observed below the Fermi level at a binding energy of 0.5 eV and another Dirac point at a binding energy of 1.7 eV. For $NiTe_2$ our measured value is more close to the Fermi level when compared with $PdTe_2$. The origin of surface states in these samples is due to the nontrivial $\mathbb{Z}2$ topology, induced by band inversion. Later, the position of Dirac cone at 1.45 eV is confirmed by other ARPES studies as well [28, 30].

Bibliography

[1] Y. Ma, L. Kou, X. Li, Y. Dai, and T. Heine, "Two-dimensional transition metal dichalcogenides with a hexagonal lattice: Room-temperature quantum spin Hall insulators," *Physical Review B*, vol. 93, jan 2016.

[2] F. Wu, T. Lovorn, E. Tutuc, I. Martin, and A. MacDonald, "Topological Insulators in Twisted Transition Metal Dichalcogenide Homobilayers," *Physical Review Letters*, vol. 122, feb 2019.

[3] J. Jiang, Z. K. Liu, Y. Sun, H. F. Yang, C. R. Rajamathi, Y. P. Qi, L. X. Yang, C. Chen, H. Peng, C. C. Hwang, S. Z. Sun, S. K. Mo, I. Vobornik, J. Fujii, S. S. P. Parkin, C. Felser, B. H. Yan, and Y. L. Chen, "Signature of type-II Weyl semimetal phase in $MoTe_2$," *Nature Communications*, vol. 8, jan 2017.

[4] P. Li, Y. Wen, X. He, Q. Zhang, C. Xia, Z.-M. Yu, S. A. Yang, Z. Zhu, H. N. Alshareef, and X.-X. Zhang, "Evidence for topological type-II Weyl semimetal WTe_2," *Nature Communications*, vol. 8, dec 2017.

[5] L. F. Mattheiss, "Band Structures of Transition-Metal-Dichalcogenide Layer Compounds," *Physical Review B*, vol. 8, pp. 3719–3740, oct 1973.

[6] Q. H. Wang, K. Kalantar-Zadeh, A. Kis, J. N. Coleman, and M. S. Strano, "Electronics and optoelectronics of two-dimensional transition metal dichalcogenides," *Nature Nanotechnology*, vol. 7, pp. 699–712, nov 2012.

[7] M. S. Fuhrer and J. Hone, "Measurement of mobility in dual-gated MoS_2 transistors," *Nature Nanotechnology*, vol. 8, pp. 146–147, mar 2013.

[8] A. T. Neal, Y. Du, H. Liu, and P. D. Ye, "Two-Dimensional $TaSe_2$ Metallic Crystals: Spin–Orbit Scattering Length and Breakdown Current Density," *ACS Nano*, vol. 8, pp. 9137–9142, sep 2014.

[9] S. Thirupathaiah, R. Jha, B. Pal, J. S. Matias, P. K. Das, P. K. Sivakumar, I. Vobornik, N. C. Plumb, M. Shi, R. A. Ribeiro, and D. D. Sarma, "$MoTe_2$: An uncompensated semimetal with extremely large magnetoresistance," *Physical Review B*, vol. 95, jun 2017.

[10] H. M. Hill, A. F. Rigosi, K. T. Rim, G. W. Flynn, and T. F. Heinz, "Band Alignment in MoS_2/WS_2 Transition Metal Dichalcogenide Heterostructures Probed by Scanning Tunneling Microscopy and Spectroscopy," *Nano Letters*, vol. 16, pp. 4831–4837, jul 2016.

[11] L. Perfetti, P. A. Loukakos, M. Lisowski, U. Bovensiepen, H. Berger, S. Biermann, P. S. Cornaglia, A. Georges, and M. Wolf, "Time Evolution of the Electronic Structure of 1T-TaS_2 through the Insulator-Metal Transition," *Physical Review Letters*, vol. 97, aug 2006.

[12] W. Choi, N. Choudhary, G. H. Han, J. Park, D. Akinwande, and Y. H. Lee, "Recent development of two-dimensional transition metal dichalcogenides and their applications," *Materials Today*, vol. 20, pp. 116–130, apr 2017.

[13] M. Porer, U. Leierseder, J.-M. Ménard, H. Dachraoui, L. Mouchliadis, I. E. Perakis, U. Heinzmann, J. Demsar, K. Rossnagel, and R. Huber, "Non-thermal separation of electronic and structural orders in a persisting charge density wave," *Nature Materials*, vol. 13, pp. 857–861, jul 2014.

[14] Y. Ma, Y. Dai, M. Guo, C. Niu, Y. Zhu, and B. Huang, "Evidence of the Existence of Magnetism in Pristine VX_2 Monolayers (X = S, Se) and Their Strain-Induced Tunable Magnetic Properties," *ACS Nano*, vol. 6, pp. 1695–1701, jan 2012.

[15] Y. I. Joe, X. M. Chen, P. Ghaemi, K. D. Finkelstein, G. A. de la Peña, Y. Gan, J. C. T. Lee, S. Yuan, J. Geck, G. J. MacDougall, T. C. Chiang, S. L. Cooper, E. Fradkin, and P. Abbamonte, "Emergence of charge density wave domain walls above the superconducting dome in 1T-$TiSe_2$," *Nature Physics*, vol. 10, pp. 421–425, apr 2014.

[16] M. Chhowalla, H. S. Shin, G. Eda, L.-J. Li, K. P. Loh, and H. Zhang, "The chemistry of two-dimensional layered transition metal dichalcogenide nanosheets," *Nature Chemistry*, vol. 5, pp. 263–275, mar 2013.

[17] M. K. Hooda, C. S. Yadav, and D. Samal, "Electronic and topological properties of group-10 transition metal dichalcogenides," *Journal of Physics: Condensed Matter*, vol. 33, p. 103001, dec 2020.

[18] A. Politano, G. Chiarello, B. Ghosh, K. Sadhukhan, C.-N. Kuo, C. S. Lue, V. Pellegrini, and A. Agarwal, "3D Dirac Plasmons in the Type-II Dirac Semimetal $PtTe_2$," *Physical Review Letters*, vol. 121, aug 2018.

[19] H. Huang, S. Zhou, and W. Duan, "Type-II Dirac fermions in the $PtSe_2$ class of transition metal dichalcogenides," *Physical Review B*, vol. 94, sep 2016.

[20] K. Zhang, M. Yan, H. Zhang, H. Huang, M. Arita, Z. Sun, W. Duan, Y. Wu, and S. Zhou, "Experimental evidence for type-II Dirac semimetal in $PtSe_2$," *Physical Review B*, vol. 96, sep 2017.

[21] K. Kim, S. Kim, J. S. Kim, H. Kim, J.-H. Park, and B. I. Min, "Importance of the van Hove singularity in superconducting $PdTe_2$," *Physical Review B*, vol. 97, apr 2018.

[22] R. C. Xiao, P. L. Gong, Q. S. Wu, W. J. Lu, M. J. Wei, J. Y. Li, H. Y. Lv, X. Luo, P. Tong, X. B. Zhu, and Y. P. Sun, "Manipulation of type-I and type-II Dirac points in $PdTe_2$ superconductor by external pressure," *Physical Review B*, vol. 96, aug 2017.

[23] H.-J. Noh, J. Jeong, E.-J. Cho, K. Kim, B. Min, and B.-G. Park, "Experimental Realization of Type-II Dirac Fermions in a $PdTe_2$ Superconductor," *Physical Review Letters*, vol. 119, jul 2017.

[24] F. Fei, X. Bo, R. Wang, B. Wu, J. Jiang, D. Fu, M. Gao, H. Zheng, Y. Chen, X. Wang, H. Bu, F. Song, X. Wan, B. Wang, and G. Wang, "Nontrivial Berry phase and type-II Dirac transport in the layered material $PdTe_2$," *Physical Review B*, vol. 96, jul 2017.

[25] O. Clark, M. Neat, K. Okawa, L. Bawden, I. Marković, F. Mazzola, J. Feng, V. Sunko, J. Riley, W. Meevasana, J. Fujii, I. Vobornik, T. Kim, M. Hoesch, T. Sasagawa, P. Wahl, M. Bahramy, and P. King, "Fermiology and Superconductivity of Topological Surface States in $PdTe_2$," *Physical Review Letters*, vol. 120, apr 2018.

[26] W. Zheng, R. Schönemann, N. Aryal, Q. Zhou, D. Rhodes, Y.-C. Chiu, K.-W. Chen, E. Kampert, T. Förster, T. J. Martin, G. T. McCandless, J. Y. Chan, E. Manousakis, and L. Balicas, "Detailed study of the Fermi surfaces of the type-II Dirac semimetallic candidates XTe_2 (X =Pd, Pt)," *Physical Review B*, vol. 97, jun 2018.

[27] C. Xu, B. Li, W. Jiao, W. Zhou, B. Qian, R. Sankar, N. D. Zhigadlo, Y. Qi, D. Qian, F.-C. Chou, and X. Xu, "Topological Type-II Dirac Fermions Approaching the Fermi Level in a Transition Metal Dichalcogenide $NiTe_2$," *Chemistry of Materials*, vol. 30, pp. 4823–4830, jun 2018.

[28] M. Nurmamat, S. V. Eremeev, X. Wang, T. Yoshikawa, T. Kono, M. Kakoki, T. Muro, Q. Jiang, Z. Sun, M. Ye, and A. Kimura, "Bulk Dirac cone and highly anisotropic electronic structure of $NiTe_2$," *Physical Review B*, vol. 104, oct 2021.

[29] I. Kar, L. Harnagea, S. Banik, SurjeetSingh, and S. Thirupathaiah, "Observation of surface Dirac state in transition metal dichalcogenide $NiTe_2$ using ARPES," in *DAE SOLID STATE PHYSICS SYMPOSIUM 2019*, AIP Publishing, 2020.

[30] B. Ghosh, D. Mondal, C.-N. Kuo, C. S. Lue, J. Nayak, J. Fujii, I. Vobornik, A. Politano, and A. Agarwal, "Observation of bulk states and spin-polarized topological surface states in transition metal dichalcogenide Dirac semimetal candidate $NiTe_2$," *Physical Review B*, vol. 100, nov 2019.

[31] Q. Liu, F. Fei, B. Chen, X. Bo, B. Wei, S. Zhang, M. Zhang, F. Xie, M. Naveed, X. Wan, F. Song, and B. Wang, "Nontopological origin of the planar Hall effect in the type-II Dirac semimetal $NiTe_2$," *Physical Review B*, vol. 99, apr 2019.

[32] P. J. Orders, J. Liesegang, R. C. G. Leckey, J. G. Jenkin, and J. D. Riley, "Angle-resolved photoemission from the valence bands of $NiTe_2$, $PdTe_2$ and $PtTe_2$," *Journal of Physics F: Metal Physics*, vol. 12, pp. 2737–2753, nov 1982.

[33] M. N. Ali, J. Xiong, S. Flynn, J. Tao, Q. D. Gibson, L. M. Schoop, T. Liang, N. Haldolaarachchige, M. Hirschberger, N. P. Ong, and R. J. Cava, "Large, non-saturating magnetoresistance in WTe_2," *Nature*, vol. 514, pp. 205–208, sep 2014.

[34] N. Kumar, Y. Sun, N. Xu, K. Manna, M. Yao, V. Süss, I. Leermakers, O. Young, T. Förster, M. Schmidt, H. Borrmann, B. Yan, U. Zeitler, M. Shi, C. Felser, and C. Shekhar, "Extremely high magnetoresistance and conductivity in the type-II Weyl semimetals WP_2 and MoP_2," *Nature Communications*, vol. 8, nov 2017.

[35] K. Wang and C. Petrovic, "Large linear magnetoresistance and magnetothermopower in layered $SrZnSb_2$," *Applied Physics Letters*, vol. 101, p. 152102, oct 2012.

[36] J. Joseph, C. Bansal, K. J. Reddy, and A. Rajanikanth, "Electron–electron interaction dominated resistivity minimum in quasi-continuous Ag nanocluster films," *AIP Advances*, vol. 10, p. 125223, dec 2020.

[37] B. L. Al'Tshuler and A. G. Aronov, "Contribution to the theory of disordered metals in strongly doped semiconductors," *Zh. Eksp. Teor. Fiz*, vol. 77, pp. 2028–2044, 1979.

[38] D. B. Poker and C. E. Klabunde, "Temperature dependence of electrical resistivity of vanadium, platinum, and copper," *Physical Review B*, vol. 26, pp. 7012–7014, dec 1982.

[39] A. Ishikawa, "Electrical Resesrivity Due to Antiferromagnetic Spin Waves in Cr," *Journal of the Physical Society of Japan*, vol. 51, pp. 441–451, feb 1982.

[40] Q. Mao, Y. Zhang, Q. Chen, R. Li, X. Geng, J. Yang, H. Hao, and M. Fang, "Metallicity and Paramagnetism of Single-Crystalline NiTe and $NiTe_2$," *physica status solidi (b)*, vol. 257, p. 1900224, aug 2019.

[41] R. Singha, A. K. Pariari, B. Satpati, and P. Mandal, "Large nonsaturating magnetoresistance and signature of nondegenerate Dirac nodes in ZrSiS," *Proceedings of the National Academy of Sciences*, vol. 114, pp. 2468–2473, feb 2017.

[42] S. Sun, Q. Wang, P.-J. Guo, K. Liu, and H. Lei, "Large magnetoresistance in LaBi: origin of field-induced resistivity upturn and plateau in compensated semimetals," *New Journal of Physics*, vol. 18, p. 082002, aug 2016.

[43] F. F. Tafti, Q. D. Gibson, S. K. Kushwaha, N. Haldolaarachchige, and R. J. Cava, "Resistivity plateau and extreme magnetoresistance in LaSb," *Nature Physics*, vol. 12, pp. 272–277, dec 2015.

[44] M. Naito and S. Tanaka, "Electrical Transport Properties in 2H-NbS_2, -$NbSe_2$, -TaS_2 and -$TaSe_2$," *Journal of the Physical Society of Japan*, vol. 51, pp. 219–227, jan 1982.

[45] R. Jha, S. Onishi, R. Higashinaka, T. D. Matsuda, R. A. Ribeiro, and Y. Aoki, "Anisotropy in the electronic transport properties of Weyl semimetal WTe_2 single crystals," *AIP Advances*, vol. 8, p. 101332, oct 2018.

[46] S. Barua, M. C. Hatnean, M. R. Lees, and G. Balakrishnan, "Signatures of the Kondo effect in VSe_2," *Scientific Reports*, vol. 7, sep 2017.

[47] L. Maritato, C. Adamo, C. Barone, G. M. D. Luca, A. Galdi, P. Orgiani, and A. Y. Petrov, "Low-temperature resistivity of $La_{0.7}Sr_{0.3}MnO_3$ ultra thin films: Role of quantum interference effects," *Physical Review B*, vol. 73, mar 2006.

[48] Y. Kumar, R. Sultana, P. Sharma, and V. P. S. Awana, "Modeling of magneto-conductivity of bismuth selenide: a topological insulator," *SN Applied Sciences*, vol. 3, mar 2021.

[49] I. Kar, J. Chatterjee, L. Harnagea, Y. Kushnirenko, A. V. Fedorov, D. Shrivastava, B. Büchner, P. Mahadevan, and S. Thirupathaiah, "Metal-chalcogen bond-length induced electronic phase transition from semiconductor to topological semimetal in ZrX_2 (X=Se and Te)," *Physical Review B*, vol. 101, apr 2020.

[50] S. Roychowdhury, S. Ghara, S. N. Guin, A. Sundaresan, and K. Biswas, "Large linear magnetoresistance in topological crystalline insulator $Pb_{0.6}Sn_{0.4}Te$," *Journal of Solid State Chemistry*, vol. 233, pp. 199–204, jan 2016.

[51] M. K. Dasoundhi, I. Rajput, D. Kumar, and A. Lakhani, "Extremely large linear magnetoresistance in antimony crystal," *Journal of Physics D: Applied Physics*, vol. 54, p. 195303, feb 2021.

Chapter 6

Electrical-transport, Magnetotransport, and Magnetic Properties Studies of VX_2 (X = Se & Te) Single Crystals

6.1 Introduction

For more than six decades, the TMDCs are widely discussed in the verge of the ground state properties like CDW and superconductivity [1–9]. Among them, from the group V TMDCs, the ditelluride-based compounds are isostructural to each other having the monoclinic crystal structure with $1T'$ phase below 300 K [10–15], while the diselenide- and the disulfur-based compounds are available in the trigonal crystal structure with $1T$ or $2H$ phase [16–21]. Despite being isostructural, these compounds show differing electronic and magnetic properties. For instance, VTe_2 shows a normal to C-CDW transition at 474 K [13, 22, 23], while $NbTe_2$ shows an IC-CDW transition at 550 K and IC-CDW to C-CDW transition at room temperature [11, 24], in addition to a superconducting transition (T_c) at ≈ 0.5 K [25, 26]. On the other hand, $TaTe_2$ shows a normal to IC-CDW transition at 170 K [27–29]. Similarly, VSe_2 shows an IC-CDW transition at around 110 K and an IC-CDW to C-CDW at 70 K [30–33]. $NbSe_2$ shows an IC-CDW transition at 33 K and superconductivity at 7.2 K [34]. $TaSe_2$ shows an IC-CDW transition at 600 K and a C-CDW transition at 473 K in the 1T phase [35], while an IC-CDW transition at 122 K and a C-CDW transition at 90 K is found in the 2H phase [16, 36]. VS_2 is reported to show a CDW transition below 304 K [21, 37, 38].

Though NbS_2 is not found to show a clear CDW order, recently it was suggested to be at the verge of a CDW order following the diverse electronic properties in NbS_2 [20, 39]. On the other hand, TaS_2 shows an IC-CDW phase below 550 K and a NC-

Most of this chapter is communicated for publication.

CDW phase below 350 K and a C-CDW phase was found below 180 K in the 1T phase [40], while a short range CDW transition is found below 75 K in the 2H phase [41]. Magnetotransport studies on $TaTe_2$ and $NbTe_2$ suggest a linear dependence of the MR [11, 27], while a quadratic MR is found for VTe_2 [42]. In contrast to $TaTe_2$ and $NbTe_2$, VTe_2 shows a weak ferromagnetic ordering at low temperature. As a result, VTe_2 is found to show a resistivity upturn due to the Kondo effect [33, 42–44]. However, the resistivity upturn found in VSe_2 is still under debate. Some reports interpreted the resistivity upturn to the Kondo effect in the paramagnetic regime [43], while the other reports interpreted it to a WL [42]. $TaSe_2$ in $2H$ phase is reported to show antiferromagnetic ordering [45]. TaS_2 in the 1T phase shows ferromagnetic ordering due to localized spins [46]. As a matter of fact, Kondo effect was not observed in $TaTe_2$ and $NbTe_2$ systems.

In this contribution, we report a comprehensive comparison study between VSe_2 and its isovalent compound VTe_2 on their electrical transport, magnetotransport, and magnetic properties. We observe a low temperature resistivity upturn in both systems due to the Kondo effect induced by the exchange interaction between localized moments and conduction electrons at low temperature. The electrical transport data of VSe_2 measured under various applied magnetic fields can be explained well with the modified Hamann equation following the Brillouin function in the quantum limit [47]. From a similar transport study on VTe_2 we find that the data can be fitted well with modified Hamann equation following the Langevin function in the classical limit [42]. Foremost these observations confirm the presence of Kondo effect in both systems, specifically for VSe_2 in which the mechanism of resistivity upturn is elusive [33, 42, 43]. Further, we find a negative MR for both systems in the Kondo state, while the MR behaves differently in the normal state.

6.2 Experimental Details

Single crystal of VTe_2 was grown by the CVT technique using iodine (crystalline, 99.99%, metals basis, Alfa Aesar) (2 mg/cm^3) as a transport agent[48]. In the first step, stoichiometric amounts of V (powder, 99.5%, metals basis, Alfa Aesar) and Te (powder, 99.99%, metals basis, Alfa Aesar) were mixed thoroughly and sealed in a quartz ampoule under vacuum. The ampoule was then slowly heated to 1000°C at a rate of 2.5°C/min and kept there for 8 h before quenching into the normal water. The powder was regrinded, sealed into a quartz ampoule under vacuum together with pieces of crystallized iodine (crystalline, 99.99%, metals basis, Alfa Aesar) (2 mg/cm^3). The ampoule was loaded into a three-zone tube furnace where the temperatures were set at 900°C at the hot-zone and 810°C was set at the cold-zone. After 5 days of

reaction, we obtained shiny single crystals with a typical dimension of 5 mm×5 mm at the cold-zone. Similarly, single crystals of VSe_2 were grown by the above method my mixing the stoichiometric amounts of V (powder, 99.5%, metals basis, Alfa Aesar) and Se (shot, 99.999%, metals basis, Alfa Aesar), except that 1000°C was set at the hot-zone and 950°C was set at the cold-zone. After 5 days of reaction, we obtained shiny single crystals of typical dimension 15 mm×6 mm at the cold-zone.

The chemical composition of the single crystals were determined by an EDX equipped with a scanning electron microscope (Quanta 250 FEG) and the phase purity was checked by XRD patterns measured using Cu-k_α-radiation (Rigaku MiniFlex II and Rigaku SmartLab 9KW). DSC (Q2000 of TA Instruments) was performed to measure the heat flow curve of the sample in both heating and cooling modes.

Electrical transport measurements were done in a PPMS (Quantum Design PPMS-9T) using a standard four-probe method, with the electrical current applied along the plane of sample (*ab*-plane). For magnetotransport measurements the magnetic field was applied at different polar angles with respect to the *ab*-plane. Copper (Cu) leads were connected to the sample by vacuum compatible silver epoxy Epo-Tek H2OE. The sample temperature was varied between 2 K and 330 K during the transport measurements. DC magnetization measurements were performed using the MPMS (Quantum Design MPMS-7T) equipped with a vibrating sample magnetometer superconducting quantum interference device (VSM-SQUID). The temperature dependence of the magnetization in ZFC and FC modes has been carried out under different applied magnetic fields up to 7 T in the temperature range of 5-300 K. Field dependent magnetization $[M(H)]$ has also been carried out at different temperatures.

6.3 Results and Discussion

Single crystals of VTe_2 and VSe_2 were structurally analyzed using the powder XRD at room temperature. High intense diffraction peaks corresponding to the (001) plane of VTe_2 are shown in Fig. 6.1(a). For the (001) plane of VSe_2, similar data are shown in Fig. 6.1(b). VTe_2 crystallizes into the monoclinic structure with the space group $C2/m$ (12) in the $1T'$ phase at room temperature, while VSe_2 crystalizes into the trigonal structure with space group of $P\bar{3}m1$ (164) in the $1T$ phase [13, 49]. From EDX measurements as shown in Figs. 6.1(c) and 6.1(d) we identify that the studied samples have actual compositions of $V_{1.08}Te_2$ and $V_{0.86}Se_2$, respectively. Thus, we obtained 8% vanadium excess VTe_2 and 14% vanadium deficient VSe_2 single crystals. Herein, for the convenience, we represent these crystals by their nominal compositions of VSe_2 and VTe_2.

Fig. 6.2(a) shows temperature dependent in-plane electrical resistance of VTe_2. The

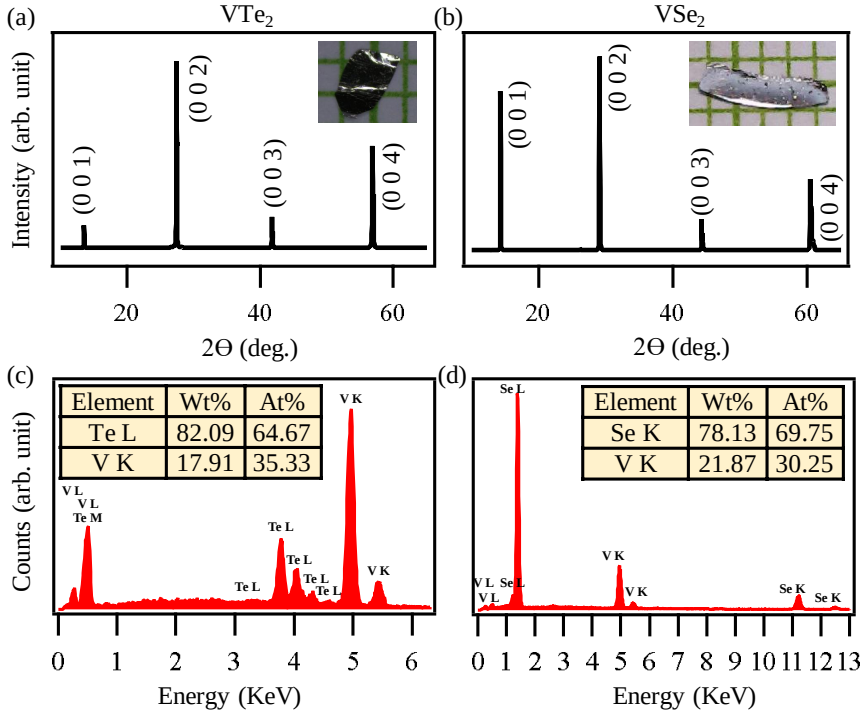

Figure 6.1: (a) and (b) Powder X-ray diffraction (XRD) pattern of VTe_2 and VSe_2 single crystals. Insets in (a) and (b) are the optical images of the single crystals. (c) and (d) Energy dispersive X-ray spectroscopy (EDX) data of VTe_2 and VSe_2 single crystals, respectively.

resistance curve shows a metallic nature, in principle, except that an upturn is noticed at low temperature with a resistance minima at T_m=17 K as can be seen from the inset of Fig. 6.2(a). To explore further on the resistance upturn mechanism, it was measured at various magnetic fields within the temperature range of 2-40 K as plotted in Fig. 6.2(b). We observe a decrease in resistance upturn with increasing magnetic field of up to 9 T. Further, the field dependent resistance curves are perfectly fitted with the Eq. 6.1 and Eq. 6.2 without and with applied magnetic field, respectively.

$$R(T) = R_0 + qT^2 + R_{KO}[1 - \frac{\ln(\frac{T_{eff}}{T_K})}{\sqrt{\ln^2(\frac{T_{eff}}{T_K}) + S(S+1)\pi^2}}] \tag{6.1}$$

$$R(T) = R_0 + qT^2 + R_{KO}[1 - \frac{\ln(\frac{T_{eff}}{T_K})}{\sqrt{\ln^2(\frac{T_{eff}}{T_K}) + S(S+1)\pi^2}}][1 - L^2(\frac{\mu B}{k_B T_e ff})] \tag{6.2}$$

In Eq. 6.1, the first term (R_0) is residual resistance, the second term (qT^2) represents

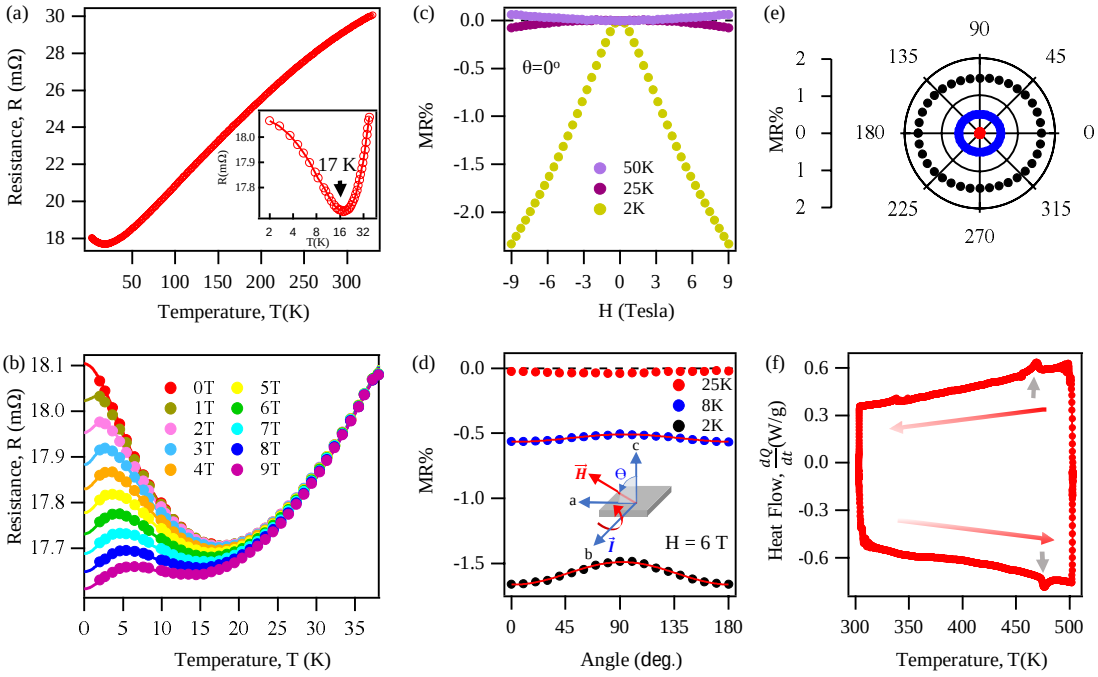

Figure 6.2: (a) In-plane electrical resistance of VTe_2 plotted as a function of temperature. Inset in (a) shows low-temperature resistance upturn at a temperature minima T_m=17 K. (b) Temperature dependent electrical resistance plotted for various magnetic fields applied parallel to c-axis. Solid lines in (b) are fittings to Eq. 6.1 and Eq. 6.2. (c) Magnetoresistance, MR (%), plotted as a function of field applied parallel to the c-axis ($\theta = 0°$). (d) MR (%) plotted as function of applied field angle. Measuring geometry is shown in the inset of (d). (e) Symmetrized MR (%) of (d) is plotted in the polar graph. (f) Differential scanning calorimetry (DSC) data is plotted as function of temperature for both cooling and heating cycle. In (f), the charge density wave ordering temperature (T_{CDW}) is marked from both heating and cooling cycles.

the electron-electron interaction, and the third term is the Hamann expression [50] due to $s-d$ exchange interaction [42, 51]. Hamann expression is an empirical equation used to calculate the exchange interaction between localized magnetic moments and conduction electrons. In the third term, R_{KO} is the temperature-independent Kondo resistance, T_K is the Kondo temperature, and S is the total spin of the magnetic impurities. $T_{eff} = \sqrt{T^2 + {T_W}^2}$, where $k_B T_W$ is the effective Ruderman-Kittel-Kasuya-Yosida (RKKY) interaction strength. From the fitting, we obtained a Kondo temperature T_K=12 K and S=0.5. These values are in good agreement with previous report on VTe_2 single crystal [42]. In Eq. 6.2, the Hamann term is multiplied by $[1 - L^2(\frac{\mu B}{k_B T_e f f})]$ where $L(x)$ is Langevin function $L(x) = \coth(x) - 1/x$ (see Table 6.1 for the fitting parameters). Primarily, Hamann equation involves Brillouin function [47] to describe the quantum mechanical behavior of magnetic moments and provides a more accurate description of their statistical distribution. In quantum theory, the magnetic moments are quantized and the orientations of magnetic moment with respect to applied mag-

netic field are specified by some possible components of magnetic moment along field direction [52]. On the other hand, the Langevin function [42] is a simplified model derived from classical statistical mechanics. In Langevin's classical theory, it is assumed that the mutual interaction between the magnetic dipoles is negligible and magnetic moments can possess any orientation with respect to applied magnetic field [52].

B(T)	R_0 ($m\Omega$)	q ($\mu\Omega/K^2$)	R_{KO} ($m\Omega$)	T_W (K)	μ (μ_B)
0	16.6140(4)	0.5719(4)	1.0782(4)	3.900(3)	
1	16.6530(4)	0.5645(4)	1.0316(4)	2.423(3)	4.042(3)
2	16.6563(4)	0.5641(4)	1.0295(4)	2.665(3)	2.569(3)
3	16.6786(4)	0.5596(4)	1.0028(4)	2.823(3)	2.045(3)
4	16.7015(4)	0.5561(4)	0.9740(4)	3.147(3)	1.789(3)
5	16.7343(4)	0.5508(4)	0.9331(4)	3.396(3)	1.631(3)
6	16.7778(4)	0.5435(4)	0.8780(4)	3.632(3)	1.510(3)
7	16.8104(4)	0.5398(4)	0.8334(4)	3.916(3)	1.445(3)
8	16.8592(4)	0.5320(4)	0.7692(4)	4.135(3)	1.379(3)
9	16.9061(4)	0.5263(4)	0.7054(4)	4.332(3)	1.329(3)

Table 6.1: Kondo fitting parameters of VTe_2

Fig. 6.2(c) depicts MR%, $MR\% = \frac{R(H)-R(0)}{R(0)} \times 100$, plotted as a function of applied field measured at below (2 K) and above (25 K & 50 K) the Kondo temperatures. We notice that at 2 K, below the Kondo temperature, VTe_2 shows a negative MR and above the Kondo temperature, the MR is negligible. This is because the magnetic field reduces fluctuations of localized impurity magnetic moments and spin dependent exchange scattering [53]. Hence, below a critical magnetic field (B_c), the MR is negative and above B_c, the Kondo effect vanishes. In case of VTe_2 the value of B_c is very high [42] which is beyond our experimental scope. Fig. 6.2(d) shows MR (%) plotted as a function of field angle with respect to the sample surface normal (c-axis) at an applied field of 6 T. The measuring geometry is shown in the inset of Fig. 6.2(d). Red solid-lines in Fig. 6.2(d) are fittings to the Eq. 6.3.

$$MR(\theta) = MR_0 + \alpha cos(2\theta) \tag{6.3}$$

In Eq. 6.3, the first tern is a constant and α is an amplitude. Fig. 6.2 (e) shows symmetrized angular dependent MR plotted in the polar graph for the temperatures 2 K, 8 K, and 50 K. As can be seen from Fig. 6.2 (e), MR shows in-plane small anisotropy in the Kondo state (2 K) but becomes completely isotropic in the normal state (8 and 50 K). Ideally, Kondo systems show an isotropic MR but a small anisotropy could be there due to the presence of a crystal anisotropy [53]. DSC measurements are performed

in both heating and cooling modes with a ramp rate of dT/dt=10 K/min as depicted in Fig. 6.2(f). During cooling and heating cycles of DSC measurements we noticed a hump and a dip, respectively, at a sample temperature of 470±5 K that is originated from the CDW [22].

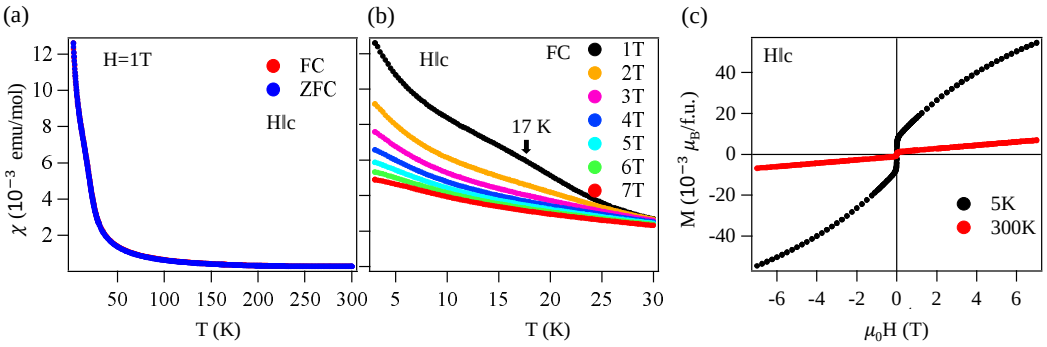

Figure 6.3: (a) Magnetic susceptibility of VTe_2 plotted as a function of temperature with a field of 1 T applied parallel to *c*-axis measured in the FC and ZFC modes. (b) Same as (a) but measured for different magnetic fields in the FC mode. (c) Magnetization isotherms $M(H)$ measured at 5 K and 300 K.

Fig. 6.3 shows magnetic measurements on VTe_2 with field applied parallel to the *c*-axis. Fig. 6.3(a) shows temperature dependent magnetic susceptibility measured with a field of 1 T within the temperature range of 3-300 K in the FC and ZFC modes. Here, it can be seen that ZFC and FC are identical. Further, we measured the temperature dependent magnetic susceptibility by varying the field in the FC mode as shown in Fig. 6.3(b). A broad hump-like structure with a maximum at around 17 K has been noticed in the susceptibility data when measured with a magnetic field of 1 T, which then eventually disappears above 3 T due to the crossover from high temperature localized moments of Kondo impurities to fully compensated moments at low temperature [42, 54]. However, at higher magnetic fields this crossover gets weaker as a result the resistance upturn decreases. Fig. 6.3(c) shows magnetization isotherms, M(H), measured at 5 and 300 K. From the M(H) data we notice a soft ferromagnetic-like ordering at the room temperature which is in agreement with previous reports on VTe_2 [47, 55, 56].

Next, Fig. 6.4(a) shows temperature dependent zero-field in-plane electrical resistance of VSe_2. Overall, the resistance curve suggests a metallic behaviour except a hump at around 100 K and a resistance upturn at low temperature is observed. The hump at 100 K is due to the IC-CDW as noticed in the previous reports from this system [30, 33, 43, 44, 57–61]. The inset in Fig. 6.4(a) shows a resistance minima (T_m) at 6 K. To understand the resistance upturn mechanism, we performed field dependent resistance measurements within the temperature range of 2 K to 12 K by varying the magnetic fields up to 9 T as plotted in Fig. 6.4(b). As can be seen from Fig. 6.4(b), re-

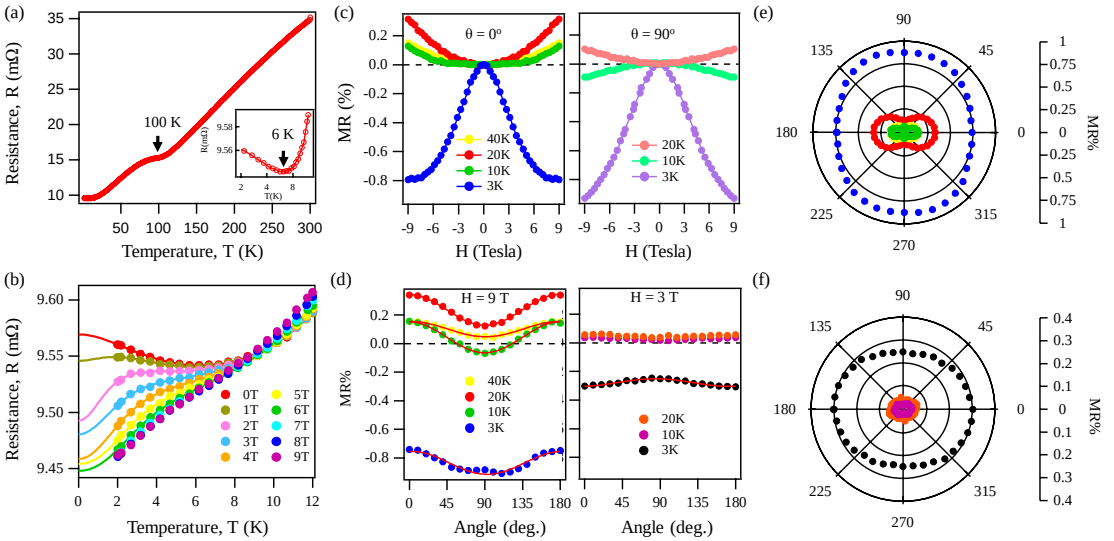

Figure 6.4: (a) In-plane electrical resistance of VSe_2 plotted as a function of temperature. A hump at the CDW transition temperature of 100 K is noticed on the resistance curve. The inset in (a) shows the resistance upturn at a temperature minima T_m=6 K. (b) Temperature dependent electrical resistance plotted for various magnetic fields applied parallel to the *c*-axis. Solid lines in (b) are fittings to Eq. 6.4 and Eq. 6.5. (c) Magnetoresistance, MR (%), plotted as a function of field applied parallel to the *c*-axis ($\theta = 0°$) is in the left panel and for the field applied perpendicular to the *c*-axis ($\theta = 90°$) is shown in the right panel. (d) The MR (%) is plotted as function of the field angle with applied field of 9 T (left panel)and 3 T (right panel). (e) Symmetrized MR (%) of (d) is plotted in the polar graph with an applied of 9 T. (f) Symmetrized MR (%) of (d) is plotted in the polar graph with an applied field of 3 T.

sistance upturn decreases with increasing field and disappears at 7 T, suggesting Kondo effect as the possible origin of the resistance upturn. Solid-lines in Fig. 6.4(b) are the fittings to Eq. 6.4 in absence of an applied magnetic field and Eq. 6.5 in presence of applied magnetic field with a modified Hamann term [43, 44, 47, 62].

$$R(T) = R_0 + qT^3 + R_{KO}[1 - \ln(\frac{T_{eff}}{T_K})\{\ln^2(\frac{T_{eff}}{T_K}) + S(S+1)\pi^2\}^{-1/2}] \tag{6.4}$$

$$R(T) = R_0 + qT^3 + R_{KO}[1 - \ln(\frac{T_{eff}}{T_K})\{\ln^2(\frac{T_{eff}}{T_K}) + S(S+1)\pi^2\}^{-1/2}][1 - B^2(\frac{g\mu_B SB}{k_B T_{eff}})] \tag{6.5}$$

Eq. 6.4 is almost similar to Eq. 6.1, except that the second term (qT^3) in Eq. 6.4 represents the interband $(s-d)$ $e-ph$ scattering while it is $e-e$ scattering (qT^2) contribution in Eq. 6.1. From the fitting, we estimated a Kondo temperature (T_K) of

about 6 K and the spin component S=0.5, which are in good agreement with previous report on VSe_2 [43]. In Eq. 6.5, the Hamann expression is modified using the Brillouin function, $B(x) = (\frac{2S+1}{2S})\coth\frac{2S+1}{2S}x - \frac{1}{2S}\coth\frac{1}{2S}x$ in the quantum limit. See Table 6.2 for the fitting parameters.

Left panel in Fig. 6.4(c) depicts the field dependent MR(%), measured at various temperatures for the field applied parallel to c-axis ($\theta = 0°$). The right panel in Fig. 6.4(c) depicts MR(%) measured perpendicular to c-axis ($\theta = 90°$). We can see from Fig. 6.4(c) that for both field orientations the MR is negative (positive) below (above) the Kondo temperature (6 K). Fig. 6.4(d) depicts the angle dependent MR(%) measured at various temperatures with a magnetic field of 9 T (left panel) and 3 T (right panel). From Fig. 6.4(d) we can see that the MR(%) has a maximum for H$\|$c and minimum for H$\perp$c under the magnetic field of 9 T. On the other hand it is reversed when the applied field is 3 T, which means that the MR(%) is minimum for H$\|$c and maximum for H$\perp$c. Nevertheless, MR (%) sinusoidally depends on the field angle in going from H$\|$c to H$\perp$c. The Red solid lines are the fits to Eq. 6.3. Figs. 6.4 (e) and 6.4 (f) represents the polar maps of the symmetrized data shown left and right panels of Fig. 6.4 (d), respectively. Figs. 6.4 (e) and 6.4 (f) clearly show the out-of-plane anisotropic MR(%) in VSe_2. Interestingly, the anisotropy is rotated by 90° between 3 T and 9 T. Anisotropic MR at 9 T is in good agreement with previous study [59]. Also, note here that the anisotropic MR is significant above the Kondo state, i.e. at higher magnetic fields (9 T) irrespective of the temperature. In the Kondo state (3 T), a small anisotropic behaviour is observed which is negligible.

B(T)	R_0 ($m\Omega$)	q ($\mu\Omega/K^3$)	R_{KO} ($m\Omega$)	T_W (K)
0	9.4223(4)	0.0483(4)	0.1121(4)	2.455(3)
1	9.3600(4)	0.0485(4)	0.1751(4)	2.023(3)
2	9.4211(4)	0.0480(4)	0.1124(4)	1.452(3)
3	9.4017(4)	0.0497(4)	0.1367(4)	2.160(3)
4	9.4301(4)	0.0497(4)	0.1061(4)	1.832(3)
5	9.4508(4)	0.0480(4)	0.0843(4)	1.385(3)
6	9.4440(4)	0.0506(4)	0.0965(4)	1.694(3)

Table 6.2: Kondo fitting parameters of VSe_2

Figure 6.5 shows magnetic properties studies on the VSe_2 single crystals. Fig. 6.5(a) shows temperature dependent magnetic susceptibility measured with a magnetic field of 1 T applied parallel to the c-axis within the temperature range of 3-300 K in the ZFC and FC modes. Here, it can be seen that ZFC and FC are identical. To observe the effect of Kondo screening on the magnetic properties, we measured the susceptibility by varying the magnetic field of up to 7 T within the temperature range of 3-30 K in FC mode as shown in Fig. 6.5(b). Unlike in VTe_2, we do not find a significant change in

the susceptibility of VSe_2 as a function of applied field, probably due to the low Kondo temperature (6 K) found in VSe_2. Fig. 6.5(b) shows the magnetization isotherm $M(H)$ measured at 5 and 300 K. We clearly notice a sigmoid like $M(H)$ curve at 5 K due to soft ferromagnetic ordering. This observation is different from previous reports where VSe_2 is found in bulk to be paramagnetic at all temperatures [60, 61, 63]. However, a strong ferromagnetic ordering is reported in monolayer VSe_2 grown on HOPG or MoS_2 substrate at the room temperature [63]. Another recent report also demonstrated a small ferromagnetic signal in stoichiometric bulk VSe_2, which they suggest to arise from vanadium impurities intercalated between the van der Waals layers.

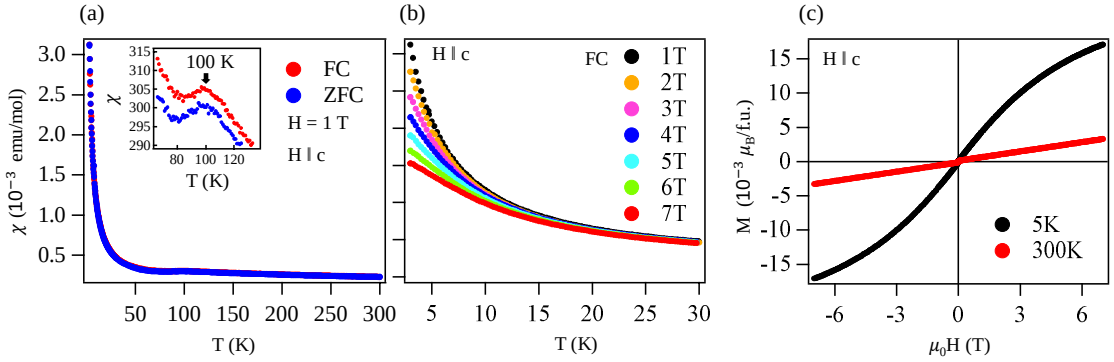

Figure 6.5: (a) Magnetic susceptibility of VSe_2 plotted as a function of temperature measured with a field of 1 T applied parallel to the c-axis in the FC and ZFC modes. (b) Same as (a) but measured for different magnetic fields in the FC mode. A hump in the magnetic susceptibility is noticed both in FC and ZFC modes at a CDW transition temperature of 100 K. (c) Magnetization isotherms $M(H)$ measured at 5 K and 300 K.

Finally, on comparing the electrical resistivity, magnetotransport, and magnetic properties between VTe_2 and VSe_2, we find that both systems show low temperature resistivity upturn due to the Kondo effect with a Kondo temperature of 12 K for the former and 6 K for the later, suggesting stronger magnetic correlations in VTe_2 compared to VSe_2. Both systems show negative MR in the Kondo state. VSe_2 shows negative to positive MR switching across the Kondo temperature of 6 K, while VTe_2 shows negligible MR above the Kondo temperature of 12 K. Moreover, above the Kondo state, a strong anisotropic MR is observed in the case of VSe_2, while it is almost negligible in VTe_2. In case of VTe_2 a weak anisotropic MR in the Kondo state is observed, whereas above the Kondo state the MR is negligible. Interestingly, though both systems show a low-temperature resistivity upturn due to the Kondo effect, under the magnetic field it behaves differently for different compounds. That means, VTe_2 follows the Hamann law modified with the classical Langevin function with dominant contribution from the $e-e$ scattering, while VSe_2 follows the Hamann law modified with the quantum Brillouin function (see Eq. 6.5) with the dominant

contribution from the interband $(s-d)$ $e-ph$ scattering. Different functions applicable to the same Kondo effect observed in different compounds can be understood from their differing Kondo temperatures. That means, the Kondo temperature of VTe_2 (12 K) is almost two times higher than the Kondo temperature of VSe_2 (6 K). On the other hand, a previous study on the single-crystalline nanoplates of VTe_2 reported a Kondo temperature of 6 K and the resistivity data was best fitted following the Brillouin function [47]. These observations suggest that the Kondo temperature of these systems is thickness sensitive [64]

6.4 Conclusions

In conclusion, we have drawn a comprehensive comparison between the transition-metal dichalcogenides VSe_2 and VTe_2 on their electrical transport, magnetotransport, and magnetic properties. We observe the Kondo effect in both systems induced by the exchange interaction between localized moments and conduction electrons at low temperature, resulting into resistance upturn at Kondo temperature of 6 K for VSe_2 and 12 K for VTe_2. From the field dependent resistance measurements we find that the data is fitted best with modified Hamann equation corrected by the quantum Brillouin function for VSe_2, while the data is best fitted with modified Hamann equation corrected by the classical Langevin function for VSe_2. Interestingly, we observe a contrasting MR properties between these systems across the Kondo temperature. In both systems examined, there is a manifestation of weak ferromagnetism at low temperatures. This phenomenon can be attributed to the presence of intercalated V atoms in both systems. While the chemical composition of VSe_2 displays a deficiency of V or excess of Se, previous studies have established that V^{4+} ions ($3d^1$) carry the localized magnetic moment in these systems [33, 42, 43]. In the case of VSe_2, some vanadium atoms are intercalated between the layers of VSe_2, similar to VTe_2, but there is also an excess of Se occupying the interstitial spaces within the crystal structure. Consequently, the overall chemical formula exhibits an excess of Se, which is p-Block element. As a result, this excess Se does not influence the Kondo effect or magnetic ordering. The Kondo effect in V deficient VSe_2 system was reported earlier [43].

Bibliography

[1] L. H. Brixner, "Preparation and properties of the single crystalline AB_2-type selenides and tellurides of niobium, tantalum, molybdenum and tungsten," *Journal of Inorganic and Nuclear Chemistry*, vol. 24, no. 3, pp. 257–263, 1962.

[2] B. E. Brown, "The crystal structures of $NbTe_2$ and $TaTe_2$," *Acta Crystallographica*, vol. 20, pp. 264–267, feb 1966.

[3] R. Nitsche, H. U. Bölsterli, and M. Lichtensteiger, "Crystal growth by chemical transport reactions—I," *Journal of Physics and Chemistry of Solids*, vol. 21, pp. 199–205, dec 1961.

[4] J. A. Wilson and A. D. Yoffe, "The transition metal dichalcogenides discussion and interpretation of the observed optical, electrical and structural properties," *Advances in Physics*, vol. 18, pp. 193–335, may 1969.

[5] J. A. Wilson, F. J. D. Salvo, and S. Mahajan, "Charge-density waves and superlattices in the metallic layered transition metal dichalcogenides," *Advances in Physics*, vol. 24, pp. 117–201, mar 1975.

[6] S. Sharma, L. Nordström, and B. Johansson, "Stabilization of charge-density waves in 1T-TaX_2 (X=S,Se,Te): First-principles total energy calculations," *Physical Review B*, vol. 66, nov 2002.

[7] R. E. Thorne, "Charge-Density-Wave Conductors," *Physics Today*, vol. 49, pp. 42–47, may 1996.

[8] C. M. WAYMAN and H. K. D. H. BHADESHIA, "PHASE TRANSFORMATIONS, NONDIFFUSIVE," in *Physical Metallurgy*, pp. 1507–1554, Elsevier, 1996.

[9] I. Kar, J. Chatterjee, L. Harnagea, Y. Kushnirenko, A. V. Fedorov, D. Shrivastava, B. Büchner, P. Mahadevan, and S. Thirupathaiah, "Metal-chalcogen bond-length induced electronic phase transition from semiconductor to topological semimetal in ZrX_2 (X=Se and Te)," *Physical Review B*, vol. 101, apr 2020.

[10] K. Selte, A. Kjekshus, H. Listou, H. Kyyhkynen, R. A. Hoffman, and A. Westerdahl, "On the Magnetic Properties of Niobium Selenides and Tellurides.," *Acta Chemica Scandinavica*, vol. 19, pp. 258–260, 1965.

[11] H. Chen, Z. Li, X. Fan, L. Guo, and X. Chen, "Quantum linear magnetoresistance in $NbTe_2$," *Solid State Communications*, vol. 275, pp. 16–20, jul 2018.

[12] F. Clerc, C. Battaglia, H. Cercellier, C. Monney, H. Berger, L. Despont, M. G. Garnier, and P. Aebi, "Fermi surface of layered compounds and bulk charge density wave systems," *Journal of Physics: Condensed Matter*, vol. 19, p. 355002, aug 2007.

[13] K. D. Bronsema, G. W. Bus, and G. A. Wiegers, "The crystal structure of vanadium ditelluride, $V_{(1+x)}Te_2$," *Journal of Solid State Chemistry*, vol. 53, pp. 415–421, jul 1984.

[14] Y. Liu, D. F. Shao, L. J. Li, W. J. Lu, X. D. Zhu, P. Tong, R. C. Xiao, L. S. Ling, C. Y. Xi, L. Pi, H. F. Tian, H. X. Yang, J. Q. Li, W. H. Song, X. B. Zhu, and Y. P. Sun, "Nature of charge density waves and superconductivity in 1T-$TaSe_{2-x}Te_x$," *Physical Review B*, vol. 94, jul 2016.

[15] T. Sörgel, J. Nuss, U. Wedig, R. K. Kremer, and M. Jansen, "A new low temperature modification of $TaTe_2$—Comparison to the room temperature and the hypothetical 1T-$TaTe_2$ modification," *Materials Research Bulletin*, vol. 41, pp. 987–1000, may 2006.

[16] T. Kumakura, H. Tan, T. Handa, M. Morishita, and H. Fukuyama, "Charge density waves and superconductivity in 2H-$TaSe_2$," *Czechoslovak Journal of Physics*, vol. 46, pp. 2611–2612, may 1996.

[17] K. Terashima, T. Sato, H. Komatsu, T. Takahashi, N. Maeda, and K. Hayashi, "Charge-density wave transition of 1T-VSe_2 studied by angle-resolved photoemission spectroscopy," *Physical Review B*, vol. 68, oct 2003.

[18] G. Gye, E. Oh, and H. W. Yeom, "Topological Landscape of Competing Charge Density Waves in 2H-$NbSe_2$," *Physical Review Letters*, vol. 122, jan 2019.

[19] T. Ritschel, J. Trinckauf, K. Koepernik, B. Büchner, M. v. Zimmermann, H. Berger, Y. I. Joe, P. Abbamonte, and J. Geck, "Orbital textures and charge density waves in transition metal dichalcogenides," *Nature Physics*, vol. 11, pp. 328–331, mar 2015.

[20] M. Leroux, L. Cario, A. Bosak, and P. Rodière, "Traces of charge density waves in NbS_2," *Physical Review B*, vol. 97, may 2018.

[21] M. Mulazzi, A. Chainani, N. Katayama, R. Eguchi, M. Matsunami, H. Ohashi, Y. Senba, M. Nohara, M. Uchida, H. Takagi, and S. Shin, "Absence of nesting in the charge-density-wave system 1T-VS_2 as seen by photoelectron spectroscopy," *Physical Review B*, vol. 82, aug 2010.

[22] T. Ohtani, K. Hayashi, M. Nakahira, and H. Nozaki, "Phase transition in $V_{1+x}Te_2$ ($0.04 \leq x \leq 0.11$)," *Solid State Communications*, vol. 40, pp. 629–631, nov 1981.

[23] T. Ohtani, S. Onoue, and M. Nakahira, "Phase relationships and properties in the V-Te system," *Materials research bulletin*, vol. 19, no. 10, pp. 1367–1375, 1984.

[24] C. Battaglia, H. Cercellier, F. Clerc, L. Despont, M. G. Garnier, C. Koitzsch, P. Aebi, H. Berger, L. Forró, and C. Ambrosch-Draxl, "Fermi-surface-induced lattice distortion in $NbTe_2$," *Physical Review B*, vol. 72, nov 2005.

[25] S. Nagata, T. Abe, S. Ebisu, Y. Ishihara, and K. Tsutsumi, "Superconductivity in the metallic layered compound $NbTe_2$," *Journal of Physics and Chemistry of Solids*, vol. 54, pp. 895–899, aug 1993.

[26] M. H. Van Maaren and G. M. Schaeffer, "Some new superconducting group V^a dichalcogenides," *Physics Letters A*, vol. 24, no. 12, pp. 645–646, 1967.

[27] H. Chen, Z. Li, L. Guo, and X. Chen, "Anisotropic magneto-transport and magnetic properties of low-temperature phase of $TaTe_2$," *EPL (Europhysics Letters)*, vol. 117, p. 27009, jan 2017.

[28] C. Chen, H.-S. Kim, A. S. Admasu, S.-W. Cheong, K. Haule, D. Vanderbilt, and W. Wu, "Trimer bonding states on the surface of the transition-metal dichalcogenide $TaTe_2$," *Physical Review B*, vol. 98, nov 2018.

[29] Y. Liu, W. J. Lu, D. F. Shao, L. Zu, X. C. Kan, W. H. Song, and Y. P. Sun, "Structural, electrical, and thermoelectric properties of distorted 1T-$Ta_{1-x}Nb_xTe_2$ single crystals," *EPL (Europhysics Letters)*, vol. 109, p. 17003, jan 2015.

[30] A. H. Thompson and B. G. Silbernagel, "Magnetic properties of VSe_2: Inferences from the study of metal-rich $V_{1+\delta}Se_2$ compounds," *Journal of Applied Physics*, vol. 49, pp. 1477–1479, mar 1978.

[31] L. F. Schneemeyer and M. J. Sienko, "The effect of niobium substitution on charge density wave anomalies in vanadium diselenide," *Journal of the Less Common Metals*, vol. 62, pp. 343–348, nov 1978.

[32] A. H. Thompson and B. G. Silbernagel, "Correlated magnetic and transport properties in the charge-density-wave states of VSe_2," *Physical Review B*, vol. 19, pp. 3420–3426, apr 1979.

[33] J. Pandey and A. Soni, "Electron-phonon interactions and two-phonon modes associated with charge density wave in single crystalline 1T-VSe_2," *Physical Review Research*, vol. 2, jul 2020.

[34] T. Valla, A. V. Fedorov, P. D. Johnson, P. A. Glans, C. McGuinness, K. E. Smith, E. Y. Andrei, and H. Berger, "Quasiparticle Spectra, Charge-Density Waves, Superconductivity, and Electron-Phonon Coupling in 2H- $NbSe_2$," *Physical review letters*, vol. 92, no. 8, p. 086401, 2004.

[35] F. J. Di Salvo, J. A. Wilson, B. G. Bagley, and J. V. Waszczak, "Effects of doping on charge-density waves in layer compounds," *Physical Review B*, vol. 12, no. 6, p. 2220, 1975.

[36] F. Borsa, D. R. Torgeson, and H. R. Shanks, "Charge-density wave amplitudes in $2H - NbSe_2$ and $2H - TaSe_2$ determined by ^{77}Se NMR," *Phys. Rev. B*, vol. 15, pp. 4576–4579, May 1977.

[37] T. Tsuda, H. Yasuoka, Y. Kitaoka, and F. J. Di Salvo, "^{51}V NMR study of the phase transition in 1T-VS_2," *Journal of Magnetism and Magnetic Materials*, vol. 31, pp. 1101–1102, 1983.

[38] X. Sun, T. Yao, Z. Hu, Y. Guo, Q. Liu, S. Wei, and C. Wu, "In situ unravelling structural modulation across the charge-density-wave transition in vanadium disulfide," *Physical Chemistry Chemical Physics*, vol. 17, no. 20, pp. 13333–13339, 2015.

[39] M. Leroux, M. Le Tacon, M. Calandra, L. Cario, M.-A. Méasson, P. Diener, E. Borrissenko, A. Bosak, and P. Rodière, "Anharmonic suppression of charge density waves in $2H$-NbS_2," *Physical Review B*, vol. 86, p. 155125, Oct 2012.

[40] Y. D. Wang, W. L. Yao, Z. M. Xin, T. T. Han, Z. G. Wang, L. Chen, C. Cai, Y. Li, and Y. Zhang, "Band insulator to Mott insulator transition in 1T-TaS_2," *Nature communications*, vol. 11, no. 1, pp. 1–7, 2020.

[41] J. Joshi, H. M. Hill, S. Chowdhury, C. D. Malliakas, F. Tavazza, U. Chatterjee, A. R. H. Walker, and P. M. Vora, "Short-range charge density wave order in 2H- TaS_2," *Physical Review B*, vol. 99, no. 24, p. 245144, 2019.

[42] X. Ding, J. Xing, G. Li, L. Balicas, K. Gofryk, and H.-H. Wen, "Crossover from Kondo to Fermi-liquid behavior induced by high magnetic field in 1T-VTe_2 single crystals," *Physical Review B*, vol. 103, mar 2021.

[43] S. Barua, M. C. Hatnean, M. R. Lees, and G. Balakrishnan, "Signatures of the Kondo effect in VSe_2," *Scientific Reports*, vol. 7, sep 2017.

[44] Q. Cao, F. F. Yun, L. Sang, F. Xiang, G. Liu, and X. Wang, "Defect introduced paramagnetism and weak localization in two-dimensional metal VSe_2," *Nanotechnology*, vol. 28, p. 475703, oct 2017.

[45] H. N. S. Lee, M. Garcia, H. McKinzie, and A. Wold, "The low-temperature electrical and magnetic properties of $TaSe_2$ and $NbSe_2$," *Journal of Solid State Chemistry*, vol. 1, no. 2, pp. 190–194, 1970.

[46] A. Furukawa, Y. Kimishima, Y. Oda, H. Nagano, and Y. Ōnuki, "Magnetic behavior of 1T-TaS_2 in the Anderson localized state," *Journal of the Physical Society of Japan*, vol. 54, no. 11, pp. 4300–4305, 1985.

[47] H. Liu, Y. Xue, J.-A. Shi, R. A. Guzman, P. Zhang, Z. Zhou, Y. He, C. Bian, L. Wu, R. Ma, J. Chen, J. Yan, H. Yang, C.-M. Shen, W. Zhou, L. Bao, and H.-J. Gao, "Observation of the Kondo Effect in Multilayer Single-Crystalline VTe_2 Nanoplates," *Nano Letters*, vol. 19, pp. 8572–8580, nov 2019.

[48] H. SCHÄFER, "Chemical Transport Processes as an Aid in Preparative Chemistry. Combination of Transport Reactions with Other Processes," in *Chemical Transport Reactions*, pp. 115–131, Elsevier, 1964.

[49] G. A. Wiegers, "Physical properties of first-row transition metal dichalcogenides and their intercalates," *Physica B+C*, vol. 99, pp. 151–165, jan 1980.

[50] D. R. Hamann, "New Solution for Exchange Scattering in Dilute Alloys," *Phys. Rev.*, vol. 158, pp. 570–580, Jun 1967.

[51] K. Yosida, "Anomalous Electrical Resistivity and Magnetoresistance Due to an $s-d$ Interaction in Cu-Mn Alloys," *Phys. Rev.*, vol. 107, pp. 396–403, Jul 1957.

[52] C. Kittel, *Introduction to solid state physics*. John Wiley & sons, inc, 2005.

[53] T. Sekitani, M. Naito, and N. Miura, "Kondo effect in underdoped n-type superconductors," *Phys. Rev. B*, vol. 67, p. 174503, May 2003.

[54] K. Park, L. S. Wu, Y. Janssen, M. S. Kim, C. Marques, and M. C. Aronson, "Field-tuned Fermi liquid in quantum critical YFe_2Al_{10}," *Phys. Rev. B*, vol. 84, p. 094425, Sep 2011.

[55] H. Pan, "Magnetic and Electronic Evolutions of Hydrogenated VTe_2 Monolayer under Tension," *Scientific Reports*, vol. 4, dec 2014.

[56] H.-R. Fuh, C.-R. Chang, Y.-K. Wang, R. F. L. Evans, R. W. Chantrell, and H.-T. Jeng, "Newtype single-layer magnetic semiconductor in transition-metal dichalcogenides VX_2 (X = S, Se and Te)," *Scientific Reports*, vol. 6, sep 2016.

[57] C. J. Sayers, L. S. Farrar, S. J. Bending, M. Cattelan, A. J. H. Jones, N. A. Fox, G. Kociok-Köhn, K. Koshmak, J. Laverock, L. Pasquali, and E. D. Como, "Correlation between crystal purity and the charge density wave in 1T-VSe_2," *Physical Review Materials*, vol. 4, feb 2020.

[58] A. O. Fumega, M. Gobbi, P. Dreher, and W. W. et al., "Absence of Ferromagnetism in VSe_2 Caused by Its Charge Density Wave Phase," *The Journal of Physical Chemistry C*, vol. 123, pp. 27802–27810, oct 2019.

[59] A. Toriumi and S. Tanaka, "Galvanomagnetic properties of 1T-VSe_2," *Physica B+C*, vol. 105, pp. 141–145, may 1981.

[60] C. F. van Bruggen and C. Haas, "Magnetic susceptibility and electrical properties of VSe_2 single crystals," *Solid State Communications*, vol. 20, pp. 251–254, oct 1976.

[61] M. Bayard and M. J. Sienko, "Anomalous electrical and magnetic properties of vanadium diselenide," *Journal of Solid State Chemistry*, vol. 19, pp. 325–329, dec 1976.

[62] S. Kondo, D. C. Johnston, and L. L. Miller, "Synthesis, characterization, and magnetic susceptibility of the heavy-fermion transition-metal oxide LiV_2O_4," *Physical Review B*, vol. 59, pp. 2609–2626, Jan 1999.

[63] M. Bonilla, S. Kolekar, Y. Ma, H. C. Diaz, V. Kalappattil, R. Das, T. Eggers, H. R. Gutierrez, M.-H. Phan, and M. Batzill, "Strong room-temperature ferromagnetism in VSe_2 monolayers on van der Waals substrates," *Nature Nanotechnology*, vol. 13, pp. 289–293, feb 2018.

[64] J. Yang, W. Wang, Y. Liu, H. Du, W. Ning, G. Zheng, C. Jin, Y. Han, N. Wang, Z. Yang, M. Tian, and Y. Zhang, "Thickness dependence of the charge-density-wave transition temperature in VSe_2," *Applied Physics Letters*, vol. 105, p. 063109, aug 2014.

Chapter 7

Electrical-transport, Magnetotransport, and Magnetic Properties Studies of V_5S_8 Single Crystal

7.1 Introduction

The discovery of magnetism in 2D layered systems [1–4] has attracted a great deal of research interest for the last few years because of their versatile technological applications in spintronics [5–9]. These systems possess loosely bound 2D layers connected by the van der Waals forces [10]. By stacking [11], twisting [12] the monolayers, or by making the heterostructured magnetic materials [13, 14], the magnetic properties can be tuned. Though magnetism is rare in the TMDCs in their bulk form, there exist few TMDCs showing ferromagnetic ordering mostly in low dimensions. For instance, monolayer 2H-$NbSe_2$ [15, 16], monolayer/bilayer VSe_2 [17, 18], monolayer VTe_2 [19], nano-2H-$NbSe_2$ [20], and atomically thin 1T-NbS_2 [21] show ferromagnetism. Nevertheless, VSe_2 is found to show ferromagnetism in its bulk phase [17]. In addition to ferromagnetism, a very few TMDCs are known to show the Kondo effect such as $ZrTe_2$ [22], VSe_2 [23, 24], and VTe_2 [25], due to low temperature magnetic ordering induced by the intercalated transition metal. Usually, the Kondo effect arises from the exchange interaction of the localized magnetic moments with the conduction electrons, leading to an increase in the electrical resistivity at extremely low temperatures. Thus, the doped or intercalated magnetic impurities with unfilled d- or f-orbitals [26–29] act as the scattering centres for this type of exchange interactions.

Since both VTe_2 and VSe_2 show ferromagnetism in addition to the low temperature Kondo effect [17, 30], whether both of these rare properties do exist in VS_2 is a natural

Most of this chapter is published as: I. Kar *et al.*, Solid State Communications **369**, 115209 (2023).

question to arise. In order to address this question, we worked on V_5S_8, which can be expressed as $V_{1.25}S_2$, having 25% excess V in the composition. Worth to mention here is that the ferromagnetism and Kondo effect arise in VTe_2 and VSe_2 by the intercalated V atoms [23–25]. Similarly, in V_5S_8, the V atoms are intercalated between the VS_2 layers [31]. The V intercalation in V_5S_8 seems to be completely changing the crystal structure and physical properties of pristine VS_2. Precisely, the pristine VS_2 is a nonmagnetic metal in the $1T$ phase with a CDW ordering at 305 K [32, 33], while V_5S_8 is an antiferromagnetic metal in the $1T'$ phase without CDW ordering [31, 34–37].

In this work, we present electrical transport, magnetotransport, and magnetic properties studies on V_5S_8 single crystals. Magnetization [$M(T)$] studies suggest an antiferromagnetic ordering at around 27 K, in agreement with previous reports [31, 34–37]. Interestingly, down to the AFM ordering temperature (>27 K) the magnetic susceptibility is found to be nearly isotropic between $H \parallel c$ and $H \perp c$. However, below the Néel temperature, T_N (<27 K) the magnetic susceptibility instantly turns to an anisotropic one. Magnetization isotherms [$M(H)$] suggest a SF transition at a critical field of 3.5 T for $H \parallel c$. Most importantly, we find an upturn in the electrical resistance at low temperature with a resistance minima at 6 K, plausibly due to the Kondo effect. A negative MR is noticed in the antiferromagnetic state, while it is negligible in the paramagnetic state (100 K).

7.2 Experimental Details

Single crystals of V_5S_8 were grown by CVT technique with iodine as a transport agent[38]. In the first step, stoichiometric quantities of V (powder, 99.5%, metals basis, Alfa Aesar) and S (pieces, 99.999%, metals basis, Alfa Aesar) were mixed thoroughly and sealed in a quartz ampoule under vacuum along with pieces of crystallized iodine (crystalline, 99.99+%, metals basis, Alfa Aesar) (2 mg/cm^3). The ampoule was kept in a three-zone tube furnace where the temperatures were set at 1000°C for the hot-zone and 950°C for the cold-zone. After 5 days of reaction, we obtained shiny single crystals of V_5S_8 with a typical dimension of 2 mm×1 mm at the cold-zone.

The chemical composition of the single crystals were determined by EDX equipped with SEM (Quanta 250 FEG). Phase purity and crystal structure were confirmed by the XRD technique using Cu k_α-radiation (Rigaku MiniFlex II and Rigaku SmartLab 9KW). Electrical transport studies were done in a PPMS (Quantum Design PPMS-9T) using a standard four-probe method, with the electrical current applied parallel to *ab*-plane. A magnetic field up to 9 T was applied at different polar angles with respect to the *c*-axis for magnetotransport measurements. Four copper (Cu) leads were connected to the sample by vacuum compatible silver epoxy (Epo-Tek H20E). The

sample temperature was varied between 2 K and 380 K during the transport measurements. DC magnetization measurements were performed using VSM (Quantum Design PPMS-9T). The temperature dependence of the magnetization in ZFC and FC modes was studied for different magnetic fields within the temperature range of 2-300 K.

7.3 Results and Discussions

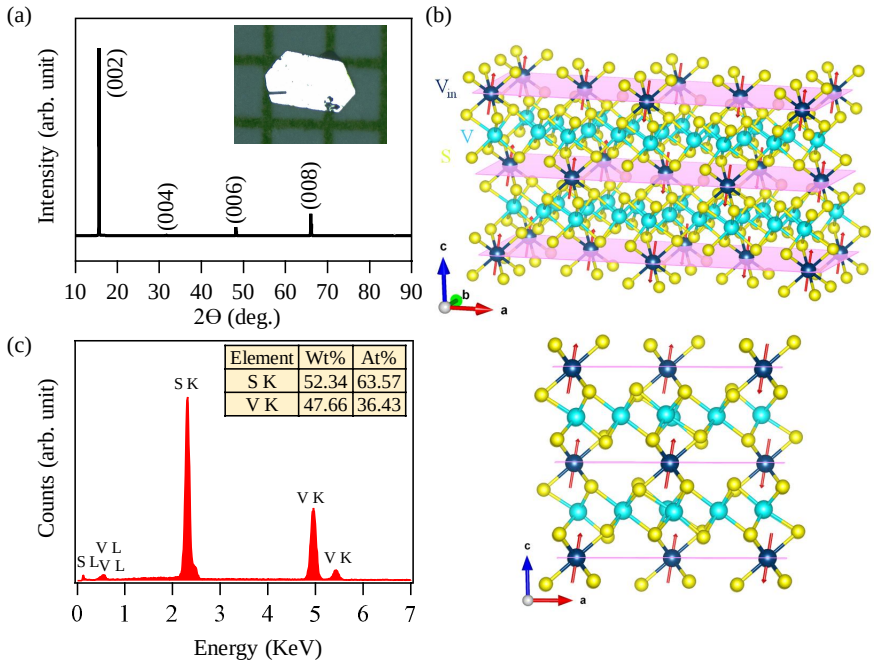

Figure 7.1: (a) Powder X-ray diffractogram (XRD) of V_5S_8 single crystals. Inset is a photographic optical image of the single crystal. The top panel in (b) is the crystal structure of V_5S_8 spanned over two unit cells. Blue color atoms are intercalated vanadium atoms in the van der Waals gap between two layers of VS_2. Bottom panel in (b) shows the V_5S_8 crystal structure projected onto the *ac*-plane. (c) Energy dispersive X-ray analysis (EDX) of V_5S_8 single crystals. Inset in (c) shows atomic and weight percentages of the elements present in the compound.

In Fig. 7.1(a) sharp Bragg peaks are observed in the XRD pattern of V_5S_8 single crystal corresponding to the $(00l)$ plane, suggesting that the crystal growth is along the *c*-axis. The single crystals were in platelike shape with metallic luster as illustrated in the inset of Fig. 7.1(a). The top panel in Fig. 7.1(b) shows the crystal structure of V_5S_8 in which the S atoms form covalent bonding with the intercalated V atoms in the octahedral coordination in between two VS_2 layers. These intercalated V atoms are responsible for the distortion in the octahedral coordination of VS_2, leading to antiferromagnetism with spins aligned at an angle of 10.4° from the *c*-axis as demonstrated in the bottom panel of Fig. 7.1(b) [39–41]. Further, V_5S_8 crystallizes into the

monoclinic structure of the space group $F12/m1(12)$ with distorted $1T$ ($1T'$) phase. From the EDX measurements, shown in Fig. 7.1(c), we estimate the actual chemical composition of the obtained single crystals to $V_{4.6}S_8$ which is very close to the nominal composition of V_5S_8.

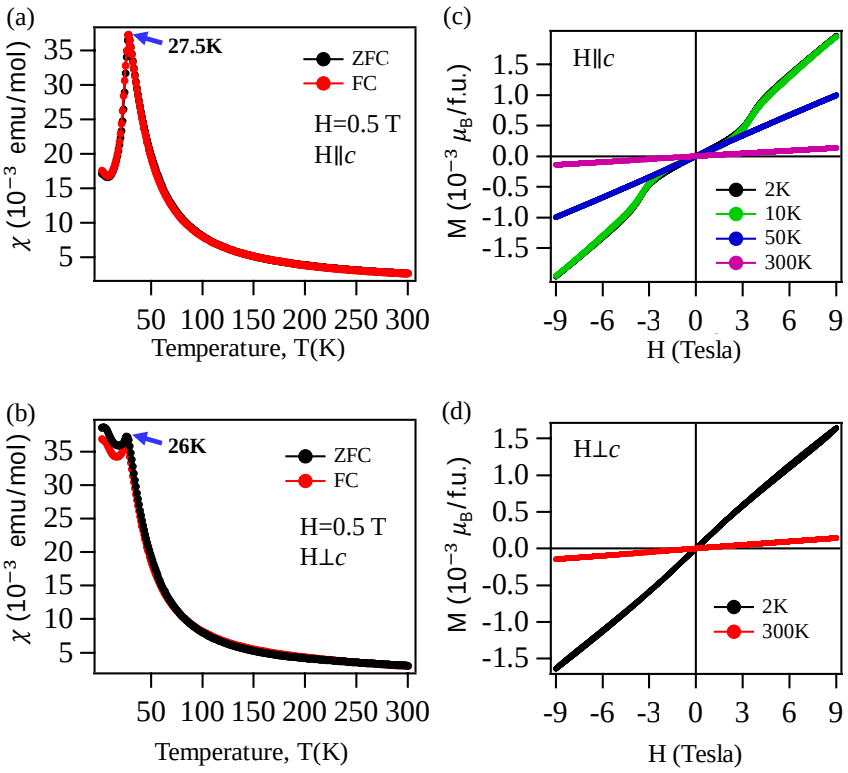

Figure 7.2: (a) Magnetic susceptibility plotted as a function of temperature measured with a field of 0.5 T in the FC and ZFC modes for $H \parallel c$. (b) Same as (a) but measured for $H \perp c$. (c) Magnetization isotherms $M(H)$ measured at different temperatures for $H \parallel c$. (d) Same as (c) but measured for $H \perp c$.

Figs. 7.2(a) and 7.2(b) show the magnetic susceptibility (χ) plotted as a function of temperature for H=0.5T applied parallel ($H \parallel c$) and perpendicular ($H \perp c$) to the c-axis, respectively. From Figs. 7.2(a) and 7.2(b) we notice similar trends of susceptibility with respect to the temperature in going from 300 K down to 27±1 K for both $H \parallel c$ and $H \perp c$, suggesting isotropic magnetic properties between 300 and 27±1 K. But below 27±1 K, we see a sudden drop in χ for $H \parallel c$ similar to an antiferromagnetic system. This observation is consistent with previous reports on these systems where an AFM order is demonstrated below T_N=27 K [31, 34–37, 40–42]. On the other hand, for $H \perp c$, though we find a slight drop in χ below 27±1 K, the susceptibility gets saturated upon decreasing the temperature down to 2 K. Thus, the system shows clear anisotropic magnetic properties below the Néel temperature. Fig. 7.2(c) depicts magnetization isotherms [$M(H)$] measured at different temperatures with field applied parallel to the c-axis. While the data largely resembles the AFM

type ordering at all the measured temperatures , at low temperatures (2 and 10 K) we observe SF like transitions at a critical field of 3.5 T, in agreement with previous reports [35, 40, 42]. Fig. 7.2(d) shows $M(H)$ data measured at different temperatures with a field applied perpendicular to the c-axis. Similar to the $H \parallel c$ data, from $H \perp c$ we also observe AFM type ordering except that SF-transition is not observed down to the lowest possible measured temperature. This indicates that c-axis is the easy-axis of magnetization in V_5S_8 [39–41].

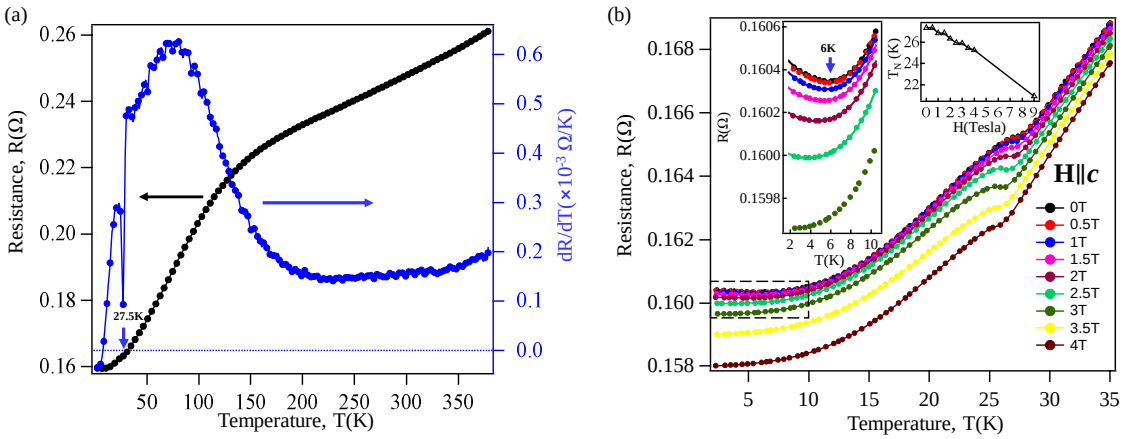

Figure 7.3: (a) In-plane electrical resistance and first derivative of resistance (dR/dT) plotted as a function of temperature. (b) Temperature dependent electrical resistance plotted for various magnetic fields applied parallel to the c-axis. Left inset in (b) is the zoomed-in image of the dash marked rectangular region. Solid lines are fitting to Eq. 7.1 at 0 T and Eq. 7.2 in presence of field. Right inset in (b) shows Néel temperature T_N plotted as a function of applied field.

Fig. 7.3(a) depicts temperature dependent zero-field in-plane electrical resistance of V_5S_8. The resistance data suggest a metallic behaviour at low temperature, consistent with previous studies [42]. We further observe a hump in the resistance at around 27 K due to antiferromagnetic ordering [42]. To better understand the electrical resistance, we derived the first derivative of the resistance with respect to temperature (dR/dT) as shown in Fig. 7.3(a). Again, we clearly see a drastic change in the slope (dR/dT) at around 27 K corresponding to the resistance hump. However from a careful observation of dR/dT, we find that below 6 K it becomes negative as the resistance increases with decreasing temperature (resistance upturn). To understand the mechanism of resistance upturn, we measured it at various applied magnetic fields within the temperature range of 2-35 K as shown in Fig. 7.3(b). Foremost, we observe in Fig. 7.3(b) that the peak temperature of hump-like structure decreases with increasing applied field from 27 K at 0 T to 21 K at 9 T ($R(T)$ at 9 T is not shown) as shown in the right inset of Fig. 7.3(b). This observation reaffirms the AFM ordering in this system. Secondly, as shown in the left inset of Fig. 7.3(b), the resistance upturn with a minima

(T_m) at 6 K disappears above 2.5 T.

In principle, there are mainly three reasons behind the resistance upturn. They are i) EEI [43], ii) WL [44], and iii) Kondo effect [45]. Among these three, EEI shows positive MR [46] whereas negative MR is observed due to the Kondo effect [22, 23, 25] and WL [22, 47]. In addition, by increasing the applied magnetic field, the resistance minima can be suppressed in the Kondo effect and WL whereas applied field strength has no effect in the case of EEI. Thus, as can be seen from inset of Fig. 7.3(b), the resistance minima is suppressed at 2.5 T. Further, we demonstrate below a negative magnetoresistance in V_5S_8. Thus, we can rule out EEI as the origin of resistance upturn. Traditionally, WL and weak antilocalization (WAL) are present in low dimensional systems [48] such as thin films [49], nanowires [50] due to the higher probability of scattering rates resulting into quantum interference [51]. Moreover, it is a well known phenomenon that a small amount of magnetic field can destroy the quantum interference and lead to a cusp-like positive or negative magnetoresistance around zero-field as a result of WL or WAL [22, 47, 49, 51, 52]. On the other hand, the Kondo effect exhibits negative MR having quadratic dependence on B in low field region [22, 23, 25, 30, 53]. As we show below, the MR of V_5S_8 depends quadratically on the field. Importantly, the cusp-like feature is not observed from our MR measurements of V_5S_8. Also, the conductivity ($\sigma(T)$) is not fitted well (not shown) with the WL equation $\sigma = \sigma_0 + kT^{p/2}$ where $k = \frac{2e^2}{ah\pi^2}$ and the factor a is defined as $L_{Th} = aT^{-p/2}$ for p=2, 3, and 3/2 [43, 50]. Thus, the WL effect also can be excluded from the discussion. Finally, we conclude that the Kondo effect is mainly causing the low temperature resistance upturn in V_5S_8.

$$R(T) = R_0 + aT^2 + bT^5 + R_{KO}[1 - \frac{\ln(\frac{T}{T_K})}{\sqrt{\ln^2(\frac{T}{T_K}) + S(S+1)\pi^2}}] \tag{7.1}$$

$$R(T) = R_0 + aT^2 + bT^5 + R_{KO}[1 - \frac{\ln(\frac{T}{T_K})}{\sqrt{\ln^2(\frac{T}{T_K}) + S(S+1)\pi^2}}][1 - B^2(\frac{g\mu_B SH}{k_B(T+T_K)})] \tag{7.2}$$

Having confirmed the Kondo effect in V_5S_8, the resistance data measured without and with magnetic fields (up to H=2.5 T) are fitted using the Eqs. 7.1 and 7.2, respectively, as shown in the inset of Fig. 7.3(b) [30]. In Eq. 7.1, the first term (R_0) is the residual resistance, the second term (aT^2) represents the Fermi-liquid contribution, third term (bT^5) represents the electron-phonon contribution, and the fourth term is the Kondo resistance described by the Hamann expression [30, 54]. In the fourth term,

H (T)	R_0 (Ω)	a ($\mu\Omega - K^{-2}$)	b ($n\Omega - K^{-5}$)	R_{KO} (Ω)
0	0.1598	0.926	1.996	0.000536
1	0.1596	1.248	1.863	0.000616
1.5	0.1597	1.209	1.890	0.000510
2	0.1597	1.621	1.679	0.000438
2.5	0.1596	2.223	1.453	0.000359

Table 7.1: Kondo fitting parameters

R_{KO} is the temperature-independent Kondo resistance, T_K is the Kondo temperature, and S is the total spin of the magnetic impurity. The resistance curves are best fitted with T_K = 6 K and S=1 since V^{3+} ($3d^2$) ions carry the localized magnetic moment in this system as reported earlier [31, 34, 36, 41]. In Eq. 7.2, the Hamann term is modified using quantum Brillouin function, $B(x) = (\frac{2S+1}{2S})\coth\frac{2S+1}{2S}x - \frac{1}{2S}\coth\frac{1}{2S}x$. Here, g is the Landè g-factor, μ_B is the Bohr magneton, and k_B is the Boltzmann constant [23, 30, 55, 56]. See Table 7.1 for the fitting parameters.

Figs. 7.4(a) and 7.4(b) depict magnetoresistance, $MR(\%) = \frac{R(H)-R(0)}{R(0)} \times 100\%$, plotted as a function of field applied parallel ($\theta = 0°$) and perpendicular ($\theta = 90°$) to the c-axis, respectively. We notice negative MR at low temperatures (2, 10, and 50 K), but it is negligible at 100 K. Mostly, the negative MR is observed in the Kondo state of the Kondo systems such as in $La_{1-x}Pr_xNiO_{3-\delta}$ [57] and VTe_2 [25], and in the AFM state of the AFM systems such as in $EuTe_2$ [58] and $FeNbTe_2$ [59, 60]. However in the studied system of V_5S_8, a negative MR is noticed above and below the Kondo temperature (6 K) and above and below the Néel temperature (27±1 K). Also, in agreement with a previous study on this system [35, 40, 42], we observe a change in MR(%) below the Néel temperature when measured with the field parallel to the c-axis($\theta = 0°$) due to SF transition at a critical field of 3.5 T. However, the same is not observed in MR(%) when measured with field perpendicular to the c-axis($\theta = 90°$). Overall, the field dependence of MR is found to be quadratic.

To explore further on the MR anisotropy, we performed angle dependent (θ) magnetoresistance (AMR) measurements, $AMR(\%) = \frac{R(\theta°)-R(0°)}{R(0°)} \times 100\%$, at various temperatures under 1T and 9T applied fields as shown in Fig. 7.4(c) by varying θ between 0° and 360°. Solid lines in Fig. 7.4(c) are the fits with equation $AMR(\theta) = C + \alpha cos2(\theta + \phi)$, where C, α are constants and ϕ is the phase [61–63]. From the AMR data, we observe that the oscillations exhibit large amplitudes under the magnetic field of 9 T measured at 2 K and 10 K with a twofold symmetry having maximal MR values for $H \perp c$ and minimal MR values for $H \parallel c$ [59, 64]. On the other hand, under the magnetic field of 1 T, measured at 2 K and 10 K, the twofold symmetry still survives, but the oscillation magnitude gets significantly reduced. For a better representation, the AMR data of Fig. 7.4(c) are plotted into the polar graphs as shown in Figs. 7.4(d) and 7.4(e) for the fields of 9T and 1T, respectively. Thus, the two-fold asymmetry of MR measured

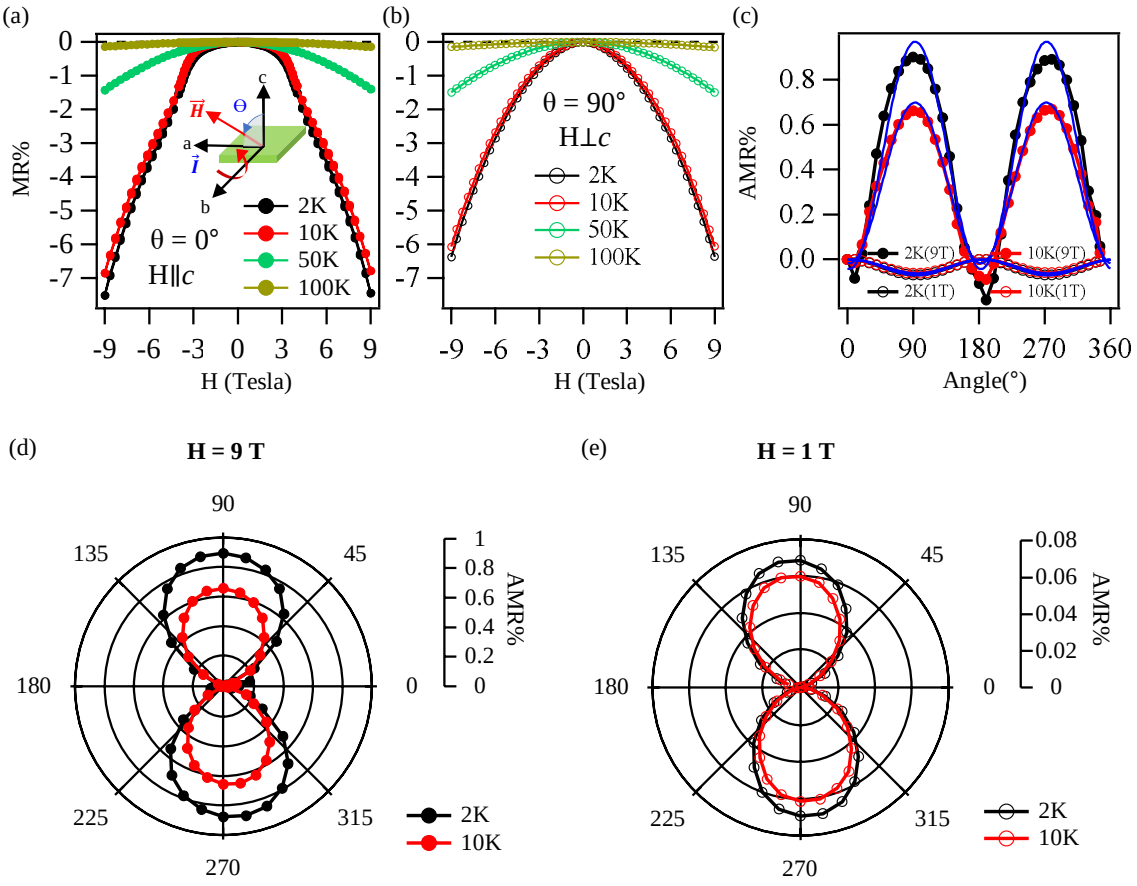

Figure 7.4: (a) Magnetoresistance, MR (%), plotted as a function of field applied parallel to the c-axis ($\theta = 0°$). (b) Same as (a) but measured for the field applied perpendicular to the c-axis ($\theta = 90°$). (c) Angle-dependent MR (%) plotted as function of field-angle under the applied fields of 1 T and 9 T. (d) and (e) AMR (%) of (c) plotted in the polar graph with an applied of 9T and 1T respectively.

at both 1 T and 9 T is clearly visible from Fig. 7.4(c).

7.4 Conclusions

In conclusion, we have systematically studied the electrical transport, magnetotransport, and magnetic properties of the V intercalated transition metal dichalcogenide V_5S_8. In this study, we show the Kondo effect in V_5S_8 originated from the exchange interaction between localized moments and conduction electrons. We find isotropic magnetic properties above T_N, while a strong magnetic anisotropy is noticed below T_N. In addition, below T_N we find an out-of-plane ($H \parallel c$) SF transition triggered at a critical field of 3.5 T that is absent for $H \perp c$. Negative MR is noticed in the antiferromagnetic state, while it is negligible in the paramagnetic state. Angle-dependent MR is found to be highly anisotropic in the antiferromagnetic state (<27 K).

Bibliography

[1] A. M. Tokmachev, D. V. Averyanov, A. N. Taldenkov, I. S. Sokolov, I. A. Karateev, O. E. Parfenov, and V. G. Storchak, "Two-Dimensional Magnets beyond the Monolayer Limit," *ACS nano*, vol. 15, no. 7, pp. 12034–12041, 2021.

[2] H. Dai, M. Cai, Q. Hao, Q. Liu, Y. Xing, H. Chen, X. Chen, X. Wang, H.-H. Fu, and J. Han, "Nonlocal Manipulation of Magnetism in an Itinerant Two-Dimensional Ferromagnet," *ACS Nano*, vol. 16, pp. 12437–12444, jul 2022.

[3] W. Ji, "2D Magnetism - Materials, Devices, and Applications Forum in ACS Applied Electronic Materials," *ACS Applied Electronic Materials*, vol. 4, no. 7, pp. 3166–3167, 2022.

[4] Y. Li, B. Yang, S. Xu, B. Huang, and W. Duan, "Emergent Phenomena in Magnetic Two-Dimensional Materials and van der Waals Heterostructures," *ACS Applied Electronic Materials*, vol. 4, no. 7, pp. 3278–3302, 2022.

[5] H. H. Kim, B. Yang, T. Patel, F. Sfigakis, C. Li, S. Tian, H. Lei, and A. W. Tsen, "One million percent tunnel magnetoresistance in a magnetic van der Waals heterostructure," *Nano Letters*, vol. 18, no. 8, pp. 4885–4890, 2018.

[6] T. Song, M. W.-Y. Tu, C. Carnahan, X. Cai, T. Taniguchi, K. Watanabe, M. A. McGuire, D. H. Cobden, D. Xiao, W. Yao, *et al.*, "Voltage control of a van der Waals spin-filter magnetic tunnel junction," *Nano Letters*, vol. 19, no. 2, pp. 915–920, 2019.

[7] Z. Wang, D. Sapkota, T. Taniguchi, K. Watanabe, D. Mandrus, and A. F. Morpurgo, "Tunneling spin valves based on Fe_3GeTe_2/hBN/Fe_3GeTe_2 van der Waals heterostructures," *Nano letters*, vol. 18, no. 7, pp. 4303–4308, 2018.

[8] H. Lin, F. Yan, C. Hu, Q. Lv, W. Zhu, Z. Wang, Z. Wei, K. Chang, and K. Wang, "Spin-valve effect in Fe_3GeTe_2/MoS_2/Fe_3GeTe_2 van der Waals heterostructures," *ACS Applied Materials & Interfaces*, vol. 12, no. 39, pp. 43921–43926, 2020.

[9] H. Ye, Y. Zhu, D. Bai, J. Zhang, X. Wu, and J. Wang, "Spin valve effect in VN/GaN/VN van der Waals heterostructures," *Phys. Rev. B*, vol. 103, p. 035423, Jan 2021.

[10] N. Sethulakshmi, A. Mishra, P. M. Ajayan, Y. Kawazoe, A. K. Roy, A. K. Singh, and C. S. Tiwary, "Magnetism in two-dimensional materials beyond graphene," *Materials Today*, vol. 27, pp. 107–122, jul 2019.

[11] R. E. Camley and R. L. Stamps, "Magnetic multilayers: spin configurations, excitations and giant magnetoresistance," *Journal of Physics: Condensed Matter*, vol. 5, no. 23, p. 3727, 1993.

[12] H. Xie, X. Luo, G. Ye, Z. Ye, H. Ge, S. H. Sung, E. Rennich, S. Yan, Y. Fu, S. Tian, *et al.*, "Twist engineering of the two-dimensional magnetism in double bilayer chromium triiodide homostructures," *Nature Physics*, vol. 18, no. 1, pp. 30–36, 2022.

[13] T. Song, X. Cai, M. W.-Y. Tu, X. Zhang, B. Huang, N. P. Wilson, K. L. Seyler, L. Zhu, T. Taniguchi, K. Watanabe, *et al.*, "Giant tunneling magnetoresistance in spin-filter van der Waals heterostructures," *Science*, vol. 360, no. 6394, pp. 1214–1218, 2018.

[14] S. V. Belim, I. V. Bychkov, I. Maltsev, D. A. Kuzmin, and V. G. Shavrov, "Tuning of 2D magnets Curie temperature via substrate," *Journal of Magnetism and Magnetic Materials*, vol. 541, p. 168553, 2022.

[15] R. Pervin, M. Krishnan, A. Sonachalam, and P. M. Shirage, "Coexistence of superconductivity and ferromagnetism in defect-induced $NbSe_2$ single crystals," *Journal of Materials Science*, vol. 54, pp. 11903–11912, jun 2019.

[16] D. Wickramaratne, S. Khmelevskyi, D. F. Agterberg, and I. I. Mazin, "Ising Superconductivity and Magnetism in $NbSe_2$," *Phys. Rev. X*, vol. 10, p. 041003, Oct 2020.

[17] F. Li, K. Tu, and Z. Chen, "Versatile Electronic Properties of VSe_2 Bulk, Few-Layers, Monolayer, Nanoribbons, and Nanotubes: A Computational Exploration," *The Journal of Physical Chemistry C*, vol. 118, pp. 21264–21274, sep 2014.

[18] M. Bonilla, S. Kolekar, Y. Ma, H. C. Diaz, V. Kalappattil, R. Das, T. Eggers, H. R. Gutierrez, M.-H. Phan, and M. Batzill, "Strong room-temperature ferromagnetism in VSe_2 monolayers on van der Waals substrates," *Nature Nanotechnology*, vol. 13, pp. 289–293, feb 2018.

[19] H.-R. Fuh, C.-R. Chang, Y.-K. Wang, R. F. L. Evans, R. W. Chantrell, and H.-T. Jeng, "Newtype single-layer magnetic semiconductor in transition-metal dichalcogenides VX_2 (X = S, Se and Te)," *Scientific Reports*, vol. 6, sep 2016.

[20] R. Gill, "Superconductivity and ferromagnetism in nanomaterial $NbSe_2$," in *AIP Conference Proceedings*, Author(s), 2017.

[21] E. Martino, C. Putzke, M. König, P. J. W. Moll, H. Berger, D. LeBoeuf, M. Leroux, C. Proust, A. Akrap, H. Kirmse, C. Koch, S. Zhang, Q. Wu, O. V. Yazyev, L. Forró, and K. Semeniuk, "Unidirectional Kondo scattering in layered NbS_2," *npj 2D Materials and Applications*, vol. 5, nov 2021.

[22] Y. Wang, C. Xie, J. Li, Z. Du, L. Cao, Y. Han, L. Zu, H. Zhang, H. Zhu, X. Zhang, Y. Xiong, and W. Zhao, "Weak Kondo effect in the monocrystalline transition metal dichalcogenide $ZrTe_2$," *Phys. Rev. B*, vol. 103, p. 174418, May 2021.

[23] S. Barua, M. C. Hatnean, M. R. Lees, and G. Balakrishnan, "Signatures of the Kondo effect in VSe_2," *Scientific Reports*, vol. 7, sep 2017.

[24] J. Pandey and A. Soni, "Electron-phonon interactions and two-phonon modes associated with charge density wave in single crystalline 1T-VSe_2," *Physical Review Research*, vol. 2, jul 2020.

[25] X. Ding, J. Xing, G. Li, L. Balicas, K. Gofryk, and H.-H. Wen, "Crossover from Kondo to Fermi-liquid behavior induced by high magnetic field in 1T-VTe_2 single crystals," *Physical Review B*, vol. 103, mar 2021.

[26] C. Krellner, N. S. Kini, E. M. Brüning, K. Koch, H. Rosner, M. Nicklas, M. Baenitz, and C. Geibel, "CeRuPO: A rare example of a ferromagnetic Kondo lattice," *Phys. Rev. B*, vol. 76, p. 104418, Sep 2007.

[27] A. H. Nevidomskyy and P. Coleman, "Kondo Resonance Narrowing in d- and f-Electron Systems," *Phys. Rev. Lett.*, vol. 103, p. 147205, Oct 2009.

[28] Y. Li, R. Deng, W. Lin, Y. Tian, H. Peng, J. Yi, B. Yao, and T. Wu, "Electrostatic tuning of Kondo effect in a rare-earth-doped wide-band-gap oxide," *Phys. Rev. B*, vol. 87, p. 155151, Apr 2013.

[29] T. P. Sarkar, K. Gopinadhan, M. Motapothula, S. Saha, Z. Huang, S. Dhar, A. Patra, W. M. Lu, F. Telesio, I. Pallecchi, Ariando, D. Marré, and T. Venkatesan, "Unexpected observation of spatially separated Kondo scattering and ferromagnetism in Ta alloyed anatase TiO2 thin films," *Scientific Reports*, vol. 5, aug 2015.

[30] H. Liu, Y. Xue, J.-A. Shi, R. A. Guzman, P. Zhang, Z. Zhou, Y. He, C. Bian, L. Wu, R. Ma, J. Chen, J. Yan, H. Yang, C.-M. Shen, W. Zhou, L. Bao, and H.-J. Gao, "Observation of the Kondo Effect in Multilayer Single-Crystalline VTe_2 Nanoplates," *Nano Letters*, vol. 19, pp. 8572–8580, nov 2019.

[31] B. G. Silbernagel, R. B. Levy, and F. R. Gamble, "Magnetic properties of V_5S_8: An NMR study," *Phys. Rev. B*, vol. 11, pp. 4563–4570, Jun 1975.

[32] M. Mulazzi, A. Chainani, N. Katayama, R. Eguchi, M. Matsunami, H. Ohashi, Y. Senba, M. Nohara, M. Uchida, H. Takagi, and S. Shin, "Absence of nesting in the charge-density-wave system 1T-VS_2 as seen by photoelectron spectroscopy," *Physical Review B*, vol. 82, aug 2010.

[33] A. Gauzzi, A. Sellam, G. Rousse, Y. Klein, D. Taverna, P. Giura, M. Calandra, G. Loupias, F. Gozzo, E. Gilioli, F. Bolzoni, G. Allodi, R. D. Renzi, G. L. Calestani, and P. Roy, "Possible phase separation and weak localization in the absence of a charge-density wave in single-phase1T-VS_2," *Physical Review B*, vol. 89, jun 2014.

[34] A. B. De Vries and C. Haas, "Magnetic susceptibility and nuclear magnetic resonance of vanadium sulfides," *Journal of Physics and Chemistry of Solids*, vol. 34, no. 4, pp. 651–659, 1973.

[35] H. Nozaki and Y. Ishizawa, "An evidence of spin flopping in V_5S_8 by magnetoresistance experiments," *Physics Letters A*, vol. 63, no. 2, pp. 131–132, 1977.

[36] Y. Kitaoka and H. Yasuoka, "NMR investigations on the spin fluctuations in itinerant antiferromagnets. II. V_3S_4 and V_5S_8," *Journal of the Physical Society of Japan*, vol. 48, no. 6, pp. 1949–1956, 1980.

[37] M. Nakanishi, K. Yoshimura, K. Kosuge, T. Goto, T. Fujii, and J. Takada, "Anomalous field-induced magnetic transitions in V_5X_8 (X=S,Se)," *Journal of Magnetism and Magnetic Materials*, vol. 221, no. 3, pp. 301–306, 2000.

[38] H. SCHÄFER, "Chemical Transport Processes as an Aid in Preparative Chemistry. Combination of Transport Reactions with Other Processes," in *Chemical Transport Reactions*, pp. 115–131, Elsevier, 1964.

[39] Y. Oka, K. Kosuge, and S. Kachi, "Magnetic properties of V_5S_8," *Physics Letters A*, vol. 50, no. 4, pp. 311–312, 1974.

[40] H. Nozaki, M. Umehara, Y. Ishizawa, M. Saeki, T. Mizoguchi, and M. Nakahira, "Magnetic properties of V_5S_8 single crystals," *Journal of Physics and Chemistry of Solids*, vol. 39, no. 8, pp. 851–858, 1978.

[41] S. Funahashi, H. Nozaki, and I. Kawada, "Magnetic structure of V_5S_8," *Journal of Physics and Chemistry of Solids*, vol. 42, no. 11, pp. 1009–1013, 1981.

[42] J. Niu, B. Yan, Q. Ji, Z. Liu, M. Li, P. Gao, Y. Zhang, D. Yu, and X. Wu, "Anomalous Hall effect and magnetic orderings in nanothick V_5S_8," *Phys. Rev. B*, vol. 96, p. 075402, Aug 2017.

[43] P. A. Lee and T. V. Ramakrishnan, "Disordered electronic systems," *Rev. Mod. Phys.*, vol. 57, pp. 287–337, Apr 1985.

[44] B. L. Altshuler, D. Khmel'nitzkii, A. I. Larkin, and P. A. Lee, "Magnetoresistance and Hall effect in a disordered two-dimensional electron gas," *Phys. Rev. B*, vol. 22, pp. 5142–5153, Dec 1980.

[45] J. Kondo, "Resistance Minimum in Dilute Magnetic Alloys," *Progress of Theoretical Physics*, vol. 32, pp. 37–49, jul 1964.

[46] T. Ghosh, T. Fukuda, T. Kakeshita, S. N. Kaul, and P. K. Mukhopadhyay, "Concomitant antiferromagnetic transition and disorder-induced weak localization in an interacting electron system," *Physical Review B*, vol. 95, apr 2017.

[47] H.-Z. Lu and S.-Q. Shen, "Weak antilocalization and localization in disordered and interacting Weyl semimetals," *Physical Review B*, vol. 92, jul 2015.

[48] H.-Z. Lu and S.-Q. Shen, "Weak localization and weak anti-localization in topological insulators," in *SPIE Proceedings* (H.-J. Drouhin, J.-E. Wegrowe, and M. Razeghi, eds.), SPIE, aug 2014.

[49] W. Niu, M. Gao, X. Wang, F. Song, J. Du, X. Wang, Y. Xu, and R. Zhang, "Evidence of weak localization in quantum interference effects observed in epitaxial $La_{0.7}Sr_{0.3}MnO_3$ ultrathin films," *Scientific Reports*, vol. 6, may 2016.

[50] S. Sett, K. Das, and A. K. Raychaudhuri, "Weak localization and the approach to metal–insulator transition in single crystalline germanium nanowires," *Journal of Physics: Condensed Matter*, vol. 29, p. 115301, feb 2017.

[51] S. Sasmal, R. Mondal, R. Kulkarni, A. Thamizhavel, and B. Singh, "Magnetotransport properties of noncentrosymmetric CaAgBi single crystal," *Journal of Physics: Condensed Matter*, vol. 32, p. 335701, may 2020.

[52] A. Laha, R. Singha, S. Mardanya, B. Singh, A. Agarwal, P. Mandal, and Z. Hossain, "Topological Hall effect in the antiferromagnetic Dirac semimetal EuAgAs," *Physical Review B*, vol. 103, jun 2021.

[53] Y. Katayama and S. Tanaka, "Resistance Anomaly and Negative Magnetoresistance in n-Type InSb at Very Low Temperatures," *Phys. Rev.*, vol. 153, pp. 873–882, Jan 1967.

[54] D. R. Hamann, "New Solution for Exchange Scattering in Dilute Alloys," *Phys. Rev.*, vol. 158, pp. 570–580, Jun 1967.

[55] S. Kondo, D. C. Johnston, and L. L. Miller, "Synthesis, characterization, and magnetic susceptibility of the heavy-fermion transition-metal oxide LiV_2O_4," *Physical Review B*, vol. 59, pp. 2609–2626, Jan 1999.

[56] Q. Cao, F. F. Yun, L. Sang, F. Xiang, G. Liu, and X. Wang, "Defect introduced paramagnetism and weak localization in two-dimensional metal VSe_2," *Nanotechnology*, vol. 28, p. 475703, oct 2017.

[57] V. Hien-Hoang, N.-K. Chung, and H.-J. Kim, "Electrical transport properties and Kondo effect in $La_{1-x}Pr_xNiO_{3-\delta}$ thin films," *Scientific Reports*, vol. 11, mar 2021.

[58] J. Yin, C. Wu, L. Li, J. Yu, H. Sun, B. Shen, B. A. Frandsen, D.-X. Yao, and M. Wang, "Large negative magnetoresistance in the antiferromagnetic rare-earth dichalcogenide $EuTe_2$," *Phys. Rev. Materials*, vol. 4, p. 013405, Jan 2020.

[59] B. tao Qi, J.-J. Guo, Y. qing Miao, M. zeng Zhong, B. Li, Z. yan Luo, X. guang Wang, Y. zhuang Nie, Q. lin Xia, and G. hua Guo, "Abnormal Magnetoresistance Transport Properties of van der Waals Antiferromagnetic $FeNbTe_2$," *Frontiers in Physics*, vol. 10, apr 2022.

[60] W. Bai, Z. Hu, S. Wang, Y. Hua, Z. Sun, C. Xiao, and Y. Xie, "Intrinsic Negative Magnetoresistance in Van Der Waals $FeNbTe_2$ Single Crystals," *Advanced Materials*, vol. 31, p. 1900246, mar 2019.

[61] V. P. Jovanović, L. Fruchter, Z. Z. Li, and H. Raffy, "Anisotropy of the in-plane angular magnetoresistance of electron-doped $Sr_{1-x}La_xCuO_2$ thin films," *Phys. Rev. B*, vol. 81, p. 134520, Apr 2010.

[62] R. Singha, A. Pariari, G. K. Gupta, T. Das, and P. Mandal, "Probing the Fermi surface and magnetotransport properties of $MoAs_2$," *Phys. Rev. B*, vol. 97, p. 155120, Apr 2018.

[63] J. Wang, J. Deng, X. Liang, G. Gao, T. Ying, S. Tian, H. Lei, Y. Song, X. Chen, J.-g. Guo, and X. Chen, "Spin-flip-driven giant magnetotransport in A-type antiferromagnet $NaCrTe_2$," *Phys. Rev. Materials*, vol. 5, p. L091401, Sep 2021.

[64] T. McGuire and R. Potter, "Anisotropic magnetoresistance in ferromagnetic 3d alloys," *IEEE Transactions on Magnetics*, vol. 11, pp. 1018–1038, jul 1975.

Chapter 8

Summary

We have systematically studied the low-energy electronic structure of $ZrTe_2$ and $ZrSe_2$ using ARPES. ARPES data of $ZrTe_2$ suggest several well disconnected hole and electron pockets at $\Gamma(A)$ and $M(L)$ points, respectively. From the ARPES data of $ZrTe_2$, we realize three holelike non-degenerate band dispersions near the $\Gamma(A)$ point and an electronlike band dispersion at the $M(L)$ point. The experimental observations are in good agreement with the DFT calculations. An equal number of hole and electron carrier density as estimated from our ARPES data suggest $ZrTe_2$ to be a semimetal. In addition, the DFT calculations of $ZrTe_2$ in the presence of spin-orbit coupling suggest a band inversion between Te p and Zr d bands near Γ point, hinting $ZrTe_2$ to be a topological semimetal. On the other hand, from the Fermi surface topology of $ZrSe_2$ we observe only the electron pockets located at $M(L)$ point, while the hole pockets are noticed well below the Fermi level. Our studies on $ZrSe_2$ further suggest it to be a semiconductor with an indirect band gap of 0.9 eV between the $\Gamma(A)$ and $M(L)$ high symmetry points. Also, our calculations demonstrate that the metal-chalcogen bond-length plays a vital role on the electronic structure changes of ZrX_2 (X = Se and Te) in such a way that an electronic phase transition takes place from a semiconductor to a topological semimetal in going from $ZrSe_2$ to $ZrTe_2$.

We have systematically studied the low-energy electronic structure of layered Tantalum ditelluride ($1T'$-$TaTe_2$) using ARPES. We find that the Fermi surface topology of $TaTe_2$ is rather different when compared to the isovalant compounds of $TaTe_2$ such as TaS_2, $TaSe_2$, and the isostructural compound like $NbTe_2$. Interestingly, we realize that the surface electronic structure of $1T'$-$TaTe_2$ has more resemblance to the $2H$-$TaTe_2$, while the bulk electronic structure $1T'$-$TaTe_2$ has more resemblance to $1T$-$TaTe_2$. These experimental observations are systematically compared with DFT calculations performed on $1T$-, $2H$- and $2H$ (monolayer)/$1T$- $TaTe_2$. We further notice that the Fermi surface topology is temperature independent up to 180 K, confirming that $2H$ phase on the top layer is very stable and the CDW order is not due to the Fermi surface nesting.

We have performed an electronic structure study on $NiTe_2$ using ARPES with a photon energy of 21.2 eV. Our ARPES data reveal a surface Dirac point in $NiTe_2$ at a biding energy of 1.45 eV. This observation is in good agreement with earlier predictions of surface Dirac states in TMDCs. Therefore, using ARPES we provide an experimental evidence that $NiTe_2$ is a topological TMDC. Also, we have grown single crystals of $NiTe_2$ and performed electrical transport and magnetotransport measurements. The Debye temperature obtained from our resistivity data using BG fitting is in good agreement with previous reports. Our BG fitting suggests this system is dominated by s-d interband electron scattering. From magnetoresistance measurements we observe a crossover from linear to quadratic dependence of the MR on B.

We have drawn a comprehensive comparison between the transition-metal dichalcogenides VSe_2 and VTe_2 on their electrical transport, magnetotransport, and magnetic properties. We observe the Kondo effect in both systems due to exchange interaction between localized moments and conduction electrons at low temperatures, resulting into a resistance upturn at a Kondo temperature of 6 K for VSe_2 and 12 K for VTe_2. From the field dependent resistance measurements we find that the data is fitted best with a modified Hamann equation corrected by the quantum Brillouin function for VSe_2, while the data is best fitted with a modified Hamann equation corrected by the classical Langevin function for VTe_2. Interestingly, we observe contrasting MR properties between these systems across the Kondo temperature. Both systems show weak ferromagnetism at low temperature due to intercalated V atoms.

We have systematically studied the electrical transport, magnetotransport, and magnetic properties of the V intercalated transition metal dichalcogenide V_5S_8. In this study, we show the Kondo effect in V_5S_8 originated from the exchange interaction between localized moments and conduction electrons. We find isotropic magnetic properties above T_N, while a strong magnetic anisotropy is noticed below T_N. In addition, below T_N we find an out-of-plane ($H \parallel c$) SF transition triggered at a critical field of 3.5 T that is absent for $H \perp c$. Negative MR is noticed in the antiferromagnetic state, while it is negligible in the paramagnetic state. Angle-dependent magnetoresistance is found to be highly anisotropic in the antiferromagnetic state (<27 K).

List of abbreviations

2D 2-Dimensional

AMR Angle Dependent (θ) Magnetoresistance

ARPES Angle Resolved Photoemission Spectroscopy

BG Bloch-Grüneisen

C-CDW Commensurate CDW

CDW Charge Density Wave

CVT Chemical Vapor Transport

DFT Density Functional Theory

DSC Differential Scanning Calorimeter

EDC Energy Distribution Curve

EDM Energy Distribution Map

EDX Energy Dispersive X-ray Analysis

EEI Electron-electron Interaction

FC Field-cooled

FS Fermi Surface

IC-CDW Incommensurate CDW

LEED Low Energy Electron Diffraction

MDC Momentum Distribution Curve

MPMS Magnetic Property Measurement System

MR Magnetoresistance

PL Photoluminescence

PPMS Physical Property Measurement System

SDW Spin Density Wave

SEM Scanning Electron Microscope

SF Spin-flop

SQUID Superconducting Quantum Interference Device

TMDC Transition Metal Dichalcogenide

VSM Vibrating Sample Magnetometer

WAL Weak Antilocalization

WL Weak Localization

XPS X-ray Photoemission Spectroscopy

XRD X-ray Diffraction Analysis

ZFC Zero-field-cooled

List of corrections

1. The publication's status has been changed from "under review" to "published", and its title has been revised to "Observation of Weak Kondo Effect and Angle-Dependent Magnetoresistance in Layered Antiferromagnetic V_5S_8 Single Crystal." Consequently, the list of publications has been rearranged to reflect these updates.

2. Footnote in page number 120 (page number 115 before) of the chapter: Electrical-transport, Magnetotransport, and Magnetic Properties Studies of V_5S_8 Single Crystal is modified as "most of this chapter is published as: I. Kar *et al.*, Solid State Communications **369**, 115209 (2023)."

Corrections recommended by the first examiner:

1. Figure numbers referred in the text are corrected in page numbers 13, 14 of the chapter: Introduction.

2. The heading "topological semimetal" is changed to "topological properties" in page number 15 of the chapter: Introduction.

3. In the chapter: Introduction, descriptions on Dirac fermions, Weyl fermions, Majorana fermions, Dirac semimetal, Weyl semimetal, topological insulator, topological superconductor are added in pages 15-16; descriptions on diamagnetism, paramagnetism, ferromagnetism, antiferromagnetism, ferrimagnetism are added in pages 19-21; descriptions on Kondo effect and Mott insulator are added in page number 23.

4. The misprints are corrected in the thesis.

5. The following sentence is removed from page number 24 (page number 20 before) in the chapter: Introduction, "also, a linear band crossing point is observed from ARPES measurements, indicating a topological nature of VTe_2."

6. The value of vacuum order is corrected in page number 43 (page number 38 before) of the chapter: Experimental details.

7. The following sentence in page number 52 (page number 47 before) of the chapter: Experimental details, "when the current flows through the junction in the absence of applied field, is proportional to the phase difference of the wave functions, is called dc Josephson effect. When the Josephson junction oscillates with a characteristic frequency proportional to the voltage applied across the junction, is called ac Josephson effect" is modified as "a current flows through the Josephson junction even in the absence of applied voltage which is proportional to the sine of the Josephson phase(phase difference accross the junction), it is called DC Josephson effect. When a DC voltage is applied accross the Josephson junction, the current passing through the junction oscillates with a characteristic frequency proportional to the voltage applied across the junction. This phenomenon is known as AC Josephson effect."

8. The difference between s and p polarized light is explained in page number 64 of the chapter: ARPES studies on ZrX_2 (X= Se and Te).

9. The following sentence is added in the caption of Figure 3.5 in page number 70 (page number 65 before) of the chapter: ARPES studies on ZrX_2 (X= Se and Te), "The blue color represents the strength of contributions.".

10. Luttinger's theorem is explained in page number 73 of the chapter: ARPES studies on ZrX_2 (X= Se and Te).

11. The temperature value of sink zone is corrected in page number 82 (page number 77 before) of the chapter: ARPES studies on CDW candidate, $TaTe_2$.

12. Figure number referred in the text is corrected in page number 83 (page number 78 before) of the chapter: ARPES studies on CDW candidate, $TaTe_2$.

13. Figure 4.5 is discussed in page number 87 of the chapter: ARPES studies on CDW candidate, $TaTe_2$.

14. The caption of Figure 5.2 is corrected in page number 97 (page number 92 before) of the chapter: Magneto-transport and ARPES Studies on type-II Dirac semimetal, $NiTe_2$.

15. The equations are rearranged according to the text in page numbers 108, 110, 112 of chapter: Electrical-transport, Magnetotransport, and Magnetic Properties Studies of VX_2 (X = Se & Te) Single Crystals.

16. The equations 6.1, 6.2 are explained in pages 109, 110.

17. The following sentence is added in pages 111 and 113 of the chapter: Electrical-transport, Magnetotransport, and Magnetic Properties Studies of VX_2 (X = Se & Te) Single Crystals, "here, it can be seen that ZFC and FC are identical."

18. The value of q is corrected in page number 113 (page number 108 before) of the chapter: Electrical-transport, Magnetotransport, and Magnetic Properties Studies of VX_2 (X = Se & Te) Single Crystals.

19. The following sentence is added in page number 115 of the chapter: Electrical-transport, Magnetotransport, and Magnetic Properties Studies of VX_2 (X = Se & Te) Single Crystals, "in both systems examined, there is a manifestation of weak ferromagnetism at low temperatures. This phenomenon can be attributed to the presence of intercalated V in both systems. While the chemical composition of VSe_2 displays a deficiency of V or excess of Se, previous studies have established that V^{4+} ions ($3d^1$) carry the localized magnetic moment in these system. In the case of VSe_2, some vanadium atoms are intercalated between the layers of VSe_2, similar to VTe_2, but there is also an excess of Se occupying the interstitial spaces within the crystal structure. Consequently, the overall chemical formula exhibits an excess of Se, which is p-Block element. As a result, this excess Se does not influence the The Kondo effect or magnetic ordering. Kondo effect in V deficient VSe_2 system was reported earlier"

20. The equations are rearranged according to the text in page number 125 of chapter: Electrical-transport, Magnetotransport, and Magnetic Properties Studies of V_5S_8 Single Crystal.

21. List of abbreviations are added to the thesis in page numbers 134, 135.

Corrections recommended by the second examiner:

1. The misprints are corrected in the thesis.

2. The following sentence in page number 25 (page number 22 before) of the chapter: Introduction, "we observe Kondo effect in both systems due to weak ferromagnetic ordering at low temperature..." is modified as "we observe the Kondo effect in both systems due to exchange interaction between localized moments and conduction electrons at low temperature...".

3. The following sentence in page number 26 (page number 22 before) of the chapter: Introduction, "in this study, for the first time, we show Kondo effect in V_5S_8 originated from the antiferromagnetic exchange interactions among the intercalated V atoms below the Néel (T_N) temperature of 27 K" is modified as "in this

study, we show the Kondo effect in V_5S_8 due to exchange interaction between localized moments and conduction electrons."

4. The following sentence in page number 43 (page number 38 before) of the chapter: Experimental details, "...by emitting X-ray of equivalent to the energy difference between the two states" is modified as "...by emitting X-ray, the energy of which is equivalent to the energy difference between the two states."

5. The following sentence in page number 106 (page number 101 before) of the chapter: Electrical-transport, Magnetotransport, and Magnetic Properties Studies of VX_2 (X = Se & Te) Single Crystals, "...Kondo effect induced by the weak ferromagnetism at low temperature" is modified as "...the Kondo effect induced by the exchange interaction between localized moments and conduction electrons at low temperature."

6. The following sentence in page number 115 (page number 110 before) of the chapter: Electrical-transport, Magnetotransport, and Magnetic Properties Studies of VX_2 (X = Se & Te) Single Crystals, "we observe the Kondo effect in both systems due to weak ferromagnetic ordering at low temperatures..." is modified as "we observe the Kondo effect in both systems induced by the exchange interaction between localized moments and conduction electrons at low temperature...".

7. The following sentence in page number 127 (page numbers 122 and 123 before) of chapter: Electrical-transport, Magnetotransport, and Magnetic Properties Studies of V_5S_8 Single Crystal, "in this study, for the first time, we show the Kondo effect in V_5S_8 originated from the antiferromagnetic exchange interactions among the intercalated V atoms below the Néel temperature" is modified as "in this study, we show the Kondo effect in V_5S_8 originated from the exchange interaction between localized moments and conduction electrons."

8. The following sentence in page number 133 (page numbers 129 before) of chapter: Summary of Works, "we observe the Kondo effect in both systems due to weak ferromagnetic ordering..." is modified as "we observe the Kondo effect in both systems due to exchange interaction between localized moments and conduction electrons...".

9. The following sentence in page number 133 (page numbers 129 before) of chapter: Summary of Works, "in this study, for the first time, we show Kondo effect in V_5S_8 originated from the antiferromagnetic exchange interactions among the intercalated V atoms below the Néel temperature" is modified as "in this study, we show the Kondo effect in V_5S_8 originated from the exchange interaction between localized moments and conduction electrons."